THERMO-PHYSICAL AND PERFORMANCE ANALYSIS OF BIO-BASED PHASE CHANGE MATERIAL FOR MEDIUM TEMPERATURE LATENT HEAT THERMAL ENERGY STORAGE APPLICATIONS

Thesis

Submitted in partial fulfillment of the requirements for the degree of

DOCTOR OF PHILOSOPHY

by

RUDRA MURTHY B V

(165009/ME16F13)

DEPARTMENT OF MECHANICAL ENGINEERING

NATIONAL INSTITUTE OF TECHNOLOGY KARNATAKA

SURATHKAL, MANGALURU-575025

JUNE 2022

THERMO-PHYSICAL AND PERFORMANCE ANALYSIS OF BIO-BASED PHASE CHANGE MATERIAL FOR MEDIUM TEMPERATURE LATENT HEAT THERMAL ENERGY STORAGE APPLICATIONS

Thesis

Submitted in partial fulfillment of the requirements for the degree of

DOCTOR OF PHILOSOPHY

By

RUDRA MURTHY B V

(165009/ME16F13)

Under the guidance of

Dr. VEERSHETTY GUMTAPURE

Associate Professor

DEPARTMENT OF MECHANICAL ENGINEERING

NATIONAL INSTITUTE OF TECHNOLOGY KARNATAKA

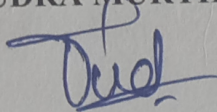SURATHKAL, MANGALURU-575025

JUNE 2022

DECLARATION

I hereby *declare* that the Research Thesis entitled "**THERMO-PHYSICAL AND PERFORMANCE ANALYSIS OF BIO-BASED PHASE CHANGE MATERIAL FOR MEDIUM TEMPERATURE LATENT HEAT THERMAL ENERGY STORAGE APPLICATIONS**," which is being submitted to the **National Institute of Technology Karnataka, Surathkal,** in partial fulfillment of the requirements for the award of the Degree of **Doctor of Philosophy** in **Mechanical Engineering** is a *bonafide report of the research work carried out by me.* The material contained in this Research Thesis has not been submitted to any University or institution to award any degree.

Register Number: **165009ME16F13**

Name of the Research Scholar: **RUDRA MURTHY B.V.**

Signature of the Research Scholar:

Department of Mechanical Engineering

Place: NITK, Surathkal

Date: 20-06-2022

CERTIFICATE

This is to *certify* that the Research Thesis entitled **"THERMO-PHYSICAL AND PERFORMANCE ANALYSIS OF BIO-BASED PHASE CHANGE MATERIAL FOR MEDIUM TEMPERATURE LATENT HEAT THERMAL ENERGY STORAGE APPLICATIONS"** submitted by **RUDRA MURTHY B.V. (Register Number: 165009ME16F13)** as the record of the research work carried out by him, is *accepted as the Research Thesis submission* in partial fulfillment of the requirements for the award of the degree of Doctor of Philosophy.

Research Guide

Dr. VEERSHETTY GUMTAPURE

Associate professor

Department of Mechanical Engineering

National Institute of Technology Karnataka, Surathkal

Chairman-DRPC

Department of Mechanical Engineering

National Institute of Technology Karnataka, Surathkal

Date: 23.6.2022

DEDICATED TO

MY BELOVED

FAMILY MEMBERS

ACKNOWLEDGEMENTS

<div align="right">RUDRA MURTHY B.V.</div>

ABSTRACT

It is well known that present and immediate future policies are focused on reducing fossil fuel consumption and thus promoting renewable energy sources for heating, cooling, and domestic hot water production. Thermal energy storage (TES) is essential to match production and demand and, therefore, provide heat or cold to consumers when required independently of when it was obtained. High energy density TES systems employ phase change materials (PCM) as storage mediums, where thermal energy is mainly stored in the form of latent heat, the so-called Latent heat thermal energy storage (LHTES) system. The most used phase change material today is paraffin. However, paraffin is highly flammable, which limits its applications. Paraffin is also a by-product of fossil fuel which implies that paraffin is a non-eco-friendly material. Only a few existing studies have investigated the thermophysical properties of Bio-PCMs (BPCM) in this detailed manner. The present research on the thermo-physical properties and performance of environmentally friendly and less flammable phase change material for medium temperature latent heat thermal energy storage applications.

Studying the effect of aspect ratio on the PCM characterization in the T-history method (THM). Conventional characterization of BPCM thermo-physical properties and compared the differential scanning calorimetry (DSC) results with the non-conventional THM. Based on the thermo-physical properties, developing the experimental and numerical model of shell and tube LHTES system.

The second fold of this study includes the performance of BPCM in the LHTES system by varying the mass flow rate and inlet temperature of heat transfer fluid (HTF). Adopting the cascaded heat transfer enhancement technique and numerically comparing the proposed tapered geometry performance with the existing cylindrical unit.

Studying the effect of aspect ratio on characterizing the PCMs in the T-history method (THM) concludes that the application of high aspect ratio tubes minimizes the error. Characterizing the BPCM (OM55 and Shellac wax) thermo-physical properties using the

conventional and non-conventional methods, concluding the OM55 and Shellac wax as potential BPCM for medium temperature LHTES applications. Experimental analysis was carried out to study the performance of the shellac wax in a vertical shell-tube LHTES system by varying the mass flow rate and inlet temperature of heat transfer fluid (HTF). The optimum flow rate and inlet temperature were obtained as 4 LPM and 120 °C, respectively, yielding a charging efficiency of 73.4%, discharging efficiency of 62.6%, and maximum reduction in the melting rate of 43.6%. It is evident from the experimental study that shellac wax is a potential bio-PCM for the medium temperature range (60-90 °C) applications.

Further, the numerical comparison of tapered type shell and tube cascaded latent heat storage (CLHS) with that of the existing cylindrical CLHS model. The mean power for the tapered model during the charging cycle is 17.6% higher than the cylindrical, attributed to convection heat transfer's dominance during the melting process. The tapered CLHS model utilizes convection heat transfer effectively by enhancing the PCM's melting rate without additional structural configurations such as fins. Hence, higher energy storage for the same volume is economically justifiable compared to conventional cylindrical CLHS units.

Keywords: *Phase change material, Latent heat thermal energy storage, Bio-based, T-history method, Shell and tube, Cascade, Shellac wax.*

TABLE OF CONTENTS

LIST OF TABLES

LIST OF FIGURES

NOMENCLATURE

Abbreviations

PCM	Phase change material
BPCM	Bio-based phase change material
TES	Thermal energy storage
LHTES	Latent heat thermal energy storage
CLHS	Cascaded latent heat storage
LMTD	Logarithmic mean temperature difference
HTF	Heat transfer fluid
DSC	Differential scanning calorimetry
TGA	Thermalgravimetric analysis
FTIR	Fourier-transform infrared spectroscopy
TCA	Thermal constant analyser
THM	T-history method
DOS	Degree of subcooling

Symbols

A	Area (m^2)
A_S	Constant parameter
A_c	Mushy zone constant
c_p	Specific heat (J/kg °C)
d	Diameter (m)
e	Sensible heat (kJ/kg)
g	Acceleration due to gravity (m/s^2)
H	Enthalpy (kJ/kg)
h	Convective heat transfer coefficient (W/m^2 °C)
k	Thermal conductivity (W/m °C)
l	Length (m)
L	Latent heat (kJ/kg)
m	Mass (kg)
$\dot{m}$	Mass flow rate (LPM)
$\bar{p}$	Mean power (kW)

q	Thermal power (W)
Q	Cumulative thermal energy (kJ)
S	Volumetric heat source term
T	Temperature (K or °C)
t	Time (s)
U	Average overall heat transfer coefficient (W/m^2°C)
v	Velocity (m/s)
$\vec{V}$	Velocity vector

Greek symbols

α	Thermal expansion coefficient (1/°C)
β	Liquid mass fraction
δ	Uncertainty
ε	Porosity
η	Efficiency
μ	Dynamic viscosity (kg/m-s)
ρ	Density (kg/m^3)
γ	Computational constant
Δ	Difference

Other symbols

∇	Laplace operator

Dimensionless numbers

Bi	Biot number
Ra	Rayleigh number
Pr	Prandtl number
Re	Reynolds number
Ste	Stefan number

Subscripts

$1,2,3,4,5$	Axial thermocouple location
A,B,C	Radial thermocouple location
a	Ambient
av	Average

c	Charge
cold	Cold fluid
d	Discharge
f	Final
H	Heat transfer tube
hot	Hot fluid
htf	Heat transfer fluid
i	Instant
in	Inlet
out	Outlet
l	Liquid
L	Loss
M	Melting or Melting peak or Fusion
o	Initial
P or pcm	Phase change material
r or Ref	Reference
S	Freezing or Solidification peak or Crystallisation
s	Solid
st	Stored
t	Tube

CHAPTER-1

INTRODUCTION

1.1. BACKGROUND

Energy is the property and is defined as the capacity to do work. For every work, we need energy. The extraordinary physics statement, i.e., energy conservation law, "Energy can neither be created nor be destroyed; rather, it transforms from one form to another." Sun is the source of all energy directly or indirectly on our planet. The interesting fact was that most energy wasted is in the form of heat energy.

The use of fossil fuels for energy production is easy but raises serious environmental concerns. The effect on the environment is not tolerable for today and in the coming days. According to the international energy agency (IEA, 2018), the current energy supply and demands are unjustifiable. Energy-related carbon dioxide emissions will be doubled by 2050, and fossil energy demand will increase over supplies security. Hence, researchers must investigate materials and systems to ensure energy storage in the domestic sector, transport, and industry to support energy security and climate change goals.

Hence, researchers must go deeper into finding materials and systems to ensure energy storage in the domestic sector, transport, and industry to support energy security and climate change goals.

Considerable efforts have been taken place for the use of solar energy. The use of solar energy is broadly classified as

1) Thermal energy production

   Solar thermal technologies can be utilized for water heating, space heating, cooking, process heat, water treatment, molten salt technology.

2) Electricity production

   Photovoltaic (PV) cells, converting sunlight to electricity directly. However, indirectly solar power to electricity through concentrated solar power (CSP) uses a heliostat and tracking system to focus the broad area of sunlight into a high-density beam.
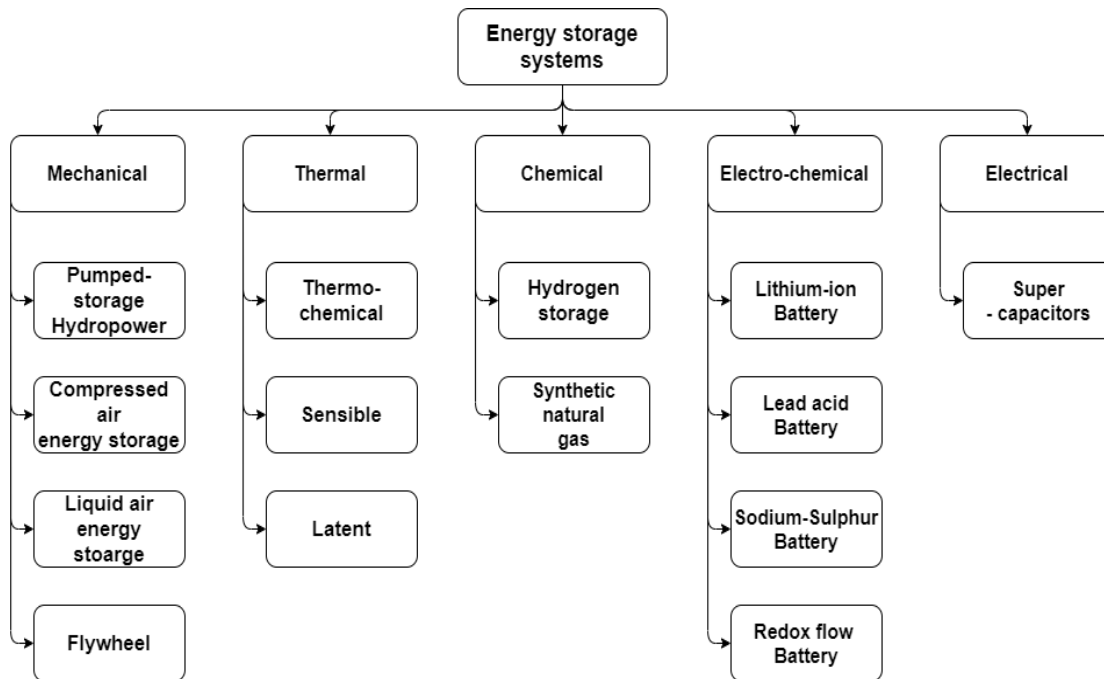
Figure 1.1. Scientific possibilities of energy storage (Source: World Energy Council 2016).

The major drawback of solar energy harnessing as thermal energy is inconsistency or intermittent, i.e., lack of synchronizing between demand and supply of energy production. To overcome the intermittent nature of solar energy harnessing and meet demand and supply, thermal energy storage (TES) is viable. Unlike, we cannot make any change with nature to make it consistent; it's out of our hands for all human beings.

Among the different energy storage technologies, as shown in Figure 1.1. TES arises as a vital technology to reduce the mismatch between energy generation and use daily, weekly, and even seasonal, increasing the potential of implementing renewable energies and reducing the energy peak demand.

TES is a technology that allows storing thermal energy by heating or cooling a storage system. Then stored energy can be used for later applications (heating and cooling) and power production. TES systems were used significantly in buildings, waste heat recovery in industrial processes, and concentrated solar power systems. The demand may often vary throughout the day and also over a year. Thus, the TES system reduces mismatch and facilitates balanced energy demand to provide daily and even seasonal. Additionally, TES declines the peak demand, energy utilization, carbon dioxide emission, and prices.
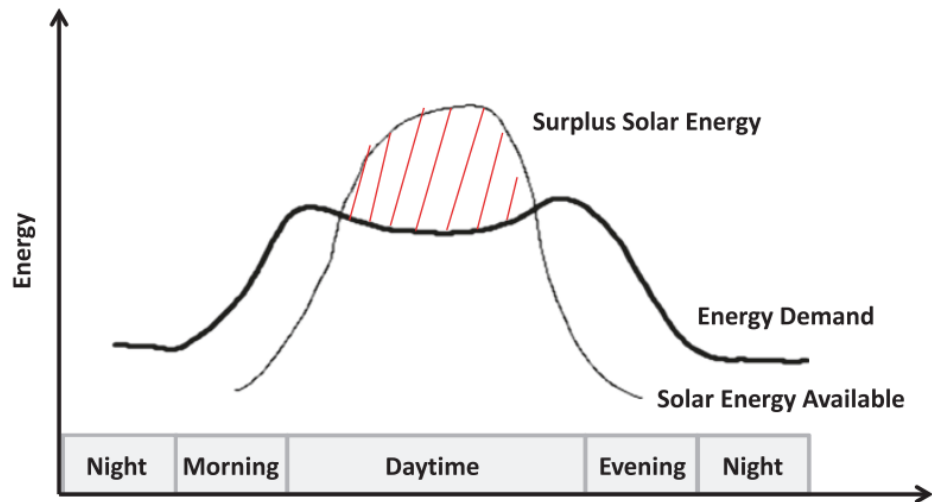
Figure 1.2. TES for solar power plant (Fleischer 2015)

Renewable energy conversion and storage as thermal energy make for more reliable solar energy utilization, as shown in Figure 1.2. TES is appropriate and significant for energy storage combined with the CSP plant for electricity generation even when sunlight is not accessible (Fleischer 2015)

1.2. THERMAL ENERGY STORAGE (TES) METHODS

TES can be stored as a change in the internal energy as sensible heat, latent heat and thermochemical, or a combination. A principal overview of the TES technique is shown in Figure 1.3.

1.2.1 Thermochemical energy storage

In thermochemical energy storage (Liu et al. 2016), the energy is stored through the reversible sorption process or chemical reaction:

$$AB + Heat \Leftrightarrow A + B \tag{1.1}$$

In the endothermic reaction Eq. (1.1), the chemical reactant AB absorbs the solar field's heat. It is dissociated into two products, A and B, which can be stored separately.

$$Q = a_r m \Delta h \tag{1.2}$$

In the reverse process (exothermic reaction), chemicals A and B are put in touch, and the initial reactant AB is formed with a heat release. The amount of heat stored in a thermochemical process is given by Eq. (1.2).
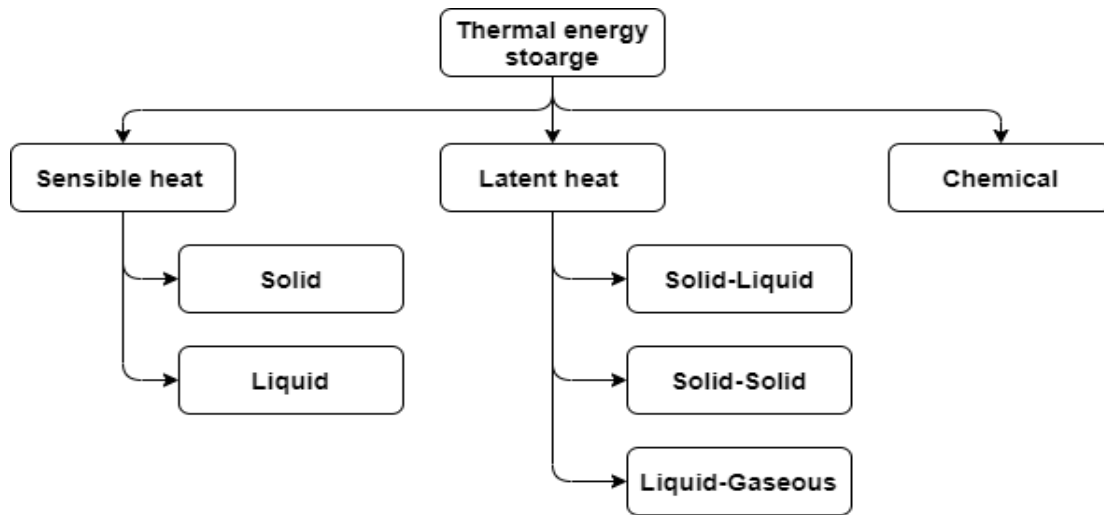
Figure 1.3. Primary techniques of TES (Sharma et al. 2009).

1.2.2 Sensible heat TES

In sensible TES systems, the energy is stored/released by raising/lowering the storage medium's temperature as solid or liquid material. The amount of heat stored as sensible heat is determined by Eq. (1.3), which is a function of specific heat (c_p) of the medium, the temperature change (ΔT), and the mass of storage material (m) (Liu et al. 2016).

$$Q = mc_p\Delta T \tag{1.3}$$

1.2.3 Latent heat TES

The latent heat thermal energy storage (LHTES) is an attractive solution due to its high-energy storage density and the slight difference between storing and discharging functions. LHTES is based on the absorption or release of latent heat when a storage material experiences a phase change from solid-liquid or solid-solid or vice versa. The storage capacity of the LHTES system is given by Eq. (1.4).

$$Q = m\left[c_{sp}\left(T_m - T_i\right) + \varepsilon \cdot \Delta h_m + c_{lp}\left(T_f - T_m\right)\right] \tag{1.4}$$

1.3 PHASE CHANGE MATERIAL (PCM)

PCMs are a class of materials that can store thermal energy in the form of latent heat. The energy is stored in or released out during the phase transition. The phase transition can occur in solid-liquid, solid-solid, and liquid-gas (Figure 1.3). The PCM to be used in the design of thermal-storage systems should possess desirable thermal, kinetics,

chemical, and economical properties as shown in Figure 1.4 (Sharma et al. 2009; "Thermal Energy Storage (TES) Methods" 2010).

1.3.2 Classification of PCM

Based on LHTES, PCMs fall into three categories: solid-solid, solid-liquid, and liquid–gas PCMs (Figure 1.3). Out of them, the solid-liquid PCMs are most appropriate for TES. The solid-liquid PCMs are subclassified as inorganic, organic, and eutectics PCMs (Figure 1.5).

1.3.2.1 Inorganic PCM

The inorganic PCMs like salt hydrates, a crystal matrix of salt and water, once they solidify and possess high latent heat and phase change temperature range from 15 to 117 °C (Lane 1983; Sharma et al. 2004). However, the molten salts are a class of ionic liquids with phase temperature ranges between 250 to 1680 °C (Kenisarin 2010). Many scientists have been extensively investigated salt hydrates as one of the most influential PCM groups and their commercial applications in TES units due to their easy availability and low cost (Sharma et al. 2004).

Salt hydrates like calcium chloride hexahydrate ($CaCl_2.6H_2O$) and disodium sulphate decahydrate ($Na_2SO_4.10H_2O$) are widely accessible and economical. Further, they are exhibit lower thermal expansion during the phase change and comparatively good thermal conductivity in the range of 0.3 to 1 W/m.`K (Lane 1983; Sharma et al. 2004; Zalba et al. 2003). The significant drawbacks of salt hydrates are incongruent melting, a high degree of subcooling (DOS), and corrosive nature that makes it incompatible with the storage container (Abhat 1983; Lane 1983). Metallic alloys are inorganic PCMs with good thermal conductivity and high latent heat, but they have not been considered for commercial usage due to a very high density.

1.3.2.2 Eutectic PCM

Eutectic PCMs mixtures are obtained with phase transition temperatures suitable for specific TES applications by mixing two or more materials. However, there is incongruent melting and phase separation after a particular thermal cycle limited its usage.
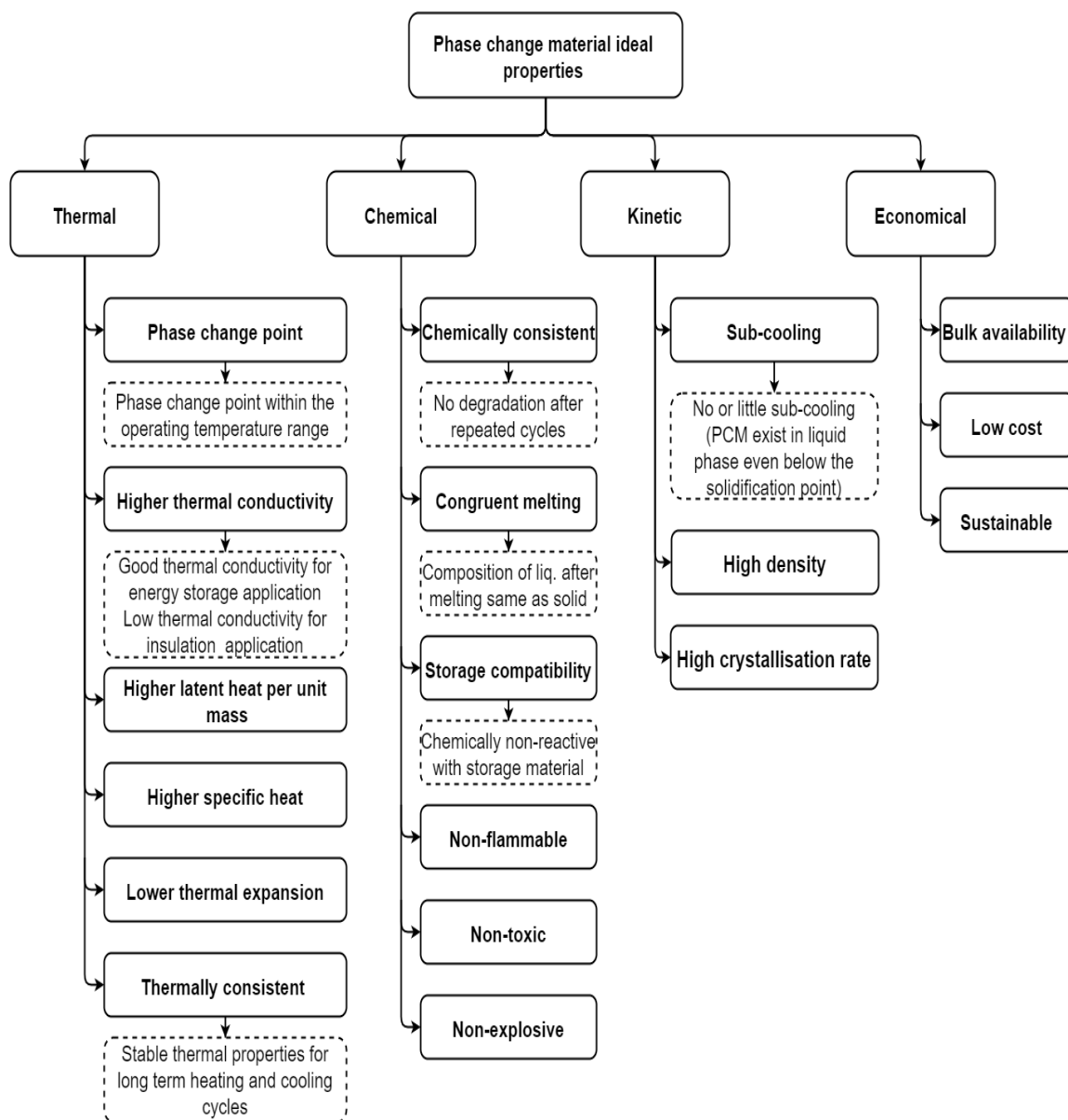
Figure 1.4. Desirable properties of PCMs (Sharma et al. 2009).

1.3.2.3 Organic PCM

Organic PCMs like paraffine are considered one of the most promising candidates due to their high latent heat, the low vapor pressure in the melt, good chemical stability, self-nucleating behavior, safety, and commercial availability at low cost (Shi et al. 2013; Zalba et al. 2003; Zhang and Fang 2006). However, paraffinic PCMs have relatively low ignition resistance compared to non-paraffinic PCMs. Yet, paraffinic PCMs have relatively low ignition resistance, and mainly, it is a fossil fuel by-product, which has geopolitical consequences leading to frequent price variations. The non-

paraffin organic material is also the most prominent classification of PCMs for TES applications. Among these, fatty acids have gained attention recently as they possess good thermophysical and kinetic properties. The general chemical formula of fatty acid is $CH_3(CH_2)_2nCOOH$ (Sharma et al. 2004). Compared to paraffin, fatty acids have a narrow phase transition range, well-defined melting point, lower expansion during phase change, and are thermally stable (Kenisarin and Mahkamov 2007).
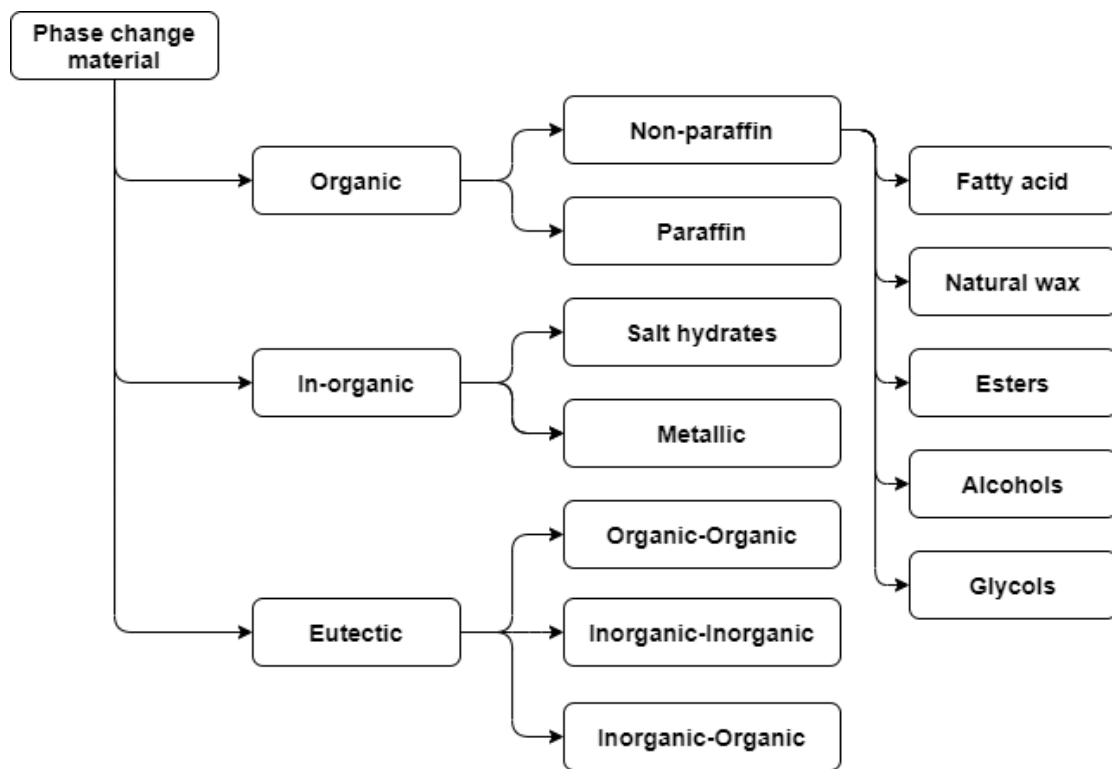
Figure 1.5. An overview of the different types of PCM (Sharma et al. 2009).

Sugar alcohols are a new type of promising organic non-paraffin type PCMs with the general chemical formula of $HOCH_2[CH(OH)]$ nCH_2OH (Mehling and Cabeza 2008); due to their high latent heat capacity and their low-cost availability for TES applications in the temperature range between 100 °C and 250 °C. However, they exhibit subcooling the same as other organic PCMs (Zhang et al., 2014). Esters are natural materials from a carboxylic acid blend with alcohol (Ravotti et al., 2019). Esters are biodegradable and even bio-based if derived from natural feedstock, like alcohols and carboxylic acid. Nonetheless, they are chemically stable and have lower oxidation as compared to other PCMs. Although esters have just been rarely tested, their thermophysical properties are still underway as PCM. There has been no considerable characterization performed on

ester's properties due to their high cost and low availability commercially (Pielichowska and Pielichowski 2014).

Bio-based phase change material (BPCM)

BPCM is an organic non-paraffinic type that contains various fatty acids and esters. It is processed from underused feedstocks, such as soybean oils, coconut oils, palm oils and natural waxes like bee wax, shellac wax, carnauba wax. BPCM is likely to exhibit high latent heat (Figure 1.6), significantly less-flammable and stable properties even after thousands of thermal cycles, without risk of oxidation.
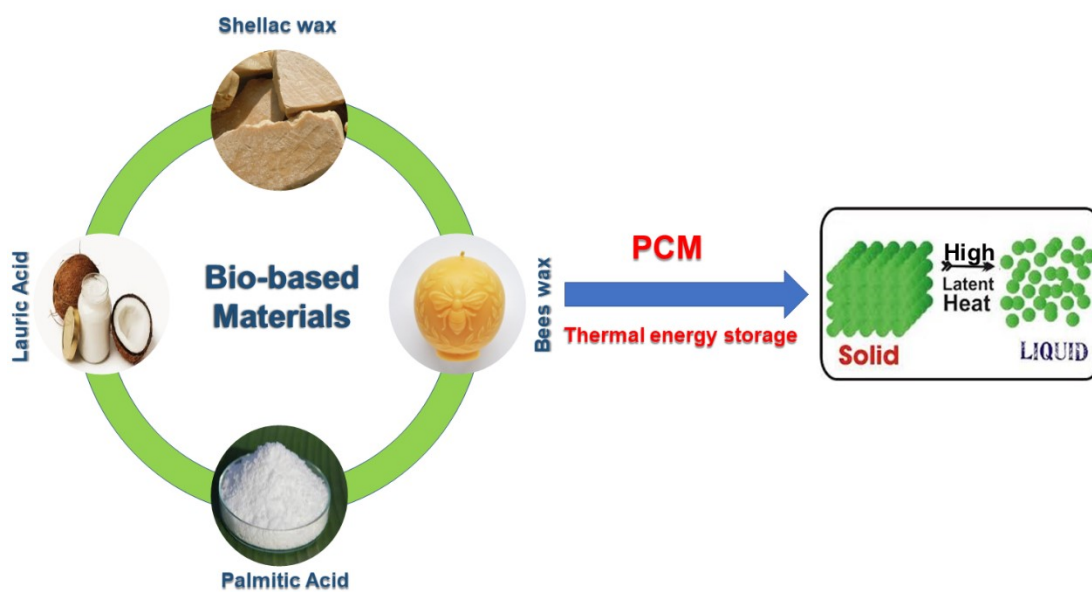
Figure 1.6. Bio-based materials as PCMs for thermal energy storage (Suppes et al. 2003).

1.4. THERMO-PHYSICAL CHARACTERIZATION

Before choosing the PCMs for TES applications, it is crucial to characterize them for efficient design, simulation, and TES system optimization. The properties like melting and solidification temperature, latent heat, specific heat, density, thermal conductivity, and viscosity were essential for the PCM in any TES application. Thorough knowledge of PCM's thermal stability for repeated heating/cooling cycles is vital to ensure long-term performance and economic viability (Shukla et al., 2008). Figure 1.7 shows the various techniques employed for the characterization of PCM for different TES applications.
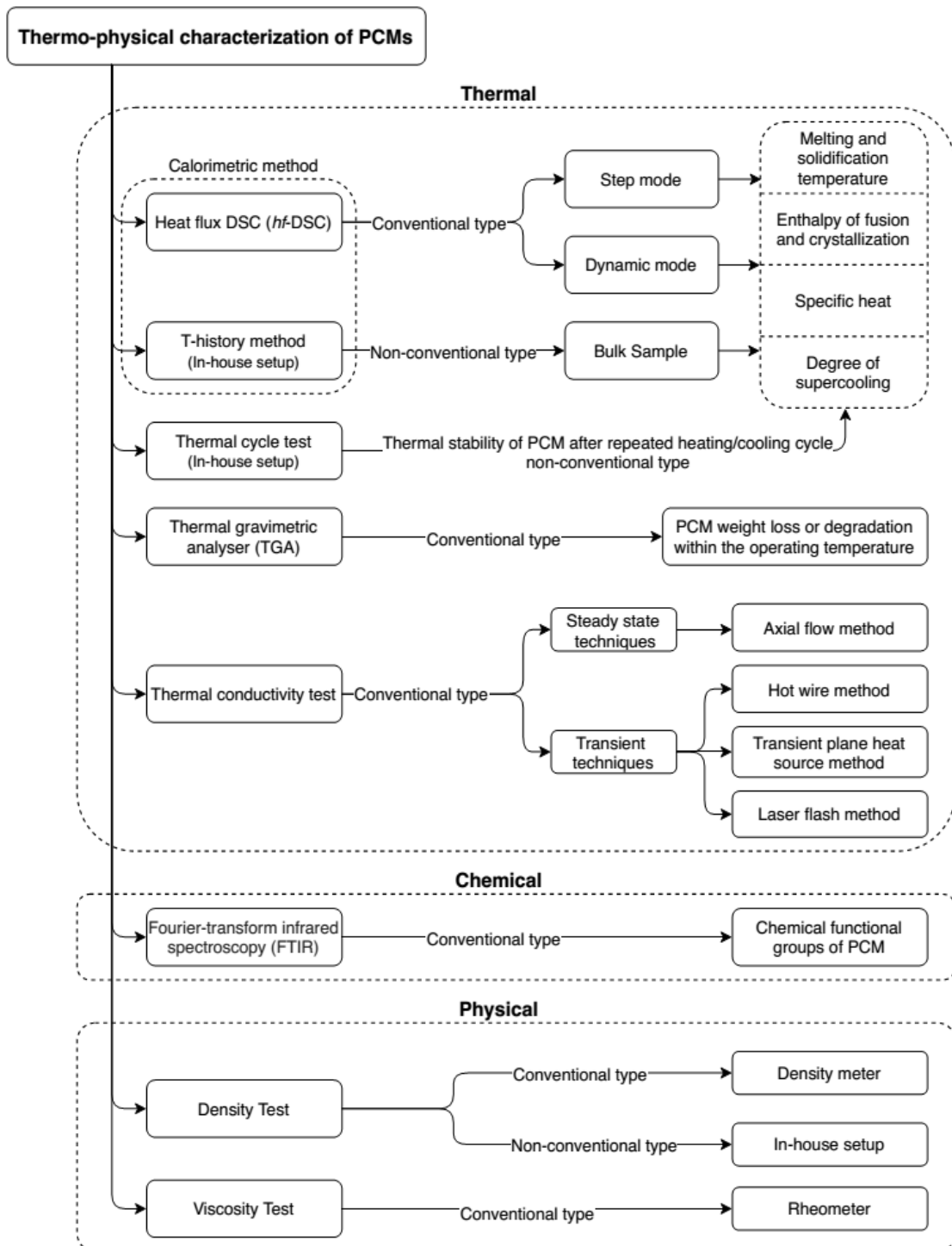
Figure 1.7. Block diagram of various techniques employed for characterization of PCMs (Cabeza et al. 2015).

1.4.1. Differential scanning calorimetry (DSC)

DSC is a conventional type calorimetric method is used to measure the difference in heat flow between sample and reference as a function of temperature. The basic

working principle of DSC is either power compensating or heat exchanging type calorimeters. However, heat exchanging type DSC is commonly used, called heat flux DSC (*hf*-DSC) (Figure 1.8).
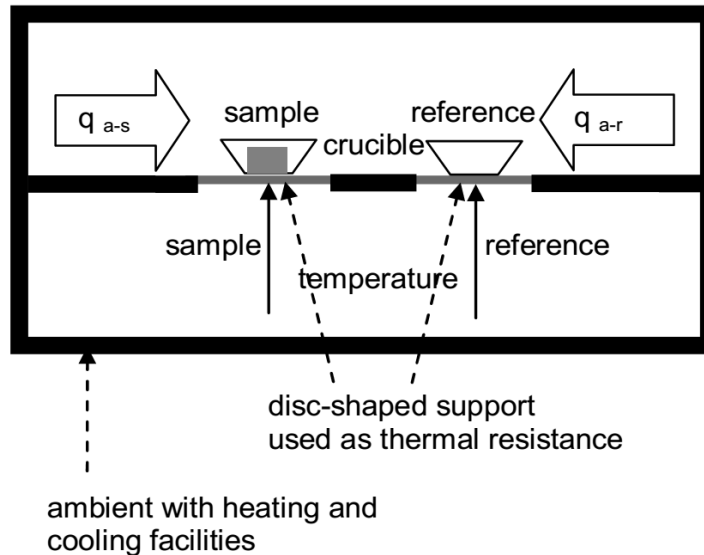
Figure 1.8 Schematic diagram of typical heat flux type DSC (hf-DSC) (Cabeza et al. 2015).

There are different methods to use a DSC in the thermal characterization of PCM. However, the foremost commonly used are the dynamic method and step method.

Dynamic mode

DSC analysis's most commonly used method is ramping temperature at a constant heating rate (Eq.1.5, dynamic method) (Cabeza et al. 2015). A typical heat flow signal and the corresponding temperature program are shown in Figure 1.9.

$$dQ = \frac{dQ}{dT}.dT = C_p.dT \qquad (1.5)$$

The DSC analysis is done mainly in dynamic mode for the determination of melting enthalpy. For TES applications, the total enthalpy value is the sum of both latent heat and sensible heat. However, in this case, the heat flow rate calibration is required to improve the sensitivity, even for small signals. For evaluation of enthalpy, the dynamic mode is performed three times:

➢ Firstly, run with the empty crucible to generate a baseline.

➢ Second, the standard sample's calibration run (sapphire or indium) within the same crucible to generate a standard line.

> ➢ Third, run with the sample (PCM) in the same crucible to generate a heat flow curve function.

PCM's specific heat as a temperature function can be interpreted with DSC software and sapphire as the baseline run's standard material. However, the PCM enthalpy is determined by integrating heat-curve with temperature (Cabeza et al. 2015).
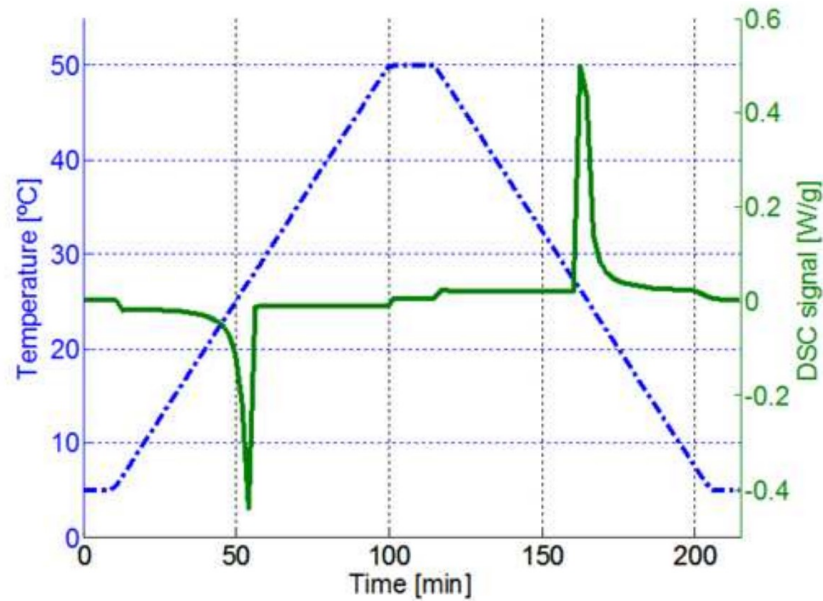
Figure 1.9. Typical DSC heat flow and temperature evolution during a dynamic mode (Barreneche et al. 2013).

1.4.2. T-history method (THM)

A common drawback with most DSC is the less sample mass, typically lower than one hundred microliters. Such small samples don't seem to be appropriate for in-homogeneous materials because the sample isn't representative anymore. Moreover, subcooling revealed during a DSC analysis is also not characteristic for larger samples. Thermal properties evaluation of an in-homogeneous, higher sample mass and different PCMs simultaneously is facilitated in the THM.

The THM is non-commercial but used as an in-house experimental setup for the PCM's thermal analysis (TA). (Yinping and Yi 1999) first proposed the THM as a calorimetry method in 1999, but later on, (Marín et al. 2003) recommended a new data assessment that lifted this method to the TA group. The T-history methodology could be a straightforward and economical approach for the PCM thermal analysis. Its origin lies within the evaluation of phase diagrams. When the PCM sample is set to cool down,

and its temperature history (T-history) curve is interpreted, as shown in Figure 1.10, any changes in its thermal properties indicate that heat release can end a change in temperature history. For example, the latent release during the cooling run ideally results in a constant sample temperature until the phase change.
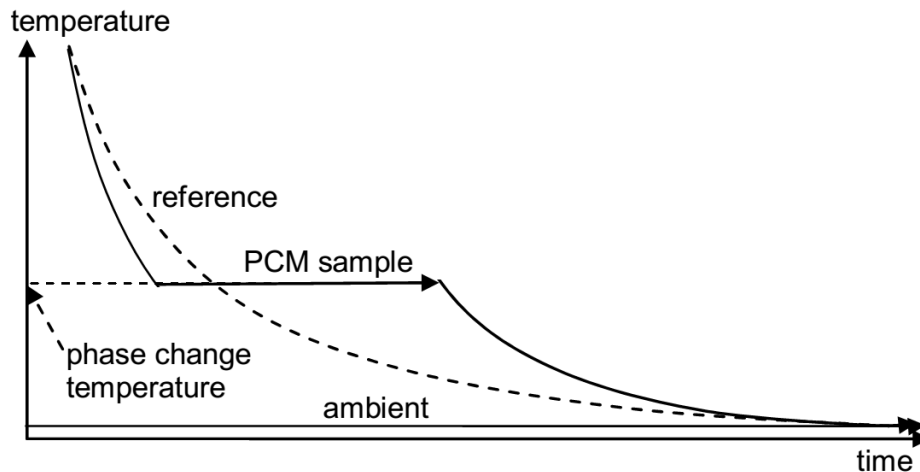
Figure 1.10. T-history cooling of a PCM and reference sample with a latent heat and only sensible heat release, respectively, at constant ambient temperature (Cabeza et al. 2015).

1.4.3. Thermal conductivity test

The period of heat stored/released by the PCM is the characteristics of thermal transport properties like thermal conductivity and diffusivity. Hence the thermal conductivity measurement is significant for the characterization of both PCMs and composite PCMs. No unique method can be used effectively to calculate the thermal conductivity of all forms of PCMs, as stated in (Joulin et al. 2011; Yavari et al. 2011). So thermal conductivity measurement is broadly classified into two primary methods: Steady-state techniques and transient techniques. Steady-state methods, commonly used as axial flow approaches, require steady-state conditions around the sample to be accomplished, taking a much longer duration and correct measurement of the thermal resistance between the specimen, sensors, and sources heating (Franco 2007). However, the transient method operates by monitoring the temperature response at a constant heat pulse supplied to the specimen initially in thermal equilibrium and obtaining effective thermal diffusivity. Well-known approaches are the hot wire method, transient plane heat source, and laser flash methods.

1.4.4. Thermogravimetric analysis (TGA)

The TGA is a group of thermal analysis techniques used to assess the change in the physical and chemical properties of the PCMs. To calculate the PCM mass loss, the TGA is typically carried out as a function of temperature increase with a constant heating rate. TGA can also investigate physical phenomena like vaporization, second-order phase transition, desorption, etc., and chemical processes like decomposition and dehydration. The TGA can easily measure the PCM specimen mass loss or gain due to degradation, oxidation, and loss of volatile compounds. The PCM's thermal stability or resistance towards degradation can also be calculated using the standardized TGA method.

1.4.5. Fourier transform infrared spectroscopy (FTIR)

FTIR is a technique for obtaining the absorption or emission spectrum of a solid, liquid, or gas in the infrared. High-resolution spectral data are acquired simultaneously by an FTIR spectrometer over a sizeable spectral scale. FTIR involves many kinds of measurement techniques, such as diffuse reflection (K-Br pellet method) and the technique of attenuated total reflection (ATR). It is vital to choose the methodology used according to the sample type. However, the K-Br pellet method has become widely used as FTIR has become more general. Attenuated total reflection (ATR) is a technique that enables powder samples to be measured directly. FTIR is used to check the chemical structure, ensuring the PCM's chemical stability before and after the thermal cycling tests.

1.4.6 Density and Viscosity test

The PCM sample density is evaluated by standard density meters and non-conventional methods like pycnometer or volume displacement using graduated pipettes sealed at the bottom. A standard rheometer evaluates the rheological behavior of PCM and composite PCMs.

1.5 PCM HEAT TRANSFER ENHANCEMENT TECHNIQUES

Large numbers of PCMs melt and solidify at a wide range of temperatures, making them attractive in several applications in the development of energy storage systems. Many organic and inorganic materials can be identified as PCM with their melting

temperature and latent heat of fusion. However, as discussed earlier, most PCMs do not satisfy the criteria required for adequate storage media except for the melting point in the operating range. Since no PCMs should have all the necessary properties for an ideal thermal storage medium, the materials available must be used to improve the insufficient physical property, i.e., heat transfer enhancement, as shown in Figure 1.11.
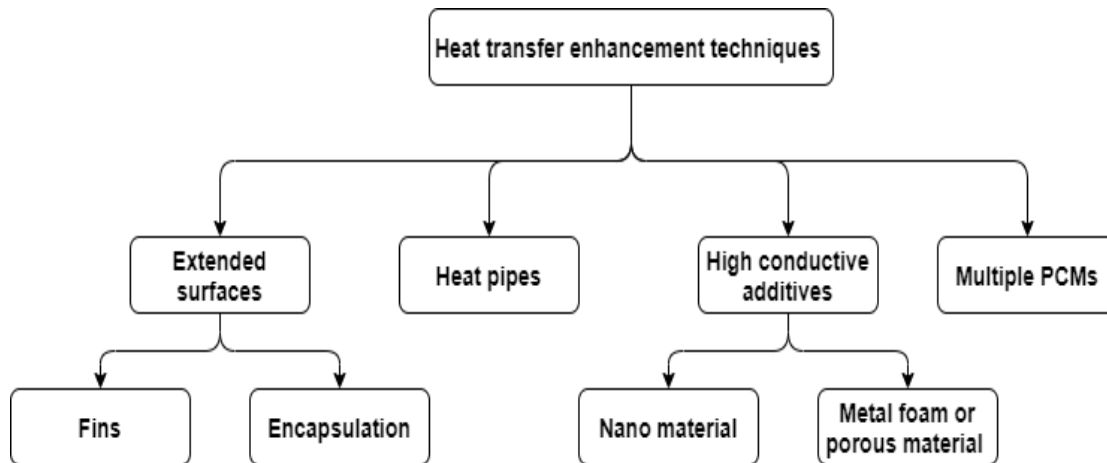
Figure 1.11. PCM heat transfer enhancement techniques.(Nasiru et al. 2017).

For example, the extended surface like fins, heat pipes, and multiple PCMs of different melting points can boost heat transfer between the PCM and HTF. Another critical choice for improving the overall thermal efficiency of LHTES systems is improving the thermal conductivity of PCMs. The thermal conductivity of PCMs can generally be enhanced by integrating high thermal conductivity porous materials, the dispersion of nanoparticles, and the dispersion into the base PCM of low-density materials.

1.6 APPLICATION OF PCM

The use of PCM in various TES applications is discussed in this section. PCM can reduce the cost of operation, volume, and capability of many systems where TES is employed. In achieving an effective and environmentally sustainable climate, PCM can play a significant role. Energy use in different types of areas. CO_2, SO_2, and NOX emissions from greenhouses using PCMs for TES can be reduced by up to 40 % (Dincer and Rosen 2001). Furthermore, PCMs in TES systems can achieve energy savings of 50% (Oró et al. 2012). PCM's various cooling and heating applications for low and medium operating temperature ranges as shown in Figure 1.12. The applications of

phase change materials in the medium range temperature from 40 °C to 90 °C, where PCMs are used in solar air heaters, solar stills, and solar domestic hot water systems for heating purpose and in electronic devices for cooling and operational performance improvements.
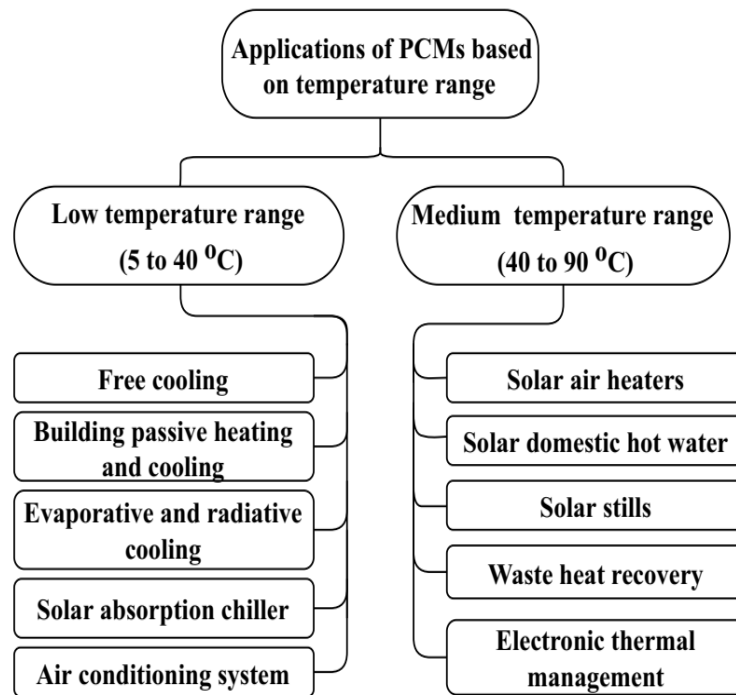
Figure 1.12. Applications of PCM based on the temperature range (Kun du et al. 2018).

The use of PCMs in a solar air heater increases the efficiency by 16-20% daily (Aymen et al. 2016). Integrating the PCM inside the evacuated tube collector along the heat pipe improves the efficiency by 26% for normal operation and 66% for stagnation mode compared to the standard solar water heater (Felnski and Sekret 2016). Solar still with external LHTES increases the freshwater productivity up to 140% higher than the conventional solar still (Faegh and Shafii 2017).

1.7 ORGANIZATION OF THE THESIS

This thesis has been divided into nine chapters. The introduction about the importance of TES and its classifications, the significance of BPCM over paraffinic PCM, desired properties, characterization methods, and PCM application based on the temperature range given in chapter 1. The review of literature pertaining to the present work is outlined in chapter 2. It also includes the objective and scope of the work undertaken.

The selection of BPCM, preparation, and methods used to study the thermophysical properties of BPCM have been highlighted in chapter 3. Chapter 4 highlights the effect of the tube aspect ratio in the THM on the subcooling and solidification behavior of PCM compared with the DSC. Thermal property study of the fatty acid mixture (OM55) as BPCM and significance of PCM isothermal enthalpy change over the non-isothermal have been discussed in chapter 5. Thermo-physical properties of natural shellac wax as novel BPCM are presented in chapter 6. Chapter 7 detailed the experimental investigation of shellac wax for medium-temperature LHTES applications. The numerical heat transfer performance analysis of tapered type shell and tube cascaded latent heat storage (CLHS) and the conventional cylindrical CLHS model emphasizes melting rates and slowest melting portions(bottom) of the shell and tube unit. The highlights and conclusion of the present study and suggestions for future work are given in chapter 9.

1.8 CLOSURE

In this chapter, the background and the motivation of the present research work have been discussed. Broad outlines of the organization of the thesis and salient features of the individual chapters have also been highlighted.

CHAPTER-2

LITERATURE REVIEW

This literature review contains five sections to know the complete idea about different aspects of work that has been done on TES. Section 2.1 of this literature review discussed the work carried out on LHTES. Section 2.2 presents a discussion on the different bio-based materials as PCMs. Section 2.3 reviews the different techniques available for the characterization of PCMs. While section 2.4 asses the experimental and numerical works on PCMs. Finally, section 2.5 presents the heat transfer optimization of PCMs.

2.1 LATENT HEAT THERMAL ENERGY STORAGE (LHTES)

The latent heat thermal energy storage (LHTES) type is more efficient than other storage systems due to its high energy storage density and less volume capacity at an almost constant temperature. By implementing proper PCMs, energy could be stored upon blackout periods and converted into electricity using photovoltaic or thermophotovoltaic converters. The most efficient way to improve the energy density and conversion efficiency of LHTES devices is to increase their operating temperature by applying high melting point PCMs.

Wang et al. (2012) performed a comparative study of a sensible and LHTES system for concentrated solar power applications. Developed the numerical model of both sensible TES system with liquid solar salt as the sensible storage material and latent heat TES system with sodium nitrate as PCM and then numerically simulated. The results indicated that the latent TES system's energy density is much higher than the sensible TES system with a faired charging /discharging rate.

Jose Pereira da Cunha and Philip Eames (2016) reviewed a PCM study with a phase-changing temperature between 0-280 °C and the design of an indirect latent heat storage unit with a feasible heat transfer enhancement technique. It is reported that PCM can store a large amount of energy within a fewer temperature range than the sensible thermal energy storage material. Its geometrical flexibility encapsulated system seems to be more since it can be attached to any existing system without significant technical modification. The compact design makes the enhanced isothermal stage more

beneficial due to its higher PCM volume ratio. However, heat transfer enhancement is vitally essential to obtain nominal thermal power.

Agyenim et al. (2010) reviewed the work that has been carried out to study the heat transfer characteristics, enhancement technique adopted in PCMs for efficient charge and discharge of the thermal energy, geometry, and configuration of the PCM container. Furthermore, this paper reviewed various numerical and experimental models studies to verify the effect of HTF flow rate and inlet temperature on the LHTES system's performance. The most commonly used geometry was the shell and tube type since heat loss is minimal. Most of the studies reported on PCM have repeated low thermal conductivity. Regarding heat transfer in PCM, numerical methods could be an excellent approach to solving the phase transition problem.

Vyshak and Jilani (2007) developed the numerical model. They studied the performance of three LHTES units of different geometric configurations: shell and tube, rectangular and cylindrical having the same volume and surface area of heat transfer. They reported a comparative study of the melting behavior of a PCM packed in three units. Obtained results indicated that the shell and tube unit stored equal amounts of energy in the least possible time and increased the PCM mass. This configuration influence is more pronounced to improve the heat transfer exchange during melting.

Fang and Chen (2007) studied the theoretical and numerical model to examine a shell and tube LHTES performance with integrated multiple PCMs. The model was developed using the enthalpy method. Numerical investigations were performed to check the numerous PCM's effects on melting fraction, stored energy, and HTF outlet temperature. However, PCMs volume fraction and melting temperature play a vital role, but the proper selection of multiple PCM is essential for LHTES performance improvement.

Li (2015) performed the LHTES system's energy analysis by considering the various parameters influenced on latent TES, including HTF mass flow rate, inlet temperature, PCM melting temperature, subcooling, storage unit dimension, and additives to enhance the thermal conductivity. The study result reported that

- The heat transfer rate and energy stored increase with an increase in the HTF mass flow rate. But energy efficiency declined due to the immense pressure drops, which signifies that the rise in the mass flow rate of HTF is largely irreversible.

- The total stored energy and the heat transfer rate increase as the HTF inlet temperature and PCM unit temperature increase while entropy generation increases.

- Imparting high thermal conductivity particles in the PCM's causes remarkable improvement in energy and exergy performance. But careful assessment is required for increasing the volume fraction of additives. Because increased additives particles decrease the volume occupied by the PCM, leading to lesser amounts of stored energy.

- The time required for the same mass of the PCM and heat transfer surface area to store an equal amount of energy is less in a cylindrical shell container compacted to the rectangular container. Increasing the tube length increases the total stored energy.

- Entropy generation can be investigated from two aspects: heat transfer and pressure drop irreversibility, and there exist the optimum for tube length.

- The efficient design and improvement in heat exchange surface positively affect energy and exergy performance. Overall energy efficiency is always greater with sensible heating before melting the PCM and subcooling after the solidification.

- The effect of reference temperature on energy performance has been more influenced than energy performance.

Sharma et al. (2009) reviewed TES with PCM. They discussed its application like the solar water heating system, solar air heating system, cooking, HVAC for building, off-peak electricity storage, and storage system for water heat recovery. A latent heat system using PCM's is an effective way of storing thermal energy. Also, it has the benefits of high energy storage density and the isothermal characteristic of storage problems. Their study also reviewed some identified PCM used in many applications for a storage system with different heat exchanger containment materials.

Al-Abidi et al. (2013) reviewed the computation fluid dynamics (CFD) applications for the LHTES system. Due to its high energy density per unit volume at a nearly constant temperature, the LHTES system gained more attention than other TES systems. This

paper reported various numerical studies of PCMs using commercial CFD software and self-developed coding to study the heat transfer behavior in PCM. The commercial software FLUENT CFD solver has been successfully adopted to simulate much PCM thermal behavior in various engineering applications. The comprehensive study reported that the CFD model of the LHTES system is supposed to be a smart way to save money and time and optimize the efficiency in solar thermal energy applications.

2.2 BIO-PCM (BPCM)

BPCM is naturally available materials derived from organic fatty acid esters, such as Soy, Palm, Sunflower, Coconut, Shellac, and Beeswax. These bio-based materials could absorb the thermal energy during melting and release the stored energy when freezing in the form of latent heat, similar to the conventional Paraffin PCM. The BPCM advantage was less flammable and eco-friendly compared to conventional PCM. Except for non-flammability, other properties of BPCM were similar to the paraffinic PCM. Over the past years, few researchers have attempted to characterize and develop the BPCM.

Suppes et al. (2003) studied Stearic, Palmitic, and Oleic fatty acid's thermal behavior to comprehend the solid-liquid transition and develop new BPCM from natural compositions. Synthesized the methyl and ethyl esters by esterifying fatty acid with methanol or ethanol using sulphuric acid as a catalyst at 55-60 °C for 4-5 hours and then characterized this derived triglycerides and alkyl esters from DSC. Results reported that Alkyl esters (purity > 90) and methyl palmitate (purity < 90) performed well and exhibited stable characteristics. This ester had latent heat comparable to paraffin PCM (~200 J/g) with absorbed and released the heat over a short temperature range. The problem reported that triglycerides in the PCM application were polymorphic. Their conclusion reported that it is possible to convert fats and oil into useful BPCM in high yield.

Putri et al. (2016) studied coconut oil thermal behavior and its possibility as PCM in the TES system. The application of coconut oil (CO) as potential material for room air conditioning system since its phase transition temperature range was just around the human thermal comfort zone. The THM was used to evaluate thermal properties like the specific heat of solid and liquid and the latent heat of coconut oil. A thermal

chamber of volume 0.64 m^3 was developed with two layers of 6 mm thick cement board, and 20 mm styrofoam as an insulator in between the thermal chamber was isolated entirely from the surrounding. They examined the amount of heat absorbed by CO in the thermal chamber, which is already heated by the 100 W bulb lamp. Results indicated that CO is a potential candidate for TES in building ventilation and air conditioning systems and reducing peak demand in electrical consumption.

Dinker et al. (2017) developed the rectangular shell with the helical tube LHTES model and studied beeswax experimentally. DSC analysis was performed to know the melting and solidification point as well as latent heat. At the same time, TGA was used to examine the material degradation temperature and residue after degradation. It was reported that the melting and freezing point was found to be 59.8 °C and 56.4 °C, respectively, and the latent heat of beeswax is 214 J/g for the temperature range 30.8 - 68 °C. TGA reported that beeswax starts and completes the degradation between 215 - 443 °C. The thermal constant analyzer measured beeswax's thermal conductivity as 0.29 W/m·°C for solid and 0.3 W/m·°C for liquid. They developed a shell and tube LHTES system and studied the beeswax thermal performance at a different HTF flow rate (0.25-1 LPM) and inlet temperature (60 °C, 70 °C, and 80 °C). Experimental results reported that the maximum efficiency of the LHTES system was 84% at a flow rate of 0.5 LPM and inlet temperature of 80 °C. It was concluded that the application of beeswax as a potential BPCM for lower temperature LHTES systems like temperature-controlled buildings, solar water, and air heaters.

Hu and Yu (2014) studied the thermal and mechanical characteristics of encapsulated BPCM with polyurethane (PU) nanofibers. SEM's characterization results reported that the electrospinning technique produced uniform core-shell and fiber morphology and homogeneous distribution of soy wax throughout the core fibers. Thermal analysis indicated that the enthalpy increased as the wax content increased with stable charge and discharge properties. Furthermore, this composite BPCM exhibited unaltered thermal properties even after 100 thermal cycles had been reported.

Cellat et al. (2015) studied fatty acid as BPCM by incorporating it into concrete to enhance its thermal property. Their study intended to utilize the naturally available fatty acid BPCM to improve building materials' thermal storage capacity. They developed

and tested two binary mixtures of capric acid-lauric acid and capric acid-myristic acid, a potential candidate for building application. The thermal and mechanical analysis was carried out and reported that both binary mixtures were thermally and chemically stable. The heating capacity recorded was 109 J/g and 155.4 J/g, with the degradation of both binary mixtures, started at 120 °C. The mechanical test reported a 12% reduction in compressive strength by adding 1 wt% of binary mixtures. This study concludes that both fatty acid binary mixtures were more suitable for self-compacting concrete used in building applications. Still, the optimum mixing ratio should be followed to maintain the compressive strength of the concrete mixture.

Zheng et al. (2011) analyzed four insect waxes thermal characterization using DSC and compared paraffin and carnauba wax. It was indicated that the melting point of the four insect waxes was varied at 90.4 °C of coccerin as the highest, 70.3 °C of beeswax as the lowest, and 86.5 °C of white insect wax, 83.8 °C of shellac wax. All of the four waxes were higher with the melting point than paraffin (63.3 °C), and the coccerin's melting point was even higher than that of carnauba wax (87.8 °C). The melting enthalpy of insect waxes ranged from 168.1 to 203.2 J/g, so did the crystallization enthalpy at 166.9 to 198.8J/g. The thermal analysis concludes that insect wax was reliable thermal properties.

2.3 THERMO-PHYSICAL CHARACTERIZATION OF PCM

For an LHTES unit's performance by simulation and practical application, it is requisite to characterize the PCM thermophysical properties like transition temperature, latent heat, specific heat, thermal conductivity, viscosity, and density as a temperature function (Lazaro et al. 2013).

Thermal analysis (TA) and calorimetric techniques were both used to evaluate the PCMs properties, such as phase-change temperature (T_m) and enthalpy (h_m), and specific heats (c_p). TA differs from calorimetry since the former investigates a sample's behavior as a temperature or time function. In contrast, calorimetry is based on recording the temperature or heat of a sample when heating/cooling as a function of time. DSC is within these two concepts, as the output property is the heat flow as a function of both time and temperature, considered a TA technique (Solé et al., 2013).

2.3.1 Conventional thermal analysis (TA)

Table 2.1 shows a comparison of four standard TA methods. The most used PCM study methods were DSC, Differential thermal analysis (DTA), and TGA. Yet, other techniques exist and are under improvement even though they are not commercially available as a THM. T-history first started as a calorimetry method but proposed a new data assessment, which lifted this method to the TA group (Marin et al., 2003).

Yinping and Yi (1999) first proposed the THM in 1998 for determining the thermophysical properties of PCMs. Compared to the conventional calorimetric method: DTA and DSC method, T-history has to be an in-house calorimetric method, and it has significant features: simple experimental setup, able to measure the transition temperature, the heat of fusion, specific heat and thermal conductivity of different samples of PCMs simultaneously and visually can observe the phase transition process.

Table 2.1. Comparison of four standard thermal analysis(TA) methods (Sole et al. 2013)

	TGA	DTA	DSC	T-history
Sample size(mg)	10-150	10-150	1-50	15,000
Measurement time (min)	100	100	100	40
Maintenance	++	++	++	+
Equipment price	++	++	++	+
Thermo physical properties	-%sample mass loss $f(T,t)$	$-\Delta T\ f(T,t)$ -h $f(T,t)$	$-c_p\ f(T,t)$ -h $f(T,t)$ $-T_m$	$-c_p\ f(T,t)$ -h $f(T,t)$ $-T_m$, - k

Reported the procedure to find the latent heat, specific heat, and thermal conductivity with the assumption of uniform heat transfer within the PCM (Bi<0.1). The ratio of the length to the diameter of a tube is larger than 15 to assume heat transfer in the radial direction only. Initially, the reference and sample tube temperature was maintained greater than the PCM melting temperature. Further, monitor the sample's and reference tube cooling temperature in a controlled chamber by a thermocouple and data acquisition system (DAQ) connected to a computer to plot the T-history curve shown in Figure 2.1.

The thermophysical properties of PCM and the error that occurred during the experiment are also discussed. Results reported that the relative deviations between the measured and those in the literature values are less than 10% and concluded this method is helpful for rapid measurement of PCMs for use in engineering applications of LHTES. Various improvements in the THM have been proposed as follows.
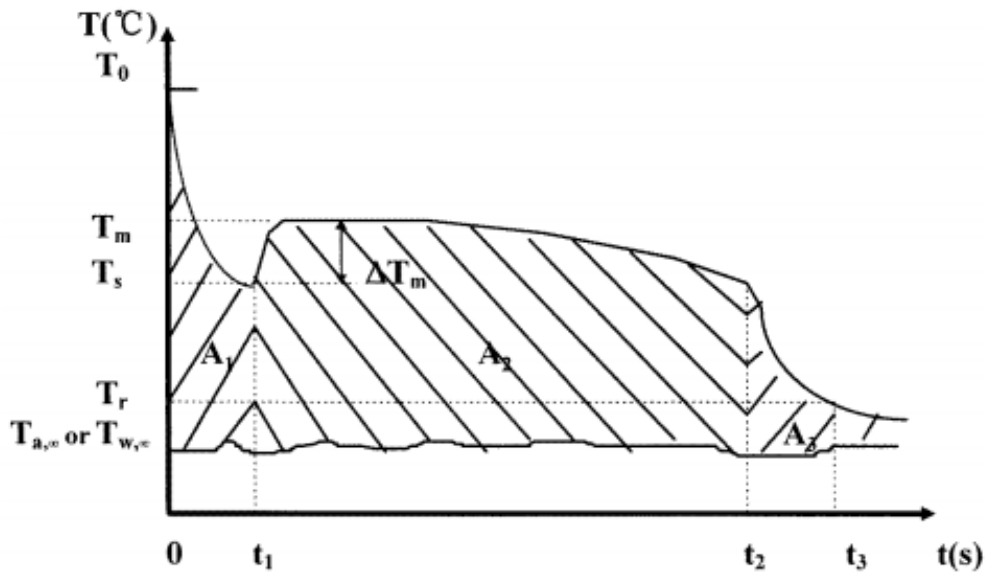
Figure 2.1. A typical T-history curve of a PCM during a cooling process (with subcooling) (Yinping and Yi 1999).

Marin et al. (2003) further improved the THM to determine the temperature-dependent properties. They included the variation of enthalpy and its relationship with the temperature, as shown in Figure 2.2. The proposed enthalpy curve was very appropriate for the impure or inhomogeneous material, for which transition enthalpy was not clearly defined. They discussed the error that occurred in their study. They suggested experimental improvements—reported that it is possible to obtain both properties and enthalpy curves simply with this method.

Hong et al. (2004) made a reasonable modification to the original THM and reported the procedure to increase the enthalpy evaluation accuracy. However, they considered the inflection point the boundary between phase change and solid-state; the temperature keeps constant or drops gradually with the latent heat release but decreases exponentially in the cooling process accompanying sensible heat alone.
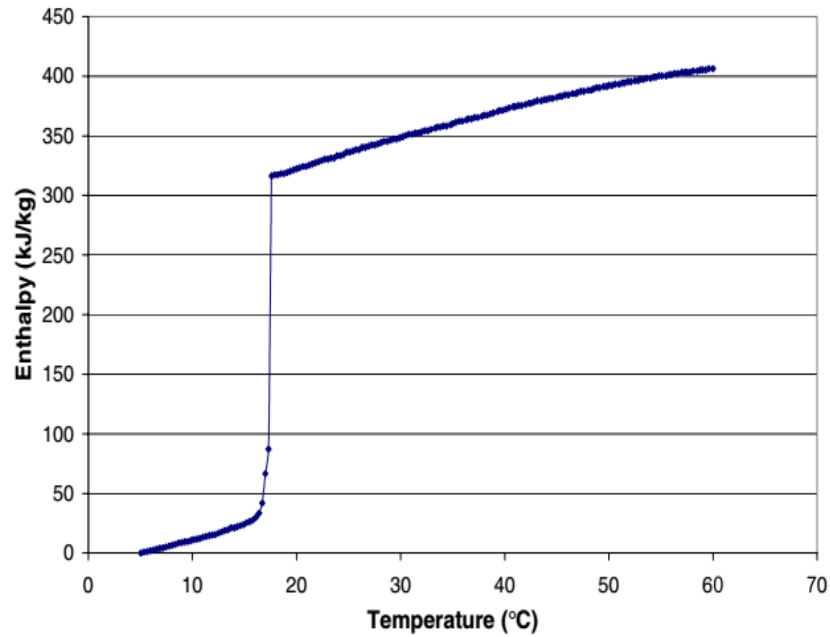
Figure 2.2. Enthalpy–temperature curve (Marin et al. 2003).

Also considered is the volumetric change of PCM in the solidification process. The conclusion of this modified THM reported that results were in good agreement with the DSC within 4%.

Lazaro et al. (2006) verified the THM using standard material water, indium, and hexadecane. They were, however, tested with two commercial PCM RT27 (Rubitherm^{TM}) and sodium acetate trihydrate. Results reported that T-history could be used to analyze different PCMs. Kravvaritis et al. (2010) suggested the improvements to the THM referred to the experiment setup, measurement processing, and presentation format of the final result. The study indicated that PCM property evaluation depends on the temperature and cooling rate. Therefore, the correctness of PCM properties in any particular application can be secured only by repeating the measurements under the application's thermal conditions. Table 2.2 further briefly reviewed the works that have been done on PCM characterization using the THM.

Table 2.2. Different work that analyzed PCM characteristics using the THM

Reference	PCM analyzed	Comments
Peck et al. (2006)	Distilled water, polyethylene glycol(PEG), and Tetrahedron	The tubes are horizontally placed to reduce the temperature gradient in the vertical direction of the tube. Results reported that agreed closely with other reference data.
Gunther et al. (2009)	Salt hydrate	T-history measurements were compared with airflow chamber calorimetric measurement, reported that good between the two results
Stankovic and Kyriacou (2012)	Commercial PCM RT-21 (Rubitherm^{R}GmbH)	Temperature uncertainty in T-history measurement was performed with thermistor sensors and two linearization techniques to increase temperature measurement accuracy.
Chiu and Martin (2012)	Salt hydrates and paraffin	It was concluded that the THM could be utilized to characterize the phase transition temperature range, specific heat, and the overall accumulated heat capacity or enthalpy over a temperature range.
Stankovic (2013)	Organic and Inorganic	They have suggested changes in T-history experimental setup, data processing techniques, and representation.
Rathgeber et al. (2014)	Stearic acid, Dimethyl terephthalate and d-mannitol	Designed the T-history setup and studied three PCMs. They analyzed the enthalpy curve's dependence on sample size and compared the DSC and T-history results.
Gunasekara et al. (2016)	Erythritol, Xylitol, and Polyethylene glycol	They have suggested these materials require comprehensive studies to estimate their PCM suitability further. This study was intended to instigate a forthcoming extensive polyol-blends phase equilibrium evaluation.

2.4 EXPERIMENTAL AND NUMERICAL STUDIES

Voller and Prakash (1987) studied the phase change problems with a fixed grid numerical modeling approach for the correction diffusion mushy region. They developed an enthalpy formulation based on fixed grid methodology to study the numerical method of convection diffusion-controlled mushy region to know the exact temperature where a phase change occurs. The proposed darcy approach was applied to simulate the motion in the mushy region. The intention of their studies has to develop a basic methodology for the analysis of mushy solidification. The thermal properties are assumed to be constant with temperature, and latent heat is specified as the linear relationship with temperature ($\Delta H = f(T)$). The analysis indicated the mushy region's size reduced towards the isothermal case, i.e., compared $\varepsilon = 0.05$ and $\varepsilon = 0.1$ deformations at t=1000s. This proposed methodology could be used to examine the real system. But care has to be taken to define the porosity source's nature—specifically the relationship between the porosity source and the mushy region, which has to be investigated. In addition to that latent heat, the source term is a function of temperature. The solid fraction and temperature may not be linear in the real system, resulting in some errors. Examined the influence of two constant (C) values: 1.6×10^3 and 160×10^3 on melting. They reported an increase in C value effects in the decline of the flow in the mushy zone. Many researchers further examined the relationship between the mushy zone and the constant (C) and considered the value of C as 1.6×10^6 and $C = 10^5$(Brent et al. 1988a; Tan and Fok 2007).

To insight the physical phenomenon that governs the melting process, Shmueli et al. (2010) studied the case: melting in a vertical cylindrical tube using numerical analysis and the experimental result. Two different diameter vertical tubes, i.e., D=4 cm and 3 cm with the same height H=17 cm, have been considered. Two tubes filled with solid PCM, a partial amount of tube was unfilled and exposed to air. However, the tube bottom was insulated to uniform heat flux transferred from the sidewall to the solid PCM.

The effect of porosity functions numerically on the melting process with C's different values as 10^5, 10^7, 10^8, $10^{9,}$ and 10^{10}. The simulation carried out for $C = 10^8$ reported a longer time, and $C = 10^5$ reported a shorter time than the experiment results. But further

increasing C constant values to 10^9 and 10^{10} approaches the results back closer to that of 10^5. This study adds to the effect of C on the melting process. They also verified the impact of the pressure velocity coupling schemes (PISO and SIMPLE) and pressure discretization schemes (PRESTO and body force weighed). They observed no difference between PISO and SIMPLE, whereas the considerable difference between PRESTO and the body force weighed scheme.

Shell and tube type latent heat energy storage unit has been studied by many researchers using a mathematical model with various complexity. Some authors studied their model with the negligible thermal resistance of PCM, i.e., and heat transfer is uniform throughout (Biot Number Bi < 0.1). A few authors neglected the effect of axial temperature change on the HTF. The majority of the studies considered the one–dimensional heat transfer problem (radial direction only) between the PCM and the HTF.

Lacroix (1993) developed a numerical and experimental shell and tubed latent heat storage unit to study the phase change problem in the tube's vicinity. He examined both radial and axial directions and connected to the convective type heat transfer from the HTF. More complexity in solving this problem is compared with the one-dimensional case because of the moving boundary and unknown wall temperature. So, to make the problem more tractable, they used the enthalpy method. Their work split into folds. First, the computational model was developed to find the heat transfer between the HTF and the PCM and then validate it with experimental data. In the second part, the parametric analysis was performed to find the effect on the heat transfer process and the system's behavior. Using the enthalpy method, the studies reported two-dimensional problems (radial and axial direction) of PCM around the tube, strongly coupled to the convective type heat transfer from the HTF. Simultaneously, the PCM parameter like shell radius, the mass flow rate, and the inlet temperature of HTF care should be taken to maximize the storage unit's performance.

Lorente et al. (2014) study cylindrical LHTES enclosure with the enclosure center's vertical tube numerically. The analytical approach is carried out using scale analysis by modeling the liquid state as the incompressible liquid inside a vertical cylindrical domain of diameter D and height H. This approach was backed by a numerical model of the cylindrical PCM tank. H=1 m and D=60 cm, and heat transfer vertical tube

diameter are 2 cm. The chosen PCM was paraffin, and simulations were done through a finite element package. Both latent and sensible heat were stored as a function of time, and the latent heat contribution was almost ten times higher than sensible heat.

They also studied melting history in which the variation of dimensionless terms $\tilde{z}$ and $\tilde{t}$ drawn and the curve shows good agreement between theoretical and numerical results. But the divergence increased as the horizontal melting front approached the bottom of the tank. Good agreement with theoretical prediction has been reported in the melting history study of both energy storage and melting front.

Lorente et al. (2015) continued their studies on the constructal approach for LHTES with helical heaters. A fixed volume of the storage and helical tube diameter was used. Heat transfer liquid inside the helical tube was maintained at a temperature of T_w with the help of solar collectors, and the helical tube surface assumed an isothermal wall. The study aims to find the TES system's efficient configuration. They split the objective into two: the lowest possible volumetric ratio between the heat transfer tube and the storage tanks. The second was the helical tube's optimum dimension, which completely melted the PCM during a fixed time of 8 hours (30×10^3 s). To find the tube volume required to melt the PCM efficiently and then the helix's geometrical parameters (pitch, diameter, number of turns). Firstly, they considered the extreme case of a helical tube with negligible pitch (P→0) as a cylindrical shell of thickness 'd'. Observed the melting fraction as a function of time for different cylindrical radii 50, 100, 150, and 200 mm. The cylindrical tube with radius R_H=50 mm melts only 50% of the PCM (melting fraction 0.5). The other three configurations, 200, 150, and 100 mm, melt the PCM entirely within 8×10^3 s, 14×10^3 s, and 15×10^3 s, respectively (melting fraction 1). Hence to decrease the tube's volume, vary the helical tube pitch. The study continued to find the tube's optimum volume required to melt the PCM completely within 3×10^4 s of operation. Helix radius increased to 20 mm with a minimum pitch of 28 mm, and PCM melts only 70%.

They changed the configuration to two concentric helices. More changes would be possible if there were more degrees of freedom, hence the additional one, in this case, helix radius. Modelled the concentric helical tubes with infinitely small pitch resembled a cylindrical shell. The three liquid pools formed with this configuration first correspond to radius R_{H1}, second corresponds to annular cross-section R_{H1+d}, and third

corresponds to R_{H2}. Based on the scale or analytical approach, the reported optimum value obtained for R_{H1} and R_{H2} was 106 mm and 232 mm, respectively. They concluded that enhancing the storage system's performance through optimum geometric parameters such as helix diameter and pitch is possible. Furthermore, scale analysis integrated with numerical analysis has effectively improved the TES system design.

Brent et al. (1988a) modelled the convection-diffusion to melt pure metal by the enthalpy porosity technique. The numerical investigation was carried out with pure gallium in a rectangular cavity to study the convection-diffusion phase change process. Employed the fixed grid technique is the more practical solution for the coupled momentum and energy equations to take on without variable transformation. They considered the two-dimensional rectangular dynamic models to study natural convection currents on the phase transition process. Found that the enthalpy-porosity technique has the right approach to converge the solution quickly and effectively produced the melt front's results at different times. The results reported that the enthalpy-porosity procedure seems to be a comprehensive validation for modelling the isothermal phase transition system.

Chen et al. (2016) performed an experimental and numerical analysis of composite PCM (Paraffin and expanded graphite) with a helical coil tube LHTES unit. The mass percentage ratio of composite PCM was paraffin (80%) and expanded graphite (20%), the expandable rate of 280 ml/g, and mesh 80 into melted paraffin. They characterized the composite PCM properties like the enthalpy, heat capacity, and thermal conductivity by DSC and thermal constant analyzer.

Further, they performed the experimental and numerical analysis to study the effect of geometrical configuration and operational parameters on the helical tube LHTES system's performance. The geometric configuration effect was studied through fixed cylindrical tank volume, helical tube diameter, and length inside the tank. They maintained a constant heat transfer area inside the tank by varying the helix radius. An operational parameter like HTF mass flow rate, inlet temperature, and bulk density was changed to study the effect of Reynolds number, temperature, heat flux, and melting fraction with time. They concluded experimental results were in good agreement with numerical, and the composite PCM bulk density enhanced the LHTES capacity.

However, the careful selection of Reynolds number, helical tube ratio (R_h/R_t), and fluid temperature value was required.

Tay et al. (2012b) developed a CFD model for tubes in-tank LHTES and validated it with experimental results. Experimental setup modelled with 290 mm diameter and 330 mm height cylindrical tank. Four coiled tubes inside the tank and 27.6 kg of water as PCM. HTF is used in an aqueous-based fluid with dissolved ionic solids and operates at a temperature below 50 °C. Experimentally examined the storage tank in both radial and axial directions. However, nine T-type thermocouples were used at a different position inside the PCM tank, and a resistance temperature detector (RTD) was placed at the HTF tube's inlet and outlet. The melting and freezing experiment continued till all the thermocouples read the steady temperature.

Computation analysis was carried out using commercial software ANSYS CFX version 12.1. They considered the three domains in which HTF and PCM are liquid, whereas the tube is solid. However, the axisymmetric model grid independence performed with three different meshes varied from coarse to fine mesh. Studies reported that the CFD model accurately estimates the behavior of TES. But the PCM thermal behavior during melting and freezing was different from the experimental result due to ignoring the effect of natural convection in the CFD model.

Tay et al. (2012c) extended work on the tube in an LHTES system using the alternative simplified method, based on the effectiveness-number of transfer units (e-NTUs) approach. Conducted the experiments with one, two, and four coiled heat transfer tubes inside the PCM cylindrical shell to validate the analytical results obtained using the e-NTU approach. Experimental results with higher heat transfer area compared well with the e-NTU model. This study concludes that the e-NTU model accurately predicts the average heat transfer effectiveness of an LHTES with a high heat transfer area.

Tay et al. (2012a) validated numerical results with a four-tube in-tank experiment using the e-NTU technique. The average tube distance was minimal (30 mm), and hence buoyant convection was insignificant. To experimentally investigate the effect of buoyant convection, they developed a bigger tank with a higher average tube distance. This study concluded that CFD with the e-NTU model accurately predicts the behavior

of the experiment phase during discharge. But deviation occurs during the melting process because of the exclusion of buoyancy in CFD.

Adine and el Qarnia (2009) developed a latent heat type shell and tube model to compare the latent heat storage thermal behavior of two-PCMs P116 and n-octadecane (melting point 50 °C and 27.7 °C) with a storage unit of a single PCM n-octadecane. The mathematical model was developed based on energy balanced between HTF and PCM's with certain assumptions to simplify the procedure. They concluded that maximum thermal storage efficiency with one and two PCM storage units was identical irrespective of HTF inlet temperature and more effective for the low value of HTF inlet temperature and mass flow rate.

Hosseini et al. (2012) studied medium-temperature range PCM experimentally and numerically to know the effect of buoyancy-driven convection and operation parameters like inlet temperature of HTF on the melting process of PCM's.

The study reported that heat transfer between the HTF tube and PCM was significantly influenced by natural convection and high rising temperature at the uppermost section of the PCM container due to the buoyancy effect. The increasing temperature of inlet fluid to 80 °C affects the decline of total melting duration to 37%.

Akgun et al. (2007) developed a novel storage unit's design and construction to study the paraffin's phase change behavior. They altered the outer shell surface with a tilting angle of 5 °C. The results reported an approximately 30% decrease in the total melting time due to 5 °C tilting the outer shell surface. It was also concluded that increasing HTF inlet temperature reasonably dropped the melting duration, and lower energy consumption lower HTF mass storage was suggested.

Khillarkar et al. (2000) developed a finite element computation model to study the free convection melting of PCM in concentric annuli of two configurations (a) square shell with a circular tube inside (b) circular shell with a square tube inside. They numerically examined Rayleigh's number effect by simultaneously heating the inside tube, outside shell, and both walls.

Table 2.3. Experimental and numerical study of a different configuration LHTES unit.

Reference	Nature of study	Description of LHTES system (Temperature range and Capacity)
Valan et al. (2013)	Numerical	Concentric double pipe heat exchanger (27-80 °C and 220 kJ)
Korti and Tlemsani (2016)	Experimental	Single helical tube made up of copper with a transparent cylindrical shell (16-82 °C).
Ling et al. (2015)	Experimental	Cylindrical shell (steel) and swirled HTF tube (30-220 °C).
Bezyan et al. (2015)	Numerical	U, W, and spiral-shaped heat transfer tubes with the cylindrical shell (18-35 °C).
Arena et al. (2015)	Experimental and Numerical	Case1: Vertical steel tube and cylindrical shell. Case 2: Triplex type, HTF flow inner and outer steel tubes in between PCM cylindrical shell. Case3: Triplex type with six circular steel fins (100-180 °C).
Gasia et al. (2016)	Experimental	U-type heat transfer tubes with a rectangular shell made up of stainless steel (48-68 °C).
Sundaram et al. (2016)	Experimental	A single tube of helical coil made of copper and cylindrical shell container made up of acrylic (30-75 °C).
Duan et al. (2017)	Experimental and Numerical	Spiral tube made of copper and cylindrical shell container made up of acrylic (22-70 °C).
Zhang et al. (2017)	Experimental	Spiral tube made of copper and cylindrical shell (25-77 °C).
Aswin et al. (2017)	Experimental	Helical copper tubes and square-type shells made of galvanized iron sheets (30.3-170 °C).

Conclusion reported that heating both surfaces simultaneously is similar to heating inside the tube and the outside surface separately until the two melt fronts interact. However, later stage melting appears to be at a faster rate because of two melt fronts' interaction. Due to this fact, there was suppressed thermal stratification in both configurations (a) and (b). The thermal stratification occurs in the annulus's upper region because the energy transferred to the system is carried upward by the melt buoyancy flow. Hence studies reported that simultaneous heating of both surfaces leads to increased sensible energy storage than latent heat.

Meng and Zhang (2017) prepared the composite PCM by vacuum-impregnated paraffin with copper foam to enhance thermal performance. However, the prepared composite PCM was studied experimentally and numerical analysis at different inlet temperatures and flow velocities of HTF. The change in a storage unit temperature with respect to time, mean power, and energy efficiency was evaluated and validated with a numerical model based on the enthalpy–porosity approach. This study reported that the LTES system with composite PCM exhibits good thermal performance. The larger the inlet velocity of HTF effects increases the temperature difference between HTF and PCM leads to enhanced heat transfer performance. Table 2.3 further briefly reviewed the experimental and numerical studies based on the different geometric configurations of the LHTES unit.

2.5 PCM HEAT TRANSFER ENHANCEMENT

As mentioned in the previous chapter, PCM-based LHTES is practically feasible. Though PCMs possess very low thermal conductivity, comparable to that of the insulators. Limits their widespread application owing to a lower energy storage rate, i.e., the time taken to store and release energy is higher Liu et al. (2016). Among various PCMs available, organic PCMs exhibit poor heat transfer characteristics due to low thermal conductivity, which lowers the energy storage and delivery rate of the LHTES. Several methods have been researched to enhance the PCM heat transfer process, such as adding nanomaterials, using metal foams, encapsulation, fins, cascading techniques (Fan and Khodadadi 2012; Hawlader et al. 2003; Peiró et al. 2015; Sharifi et al. 2011; Wu and Zhao 2011)

2.5.1 Heat transfer enhancement through the extended surface (Fins)

Fins being cost-effective due to easy construction and exhibiting uniform temperature fields without affecting the PCM properties, have been widely employed to enhance the thermal performance (Hosseinizadeh et al. 2011; Huang et al. 2004).

Huang et al. (2011) employed fins in PCM used in PV systems and reported significant thermal performance improvement due to the uniform temperature distribution. However, they also stated that natural convection benefits could be offset by increasing the number of fins.

Jmal and Baccar (2018) studied solidification time in a finned rectangular heat exchanger with paraffin and commercial composite RT27 PCMs. The study revealed that fins had no significant effect on heat transfer during solidification. More fins caused a confinement effect and contributed significantly to conductive heat transfer rather than the convective mode.

Stritih (2004) experimentally compared finned over plain PCM for thermal storage applications in buildings and compared the PCM's thermal-convective features for both melting and solidification stages. The conduction mode of heat transfer was dominant during solidification, whereas natural convection had a substantial impact during melting.

Ji et al. (2018) numerically investigated the LHTES units with double-fins of unequal length to explore natural convective currents' effects in a phase change process. The short upper fin and long lower fin improved the PCM melting rate. The arrangement of a long upper fin and a shorter lower fin had an adverse impact on PCM's melting.

Joshi and Rathod (2019) employed the fin in shell and tube LHTES unit. To minimize the total melting time for the given fins to the PCM volume ratio, the study emphasized obtaining the fins' best size and location. Shorter fins at the top gradually increased the fin length to the bottom regions of higher temperature gradient and reported a 4.38% enhancement in thermal performance compared to uniform fin configuration. The fin volume reduction also contributed to increased thermal storage space for a lower-weight energy storage unit.

Rudonja et al. (2016) studied the effect of longitudinal rectangular copper fins as shell and tube LHTES units. Longitudinal rectangular copper fins were attached to the HTF tube and annular gap between shell and tube filled with paraffin E53. Both numerical and experimental results reported that increased heat transfer surface ratio leads to decreased charging and discharging time.

Yang et al. (2017) investigated the annular fin's effect in shell and tube LHTES system. A numerical study was carried out using paraffin wax as PCM and water as HTF. Performed the optimal fin number to maximize the heat transfer and energy saving from an engineering perspective. The numerical study concluded that the LHTES unit with an optimum number of annular fins (fin number N=31, thickness t/l=0.0248, and interval l/L=0.0313) inherently enhanced the melting heat transfer. Quantitatively reported a 65% reduction in full melting time by annular fin into the PCM.

Pu et al. (2020) numerically studied the suitable arrangement of radial fins to enhance the heat transfer between PCM and HTF in a vertical LHTES unit. The finned LHTES model melting time is 44% lesser than the no fin model. However, the different radial fins arrangements (lower fins, upper fins, middle fins, and arithmetic fins) exhibit a 49.9 % reduction in melting time by arithmetic fins type. So, to maximize the thermal performance, arithmetic fins to LHTES were recommended.

Anish et al. (2019) experimentally investigated the heat transfer mechanism in a horizontal shell-and-multi-finned-tube energy storage unit. They studied the operating parameters, such as volume flow rate and HTF inlet temperature, on the melting and solidification time. Natural convection had a pronounced impact on the thermal performance of the unit during melting. It was found that the effect of inlet temperature was more significant than the flow rate.

Yagci et al. (2019) experimentally performed the effect of fin edge length ratio (tapered angle) on the shell and tube LHTES system's thermal performance. The analyzed results depict that melting time shortened by 21% as the edge length ratio reduced from 1 to 0—however, the fin with edge length ratio 0 (maximum tapered angle) confirmations good melting performances. Further, fin edge length has no significant effect on solidification time.

2.5.2 Heat transfer enhancement through the application of multiple PCMs

Among all the possible TES configurations, multiple PCMs, also known as cascaded type LHTES, uses PCMs of the different transition temperatures and latent heat. The CLHS method improves the HTF storage capacity and heat transfer by a series arrangement of PCMs and relative differences in melting temperature. The PCMs are arranged in decreasing order of their melting point and increasing order of their enthalpy. The HTF fluid flow direction during the charging and discharging process is opposite to each other.

Farid et al. (1990), Farid and Kanzawa (1989) carried out numerical and experimental analyses with three different PCMs. They observed a significant increase in heat transfer rate (15%) during the charging and discharging process of the latent heat period. However, the heat transfer rate increase reduces the TES unit's volume and mass, making it more economical.

Domański and Fellah (1996) the exergy analysis for TES by employing PCMs with different melting temperatures in series. However, the exergy analysis directs the combination of different PCMs improves the second law efficiency compared to the single PCM unit. To have the best second-law efficiency, the downstream units melting temperature should be close to ambient temperature.

Aldoss and Rahman (2014) studied the spherical capsules packed bed LHTES unit and compared a single PCM unit's performance with a CLHS system. The melting temperature variation is selected to match the HTF temperature profile along the bed. This is to maximize the heat transfer rate between HTF and PCMs. They reported that the heat transfer enhancement in CLHS than single PCM unit. However, in more than three stages, there was no significant improvement in heat transfer.

Chiu and Martin (2013) numerically compared the performance of single and multi-stage PCMs in a finned-type shell and tube heat exchanger. An outcome is that a multi-stage TES unit improves 10-40 % in heat transfer than that of a single PCM TES unit. This is due to the CLHS unit maintaining a higher driving temperature difference for the heat transfer process in the charging and discharging cycles. Multi-PCM is recommended for use in applications where a higher thermal power rate is required, and charge/discharge thermal rates are equally important.

Cui et al. (2003) observed the heat transfer problem by employing a single PCM in the heat receiver for the NASA 2kW solar dynamic power system. So numerically analyzing by replacing single PCM with three PCM LHTES units and compared. It is shown that the fraction of PCM increases by 12%, which means that the PCMs absorb more heat in the CLHS unit than in the single-PCM unit. Using 3-PCM to transfer the same amount of heat can enhance the heat transfer rate, reduce heat receiver weight, and minimize HTF temperature fluctuation.

Xu et al. (2016) developed a mathematical model for studying the overall exergy efficiency of multi-stage PCMs for the charging-discharging process. The analysis was based on a lumped model for the PCMs, which assumes that PCM is a thermal reservoir of its melting point's constant temperature. The results show that an increase in HTF temperature increases the maximum overall exergy efficiency. In contrast to increasing the number of transfer units (NTUs) of the TES system HTF, increasing the NTUs of the solar field HTF effectively improved the maximum overall exergy efficiency.

Seeniraj and Lakshmi Narasimhan (2008) numerically examined the performance of the finned CLHS unit. The result shows a significant increase in PCM's melting rate and nearly uniform exit temperature of HTF. Xu et al. (2017a, 2017b) developed the analytical solution to examine the CLHS model's performance for a steady and unsteady case. Comparative results show optimal thermal performance in steady cases superior to the unsteady case for entropy and entrance optimization.

Peiro et al. (2015) experimentally evaluated the advantages of multiple PCM over a single PCM configuration. They have selected two PCMs of melting temperature range 150-200 °C and three configurations a) LHTES unit with single PCM hydroquinone, b) D-mannitol, and c) combination of two PCM CLHS units. Experimental results showed that multiple PCM increases the effectiveness by 19.3% and uniform HTF temperature at the outlet than the single PCM system. A similar analysis showed a significant increase in the melting rate for multiple PCM units, which resulted in uniform HTF temperature. It ensured a nearly isothermal operation beneficial for solar-thermal power plant applications (Seeniraj and Lakshmi Narasimhan 2008).

Table 2.4. Summary of works carried out to enhance the thermal behavior of PCM using nano additives.

References	Base PCM and nano additives	Fraction of nano additives	Remarks
Eman et al.(2007)	Paraffin with Aluminium	1, 3,4 & 5% mass fraction of Aluminium	Addition of aluminium powder reduces the melting time 60% and improved in heat discharge as well as averaged heat transfer coefficient of composite PCM than pure PCM.
Teng and Yu(2012)	Paraffin with TiO_2, Al_2O_3, ZnO & SiO_2	1, 2 & 3 wt.% concentration of Nano particles	Experimentally investigated and found that TiO_2 was more effective than other additives.it reduces the melting onset temperature and increases the solidification onset temperature of paraffin
Ho and Gao(2013)	Paraffin with Al_2O_3	1 & 3 vol.% concentration of nanoparticles	Experimentally investigated the performance of square enclosure reported that enhancement in the thermal conductivity of the Nano-PCM due to dispersing the Al_2O_3 nanoparticles but mean while greater enhancement in the dynamic viscosity of the liquid Nano-PCM.
Jogi et.al.(2017)	Tricosane and Al_2O_3	0.5%,1% & 2 vol.% concentrations	The thermal conductivity of the composite PCM found to be enhanced to a maximum of 32% compared to the pure Tricosane.

2.6 SUMMARY OF LITERATURE REVIEW

➢ The latent heat storage system has a higher energy storage density in small temperature intervals and is more compact than another storage system.

➢ Thermophysical and rheological characterization of PCMs very a crucial step for the proper design of the LHTES system.

➢ Compared to the conventional DTA/DSC calorimetric method, the T-history in-house calorimetric process has significant features like a simple setup, measuring different properties of different PCMs simultaneously, higher sample weight useful for inhomogeneous material, and less measurement time.

➢ BPCM is an eco-friendly, less-flammable, and alternative potential candidate for commercial paraffin.

➢ DOS affects the latent enthalpy of the material and the requisite property for the storage system's proper design.

➢ Shell and tube TES units stored equal amounts of energy storage in the least possible time and increased PCM mass compared to other TES configurations. This configuration influence is more pronounced to improve the heat transfer exchange during melting.

➢ CFD model of the LHTES system is supposed to be a smart approach to saving money and time and an optimization tool to deliver maximum efficiency in latent heat energy storage applications.

➢ The enthalpy-porosity technique has been found that the right approach to converge the solution quickly and effectively produce the accurate results of the melt front at different times. The enthalpy-porosity methods seem to be a comprehensive validation for modelling an isothermal phase transition system.

➢ The main drawback of the LHTES unit is the low thermal conductivity of PCM. Hence heat transfer enhancement techniques are vitally essential to obtain nominal thermal power performance.

2.7 RESEARCH GAP AND ANALYSIS

Globally growing demand for energy production, meeting the demand by burning fossil fuel, is not the solution because of its environmental effects or greenhouse emissions.

Renewable energy utilization is only the solution to meet the demand, even though their cost investments are high in contrast to fossil fuel energy production.

The major problem of renewable energy is intermittent. Integrating TES systems into renewable energy production is an efficient way to overcome the problem and supply energy according to demand. Latent heat type energy storage is the most promising nowadays than another type of TES due to its high energy density at the nearly isothermal condition.

Today paraffin is the most widely used PCM in all latent heat applications. Since paraffin is derived from crude oil, its prices vary randomly and geopolitical scenario. Crude oil prices have been on the upsurge in recent years. Perhaps all these factors need to shift the motivation from paraffinic PCM to alternative paraffin PCMs, i.e., BPCM

BPCMs are a renewable, less flammable, and eco-friendly option to commercial paraffin-based PCMs. In the open literature, few works have been reported on bio-based PCMs. More research on bio-based materials characterization and performance study is required to find potential BPCMs suitable to different LHTES applications.

2.8 AIM

The aim is to investigate BPCMs that are eco-friendly, cheap, and have efficient energy storage capacity. BPCM can be applied to different solar thermal applications: district heating, desalination and electronics thermal management, waste heat recovery systems, and building thermal systems management applications.

2.9 OBJECTIVES

➢ Development of experimental setup to study the effect of the tube's length to diameter ratio on PCM's characterization in the T-history method (THM).

➢ Thermo-physical characterization of the fatty acid mixture (commercial OM55) as bio-based phase change material (BPCM).

➢ Thermo-physical characterization of shellac wax (in-house calorimetric and conventional method) and evaluating required properties for BPCM.

➢ Heat transfer evaluation of BPCM experimentally in vertical shell and tube latent heat thermal energy storage (LHTES) system.

➤ Numerically studying the heat transfer enhancement techniques by geometrical modification of storage unit.

2.10 SCOPE AND METHODOLOGY OF THE PROPOSED STUDY

The scope and methodology of the research study shown in Figure 2.3 is split into two folds material properties investigation and performance study as follows,

2.10.1 Material properties investigation

To select a good phase change material and successfully design of a storage system, the material properties must be known. The most prominent property is the phase change temperature. The specific heat (c_p) of the solid and liquid states are almost constant in small temperature ranges. The storage capacity is then well defined via the four parameters solid and liquid specific heat, transition temperature and the phase change enthalpy (Δh). PCM can be investigated through conventional and non-conventional characterization methods.
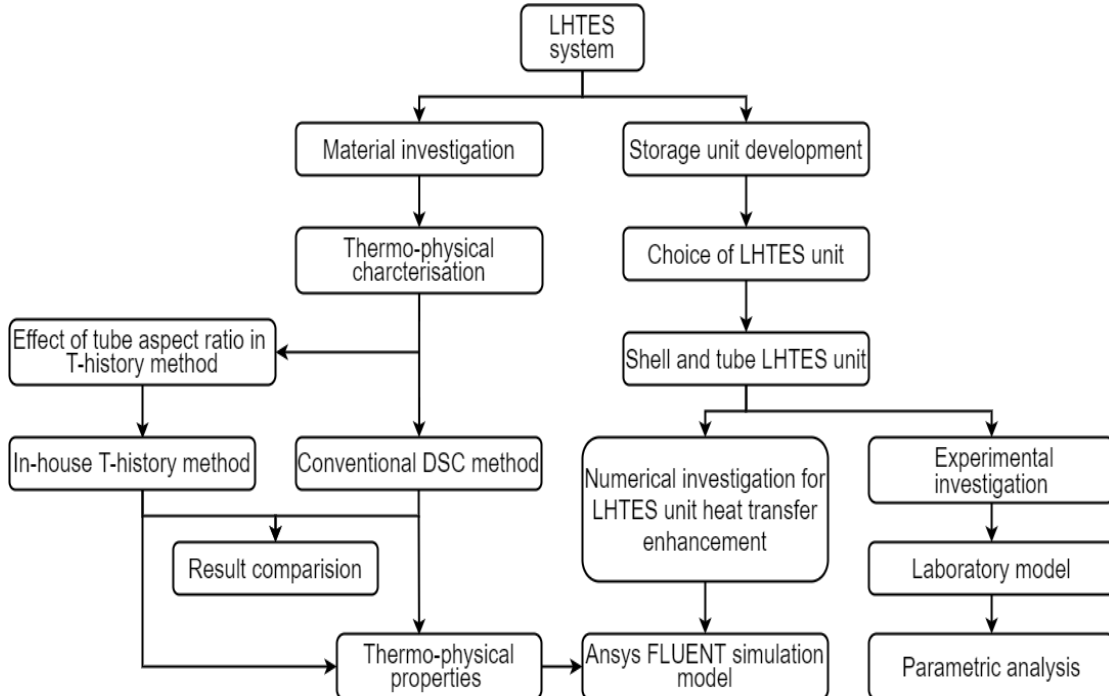
Figure 2.3. Scope and methodology of the proposed research study

1) The non-conventional calorimetric method or in-house calorimetric process: T-history method.

i) Development of experimental setup to investigate the thermophysical properties of PCM

ii) To study the effect of length to diameter ratio of the tube in the T-history process.

iii) Characterizing the BPCM using the THM.

2) Conventional method: Characterizing the BPCM using thermoanalytical methods like DSC, TGA, TCA (Thermal constant analyzer), FTIR, and rheometer.

3) Comparision of T-history results with the conventional DSC method.

2.10.2 Performance study

1) Heat transfer evaluation of BPCM experimentally in vertical shell and tube LHTES system.

2) Development of numerical model using ANSYS workbench and solved through FLUENT solver to compare the existing heat transfer enhancement techniques like conventional cascaded storage with the proposed storage design.

2.11 CLOSURE

A review of literature relevant to the present work has been presented in this chapter. The research gap, objectives, and scope of the present research work were highlighted. The next chapter establishes the material selection, preparation, and methods used to characterize the BPCM.

CHAPTER-3

MATERIALS AND CHARACTERISATION METHODS

3.1 INTRODUCTION

This chapter describes the material used and the thermo-physical characterization methods of the BPCM. The conventional characterization techniques discussed are DSC, TGA, FTIR, TCA, and Rheometer. This study also encompassed non-conventional methods like the THM, pycnometer, and thermal stability through thermal cycle test.

3.2 MATERIALS USED FOR PRESENT RESEARCH ANALYSIS

3.2.1 Commercial bio-phase change material (BPCM)

Four bio-based commercials PCMs OM-42, 46, 48, and 55 (PLUSS^{TM}) derived from the mixture of organic fatty acids selected for this study. The selection criteria for this BPCM are mainly based on their transition temperature and are well suited for medium-temperature thermal storage applications. Thermo-physical properties and performance behavior of this BPCM were analyzed for the heat transfer enhancement and storage applications.

3.2.2 Bio-wax

The motivation to study the natural shellac wax is bio-based material. Moreover, shellac wax has potential thermal properties similar to the existing non-paraffin wax like beeswax, carnauba wax and is the best alternative for petroleum paraffin wax. Shellac is a natural product derived from Kerria lacca and Laccifer lacca insects. Shellac contains approximately 4-6% wax and is separated as a by-product during shellac processing. All over the world, India and Thailand are the leading countries where lac is cultivated. The processing of shellac wax from sticklac is as shown in Figure 3.1(Farag and Leopold 2009). Shellac is natural polyester of mainly aleuretic acid and shellolic acid. The harvested stick lac is processed and washed, which removes the water-soluble laccaic acid to obtain the raw seedlac. It is further processed and refined, resulting in different shellac qualities. A significant amount of shellac wax

is produced by bleaching the seedlac in the alkaline solution and dewaxed process. Shellac wax is made up of long-chain esters of monovalent alcohols and acids. It contains more than 30% of free wax alcohol with a chain length of C28-C32. It also includes a small number of hydrocarbons and about 1% lactic acid. Shellac can be used as a natural thermoplastic (Lausecker et al. 2016), and it is also eco-friendly. Natural shellac wax is obtained from the Indian Institute of Natural Resins and Gums (IINRG), process and product development division, Ranchi. It is purified by petroleum ether and then grinded into 75-micron mesh powder as the pre-treatment to reduce the particle size. Shellac wax is used to study its thermophysical properties and performance analysis as a novel BPCM for medium temperature storage applications.
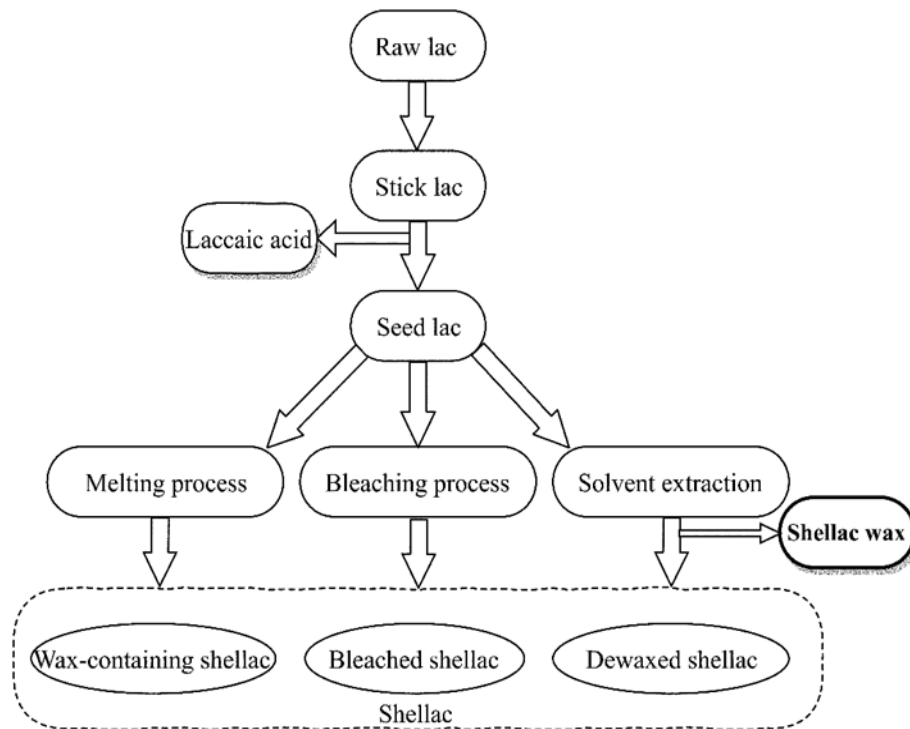
Figure 3.1. The process flow is involved in the production of shellac wax.

3.3 THERMO-PHYSICAL CHARACTERIZATION OF BPCM BY CONVENTIONAL AND NON-CONVENTIONAL METHODS

The material's properties must be well known to choose a good PCM and successfully design a TES system. PCM can be investigated through the conventional and non-conventional calorimetric methods. A conventional approach is usually used or has been used for a long time, such as differential scanning calorimetry, thermal conductivity measurement, thermal gravimetric analysis, and fourier transforms

infrared spectrophotometer and measurement of viscosity. Non-conventional methods are non-commercialized, such as the T-history method, density measurement using a pycnometer, and thermal cycle test.

3.3.1 Differential scanning calorimetry (DSC)

Thermal properties like first and second-order transition temperature, latent and specific heat of BPCMs are investigated in dynamic mode using Perkin Elmer DSC 8500 (accuracy ± 0.1 ºC), as shown in Figure 3.2. Pulverized samples are weighed and kept in 40 microliters (μL) aluminium crucible with pierced lid. For heating and cooling of the sample, an inert atmosphere was created with argon/nitrogen (20 ml/min) as a purge gas. The sample was heated from 0 ºC to above the sample's melting temperature at a preset heating rate (1 to 10 ºC/min) and then kept isothermally at this temperature for 2 min in the DSC chamber. Further, it is cooled to 0 ºC, with the same cooling rate followed by an isothermal segment for 2 min.
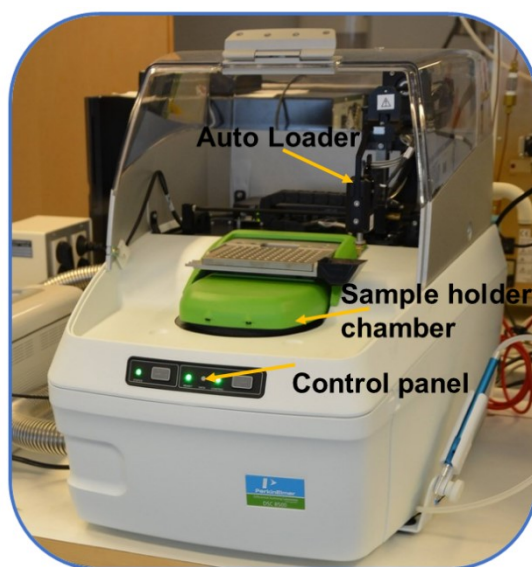
Figure 3.2. Differential scanning calorimetry (DSC) (Perkin Elmer DSC 8500, PerkinElmer laboratory, Mumbai).

To achieve stability during heating and cooling, the isothermal condition is initially maintained for 2 min. Isothermal steps help to reduce the temperature lag compensation and also improve the results. This heating-cooling cycle was repeated three times to obtain an acceptable reproducibility (Hong et al., 2004; Marín et al., 2003; Yinping et

al., 1999). The first cycle was discarded as (Gallart-Sirvent et al. 2017) recommended, though the second and third cycles were considered for the study analysis.

3.3.2 Thermal conductivity measurement

A hot disk TPS 500 (accuracy 0.5%) thermal constants analyzer is used to measure the thermal conductivity of given PCM for both liquid and solid states. The facility is available at NIT Warangal and is shown in Figure 3.3. The setup consists of a hot disk analyzer, sample holder, and oil bath. The sample holder and Kapton disk are shown in Figure 3.4 (a) and (b), respectively. The principal operation of the instrument is the transient plane source (TPS). The TPS method is based on the effective use of a transient heated sensor equipped with a hot oil bath. A Kapton disk sensor of radius 3.18 mm is placed inside a sample holder. Prior to measurements, the sample holder is well cleaned and dried.
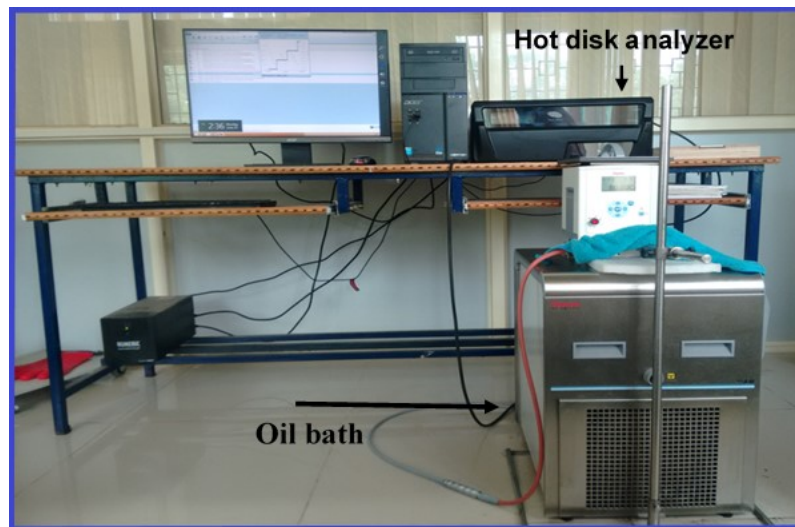
Figure 3.3. Thermal constants analyzer with an oil bath at NIT Warangal.

A rectangular sample holder with 80 mm×65 mm is used to hold the samples. Measuring 10 seconds with a pre-determined heating power of 50 mW is used to measure the 200 data points at room temperature. The data points 50 to 190 are then used for thermal analysis to reduce the initial error. The thermal conductivities of selected PCMs viz. Shellac wax and organic fatty acid mixtures (OM-42, 46, 48, and 55) are obtained at solid and liquid states. The power and time are adjusted so that total temperature and total characteristic time come in between 4 to 7 K and 0.3 to 1 s. This

range shows that heat is uniformly distributed around the PCM. The flow chart of the experimental procedure adopted in the present work is shown in Figure 3.5.

<table>
<tr><td>(a)</td><td>(b)</td></tr>
</table>
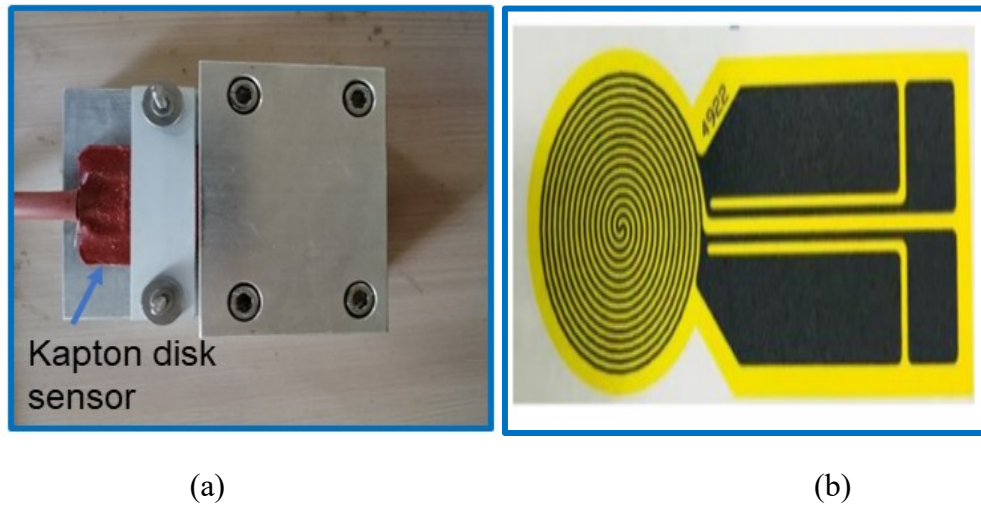
Figure 3.4. Thermal constants analyzer a) Sample holder and b) Kapton disk sensor.
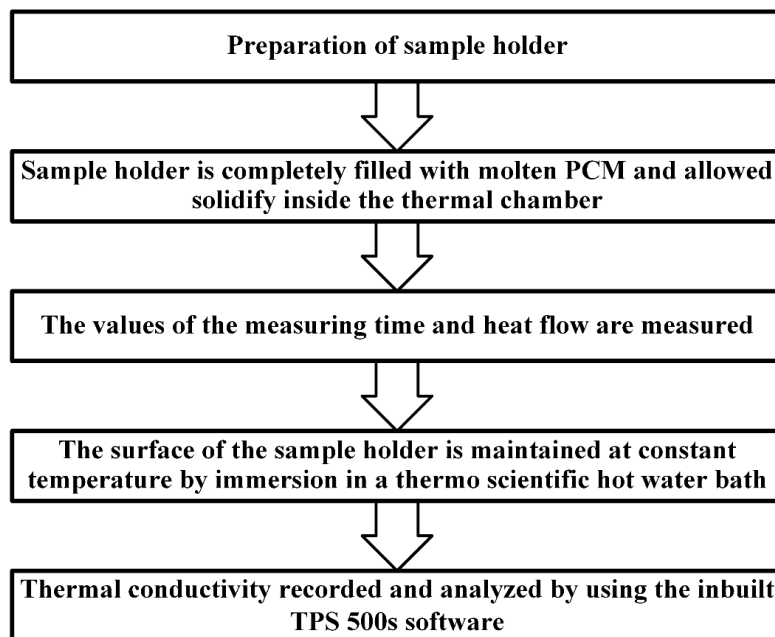
Figure 3.5. Flow chart of the experimental procedure for thermal conductivity measurement.

3.3.3 Thermal gravimetric analysis (TGA)

The PCM thermal stability is determined by utilizing the hyphenated TG/DTA thermal analyzer apparatus (Seiko TG/DTA 6300) and its schematic as shown in Figure 3.6. TGA is a method where mass is obtained as a function of temperature. The calibration

of TGA is done with calcium oxalate and indium, respectively; as per ASTM standards, the measured temperature and mass accuracy is ±0.2 °C and ±0.01 mg. The testing chamber contains an open lid sample and the reference pan, which serves as a heater and a sensitive scale. The chamber is sealed, and purge gas is made to flow through the chamber at a fixed rate. As the sample is heated (or cooled in some cases), it may lose or gain mass through oxidation, decomposition, deposition, or evaporation. The scale measures the sample's mass throughout the process as a function of temperature. In the presence of nitrogen in the atmosphere as purge gas at the flow rate of 20 mL/min, the PCM sample is heated in an open lid aluminium pan, compared with an empty reference pan. The PCM investigation is carried out from ambient temperature to 500 °C at the heating rate of 10 °C/min.
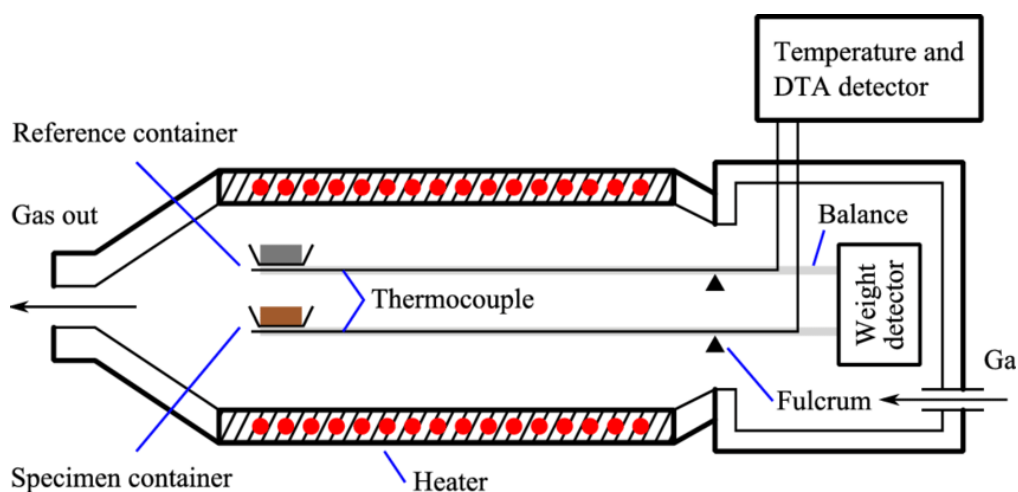
Figure 3.6. Schematic representation of the TGA with DTA detector

3.3.4 Fourier transforms infrared spectrophotometer (FTIR)
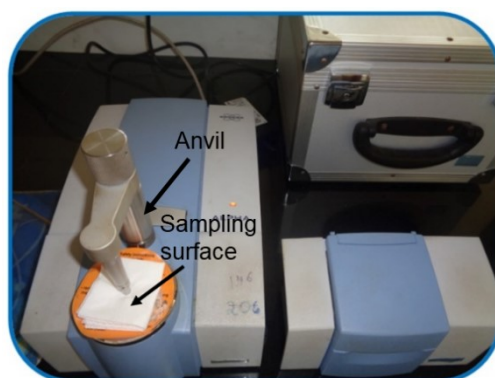
Figure 3.7. Fourier transforms infrared spectrophotometer, NITK Surathkal.

Infrared spectra of PCM are obtained from FTIR (ALPHA FTIR by BRUKER^{TM}), as shown in Figure 3.7. This test determines the samples' functional groups within a range of 400–4000 cm^{-1} at room temperature for a scanning resolution of 2 cm^{-1}. The investigation has been performed by mixing the PCM sample with potassium bromide in the ratio of 1:100 (Kbr method). A thin film is prepared and analyzed with FTIR to obtain a spectrum.

3.3.5 Measurement of viscosity

PCM's dynamic viscosity is determined using a rotational rheometer (Anton Paar^{TM}: Rheolab C-LTD180/QC). External computerized thermostat circulator with silicon oil as the heat transfer liquid is used to control the device temperature ranging from -20 ºC to 180 ºC. The rheometer is a rotational device that works according to the interrelation between force and deformation. The experimental setup is shown in Figure 3.8.

Figure 3.8. Rotational Rheometer (Anton Paar^{TM}: Rheolab C-LTD180/QC), NIT Warangal.

Prior to the experiment, the PCM sample holder was well cleaned and dried. The HTF is circulated through the cup holder to maintain the PCM sample's specific temperature. Then, viscosity readings are recorded and analyzed by using the inbuilt Anton Paar software.

3.3.6. Density measurement

The solid and liquid PCM density is found using a pycnometer and n-dodecane displacement liquid (Ushak et al., 2015). The n-dodecane density temperature dependence is evaluated analytically by digital density meter (DDM 2911-Rudolph research analytical™) over a temperature range of 25–95 °C. Figure 3.9 shows the linear variation of n-dodecane density with temperature. The pycnometer nominal volume of 2.5×10^{-5} m^3 is shown in Figure 3.10(a).
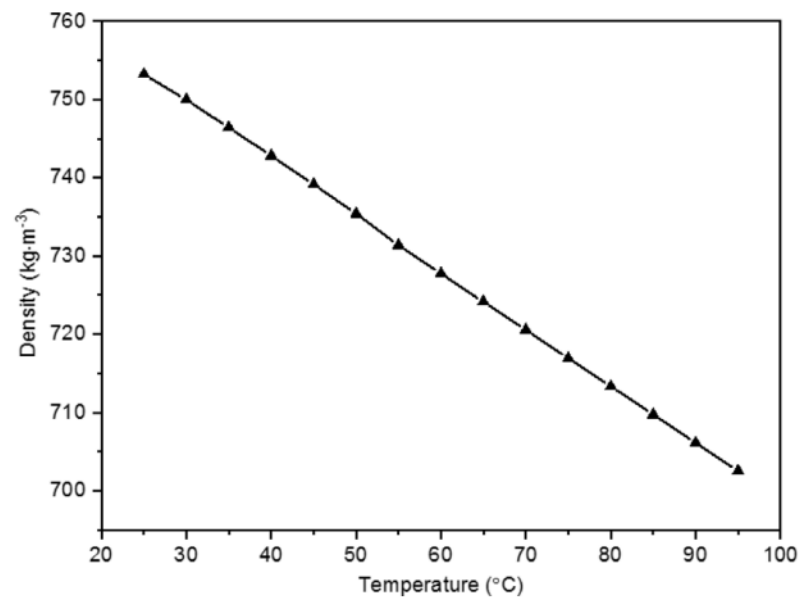
Figure 3.9. The density of n-dodecane with reference to temperature.

The density temperature relation expressed in Eq. (3.1) has an R^2 value of 0.99. Initially, an empty and filled pycnometer of 2/3 volume with solid PCM and n-dodecane is weighed using an analytical balance (Model: Contech^R CAI 234, accuracy: ± 0.1 mg).

$$\rho_{Dod} \, (kg/m^3) = -0.7302(T) + 771.14 \tag{3.1}$$

Then pycnometer is uniformly heated in a thermostatic water bath till the PCM sample reaches the desired temperature, as shown in Figure 3.10(b). Excess displacement liquid above the reference marks is pippeted out, and the weight difference is measured. Then PCM density is evaluated by considering the n-dodecane density at the corresponding temperature using relation Eq. (3.1). The PCM liquid density is obtained by heating above the melting point inside the thermostatic bath, and the weight difference is

calculated. PCM's solid and liquid density is obtained by considering the average of four repeated trials at different specified temperatures

(a)   (b)
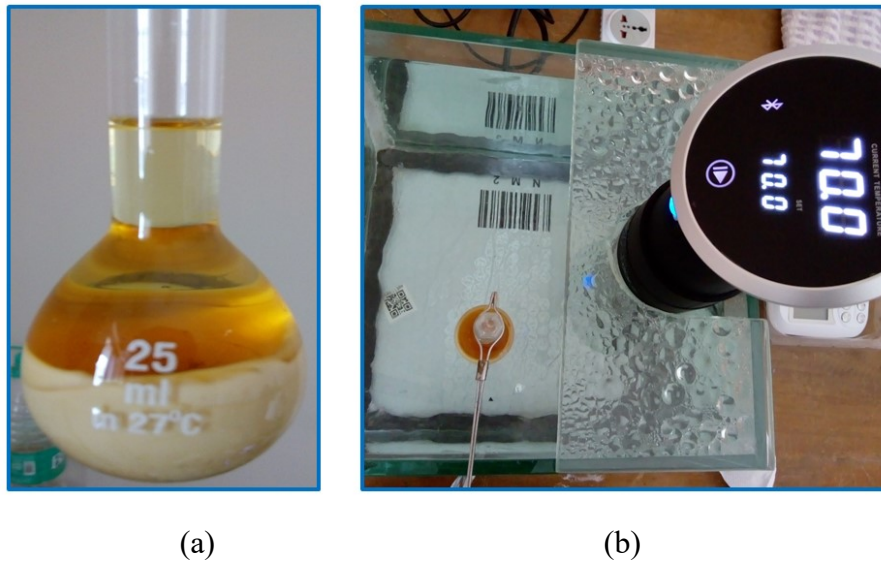
Figure 3.10. Density measurement (a) Pycnometer (25 ml) containing N-dodecane and solid PCM sample (b) Heating the pycnometer containing PCM sample to set temperature inside the thermostatic bath, NITK Surathkal.

3.3.7 T-history experimental method

T-history is an in-house calorimetric method and has significant features compared to the conventional DSC method. THM can simultaneously measure the transition temperature and the latent and specific heat of different bulk PCM samples with the phase transition process's visuals. Figure 3.11 shows the T-history in-house experimental setup, which includes a constant temperature water bath (accuracy: ± 0.5 °C) of volume 0.0155 m^3 and heating capacity of 800 W. The PCM and reference sample holder tubes are made up of borosilicate glass manufactured by Wilmad™, and the tube aspect ratio is much greater than 15 and satisfies the criterion Bi < 0.1. Due to the glass tube's geometry (aspect ratio), most heat transfer is expected from the tube to the ambient through the lateral cylindrical surface area. RS™ Pro K-type twisted thermocouple insulated with a durable PTFE placed at the center of the each tubes. Pt.100 temperature sensors are used to calibrate thermocouples with an accuracy of ± 0.1 °C: the sample and reference tube filled at atmospheric pressure with PCM and distilled water, respectively. Contech^R (CAI 234, accuracy:0.1 mg) analytical balance

with a least count of 10 mg is employed to measure the mass of the sample. A styrofoam motionless air chamber of thickness 0.03 m has been used to cool the testing samples without ambient fluctuations. Design, fabrication procedures and uncertainty analysis of measuring probes detailed in Appendix-A.
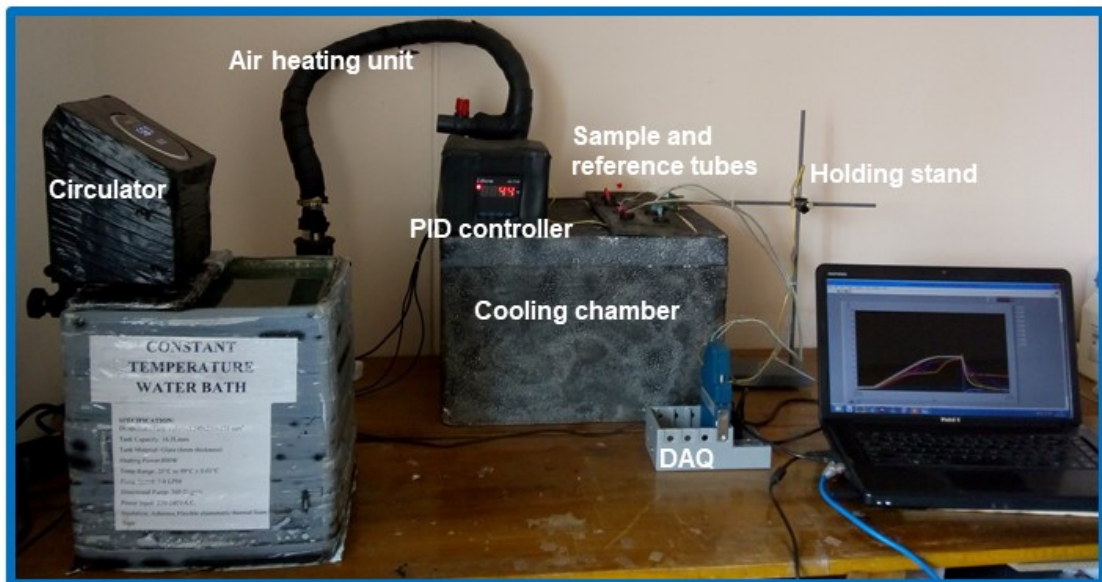
Figure 3.11. In-house T-history experimental setup, NITK Surathkal.

The reference and sample tube are held vertically in a constant temperature water bath to attain a steady temperature (higher than the PCM's melting temperature). Then it is exposed to the ambient temperature (inside the motionless air chamber). National Instruments™ TB-9214 module and NI cDAQ 9174 chassis data acquisition system with LabVIEW software is used to acquire the sample and reference temperature variation to time with a sampling rate of 1 Hz. However, the sample and reference holders are insulated with one layer of nitrile foam insulation of thickness 3 mm. Provision of heating and cooling both tubes are made simultaneously to achieve uniform conditions. Four repeated trials have been performed to check the recurrence of the results, and the mean of four trials with standard deviation is computed and considered for property evaluation.

3.3.7.1 Mathematical model

The areas under the THM curve of PCM and reference material are shown in Figure. 3.12 represented as $A_{p,i}$ and $A_{r,i}$, respectively. The Area $A_{p,i}$, and $A_{r,i}$ are calculated by integrating the temperature to the time curve using the standard numerical tool. To

simplify T-history evaluation, it is crucial to consider the following assumptions (Badenhorst and Cabeza 2017).

1) Both sample and reference tubes have equal heat transfer coefficients as measured at the same temperature and the same instance of time.

2) The heat transfer coefficients for both tubes are constant over a small interval of time.

The natural convection heat transfer coefficient of air outside the tube is 4-5 W/m^2·°C (Yinping et al. 1999), and the Biot number Eq. (3.2) for lumped system analysis is evaluated as described in the literature (Marín et al. 2003).

$$Bi = \frac{hR}{k} < 0.1 \qquad (3.2)$$

where, R is the inner radius of the sample tube, h is the convective heat transfer coefficient between the tube and the air, and k is the thermal conductivity of the PCM.
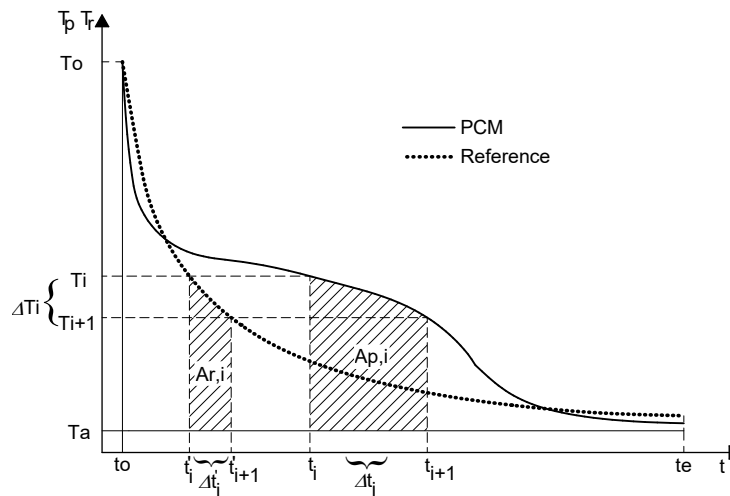
Figure 3.12. THM model graph, temperature versus time (Hong et al. 2004; Marín et al. 2003; Yinping et al. 1999).

The energy balance between the PCM and reference material with the ambient condition during the experiment is as follows (Hong et al. 2004; Marín et al. 2003; Yinping et al. 1999).

$$m_p \Delta H_p(T_i) + m_t c_{p,t}(T_i)\,(T_i - T_{i+1}) = hA_t A_{p,i} \qquad (3.3)$$

$$m_t c_{p,t}\left(T_i\right) + m_r c_{p,r}\left(T_i\right)(T_i - T_{i+1}) = hA_t A_{r,i} \qquad (3.4)$$

where, $A_{\mathrm{p,i}} = \displaystyle\int_{t_i}^{t_i + \Delta t_i} (T_i - T_a)dt$ and

$$A_{\mathrm{r,i}} = \int_{t_i'}^{t_i' + \Delta t_i'} (T_i - T_a)dt$$

By simplifying Eq. (3.3) and (3.4) obtained the $\Delta H_{\mathrm{p}}(T_i)$ relation.

$$\Delta H_{\mathrm{p}}(T_i) = \left(\frac{m_r c_{\mathrm{p,r}}(T_i) + m_t c_{\mathrm{p,t}}(T_i)}{m_{\mathrm{p}}} \right) \frac{A_{\mathrm{p,i}}}{A_{\mathrm{r,i}}} \times \Delta T_i - \frac{m_t}{m_{\mathrm{p}}} c_{\mathrm{p,t}}(T_i) \times \Delta T_i$$

(3.5)

Eq. (3.5) is the enthalpy change of the PCM in a small interval of time is coded using MATLAB R2017a (Appendix-A). The obtained values of $H_{\mathrm{p}}(T_i)$ are plotted and then compared with the DSC enthalpy graph. However, enthalpy curves are more useful for the PCM analysis and comparison with DSC values. Total enthalpy determined as the sum of the enthalpy intervals, assuming a constant value of $H_{\mathrm{p,o}}$ as a reference,

$$H_{\mathrm{p}}(T) = \sum_{i=1}^{N} \Delta H_{\mathrm{p,i}} + H_{\mathrm{p,o}}$$

(3.6)
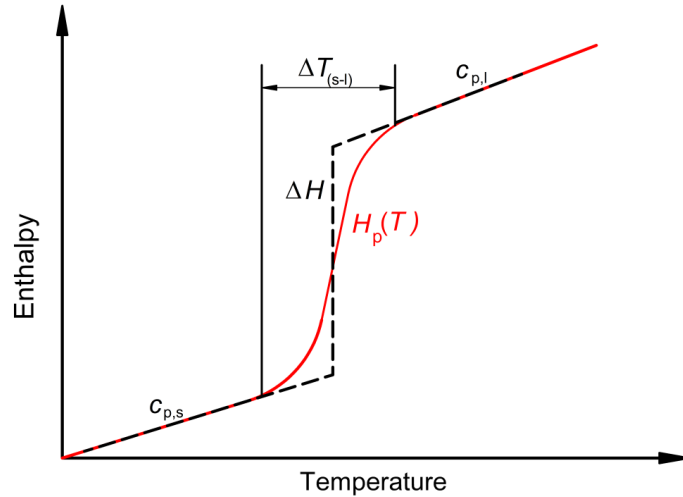
Figure 3.13. The enthalpy-temperature curve for an ideal and actual PCM.

For a non-isothermal phase transition process, a considerable amount of sensible heat part also affects the phase change, as shown in Figure 3.13. However, evaluating the enthalpy over a temperature range $H_{\mathrm{p}}(T)$ always raises the error and would not give the

PCM's actual enthalpy. To assess the enthalpy of transition accurately, heat capacity change concerning transition temperature interval should be subtracted from $H_p(T)$ term (Chernik 1993) , and it is given by

$$\Delta H = H_p(T) - c'_{p(s-l)}\Delta T_{(s-l)}$$
(3.7)

Where, $c'_{p(s-l)} = xc_{p,s}+(1-x)c_{p,l}$ is the sensible heat capacity of the PCM for an non-isothermal phase transition region ($\Delta T_{(s-l)}$). The phase transition region for a non-isothermal process referred to as the mushy zone is neither completely liquid nor solid

Based on eq. (3.6), The PCM's specific capacity, while the temperature equals T_i, is given by calculating the slope of the enthalpy-temperature curve.

$$c_p = \frac{\partial H}{\partial T}$$
(3.8)

Eq. (3.2) can also be written as

$$(m_p c_{p,p}(T_i) + m_t c_{p,t}(T_i))(T_i - T_{i+1}) = hA_t \int_{t_i}^{t_i+\Delta t_i} (T_i - T_a)dt$$
(3.9)

$$(m_p c_{p,p}(T_i) + m_t c_{p,t}(T_i))(\Delta T_i) = hA_t(T_i - T_a)\Delta t_i$$
(3.10)

For a small temperature difference ΔT_i and time increment Δt_i Eq. (3.9) becomes

$$\frac{dT_i}{dt_i} = -\frac{hA_t}{m_p c_{p,p}(T_i) + m_t c_{p,t}(T_i)}(T_i - T_a)$$
(3.11)

According to Newton's law of cooling, the cooling rate follows the exponential decay with time, Eq. (3.10) becomes

$$\frac{dT_i}{dt_i} = -\frac{hA_t}{m_p c_{p,p}(T_i) + m_t c_{p,t}(T_i)}(T_o - T_a).e^{\left(\frac{-hA_t}{m_p c_{p,p}(T_i) + m_t c_{p,t}(T_i)}t\right)}$$
(3.12)

3.3.8 Thermal cycle test

The schematic of the thermal cycle experimental setup is shown in Figure. 3.14. It consists of a hot air blower with a controlled flow rate, and the temperature is connected through well insulated flexible pipe to the heating and cooling chamber. The PCM of 3 gm is placed inside the borosilicate glass tube of 3 mm diameter and length 178 mm (Wilmad^{TM}). The sample tube is held vertically in a testing chamber. The temperature varied from room temperature to above the PCM melting point by integrating the proportional integral derivative (PID) controller and thermocouple (ambient conditions). The PCM temperature is monitored with the RS^{TM}Pro K-type thermocouple, connected to the data acquisition module (DAQ: National Instruments™ TB-9214 module and NI cDAQ 9174) worked on the LabVIEW platform to access the thermal cycle counts.

(a)　　　　　　　　　　　　　　　　(b)
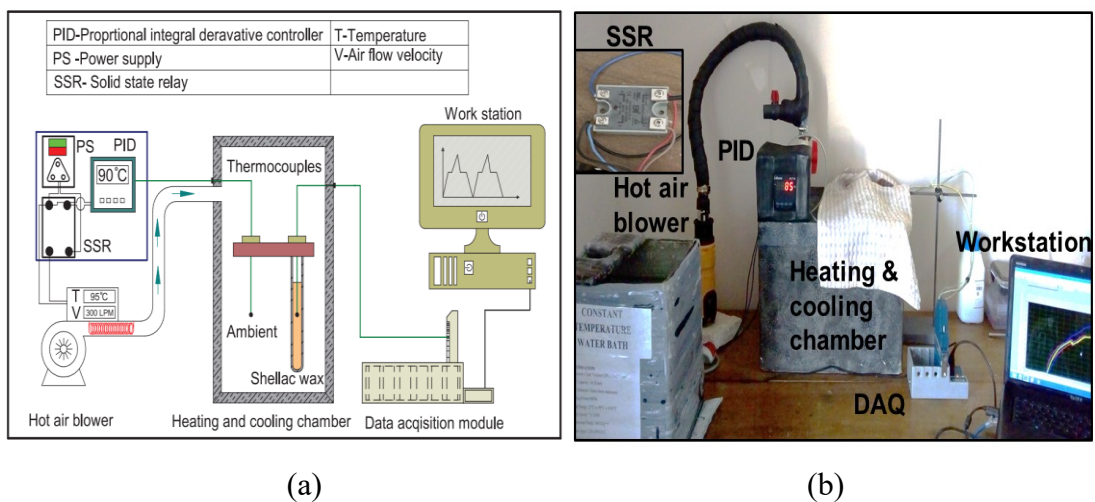
Figure 3.14. Thermal cycle experimental setup (a) Schematic view (b) Pictorial view, NITK Surathkal.

3.4 CLOSURE

Conventional and non-conventional characterization methods, procedures, and mathematical formulation are highlighted in this chapter. The next chapter deals with the effect of the tube aspect ratio in the THM on the thermal properties of PCM.

T-HISTORY ANALYSIS OF ASPECT RATIO EFFECT ON SUBCOOLING AND SOLIDIFICATION BEHAVIOUR OF PHASE CHANGE MATERIAL IN VERTICAL GLASS TUBES

4.1 INTRODUCTION

Subcooling is the effect of cooling a material below its melting temperature without becoming solid. When the temperature is low (at any point in a volume), nucleation starts and the material begins to solidify, called nucleation temperature, for homogeneous nucleation. These are relevant for heterogeneous nucleation, being started by other substances, e.g., nucleators in the PCM or at container walls. Further nucleation depends on time. The PCM exists in the metastable subcooled state below the melting temperature and before the nucleation point. The difference in temperature level between the melting and nucleation point is the DOS. The novelty of this work is to study the effect of aspect ratio on subcooling in THM. DOS affects the latent enthalpy of the material and the requisite property for the proper design of the storage system. It is essential to study the correlation between aspect ratio, cooling rate, sample mass, and subcooling. The data are provided in the certificate of analysis (COA); OM-46 has desired properties is shown in Table. 4.1.

Table 4.1. Thermophysical properties of OM46.

Property (Solid / Liquid)	Value
Melting temperature[a]	48 °C
Freezing temperature[a]	45 °C
Latent heat (48 to 39 °C)[a]	196 kJ/kg
Specific heat (28 °C / 53 °C)[a]	2.5/2.7 kJ/kg·°C
Thermal conductivity (5 °C / 60 °C)[b]	0.2/0.1 W/m·°C
Density (28 °C / 55 °C)[b]	917/880 kg/m^3
Thermal stability[b]	~2000 cycles
Maximum operating temperature[b]	120 °C

Note: [a] Measured data (DSC), [b] Manufacturer's nominal data (PLUSS[R],2019)
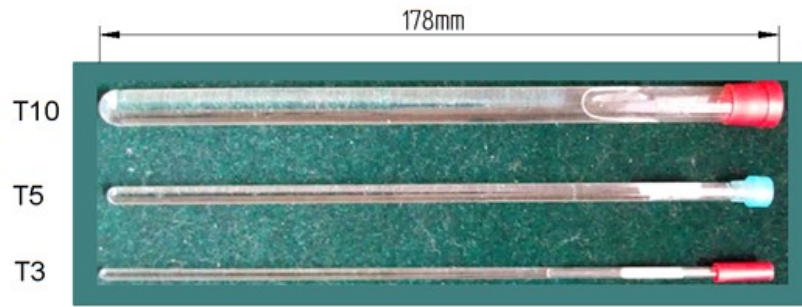
Figure 4.1. The Sample holder of different aspect ratios keeps the length of the tube constant.

Each of the PCM samples, reference, and tubes weighed in analytical balance (Contech[R]-CAI 234) of least count 10 mg and are listed in Table. 4.2.

Table 4.2. Details of T3, T5, and T10 tubes used in THM.

Parameters	T 10	T5	T3
Outer diameter (mm)[a]	9.9935 ± 0.0065	4.97 ± 0.070	2.99 ± 0.030
Inner diameter (mm)[a]	9.070 ± 0.013	4.20 ± 0.070	2.41 ± 0.030
Length (mm)[a]	178	178	178
Mass of PCM (g)	8.31	1.68	0.55
Mass of reference (g)	9.21	1.8	0.62
Mass of tube (g)	5.44	2.55	1
Aspect ratio (Length/Inner diameter)	19.6	42.3	73.8
Biot number (Bi < 0.1)	0.05	0.02	0.01

Note: [a] Manufacturers Data's

The T-history analysis is carried out in two cases, with and without insulation of the tube. Three repeated trials were performed on all the tubes to check the recurrence and deviation of the results.

4.2 Differential scanning calorimetry (DSC)

The DSC heat flow curve of PCM OM46 is shown in Figure 4.2. The zero slopes of the heat flow curve signify sensible heat absorption and discharge without a phase transition. However, the instantaneous slope changes to infinite value revealing the

latent heat absorption or release at a nearly isothermal state with phase change. Extrapolation onset and the endset temperature are used to identify the melting and solidification range of PCM. The heat flow curve from Figure 4.2 shows the onset melting point, and the crystallization point is 47.8 °C and 46.2 °C, respectively. However, the corresponding melting and crystallization peaks are observed at 50.2 °C and 45.1 °C, respectively. DOS evaluated from the DSC heat-flow curve based on the onset-onset approach is 1.6 °C (Wiki PCM, 2019).
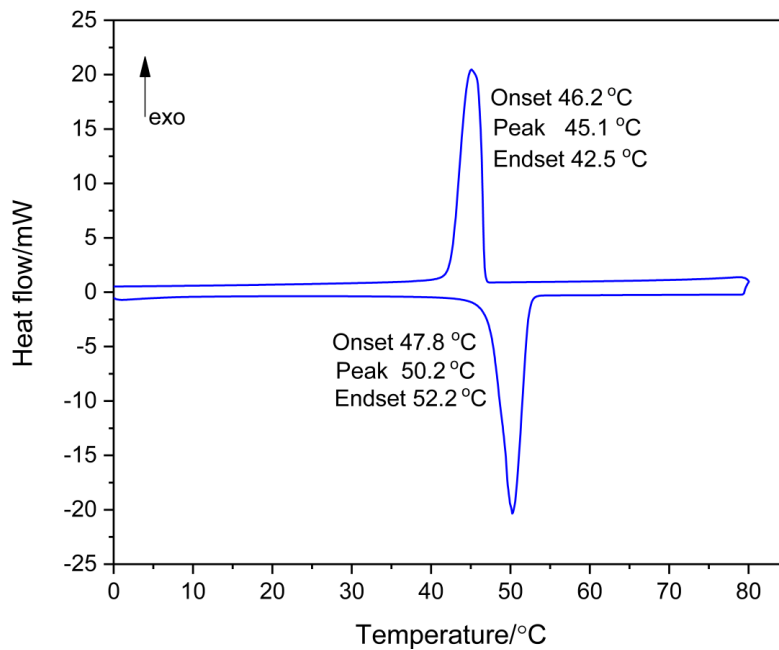
Figure 4.2. DSC heat flow graph of OM46 for heating and cooling run.

4.3 T-HISTORY COOLING INFRARED (I.R.) IMAGE OF THE SAMPLE AND REFERENCE TUBES (T10, T5, AND T3) AT DIFFERENT TIME SPAN.

All three tubes' melting contour at different times is captured using an I.R. thermal camera (Testo 865) of accuracy ± 2 °C as shown in Figure 4.3. The sample (T10S, T5S and T3S) and reference (T10R, T5R, and T3R) tubes were initially at a thermal equilibrium temperature of 60 °C. K- type thermocouple is placed at the center of the tubes to monitor sample variation and reference temperature with time. The cooling process is divided into three regions: the start of the cooling process associated with natural convective motion. The nucleation and phase change process release latent heat, and then solidification is dominated by conduction heat transfer. The I.R. image captured at the different cooling times indicates the time required for temperature

reduction in sensible cooling of PCM before solidification is faster than reference material (distilled water). As the PCM sample undergoes phase change or nucleation, it triggers the latent heat release at an almost constant temperature. At this instant, temperature decrement in PCM tubes is lesser than in reference tubes, as shown in the image captured from 300 to 2500 s. A similar effect is perceived in the temperature-time curve of all three tubes is illustrated in Figure 4.5. The image captured at 30 s indicates that T3R (3mm reference tube) cools faster than T3S (3 mm sample tube).
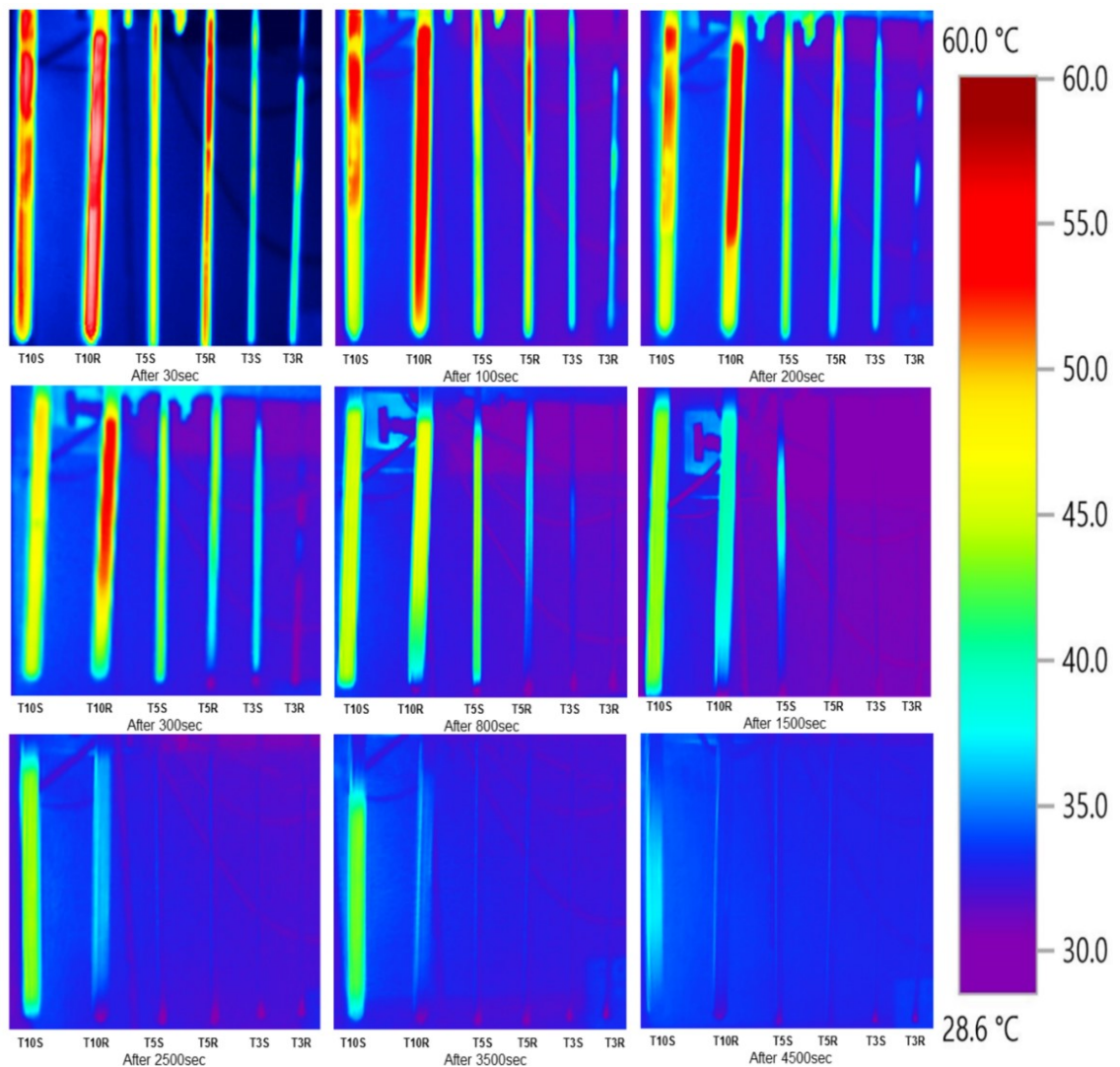
Figure 4.3. I.R. image of T10, T5, and T3 tubes at a different cooling time.

Non-uniform temperature is observed (yellow patches at the center of T3S) even the aspect ratio of the T3S tube is very high. However, this indicates that the achievement of the uniform temperature inside the PCM tubes is hypothetical. Due to the PCM's

density effect, the temperature at the top, bottom, and portion of the PCM, which is in contact with the inner surface of the glass tube, becomes a cold spot, as shown in Figure 4.3 at a different time interval. It is noticed that in different intervals of I.R. contour, nucleation triggers form the inner surface of the glass tube towards the center. Because of adhesion force, the contraction of PCM upon cooling occurs, which makes the cavity at the top face of the PCM, as shown in Figure 4.4.

Figure 4.4. PCM cavity formation inside the tube during the cooling process.

Table 4.3. DOS mean and standard deviation (S.D.) for T3, T5, and T10 trials without insulation

Tubes	Trials	Nucleation temperature (°C)	Melting temperature (°C)	DOS (°C)	DOS (mean ±S.D.) (°C)
T3	1st	44.9	46.5	1.6	1.3 ± 0.2
	2nd	45.3	46.5	1.2	
	3rd	45.2	46.5	1.3	
T5	1st	44.9	46.1	1.2	1.1 ± 0.1
	2nd	45.2	46.2	1.0	
	3rd	45.4	46.6	1.2	
T10	1st	44.6	45.5	0.9	0.8 ± 0.1
	2nd	45.2	45.9	0.7	
	3rd	44.9	45.8	0.9	

This phenomenon is regarded as heterogeneous nucleation. Nucleation points are triggered near the inside glass surface, releasing the latent heat to subcooled liquid PCM to raise its temperature suddenly from subcooling to the temperature near the melting point, where the plateau is formed, as shown in Figure 4.5. T3 tubes cool faster and reach the ambient condition compared to the T5 and T10 due to less material.
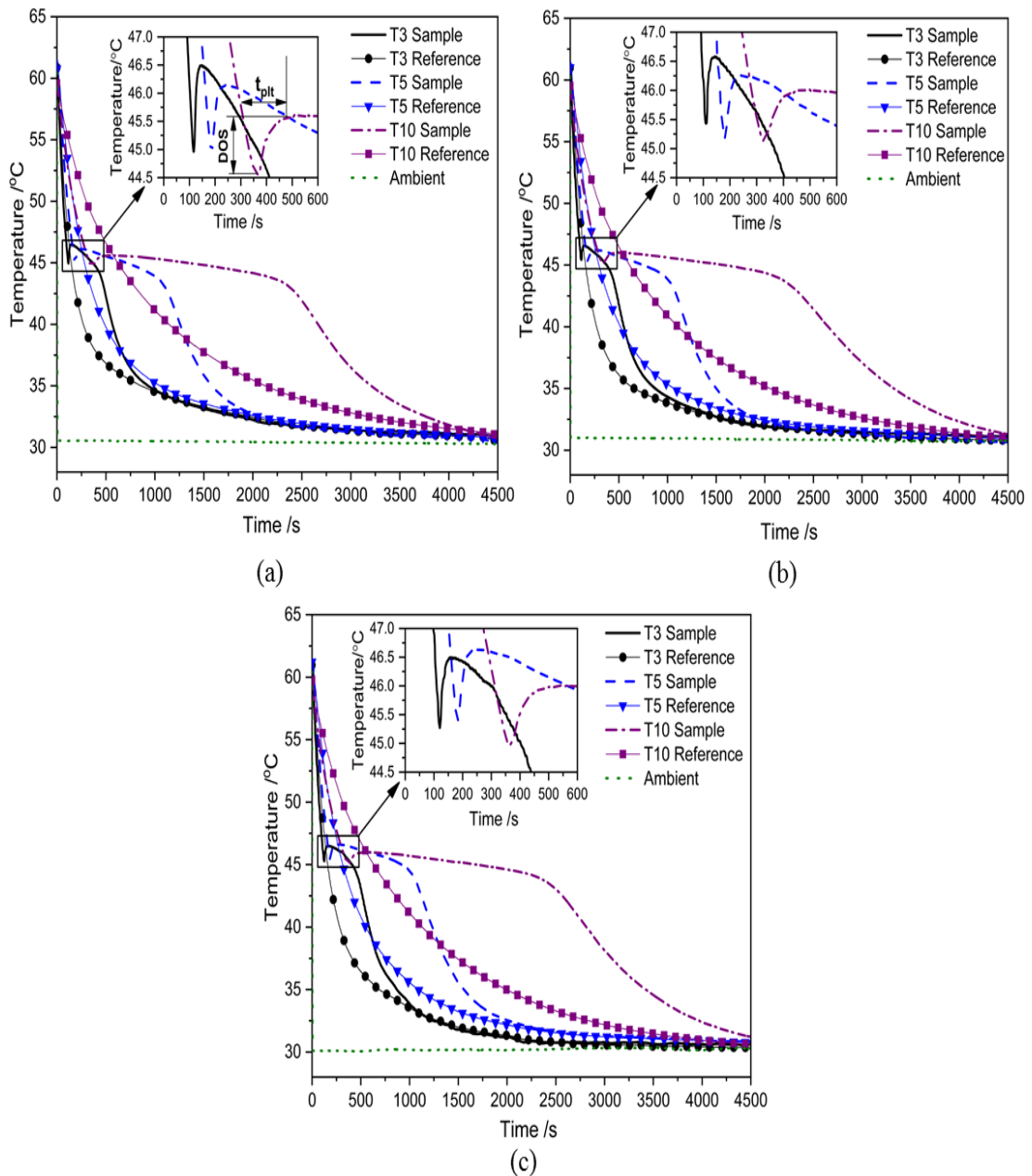
Figure 4.5. Temperature-time cooling curve of T3, T5 and T10 without insulation (a) First trial (b) Second trial (c)Third trial.

However, the I.R. image captured at 800 s indicates that the T3 sample and reference tubes attain a temperature of less than 35 °C. Similar behavior was observed in the T5 tube. Still, the cooling rate of the T5 tube is lesser than the T3 tube due to the higher radius of the tube and more sample material.T5 reference and sample tubes attain ambient condition, and it is shown in the I.R. image captured at 2500 s. The image captured at 4500 s indicates the T10 tube approaches the ambient conditions.

4.4 T-HISTORY COOLING WITHOUT INSULATION

Three repeated trials had been conducted using tubes of different diameters keeping lengths the same, i.e., T10, T5, and T3, respectively. Heating and cooling for all three tubes were carried out in a similar condition, and observation has been made to study the effect of diameter on subcooling. Even though all the tubes cooled at similar conditions, from Figure 4.5, the cooling rate of T3 tubes is higher than that of T5 and T10 tubes due to less diameter and sample mass. The average DOS for three trials is more in the T3 tube due to the high cooling rate. However, the heat released from nucleating points inside the T3 tubes reaches the tube's center very fast compared to the T5 and T10 due to less PCM radial thickness between the inner glass surface and the thermocouple point. Hence, the period in the T3 tube to raise its temperature from the sub-cooling point to the melting point plateau is less. This factor is evident from the temperature-time curve obtained for all the three repeated trials and is shown in Figure 4.5. The DOS for the individual trials of all three tubes and their average value is listed in Table 4.3.

4.5 T-HISTORY COOLING WITH ONE LAYER OF INSULATION

To study the effect of cooling rate on subcooling, T3, T5, and T10 tubes were provided with one layer of nitrile foam insulation of thickness 3 mm and the trials are repeated with the similar cooling condition as considered for the tubes without insulation case. In THM, three cooling trial data of all three tubes were obtained and are plotted as shown in Figure 4.6. The quantitative values obtained from the T-history cooling curve, i.e., nucleation point, melting temperature, and DOS of three trials, are tabulated in Table 4.4. From the calculated average and standard deviation values, it is observed that DOS is in the order of T3 >T5>T10.
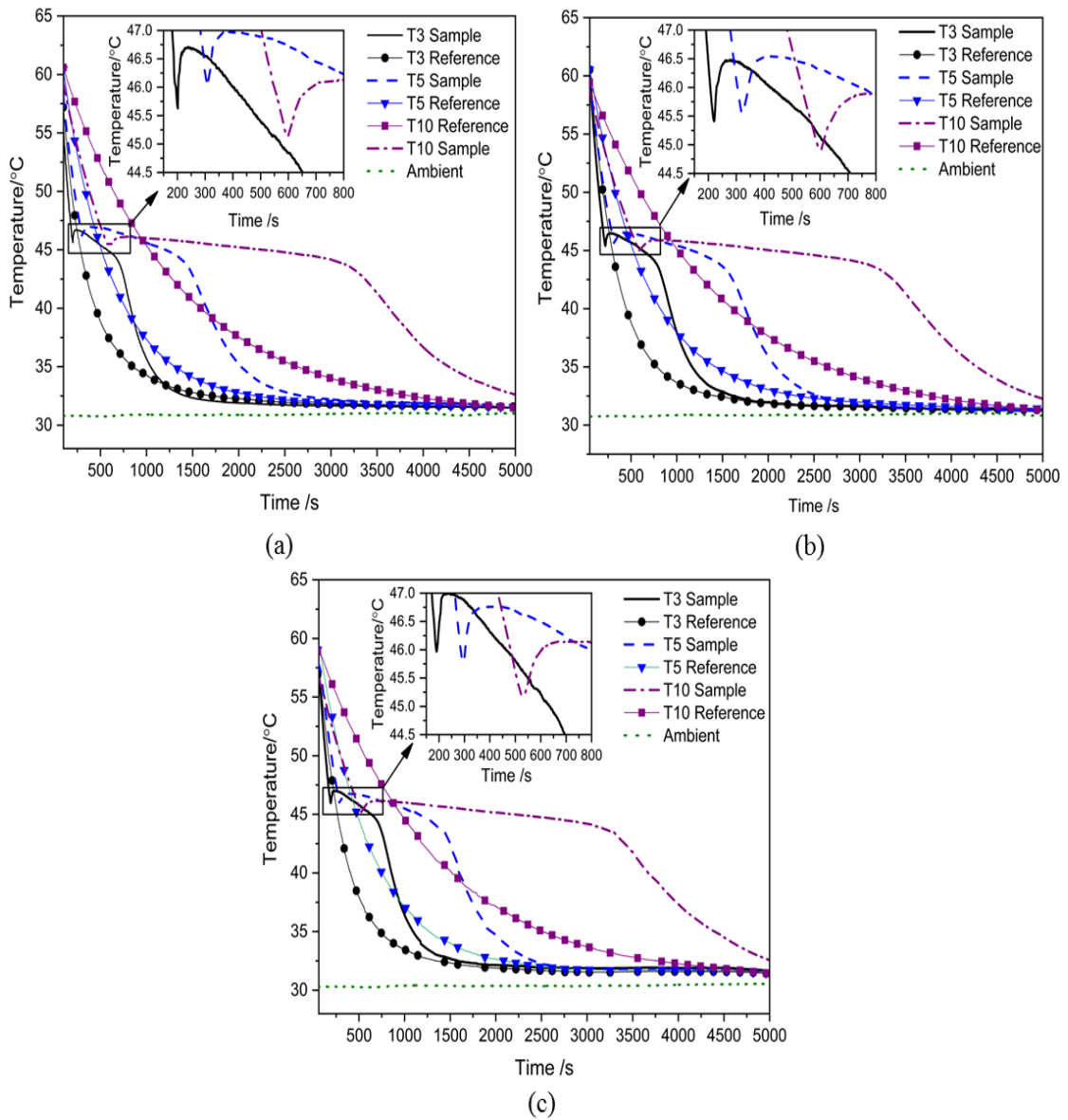
Figure 4.6. Temperature-time cooling curve of T3, T5, and T10 with insulation
(a) First trial (b) Second trial (c) Third trial.

4.6 COMPARISION OF DEGREE OF SUBCOOLING (DOS) WITH AND WITHOUT INSULATION.

Quantitative comparison of DOS values in Table 4.3 and Table 4.4 yields that DOS is less in all insulated tubes indicating that the provision of insulation reduces the cooling rate, and the reduction in the DOS value proves the relation (Eq. 4.1). The hypothetical DOS triangle is shown in Figure 4.7, where the height and base of the triangle indicate

DOS and time to reach a plateau (t_{plt}), respectively. From Figures 4.5 and 4.6, it is observed that the DOS is increasing with an increase in the aspect ratio (i.e., T3>T5>T10). However, the t_{plt} is decreasing with an increase in the aspect ratio (i.e., T3<T5<T10). From the analysis of tubes with one layer of insulation, a reduction is noticed in DOS as compared with the respective tubes without insulation.

Table 4.4. DOS mean and standard deviation (S.D) for T3, T5, and T10 trials with insulation.

Tubes	Trials	Nucleation temperature (°C)	Melting temperature (°C)	DOS (°C)	DOS (mean ± S.D) (°C)
T3	1st	45.6	46.6	1	1 ± 0.1
	2nd	45.4	46.3	0.9	
	3rd	45.9	47	1.1	
T5	1st	46	47	1	0.8± 0.15
	2nd	45.7	46.4	0.7	
	3rd	45.9	46.7	0.6	
T10	1st	45.1	45.6	0.5	0.6± 0.1
	2nd	44.8	45.5	0.7	
	3rd	45.2	45.8	0.6	
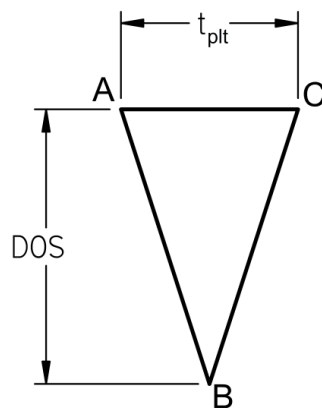
Figure 4.7. DOS triangle

$$(dT/dt)_{cooling} \alpha \; DOS \hspace{5cm} (4.1)$$

However, the t_{plt} has no considerable changes noticed between insulated and non-insulated tubes during a similar cooling condition. In insulated tubes, heat exchange is controlled between PCM and ambient as compared with the non-insulated tubes. The insulated tube facilitates more sensible heat transfer from nucleation sites to the PCM around the thermocouple. However, it proves that insulation affects the cooling rate (*dT/dt*) only. Neither it affects the nucleation progress nor the release of sensible heat at the nucleation site to reach the plateau or melting point (t_{plt}). Due to more sample mass in higher diameter tube, heterogeneous nucleation triggers at the inner surface of the glass tube take more time to reach the released sensible heat towards the tube center where the thermocouple is placed. So discharge time or time required to attain a plateau (t_{plt}) is more in higher diameter tubes (Eq. 4.2). Therefore,

$$d_t \text{ or } m_p \alpha \ t_{plt} \tag{4.2}$$

Where d_t - Tube diameter, m_p - Sample mass (PCM) and t_{plt} - Time required to reach plateau or melting point.

4.7 CLOSURE

This chapter deals with the effect of the tube aspect ratio on subcooling and the solidification behavior of PCM using the THM and is compared with the DSC analysis. The next chapter deals with the thermal property study of the fatty acid mixture as BPCM.

CHAPTER-5

THERMAL PROPERTY STUDY OF THE FATTY ACID MIXTURE AS BIO-BASED PHASE CHANGE MATERIAL FOR SOLAR THERMAL ENERGY STORAGE USAGE IN DOMESTIC HOT WATER APPLICATION

5.1 INTRODUCTION

The PCM should have suitable thermal properties such as a phase-transition within the operating temperature range, a high latent heat of enthalpy per unit volume to permit a small size of the storage container, a high specific heat to deliver or store sensible heat storage, a high thermal conductivity, less volume change during the phase transition and economically less expensive (Sharma et al. 2009). Since the PCM is the core material for LHTES, studying the PCM thermal properties forms a crucial part of the proper design, simulation, and applications in various aspects (Sukontasukkul et al. 2019). Generally, thermal characterization of PCM is performed through differential scanning calorimetry (DSC). This technique is significant for thermal characterization because PCM transition temperature, enthalpy, and specific heat can be found in fewer periods and considerably less procedure. DSC heating and cooling rate are higher than the practical application. The sample mass is considered to range from 2 to 50 milligrams, leading to subcooling and shifting phase change temperature in the bulk application (Lazaro et al. 2006; Gunther et al. 2009). THM has the great benefits of simple construction, economical and simultaneous evaluation of bulk and inhomogeneous PCM samples. However, the suitable operating temperature for domestic water heating ranges from 49 to 60 °C (Levesque et al. 2004). The occupational safety & health administration (OSHA) recommends water temperature between 52 to 60 °C to minimize the growth of Legionella and other micro-organisms. In this regard, the OM55 with a nominal melting point of 57 °C has been chosen for this study. Commercially accessible PCMs are generally proprietary, and fewer technical details hinder the performance evaluation in an application. A thorough PCM study is required to get the correct thermo-physical properties of PCMs for design, simulation, and its applications. This study aims to analyze the thermal properties of the organic PCMs using TGA, DSC, TCA, and THM for application in domestic solar water heating (DSWH).

5.2 Thermo gravimetric analyser (TGA)

Thermal stability analysis is performed for the BPCM OM55 to study the thermal degradation within the operating temperature. In this analysis, the maximum stable temperature and final degradation temperature are measured.
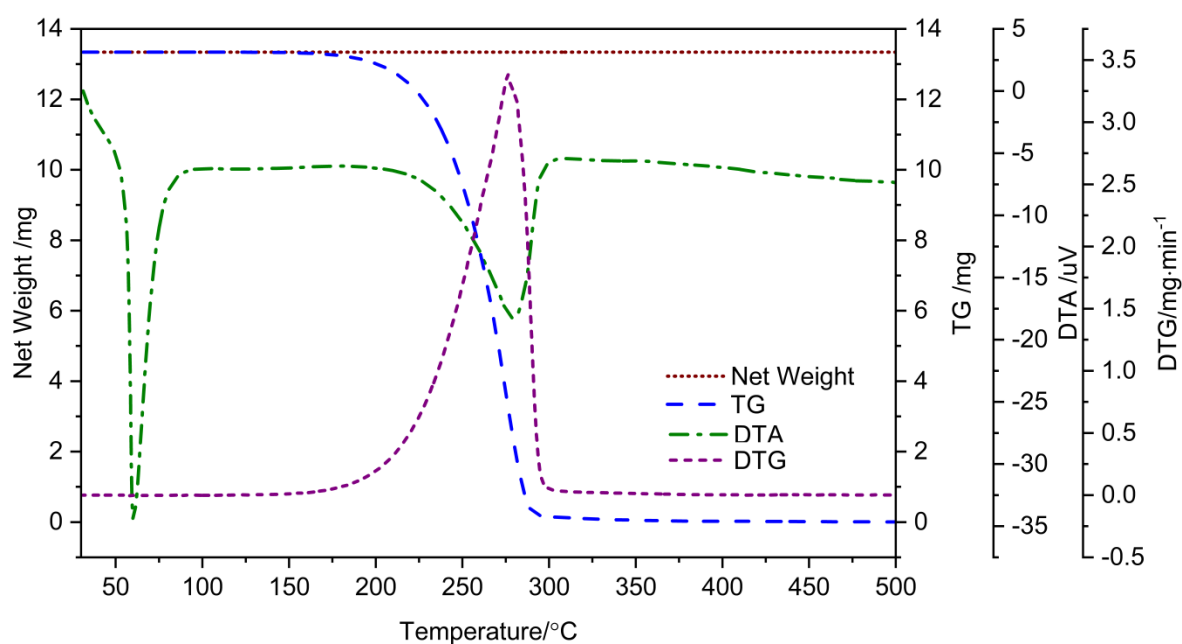
Figure 5.1. TG, DTA and DTG curves for OM55 at 10 °C/min heating rate under an inert atmosphere.

The maximum stable temperature is defined as the sample's temperature to lose 1.5 wt% of the initial weight. T.G. curve of OM55 is shown in Figure 5.1, indicating the maximum stable temperature is 154.6 °C. Above this point, a higher reduction in PCM mass due to vaporization and hydrocarbon degradation. The final degradation temperature is 297 °C. At this point, almost complete weight loss occurs. Derivative T.G. (DTG) curve permits the direct application of the rate function of the transformation in weight during TGA (Zhang et al. 2016). DTG curve degradation peaks are observed at 275.7 °C. Differential thermal analysis (DTA) curve indicates two maximum endothermic transition peaks, one at 59.5 °C due to phase change from solid to the liquid state and the second peak at 278.3 °C due to vaporization (liquid to vapor). This study signifies that the maximum stable temperature of OM55 is much higher than the operating temperature range. However, OM55 is thermally stable for the DSWH application temperature range.

5.3 Differential scanning calorimetry (DSC)

The variation of heat flow with temperature is shown in Figure 5.2. Zero curve slopes indicate the sensible heat storage and discharge before and after the phase transition as the PCM sample starts heating and cooling in the crucible. The instant slope changes remarkably and reaches the infinite value, which means heat is being absorbed or released at a nearly constant temperature in the PCM sample, which shows melting and solidification onset temperature. In the heating curve, the slope change reaches the maximum point or endothermic peak at 57.7 °C. However, the end of the melting process is at 58.7 °C. The melting point of OM55 is considered using an extrapolated onset temperature of 54.8 °C.
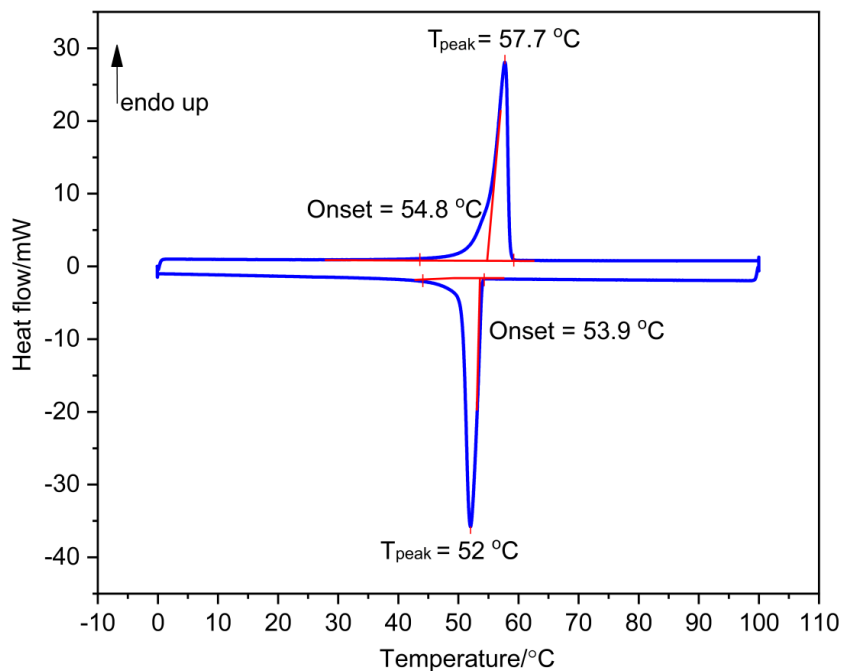
Figure 5.2. DSC heat flow graph of OM55 for heating and cooling run.

The cooling curve infers extrapolated onset solidification point at 53.9 °C and an exothermic peak temperature at 52.0 °C. There is no indication of solid-solid transition before melting and after solidifying the heating and cooling process the enthalpy's change during the heating and cooling cycle over a narrow temperature range. The hysteresis between melting and solidification peak is 5.7 °C. The isothermal enthalpy of fusion over the melting process is found to be 175 kJ/kg. However, the isothermal crystallization enthalpy is found to be 170.1 kJ/kg. DOS of OM55 is evaluated based

on the onset-onset approach, and it is calculated as 0.9 °C. The variation of specific heat with the respective temperature is shown in Figure 5.3. The mean value and the standard deviation (S.D.) of the solid specific heat for the sensible cooling over the temperature range of 40 to 0 °C is found to be 2.7 ± 0.3 kJ/kg·°C. However, the liquid-specific heat over the temperature range of 99 to 60 °C is 3.1 ± 0.1 kJ/kg·°C.
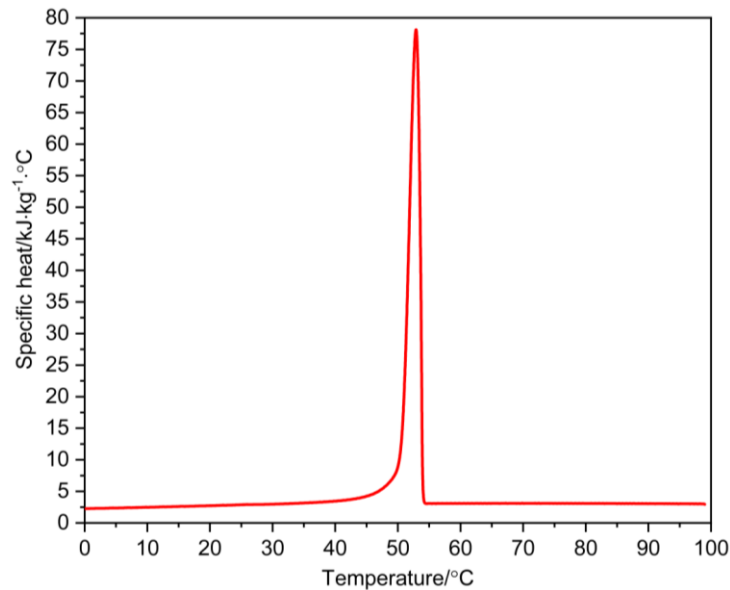
Figure 5.3. Variation of specific heat of OM55 with temperature during the cooling run.

5.4 Thermal constant analyser (TCA)

The thermal conductivity of OM55 is evaluated based on the mean and standard deviation of four repeated trials conducted at the specified temperature. The measured heat conductivity in the solid-state at 30 °C is 0.21 ± 0.018 W/m·°C and liquid sample at 66 °C is 0.19 ± 0.015 W/m·°C. The solid and liquid conductivity is 0.9 W/m·°C and 0.2 W/m·°C, which is higher than the supplier's data due to the measuring condition and equipment accuracy.

5.5 T-history method (THM)

The tube holder contains the sample and reference material placed inside the thermostatic water bath. The water bath temperature is maintained at 70±0.2 °C and is well above the PCM's nominal melting temperature. Four repeated heating and cooling trials of the sample and the reference material are shown in Figure 5.4. All the results obtained in the THM method is based on consideration of the mean of the four trials

and standard deviations. For the quantification of the specific heat and enthalpy, both heating and cooling curves have been evaluated. The repeated four THM sample and reference heating curve tests, heating rate, and ambient curve are shown in Figure 5.5.
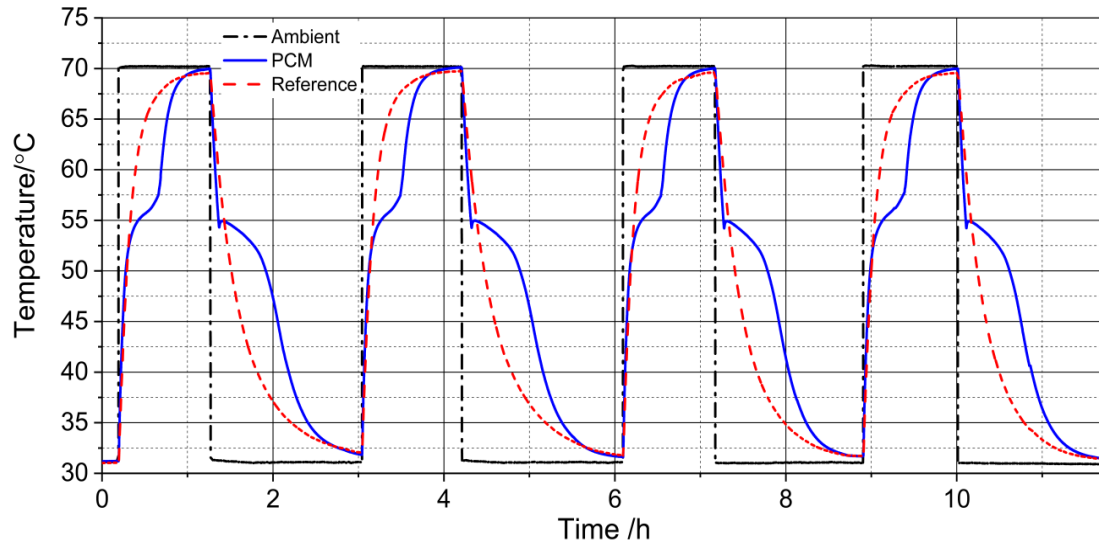
Figure 5.4. THM (experimental) variation of temperature to time during heating and cooling trials.

The sample and reference temperature increase steeply from ambient conditions at 31 ± 0.2 °C (A). On continuing the heating process, the PCM sample curve temperature is deviating and incrementing forehead than the reference material, observed between temperature ranges from 32 to 50 °C as illustrated in Figure 5.4. This behavior is due to PCM's lesser heat capacity than the reference material within the PCM sensible heat solid region (A-B). As the heating time proceeds further, it is notable that the PCM heating curve approaches towards the reference curve and intersects at 51.5 ± 0.6 °C. However, above the intersection point, the heating rate comes close to zero between points B to C due to more energy absorption (non-isothermal phase transition). Point C is the inflection point (Hong et al. 2004; Peck et al. 2006), which denotes the end of phase transition at 59 ± 0.5 °C. Furthermore, PCM drastically increases the temperature and changes its slope due to PCM's sensible heat liquid region (CD), associated with less heat capacity than reference material. A similar trend has been observed in DSC endothermic reaction as shown in Figure 5.2 with minor differences due to the PCM

volume considered and high precision of the DSC instrument than THM experimental method.
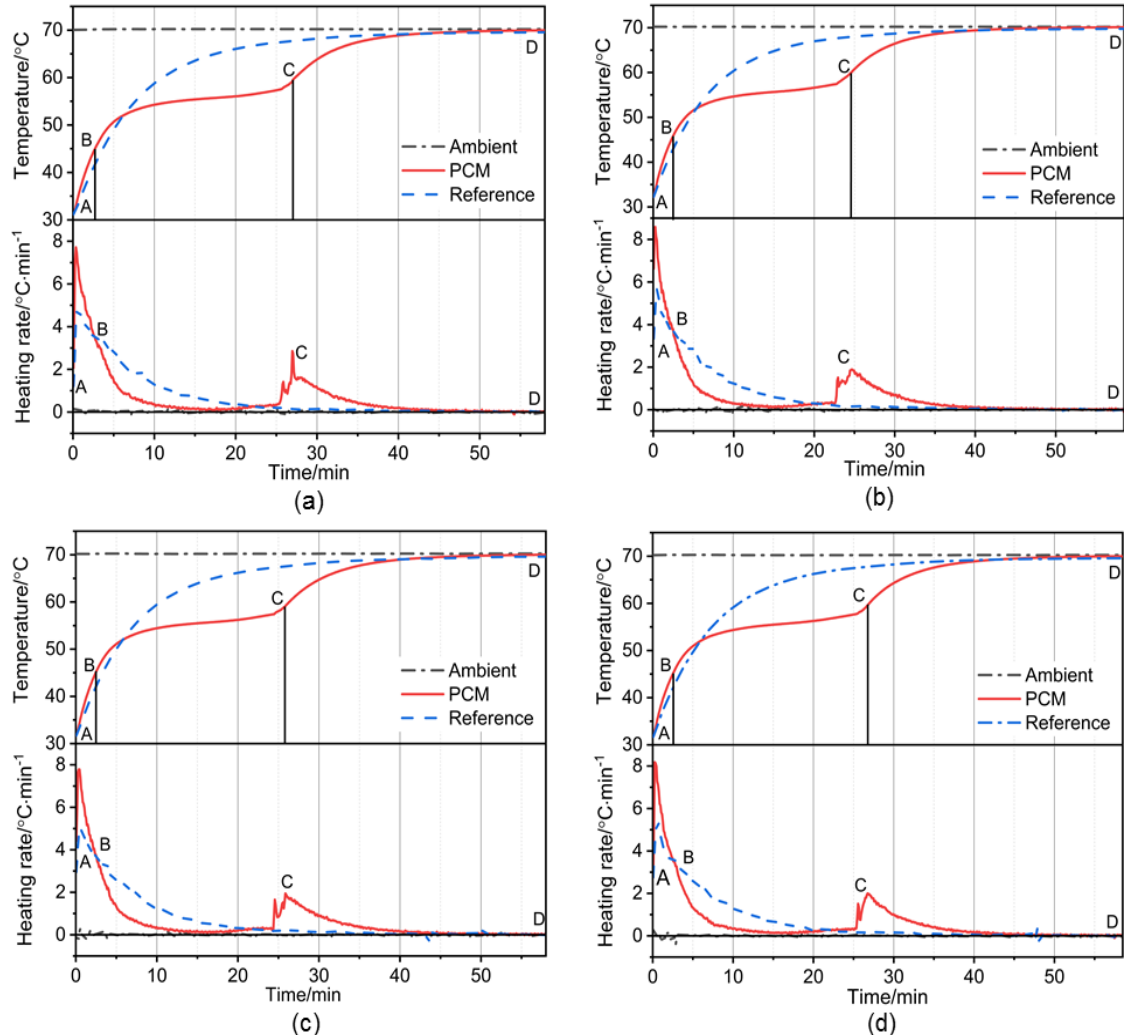
Figure 5.5. Variation of temperature and heating rate to time (a) THM-I (b) THM-II (c) THM-III (d) THM-IV.

However, as the PCM and reference sample temperature approaches the water bath temperature, both tubes are placed in the motionless air chamber in which cooling takes place. The repeated four THM samples and reference cooling curve, cooling rate, and ambient curves are shown in Figure 5.6, which is considered to evaluate the end of the phase transition and DOS. However, enthalpy and specific heat are assessed based on the enthalpy curve (Marin et al., 2003) obtained from the numerically coded mathematical relation. Point E indicates the starting point of the cooling temperature, 69.6 ± 0.2 °C. The curve EF signifies the sensible cooling of liquid PCM. Point F is the

subcooling point below the phase change temperature, where the nucleation is triggered and found to be 54.3 ± 0.1 °C. From point F, some sensible heat is utilized to raise the temperature to the melting temperature (point G). This effect can be observed in the PCM cooling rate curve crossing 0 datum to the positive value, signifying the utilization of heat released by nucleating molecules with the surrounding molecules in the PCM domain.
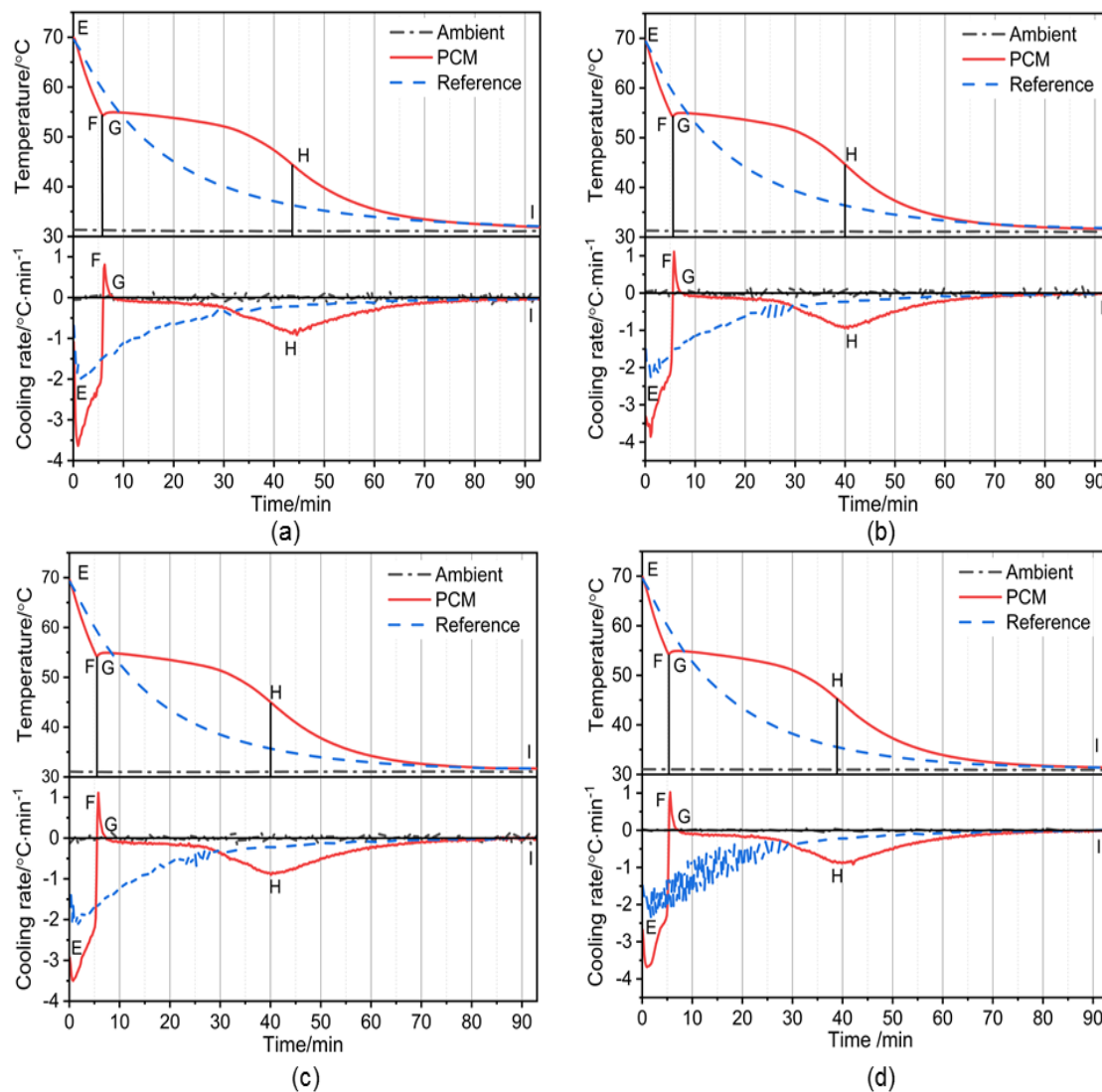
Figure 5.6. Variation of temperature and cooling rate to time (a) THM-I (b) THM-II (c) THM-III (d) THM-IV.

This amount of heat released is thus not obtainable to keep the PCM's temperature at the end of the plateau, and the temperature falls sooner. The phase change plateau is formed at 55 ± 0.1 °C, and phase transition ends at point H found to be 46 ± 0.5 °C. H

is the point at which the cooling rate of the PCM curve becomes minimum, so-called the point of inflection (Hong et al. 2004), which signifies the end of the phase change period (G-H). However, sensible heat release to the surrounding is marked as H to I in the solid region. The latent heat evaluated considering the inflection point as the end of the phase transition is in good agreement with the DSC data presented in Table 5.1.

5.6 COMPARISON OF DSC AND THM
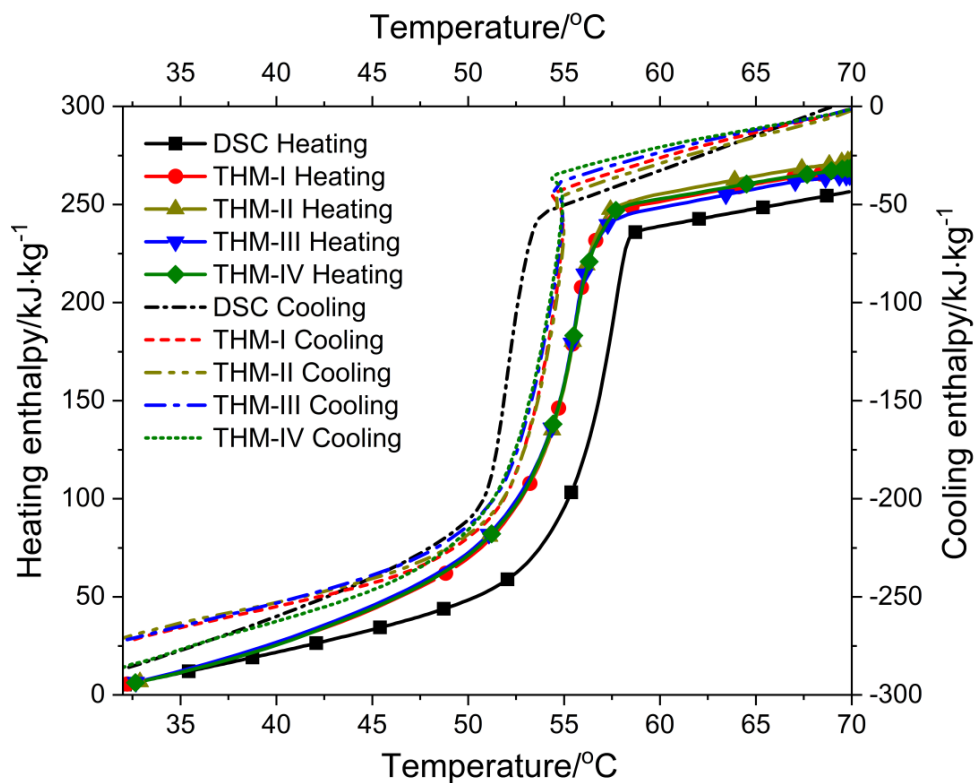
Figure 5.7. Non-isothermal heating and cooling enthalpy (ΔHp (T)) of DSC and THM trials.

Figure 5.7 shows a non-isothermal heating and cooling enthalpy of DSC and THM trials. The enthalpy evaluated in the four repeated THM trials is 209 ± 3 kJ/kg in a range between B to C. However, the DSC non-isothermal enthalpy is 201.2 kJ/kg. Iso-thermal heating enthalpy of THM and DSC evaluated as 180 ± 2 kJ/kg and 175 kJ/kg respectively. The solidification point in DSC is 53.9 °C, and the DOS is found to be 0.9 °C. However, less sample material and a high cooling rate (5 °C/min) are considered in the DSC than THM, which is marginally higher. The phase change heat released by the nucleating molecules is insufficient to raise the neighbouring molecule's sensible

temperature towards the melting temperature. Hence, in DSC crystallization enthalpy, no peak or slope change after the nucleation has been noticed. The THM cooling nucleation triggers at 54.3 ± 0.1 °C, and then raises the sensible temperature of neighbouring molecules to the melting temperature of 55 ± 0.1 °C.

Table 5.1. Comparison of OM55 results obtained in THM trials, DSC, and supplier's data.

Test method	Melting point	Solidification or nucleation Point	Degree of subcooling ($\Delta T_{sc}=T_m-T_s$)	Solid specific heat	Liquid specific heat	Sensible heat during the transition	Non-isothermal enthalpy change	Isothermal enthalpy change
	T_m (°C)	T_s (°C)	ΔT_{sc} (°C)	$c_{p,s}$ (kJ/kg·°C)	$c_{p,l}$ (kJ/kg·°C)	$c_{p\,(s\text{-}l)}^{'}\Delta T_{(s\text{-}l)}$ (kJ/kg)	$\Delta H_p(T)$ (kJ/kg)	ΔH (kJ/kg)
THM Mean±SD	55 ± 0.1	54.3±0.1	0.7± 0.1	2.3± 0.3	2.6± 0.4	29 ± 1[a] 22 ± 1[b]	209± 3[a] 198± 2[b]	180± 2[a] 176 ± 3[b]
DSC	54.8	53.9	0.9	2.7 ± 0.3	3.1± 0.1	26.2[a] 19.8[b]	201.2[a] 189.9[b]	175[a] 170.1[b]
Supplier data	57	55	N.A[c]	2.68	2.76	N.A[c]	188	

Note: [a]Heating run, [b]Cooling run, [c] NA-Not Available

Which effect the significant difference in THM and DSC analysis, and the quantitative results are tabulated in Table 5.1. Further on, the continuous release of the latent heat over a temperature range of 8 ± 0.3 °C is 198 ± 2 kJ/kg in THM and DSC temperature range is 6.8 °C and 189.9 kJ/kg. To obtain the actual latent enthalpy independent of the phase transition temperature by subtraction of sensible heat contribution over the non-isothermal phase change calculated using Eq. 3.7. For THM repeated trials, the sensible heat absorbed and released during the phase change is 29 ± 1 kJ/kg and 22 ± 1 kJ/kg, respectively. However, in DSC, sensible heat absorption and release during the phase change are evaluated as 26.2 kJ/kg and 19.8 kJ/kg [$\Delta T_{(s\text{-}l)}$], respectively. The mean and standard deviation of isothermal enthalpy change (ΔH), the specific heat of solid and liquid state of four THM trials, and DSC result are calculated and listed in Table 5.1.

5.7 CLOSURE

In this chapter thermal property study of fatty acid mixture as BPCM using DSC and THM. Simple correlations are proposed for the isothermal enthalpy change of BPCM. The evaluation of transition temperature, isothermal enthalpy, and specific heat by THM are well compared with the DSC analysis. The next chapter deals with the thermophysical and rheological analysis of natural shellac wax as BPCM.

CHAPTER-6

THERMO-PHYSICAL ANALYSIS OF NATURAL SHELLAC WAX AS NOVEL BIO-BASED PHASE CHANGE MATERIAL FOR MEDIUM TEMPERATURE THERMAL ENERGY STORAGE APPLICATIONS

6.1 INTRODUCTION

The high energy density of latent heat storage makes it more competent than other types of TES systems. Studying thermophysical and rheological properties of PCM is required for effective storage design, simulation, and applications. BPCM is renewable and eco-friendly. This chapter aims to characterize the shellac wax, a BPCM, as a feasible TES alternative for medium-temperature applications. FTIR, TGA, DSC, TCA, Rheometer, and Pycnometer are employed to study thermo-physical properties. The behavior of bulk quantity is tested with THM and compared with that of DSC. Finally, the thermal stability and reliability of shellac wax are established using the thermal cycle test.

6.2 FOURIER TRANSFORMS INFRARED SPECTROPHOTOMETER (FTIR)

All organic compounds have a C-H set of vibrations observed in the hydrocarbon spectra. The simple C-H stretching vibrations and the corresponding simple bending vibrations of saturated aliphatic species arise between 2800 to 3000 cm^{-1} and 1500 to 1300 cm^{-1}. The methylene groups' C-H asymmetric and symmetric stretch vibration occurs at 2915 cm^{-1} and 2855 cm^{-1}, respectively. In common, this standard matches most sets of vibrations. Indeed, there is always a difference, and correction of the interpretation is due to entropy-related and induced electronic effects. The FTIR spectra of shellac wax (Figure 6.1) predict the C-H stretching vibrations at 2915 and 2847 cm^{-1} due to strong CH_2 bonds and a small band at 2956 cm^{-1} due to the CH_3 group. The sharp band at 1465 cm^{-1} signifies CH_2 is bending and rocking vibrations at 721 cm^{-1} due to methylene and C-H bending vibrations at 1465-1377 cm^{-1} region due to aliphatic hydrocarbon. Stretching vibration is at 1737 and 1171 cm^{-1} due to vC=O and vC-O, the fatty acid ester of carboxylic groups. The band's overall absorption is not more than 3000 cm^{-1}, indicating the absence of unsaturated (C=C group) or aromatics and the presence of aliphatic compounds. The main absorption is 2915cm^{-1}, 2847 cm^{-1}, 1465

cm^{-1}, and 721cm^{-1} due to the presence of long linear aliphatic chain (Coates 2006). Aliphatic saturated hydrocarbon is the main constituent in paraffin wax and fatty acids (methylene esters) (Fortuniak et al., 2013). The melting temperature of the organic PCM depends on the length of the hydrocarbon chain.
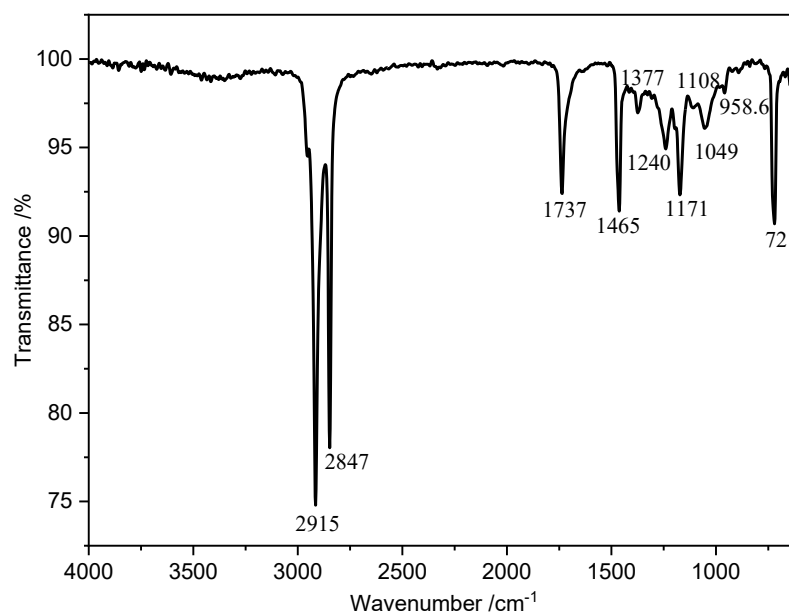
Figure 6.1. The infrared spectrum of shellac wax.

6.3 THERMO GRAVIMETRIC ANALYSIS (TGA)
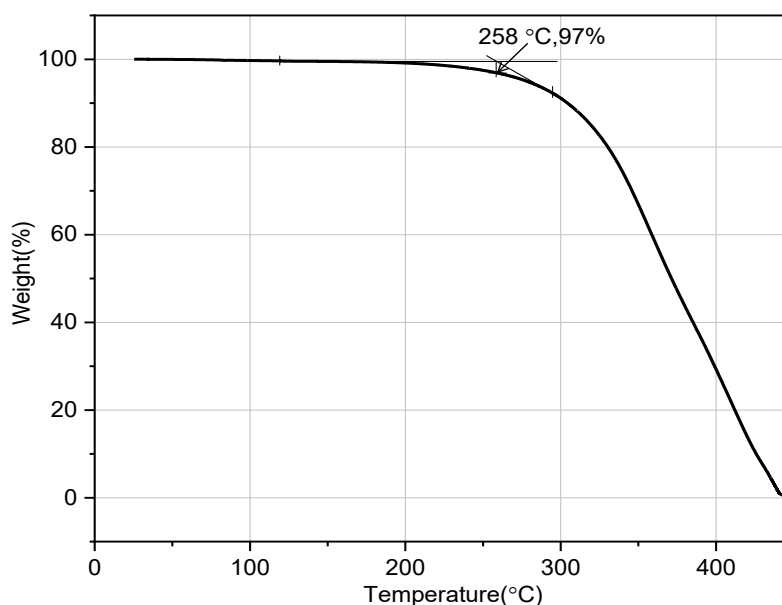
Figure 6.2. TGA curves for shellac wax at heating rates of 5 °C/min under an inert atmosphere.

The weight of the sample is measured during the analysis, as shown in Figure 6.2. The decomposition's onset temperature is reported at 258 °C, and the weight loss at the instant is 3.0 %, with the complete decomposition temperature being about 448 °C. Shellac wax has thermal stability (~ 258 °C) above its operating temperature range.

6.4 THERMAL CONDUCTIVITY

Four repeated trials were conducted on the same sample to calculate the mean and standard deviation (SD). The measured thermal conductivity of solid shellac wax is 0.33 ± 0.05 W/m·°C at 24 °C, and the liquid state is 0.31 ± 0.02 W/m·°C at 85 °C. It signifies that thermal conductivity decrease with an increase in temperature. The thermal conductivity of shellac wax in a solid and liquid state is comparable with the present PCMs.

6.5 DSC ANALYSIS

Extrapolation onset and offset temperature are used to identify the melting and solidification range of PCM. The heat flow curve from the Figure 6.3 depicts three melting and crystallization peaks between onset and offset temperature of 50.5 to 81.5 °C and 73 to 48 °C, respectively.
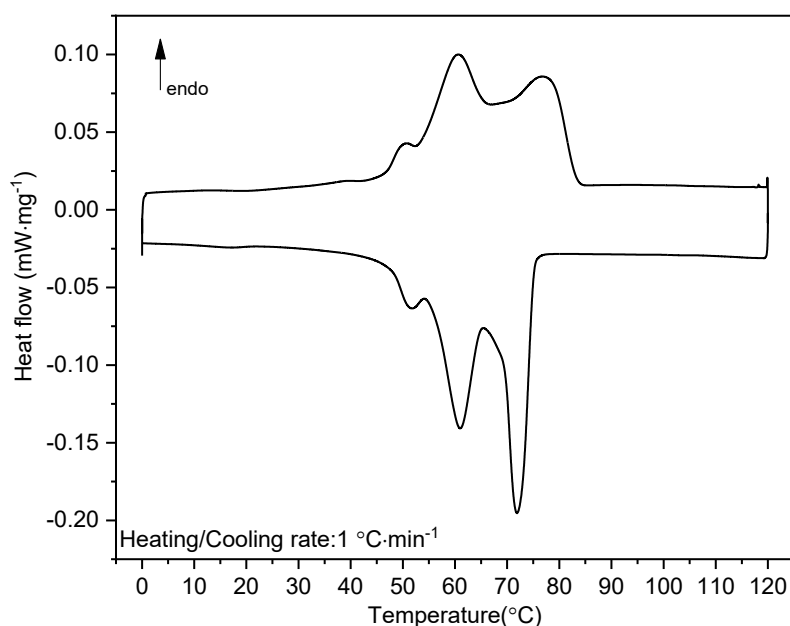
Figure 6.3. DSC heat flow Curve for heating and cooling run.

The three peaks formed during the melting and solidification cycle are due to the wax content's first and second-order transition, resulting in wider endothermic and exothermic peaks. From the DSC graph in Figure 6.3, the melting and solidification peak is 79.5 °C and 71.5 °C. Melting enthalpy of 148 kJ/kg and crystallization enthalpy of 161 kJ/kg for a temperature range of 50.5 to 81.5 °C and 73 to 48 °C, respectively (Figure 6.4 (a)).
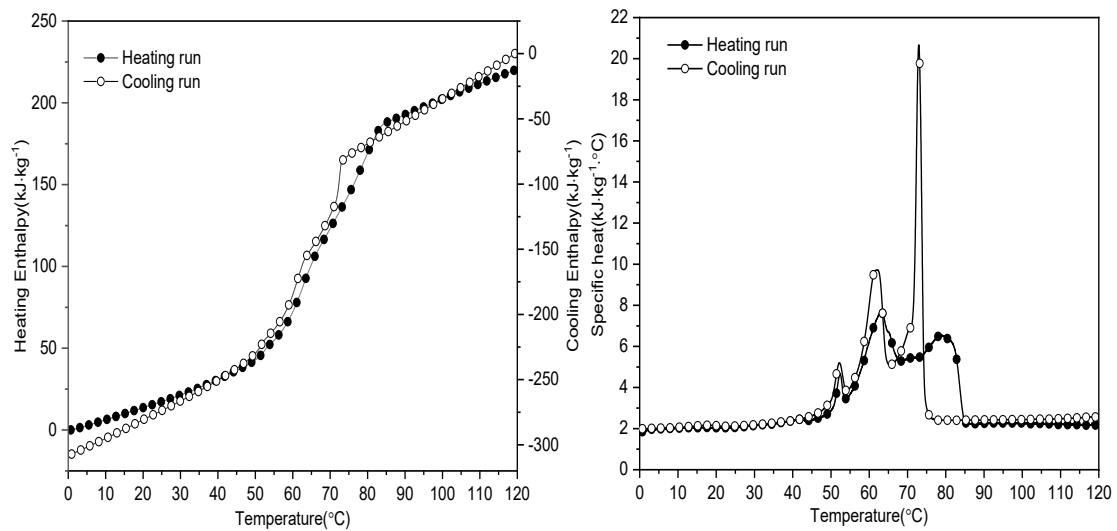
Figure 6.4. DSC (a) Enthalpy variation with temperature and (b) Specific heat variation with temperature.

The difference in enthalpy of fusion and crystallization, i.e., due to supercooling phenomena or hysteresis shown in Figure 6.4(a), can be controlled by opting for lower heating-cooling rates with a higher thermal mass. The specific heat curves for the heating and cooling run are depicted in Figure 6.4(b). The mean specific heat of solid and liquid state is obtained as 1.9 kJ/kg·°C (for a temperature range of 25 to 40 °C) and 2.1 kJ/kg·°C (for a temperature range of 85 to 100 °C), respectively.

6.6 EXPERIMENTAL T-HISTORY METHOD

Initially, it is observed that the rise in temperature for the sample is higher than the reference material upon heating. However, a counter-trend is obtained above 50 °C up to 81.7 °C. After the phase transition, the sample temperature rises higher than the reference material (Figure 6.5). It indicates that the shellac wax's specific heat capacity is lower than the reference material in a solid and liquid state. However, as the transition progresses, it absorbs higher energy than the reference material. The specific heat and

latent enthalpy of shellac are quantified by interpreting the energy discharge graph (Figure 6.6(a)). The inflection point is marked to identify the end of a phase change process (Hong et al. 2004). However, the determination of solid specific heat was reported with discrepancies in the literature.
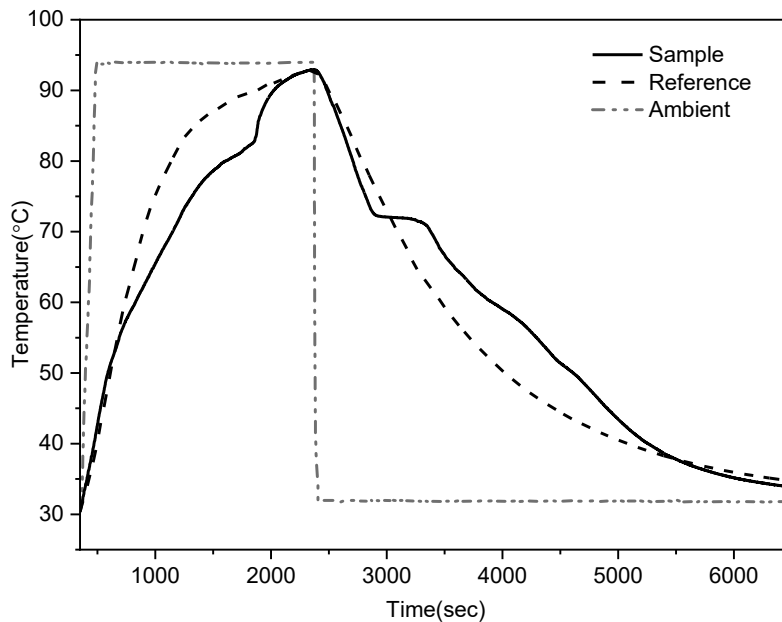
Figure 6.5. Temperature variation with charging and discharging time for the shellac wax and reference sample.

Hence, the cooling rate has been adopted only to define the transition period (A-D) in the temperature-time curve (Figure 6.6(a)). Another methodology is adopted to determine the specific heat of solid and liquid states (Marin et al., 2003). A significant variation in the PCM's sensible heat capacity is observed during the transition period. Due to this, a noticeable change is found in the shape of the cooling rate curve. AB and BD represent the phase change period and the second-order transition, respectively (Figure 6.6(a)). The crystallization temperature of the shellac wax is found to be 72.3 °C. Enthalpy is computed from the temperature-time curve and is as shown in Figure 6.6(b). The specific heat variation with temperature is plotted in Figure 6.6(c). The shellac wax's latent heat is 210.5 kJ/kg (for curves A to D). The specific heat of solid and liquid shellac wax is calculated over a temperature range is 2.1 ± 0.2 kJ/kg·°C and 2.2 ± 0.2 kJ/kg·°C, respectively.
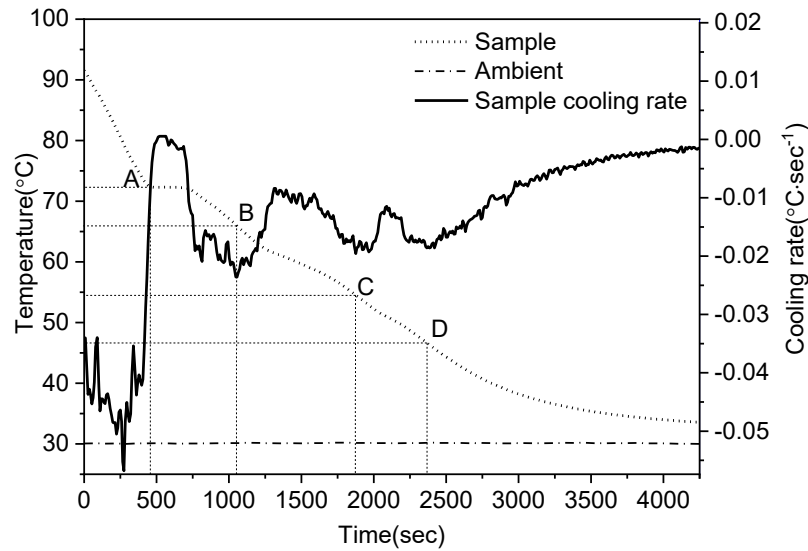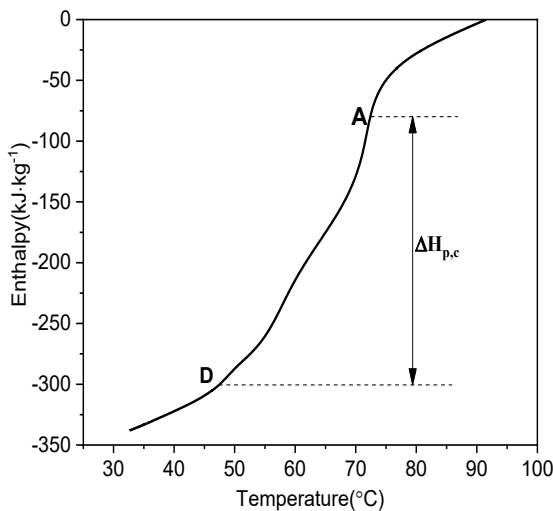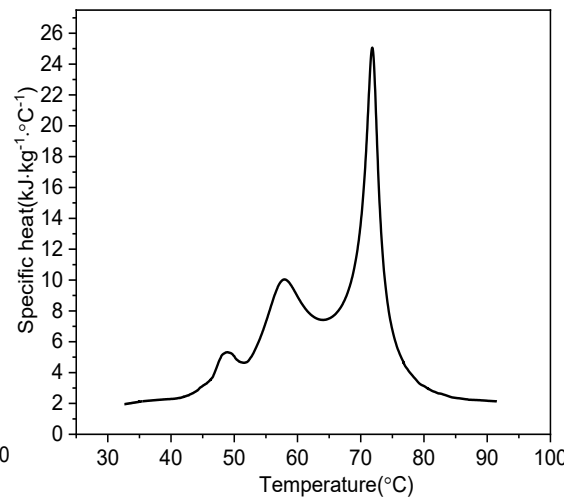
Figure 6.6. Experimental analysis of T-history method for the variation of shellac wax (a) temperature and cooling rate with time (b) enthalpy with temperature (c) specific heat with temperature.

6.7 COMPARISON OF DSC AND THM

A DSC enthalpy and specific heat comparison with the experimental THM is shown in Figures 6.7 (a) and (b). The crystallization enthalpy and peak difference between THM and DSC analysis is 49.5 kJ/kg·°C and 0.8 °C, respectively.

$$\Delta T_{sc} = T_{p,m}^{peak} - T_{p,c}^{peak}$$

(6.1)
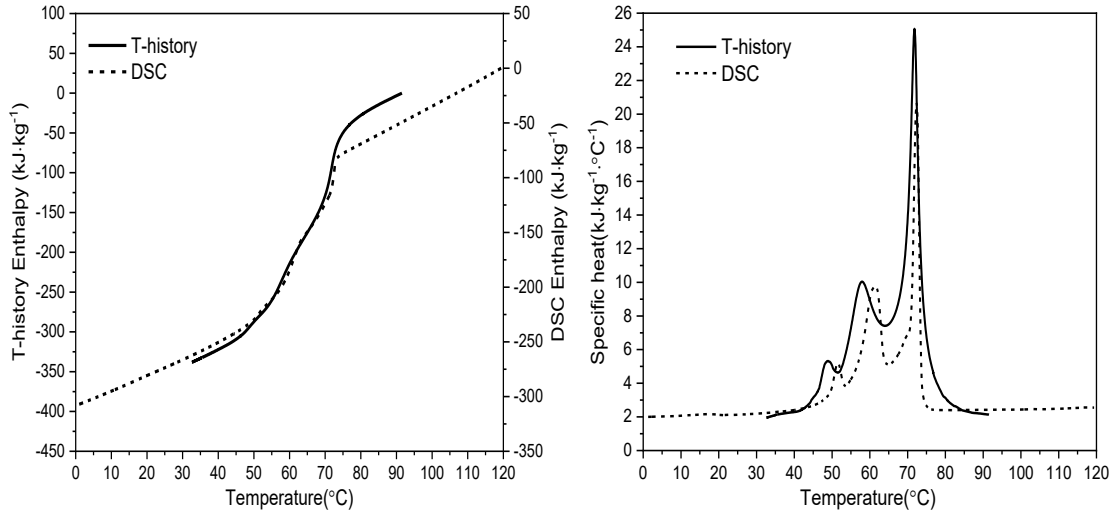
Figure 6.7. Comparison of DSC and THM results (a) Crystallisation Enthalpy-Temperature and (b) Specific heat -Temperature.

Table 6.1. Comparison of DSC, THM and the literature data.

	Melting peak	Crystallization peak	DOS	Latent Heat (kJ/kg)		Heat Capacity (kJ/kg·°C)	
				Heating	Cooling	Solid	Liquid
	$T_{p,m}^{peak}$ (°C)	$T_{p,c}^{peak}$ (°C)	ΔT_{sc} (°C)	$\Delta H_{p,m}$	$\Delta H_{p,c}$	$c_{p,p,s}$	$c_{p,p,l}$
DSC	79.5	71.5	7.5	148 ± 3	161 ± 2	1.9 ± 0.1	2.1 ± 0.2
THM	81.7	72.3	9.4	-	210.5 ± 13	2.1 ± 0.2	2.2 ± 0.2
Literature (Zheng et al. 2011)	75.19	67.81	7.38	203.2	198.8	NA[*]	NA[*]

Note: [*]NA-Not Available

This deviation is due to the shellac wax's volume-dependent behavior and a difference in measuring conditions. However, the solid and liquid specific heat calculated in THM agrees with the DSC results. DSC curve has a sharp deviation due to less sample

thermal mass as compared to the THM. The DOS is evaluated based on the peak-peak method and it is defined as the temperature difference between melting and crystallization peak is given by Eq. (6.1). DSC, THM, and literature data are given in Table 6.1. The DOS in THM and DSC analysis is 9.4 and 7.5 °C, respectively. The literature data (Zheng et al. 2011) presented in Table 6.1 is based on the DSC analysis of crude shellac wax.

6.8 THERMAL CYCLE TEST
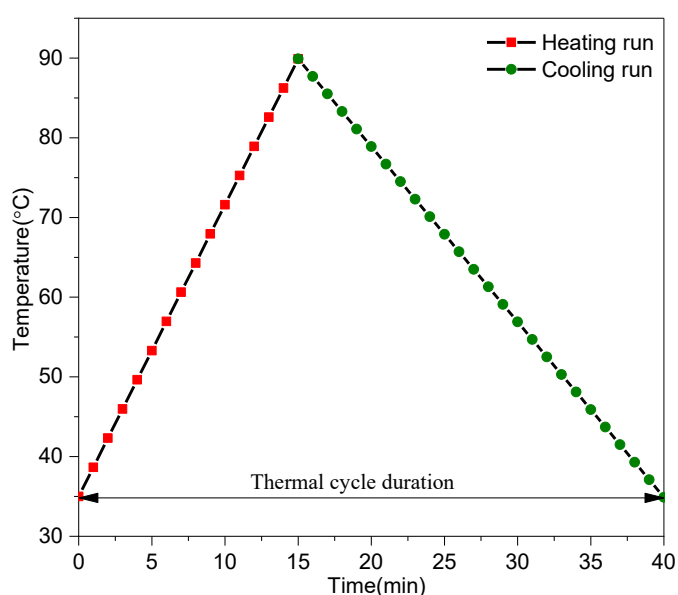
Figure 6.8. Thermal cycle duration for each heating and cooling cycle.

(a)   (b)
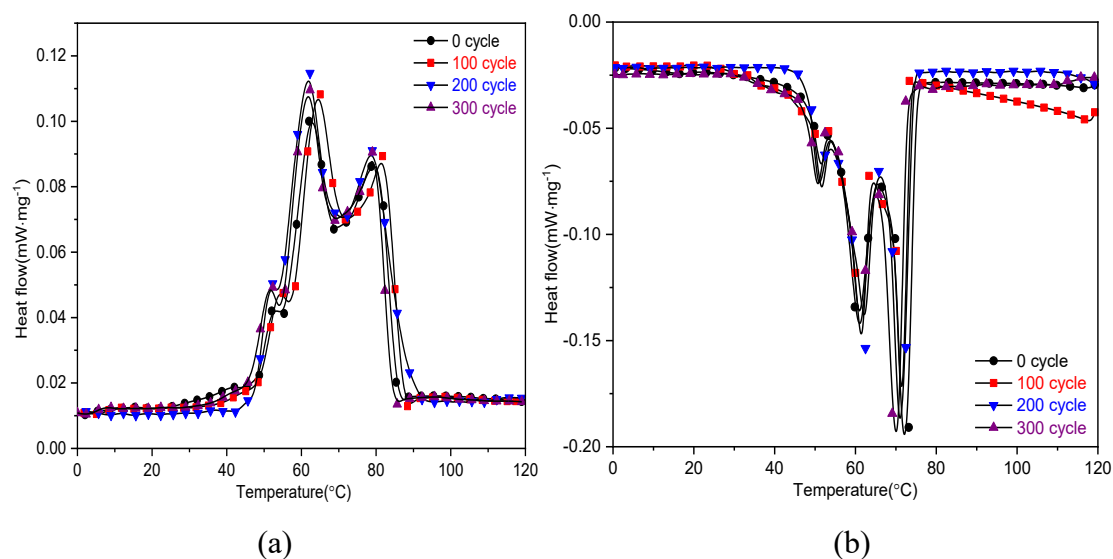
Figure 6.9. DSC analysis of shellac wax for 0,100, 200 and 300 thermal cycles (a) Heating run (b) Cooling run.

Figure 6.8 shows the duration of each thermal cycle (heating and cooling). The DSC curves of shellac wax obtained for 0, 100, 200, and 300 thermal cycles – are shown in Figure 6.9 (a) and (b). From 0 to 300 cycles, the latent heat of melting and crystallization varied by 1.6 % and 1.1 %, respectively. However, the melting and crystallization peak percentage deviation is obtained as 1.3% and 1.6%, respectively. The DOS after 300 thermal cycles is 6.9 °C as to 7.5 °C obtained initially. DSC analysis of 0,100, 200, and 300 cycles shows that shellac wax has no significant transition temperature and latent heat change. The minor changes noticed in thermal properties may be due to impurities within the shellac wax.

6.9 DENSITY

The obtained mean density and standard deviation (S.D) of four repeated trials at different temperatures are listed in Table 6.2. The sharp decline in the shellac wax density from 50 to 80 °C, noted in Figure 6.10, is due to the solid and phase transitions.
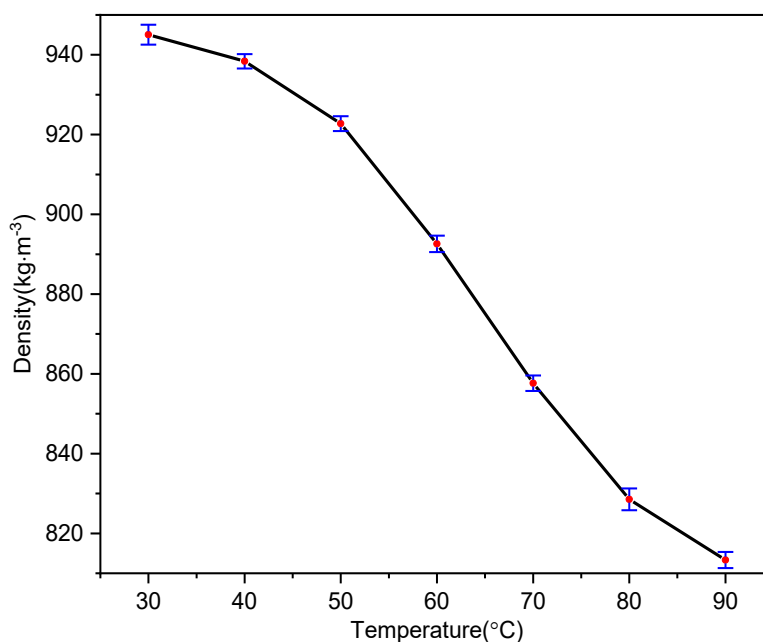
Figure 6.10. Shellac wax density-temperature behavior.

However, the density progressively decreases for sensible heat solid and liquid states. The solid density percentage difference at 30 °C is 2.1 % compared with the literature data due to the nature of Seedlac origin and purity of the shellac wax. The density change with temperature signifies the information to know the volumetric thermal expansion coefficient (Eq. (6.2)) of shellac wax over the phase transition period. The α

value obtained over a temperature range from 30 to 90 °C is 0.00269 °C^{-1}. The α value of the shellac wax is within the comparable range of PCMs used in storage applications. It is an essential property for the proper storage volume design and simulation.

$$dV = V_s \times \alpha \times (T_L - T_S)$$ (6.2)

The relative volume expansion is defined in Eq. (6.3) (Cabeza et al. 2020)

$$\Delta V(\%) = \left(\frac{V_L}{V_S} - 1 \right) \cdot 100$$ (6.3)

V_S and V_L are the shellac wax volume in solid-state (T_S is 30 °C) and liquid state (T_L is 90 °C).

Table 6.2. Shellac wax solid and liquid density.

Temperature (°C)	Density(kg/m³) (Mean ± S.D)	Density(kg/m³) Literature	Phase	ΔV(%)
30	945.0 ± 2.5	965	Solid	16.1 ± 0.4
40	938.3 ± 1.8	NA*		
50	922.7 ± 1.9	NA*		
90	813.3 ± 2.0	NA*	Liquid	

Note: *NA-Not Available

6.10 VISCOSITY

Four sets of experimental trials were carried out at four different temperatures 80 °C, 85 °C, 90 °C, and 95 °C. The average of the two closest values was used to plot the dynamic viscosity from 80 to 95 °C, as shown in Figure 6.11. Due to the phase transition advancement, an abrupt decline in dynamic viscosity is observed from 80 to 85 °C. Towards the end of the phase transition (~85 °C), an increase in temperature (95 °C) causes a gradual decrease in viscosity since sensible heating in the liquid state.
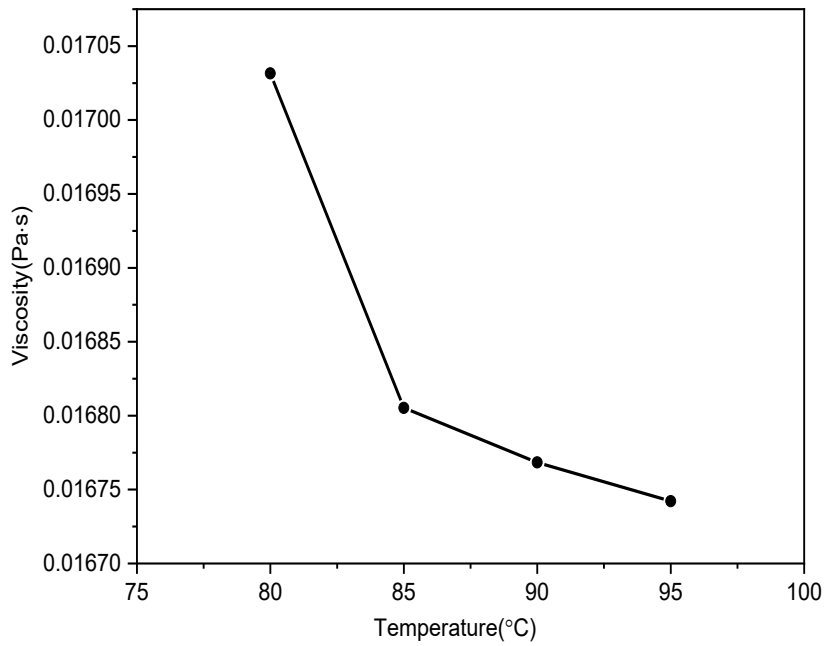
Figure 6.11. Shellac wax viscosity with reference to temperature.

6.11 CLOSURE

This chapter deals with the thermophysical and rheological analysis of natural shellac wax as BPCM for medium-temperature applications. The overall study outcome is that shellac wax is thermally stable and is a potential BPCM for TES applications like solar desalination, district heating, waste heat recovery, and solar cooking. The next chapter deals with the experimental investigation of shellac wax heat transfer performance as BPCM using vertical shell and tubes LHTES.

CHAPTER-7

EXPERIMENTAL INVESTIGATION OF SHELLAC WAX FOR MEDIUM TEMPERATURE LATENT HEAT THERMAL ENERGY STORAGE APPLICATIONS.

7.1 INTRODUCTION

Shellac wax, a potential BPCM, possesses significant latent heat values, thermal conductivity, congruent phase change, and chemical stability. In addition, it exhibits stable thermal properties with no deviation in transition range and latent heat even after 300 thermal cycles (Rudra and Gumtapure, 2020). In this regard, detailed performance analysis of a shellac wax, as novel BPCM is carried out in a vertical shell and tube heat exchanger. Thermo-fluidic phenomena of shellac wax in the vertical shell and tube heat exchanger for both the charging and discharging process are experimentally analyzed for different HTF flow rates and inlet temperature. Furthermore, the heat transfer coefficient and efficiency of the same for charging and discharging are studied in detail and quantifying the losses occurring in each case.

7.2 EXPERIMENTAL SETUP AND PROCEDURE

7.2.1 Apparatus

The lab-scale experimental setup and its schematic to perform the thermal behavior of shellac wax, as shown in Figures 7.1 and 7.2. The apparatus mainly includes as follows

➤ Twenty-five liters capacity hot fluid tank consists of an immersion heater of 1000 W (Tempsens Instruments) and a 120 RPM stirrer to maintain a uniform fluid temperature inside the tank. However, the hot fluid tank temperature is stabilized with the calibrated PT-100 temperature sensor (BS1904 class A ±0.15 °C) and proportional-integral-derivative (PID) controller.

➤ Therminol®-55 is the synthetic HTF used for this study because of its excellent low-temperature pumping ability, high resistance to fouling, low corrosion of metals, and long life. To employ water as an HTF above 100 °C would require greater than atmospheric pressure of one bar. It delivers efficient, dependable, uniform process heat with no need for high pressures—thermo-physical properties of Therminol®-55 for an operating temperature outlined in Table 7.1.

- High-temperature rotary gear pump (Rotodel™ HGN 050) capacity 20 LPM and maximum operating temperature is 200 °C. However, the DC motor of 180 Watt and 1800 rpm coupled with the rotary gear pump and speed varied with the D.C. speed controller for different flow rates. The gear pump and volumetric flask calibration were performed at a specified flow rate and temperature for 8 hours, and the noted deviation is ±0.05 x (flow rate) for a flow rate varied between 2 to 5 LPM.

- HTF inlet and outlet temperature are monitored with a four-wire ultra-precise immersion RTD sensor (Omega™: P-M-1/10-1/4-4-0-P-3 and accuracy (±1/10 (0.3 + 0.005 |T|) °C). However, the PCM temperature is monitored with calibrated 15 K-type thermocouples (accuracy ± 0.5 °C within the temperature range -20 to 120 °C). However, the temperature sensors are connected with the data acquisition module to collect the temperature data for further analysis (National Instruments®, cDAQ—9174 base, NI-9217, DAQ NI-9214, and NI TB-9214, LabVIEW workbench).

Table 7.1. Thermo-physical properties of HTF (Therminol 55a).

Temperature T (°C)	Density, ρ (kg/m³)	Specific heat, c_p (kJ/kg°C)	Thermal conductivity K (W/m°C)	Viscosity μ (mPa.s)
30	865	1.94	0.1273	25.2
100	818	2.19	0.1191	2.88
110	811	2.23	0.1179	2.38
120	804	2.26	0.1168	2.00

Note: [a]HB Tech Services, Pune, India

- HTF flow rate measurement is done with a graduated volumetric flask (borosilicate), and the reading marked over the flask measures the volume of HTF to time.

- The cooling unit consists of a compressor, evaporating coil, condenser coil, and refrigerant. Which maintains the uniform HTF temperature in the cooling tank (32 liters) during the discharge cycle.
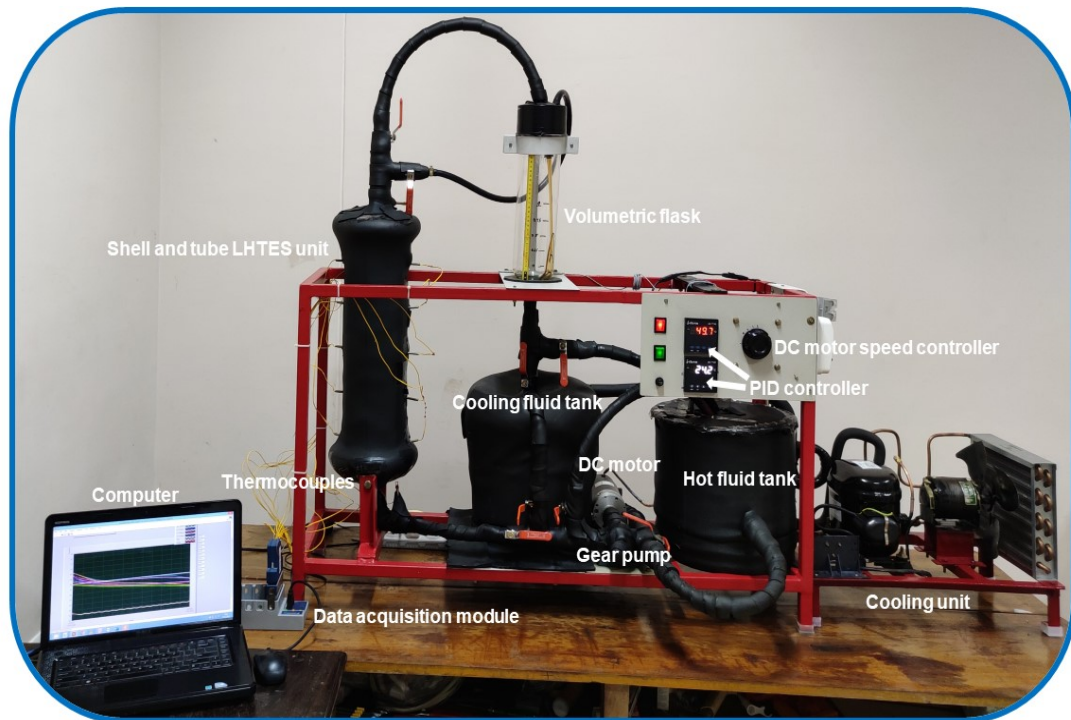
Figure 7.1. Experimental setup to evaluate the thermal behavior of the BPCM, NITK Surathkal.

1	Hot fluid tank	5	Volumetric flask	10	RTD sensor
2	Cold fluid tank	6	PID controller	11	Thermocouples
3	Gear Pump	7	Cooling unit	←	Hot HTF
4	Shell and tube LHTES unit	8	Computer	⇐	Cold HTF
		9	DAQ	←	Refrigerant flow
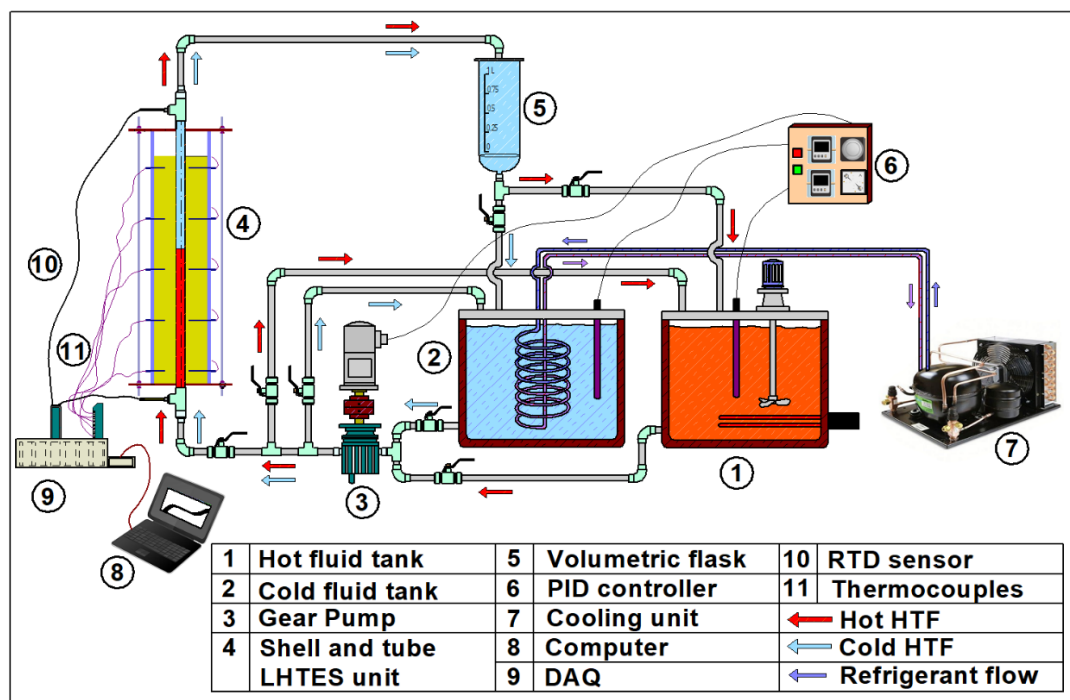
Figure 7.2. Schematic of the experimental setup to evaluate the thermal behavior of the BPCM, NITK Surathkal.

7.2.2 Latent heat thermal energy storage (LHTES) unit

The lab-scale shell and tube LHTES unit is designed, and the thermocouples are fixed in three columns (A, B, and C) and five rows (1, 2, 3, 4, and 5), as shown in Figure 7.3. The heat transfer tube inside the shell is copper with an inner diameter of 15 mm and an outer diameter of 19 mm. The outer shell, made of borosilicate glass, has a height of 500 mm with an inner and outer diameter of 101 mm and 115 mm, respectively. Insulation is provided with one layer of glass fiber (15 mm thick) and two nitrile foam layers of class c-type (5 mm thick). Based on previous studies, optimum configuration, shell to the tube (r_i/r_o) aspect ratio is chosen as 5.3 (Seddegh et al. 2017; Shen et al. 2020). The BPCM is filled to a height of 448 mm with 52 mm clearance at the top to accommodate the expansion of BPCM during phase transition.
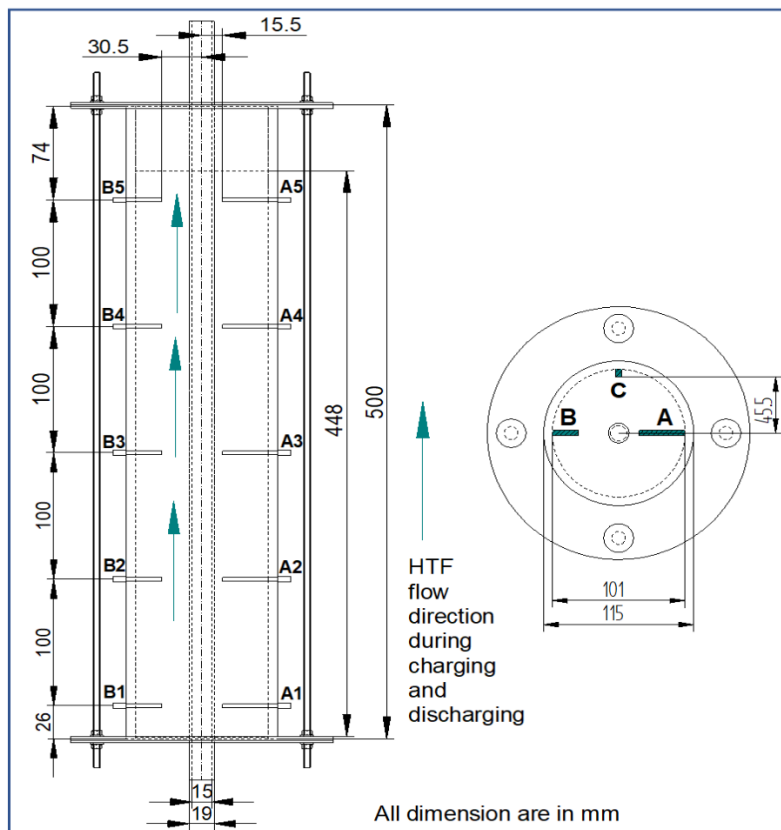
Figure 7.3. LHTES unit with dimension specification and thermocouple position.

7.2.3 Experimental procedure

The HTF is uniformly heated to the required temperature inside the hot fluid tank and circulated through the LHTES unit for the charging process. With temperature monitoring, this process is continued until the entire volume of the PCM has melted. Similarly, for the discharge process, the HTF is uniformly cooled and circulated through the LHTES unit. The experimental parameters used are outlined in Table 7.2. The HTF inlet and outlet temperature is given by Stefan number;

$$Ste = \frac{c_{p,pcm} \cdot \Delta T}{L}$$
(7.1)

In phase change systems, the Stefan number is the ratio of sensible heat to latent heat. In Eq. (7.1), where c_p is the specific heat capacity of the PCM and temperature difference ($T_{hot,in}$ -T_M) for the charging process and (T_S-$T_{cold,in}$) for the discharging process.

The HTF flow rate effect is defined by the Reynolds number (Re);

$$Re = \frac{\rho_{htf} v_{htf} D_h}{\mu_{htf}}$$
(7.2)

Table 7.2. List of experiments performed and operating parameters used.

List of experimental trials	HTF inlet temperature (°C)	HTF flow rate (LPM)
Repeatability	110	4
Charging	Variables: 100, 105, 110, 115 and 120	Variables: 2, 3, 4 and 5
Discharging	26	Variables: 2, 3, 4 and 5

7.2.4 Data reduction

By considering the LHTES unit as a control volume and applying the energy balance, the LHTES unit's performance is evaluated based on control volume and energy balance equations. The instantaneous thermal power (q) released and gained by the HTF

(Eq. (7.3) and Eq. (7.4)) was evaluated using the measured temperature of HTF at the inlet and outlet for a 1 min interval ($\Delta t = 60$ s).

$$q_c = \dot{m}_{htf} c_{p,htf} \left(T_{hot,in} - T_{hot,out} \right)$$

(7.3)

$$q_d = \dot{m}_{htf} c_{p,htf} \left(T_{cold,out} - T_{cold,in} \right)$$

(7.4)

Where $\dot{m}$ is the mass flow rate of the HTF, c_p is the specific heat of HTF at the operating temperature, and ΔT is the temperature difference between the inlet and outlet of the HTF.

The cumulative energy (Q) input and gained by the HTF can be evaluated by summing up the instantaneous thermal power throughout the charging and discharging process. It is expressed by Eq. (7.5)

$$Q_{c \& d} = \sum_{i=1}^{n} \Delta t \cdot q_{c \& d}$$

(7.5)

The average overall heat transfer coefficient between the HTF tube and the PCM is evaluated as

$$U = \frac{\int_0^t \left(q / \left(A_{H,inside} \times LMTD \right) \right) dt}{t}$$

(7.6)

Where $A_{H, inside}$ is the area based on the inside diameter of the HTF tube, LMTD is the logarithmic mean temperature difference during the PCM melting, which is defined by

$$LMTD = \frac{\left(T_{hot,in} - T_{A1} \right) - \left(T_{hot,out} - T_{A5} \right)}{ln \left(\left(T_{hot,in} - T_{A1} \right) / \left(T_{hot,out} - T_{A5} \right) \right)}$$

(7.7)

Where T_{A5} and T_{A1} are the PCM temperature near to the tube at the top and bottom of the LHTES unit (Ettouney et al. 2004; Wang et al. 2016)

The actual energy stored and discharged within the PCM is expressed as follows

$$Q_{s,c} = m_{pcm} \left[c_{p,s} \left(T_{onset,M} - T_o \right) + L_M + c_{p,l} \left(T_{pcm,f,av} - T_{offset,M} \right) \right]$$

(7.8)

$$Q_{s,d} = m_{pcm} \left[c_{p,l} \left(T_{pcm,o,av} - T_{onset,S} \right) + L_S + c_{p,s} \left(T_{offset,S} - T_f \right) \right]$$

(7.9)

The thermal performance of the shellac wax-based LHTES unit during the charging and discharging process is expressed as follows

$$\eta_c = \frac{Q_{s,c}}{Q_c}$$

(7.10)

$$\eta_d = \frac{Q_d}{Q_{s,d}}$$

(7.11)

7.2.5 Heat loss calculation

The heat dissipated from the LHTES unit is determined by charging the storage unit to the steady-state temperature. Then experimentally assessed the additional heat required to maintain that steady-state by heat balance method, i.e., heat added to the storage unit was equal to heat loss (Murray and Groulx, 2014)

The experiment was performed to estimate the heat loss at a maximum trial temperature of 120 °C over a period of 24 h and calculated the thermal power for every 30 s. The estimated maximum heat loss through the storage unit is denoted as H_L. As no heat loss occurs through LHTES at room temperature, the heat dissipation is assumed to be linear throughout the experiment and is estimated based on the PCM average temperature.

$$\dot{Q}_{loss} = \frac{H_L}{\left(T_{hot,in} - T_a\right)} \times \left(T_{pcm,av} - T_a\right)$$

(7.12)

$T_{hot,\,in}$ is the HTF temperature (°C), $T_{pcm,\,av}$ is the average PCM temperature (°C), and T_a is the ambient temperature. Heat loss would be overrated due to the thin layer of PCM present between the thermocouple probe and inside of the shell surface.

7.2.6 Uncertainty analysis

When considering the measurements taken by flow meters and thermocouples, uncertainty analysis is required to identify the range of measured values within which the true value lies. The detailed fabrication procedure and uncertainty analysis of measuring instruments explained in Appendix-B.

The calibrated results obtained from the instrument suppliers and measured uncertainty values are outlined in Table 7.3.

The calculation uncertainty in HTF temperature (δT) and flowrate ($\delta \dot{m}$): is evaluated employing rectangular probability distributions (Eq. 7.13 and Eq. 7.14) (Koukou et al. 2019).

$$\delta T_{RTD} = \frac{\pm 1/10 \left(0.3 + 0.005 \left|T\right| \right) ^\circ C}{\sqrt{3}}$$

(7.13)

Table 7.3. Accuracy of the measuring instruments.

Instruments	Accuracy
Thermocouple sensor (K-type)	±0.5 °C
Pt-100 RTD sensor	±0.15 °C
Ultra-precise RTD sensor	±1/10 (0.3 + 0.005 |T|) °C
Flowmeter	± (0.05·flowrate) LPM
Mass	±0.1 g
Dimension	±0.2 mm

$$\delta \dot{m} = \frac{0.05 \cdot \text{flow-rate}}{\sqrt{3}}$$

(7.14)

The relative error for a confidence level of 95% is given by:

$$\text{Relative error} = \frac{\text{Absolute error} \times 2}{\text{Measured value}}$$

(7.15)

The thermal power that HTF (Therminol-55) transfers to or from the storage system is given in Eq. (7.3) and (7.4). The uncertainty is calculated using the methodology adopted by Kline and McClintock (Moffat 1988).

$$\delta Q = \sum_{j=1}^{n} \sqrt{\left(\frac{\partial q_j}{\partial \dot{m}} \cdot \delta \dot{m}\right)^2 + 2\left(\frac{\partial q_j}{\partial T} \cdot \delta T\right)^2}$$

(7.16)

The relative error of ultra-precise RTD sensors is assumed as diminutive compared to the error in flow-rate measurement. Based on the uncertainty propagation (Eq. 7.16), the cumulative energy error is estimated as ±5.7%.

7.3 EXPERIMENT REPEATABILITY

Two repeated charging trials were conducted to verify the result's consistency under similar input conditions, as presented in Table 7.2. Figure 7.4 shows the transient temperature profile measured at different locations within the PCM. Based on the results plotted in Figure 7.4, it is observed that the experimental setup has good repeatability, and formal experiments can be carried out.
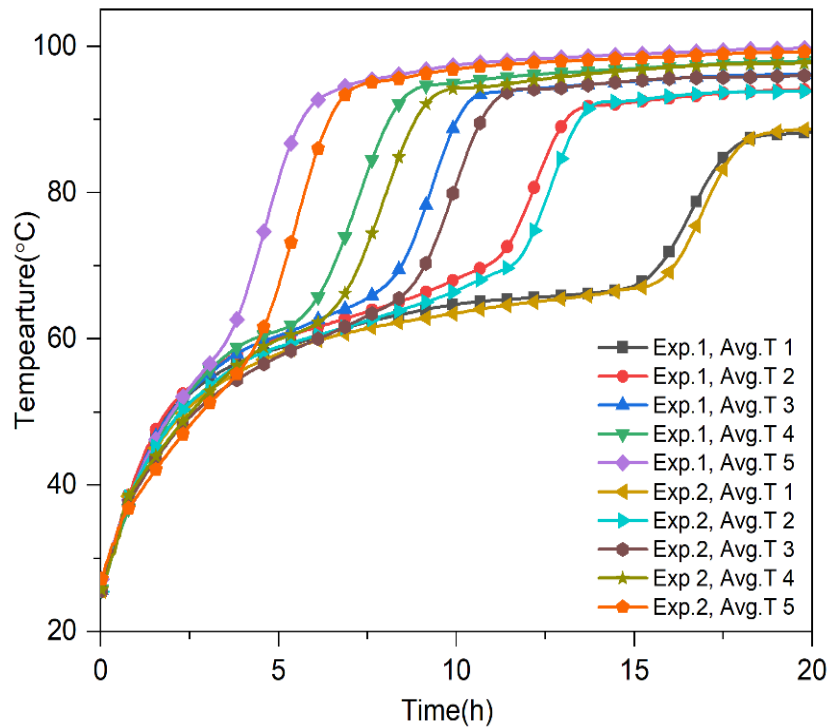
Figure 7.4. PCM transient temperature variation for two charging trials under similar input conditions: $T_{PCM,i} = 26\ °C$, $T_{hot,in} = 110\ °C$, and flow-rate = 4.0 LPM.

7.4 HEAT TRANSFER DURING THE CHARGING PROCESS

The temporal variation of inlet and outlet temperature of HTF (Therminol®-55) and the temperature difference during the charging process for an input condition of 110 °C and flow rate of 4 LPM is shown in Figure 7.5. Owing to the temperature controller dynamics of the 1 kW heating coil in the hot fluid tank, a serrated shape is obtained in the inlet and outlet temperature profile. As the electric heater and pipeline require initially warming up, the inlet temperature of HTF attains a steady state after 0.2 hrs of the charging process. In the initial stages, a maximum temperature gradient of 1.1 °C is obtained, and with time it drops to an average value of 0.3 °C. This is attributed to the

attainment of melting temperature and less heat absorption during the further charging process.
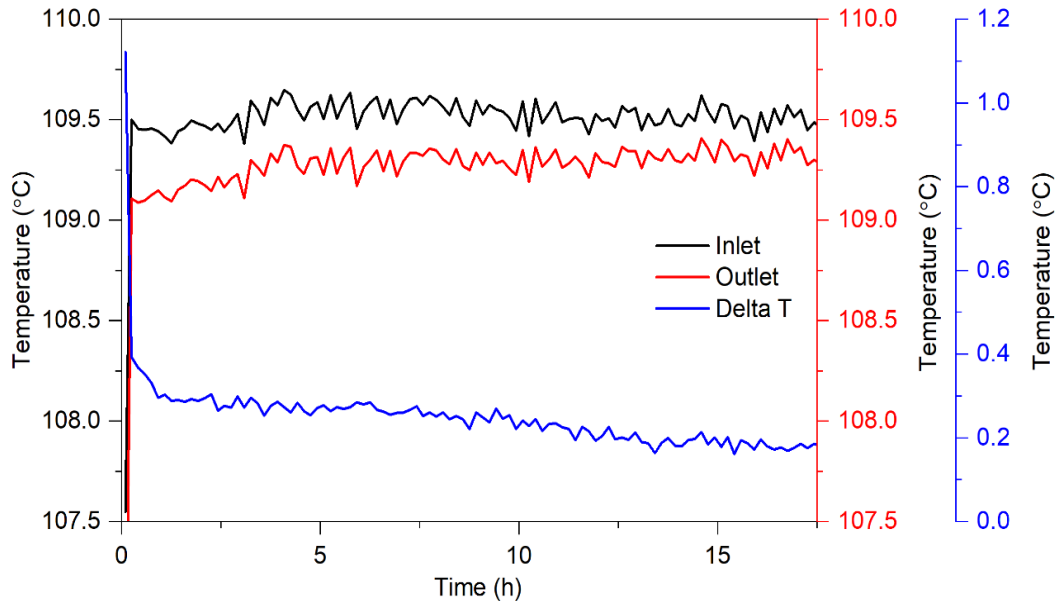
Figure 7.5. HTF temperature variation at the inlet, outlet, and temperature gradient with time during charging process: $T_{PCM,i} = 26\ °C$, $T_{hot,in} = 110\ °C$, and flow rate = 4.0 LPM.

7.5 EFFECT OF HTF FLOW RATE ON CHARGING PROCESS
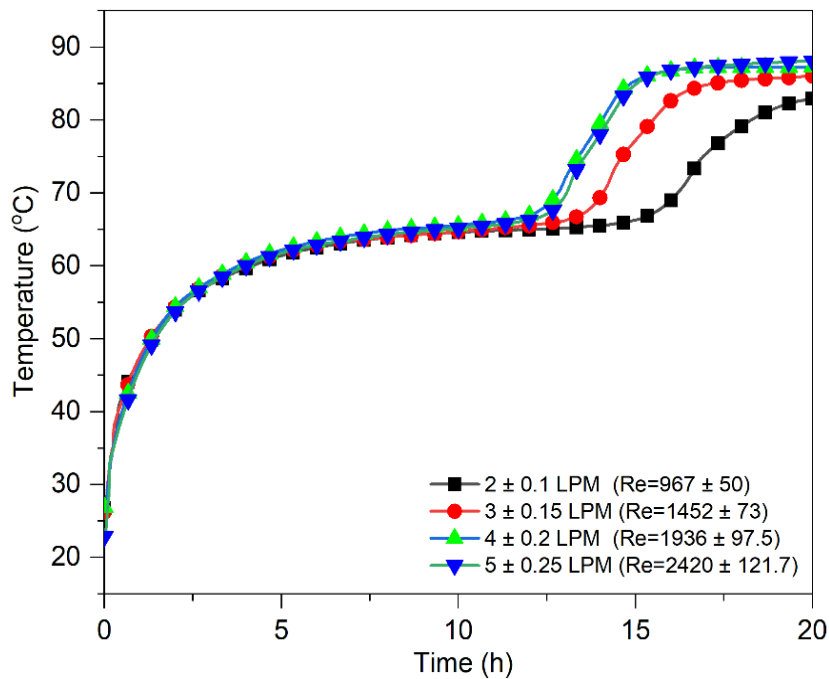
Figure 7.6. Effect of HTF flow rate on charging time. (Average of A1, B1, and C1 probe locations).

The impact of HTF flow rate on the melting process is parametrically studied for different flow rates - 2, 3, 4, and 5 LPM at a fluid inlet temperature of 110 °C. Figure 7.6 illustrates the timewise variation of PCM average temperature at the bottom location (A_1, B_1, and C_1). The bottom portion of PCM is less influenced by natural buoyancy and considering the delayed melting at other locations. Total melting time reduction of 31.2%, 43.6%, and 43.1% is obtained for flow rates of 3, 4, and 5 LPM upon comparison to 2 LPM flow rate. As the flow rate increases, the melting time reduces due to flow instability owing to flow transition, indicating that the optimum is a 4 LPM flow rate. Figure 7.7 illustrates the average overall heat transfer coefficient (U) variation for varying flow rates. The U value increases as the mass flow rate increases, indicating increased heat transfer between HTF and PCM. For 5 LPM, U value drops due to flow instability leading to lower heat transfer.
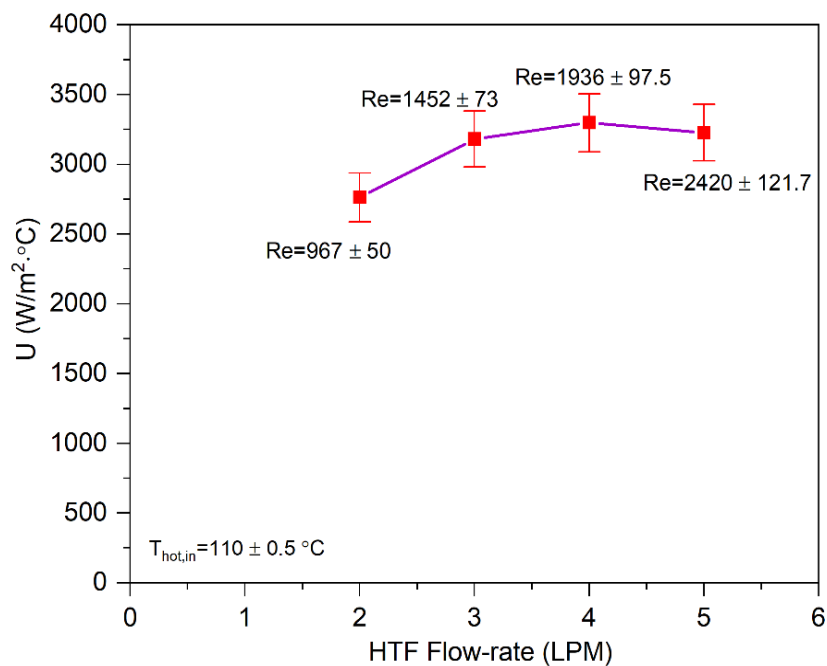
Figure 7.7. The average overall heat transfer coefficient at different HTF flow rates.

7.6 EFFECT OF HTF TEMPERATURE ON CHARGING PROCESS

The effect of operational parameters like HTF inlet temperature on the heat transfer characteristics of the PCM is conducted using four trials with 100 °C, 105 °C, 110 °C, 115 °C, and 120 °C at a fixed optimum flow rate of 4 LPM as shown in Figure 7.8. For

an HTF inlet temperature of 100 °C, the PCM attained an average temperature of 84.5 °C, a few degrees above the shellac wax melting point.
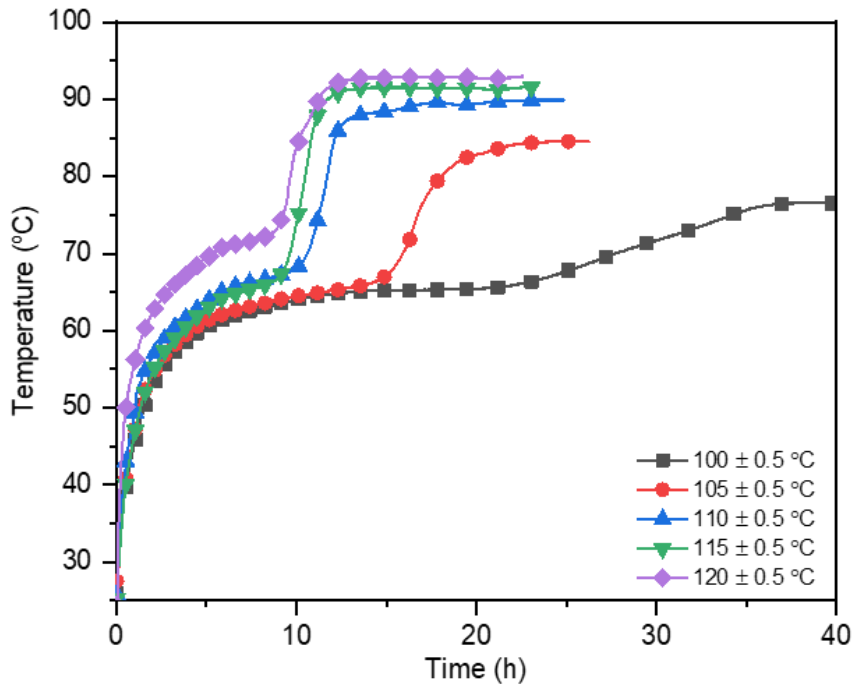
Figure 7.8. Effect of HTF input temperature on charging time (Data used an average of A1, B1, and C1 probe locations).
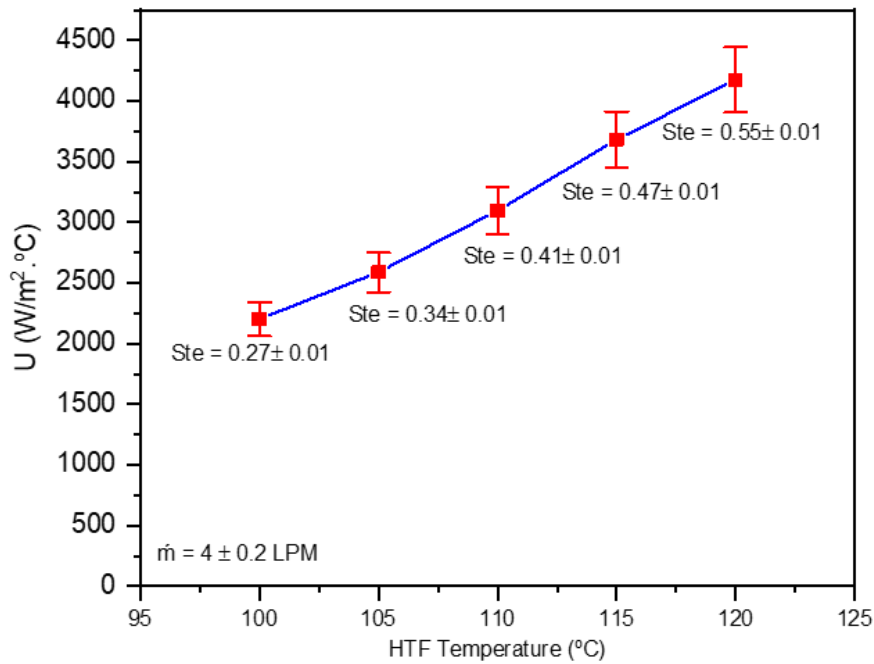
Figure 7.9. Variation of the average overall heat transfer coefficient with inlet HTF temperature.

Indicating that the temperature in the bottom regions is still below the melting temperature of shellac wax (average PCM temperature of all three-probe at the bottom, i.e., A1, B1, and C1 is 76±0.5 °C), and the same can be visually inspected. A reduction of 42.2% is obtained in time to attain a steady-state for 120 °C relative to 105 °C HTF temperature. In this regard, heat transfer gets augmented and reduces the actual energy required to charge (Q_c) the LHTES for 120 °C and gives the minimum melting time. As compared to the 100 °C trials, the percentage reduction in accumulated energy utilized to charge the unit is obtained as 11%, 34.3%, 38.1%, and 39.7% for 105 °C, 110 °C, 115 °C, and 120 °C, respectively.

Figure 7.9 illustrates the variation of U with the inlet HTF temperature. The average overall heat transfer coefficient increased linearly with the HTF inlet temperature. Correspondingly, the Stefan number also increased due to the higher temperature gradient between HTF and the PCM.

7.7 TEMPORAL VARIATION OF THE TEMPERATURE INSIDE THE PCM DURING THE CHARGING PROCESS
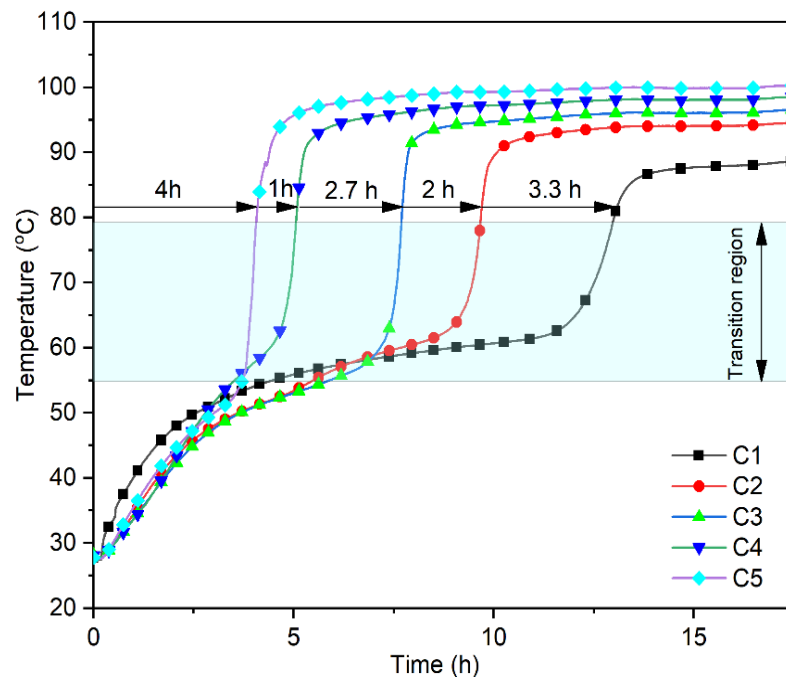
Figure 7.10. Temporal variation of the PCM temperature at the different probe locations axially during charging: $T_{PCM,i} = 26$ °C, $T_{hot,in} = 110$ °C, and flow rate = 4.0 LPM.

The temporal variation of axial temperature throughout the charging process for a fluid inlet temperature of 110 °C and the flow rate of 4 LPM is as shown in Figure 7.10. Due to the maximum charging time near the inner shell surface C1-C5, the same is considered to study the PCMs axial temperature distribution. To analyze in detail, the PCM temperature distribution contour is plotted employing the kriging spatial interpolation method, as shown in Figure 7.11. The temperature rises uniformly along the axial direction (Figure 7.10 and Figure 7.11, before 3 h), signifying that heat transfer occurs primarily by conduction within the solid PCM. As the PCM around the tube melts first, it creates a density gradient between liquid and solid PCM, driving the liquid PCM upward as charging proceeds. Further, as charging proceeds, the high-energy liquid PCM carried to the top interacts with adjacent solid PCM, increasing the melting rate (Figure 7.11, t=6 h and t=9 h). The reference for the melting front is taken as the melting peak temperature (79.5 °C).
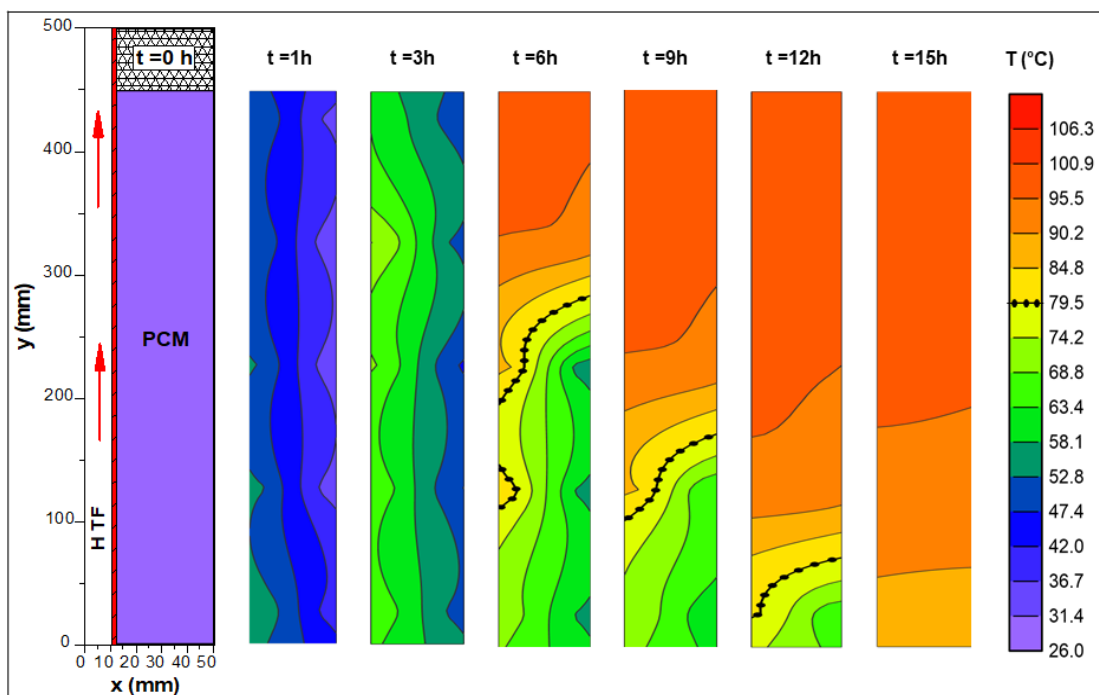
Figure 7.11. Temporal variation of temperature contours for charging process: $T_{PCM,i}$ = 26 °C, $T_{hot,in}$ = 110 °C, and flow rate = 4.0 LPM.

During 6 h to 12 h (Figure 7.11), the melt front propagates from top to down, as evident. The time gap to reach melt front at different axial positions is shown in Figure 7.10. The period between C2 and C1 axial position to reach the melting peak was more

(approximately 3.3 h) due to the partial energy dissipation through the shell wall as the PCM around the C1 location is in contact with the bottom wall and sidewalls. In addition, due to weaker convective heat transfer, the PCM near C1 attained lower temperatures than other areas.
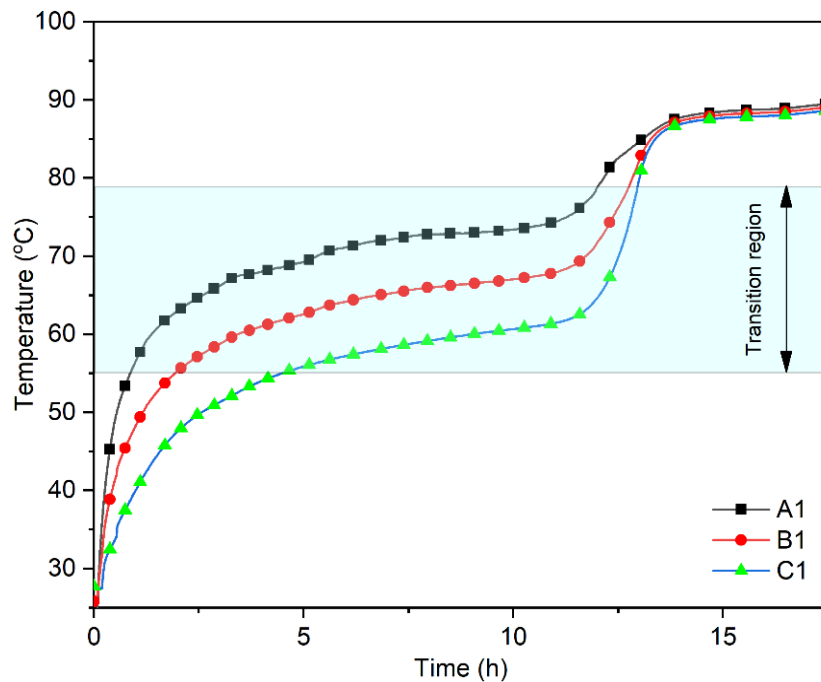
Figure 7.12. Temporal variation of the PCM temperature at the different probe locations radially during the charging process: $T_{PCM,i} = 26\ °C$, $T_{hot,in} = 110\ °C$, and flow-rate = 4.0 LPM.

Figure 7.12 illustrates the temporal variation of PCM temperature radially at the bottom of the storage unit, i.e., at A1, B1, and C1 locations. The PCM around location A1 melts faster as it is close to the HTF tube. The curve indicates the temperature gradient at different radial locations is higher during the sensible heat transfer in solid-state. During the phase change period, low conductive heat transfer influences the melting plateau formed at different temperature values (Figure 7.11, t=1 to 3 h). However, the radial temperature gradient approaches minimal after the shellac wax melts, owing to natural convection (t= 6 to 15, Figure 7.11).

7.8 HEAT TRANSFER DURING THE DISCHARGING PROCESS

Figure 7.13 illustrates the inlet and outlet temperature and the temperature difference between them during the discharging process.
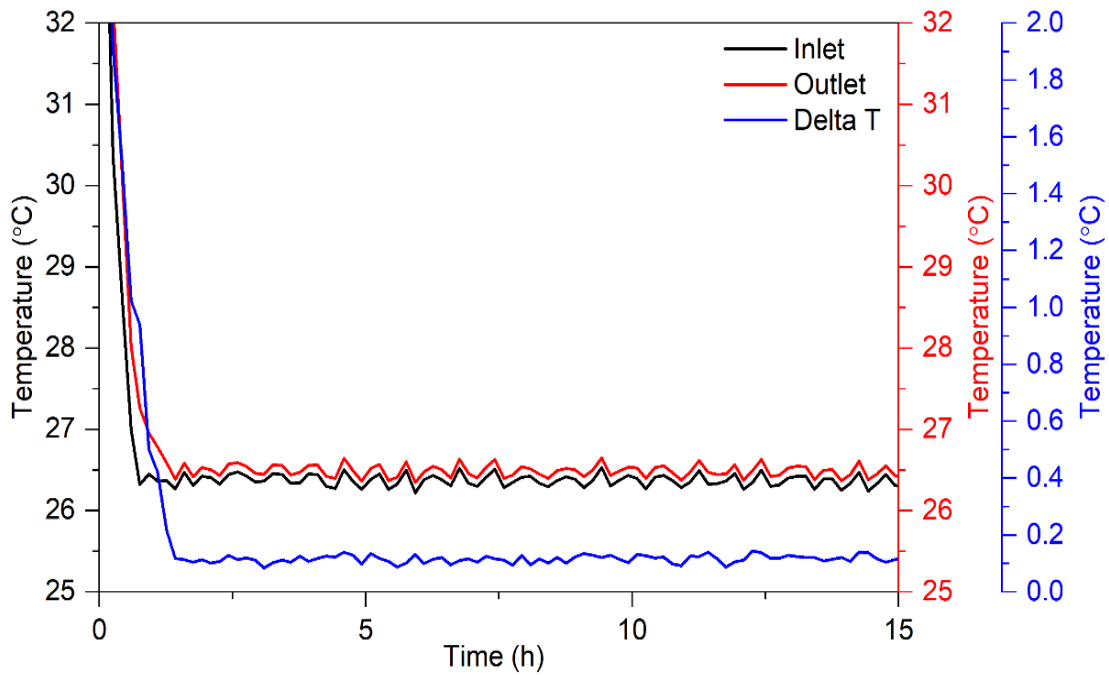
Figure 7.13. Temporal variation of HTF temperature at the inlet, outlet, and difference during discharging.

7.9 EFFECT OF FLOW-RATE ON DISCHARGING PROCESS
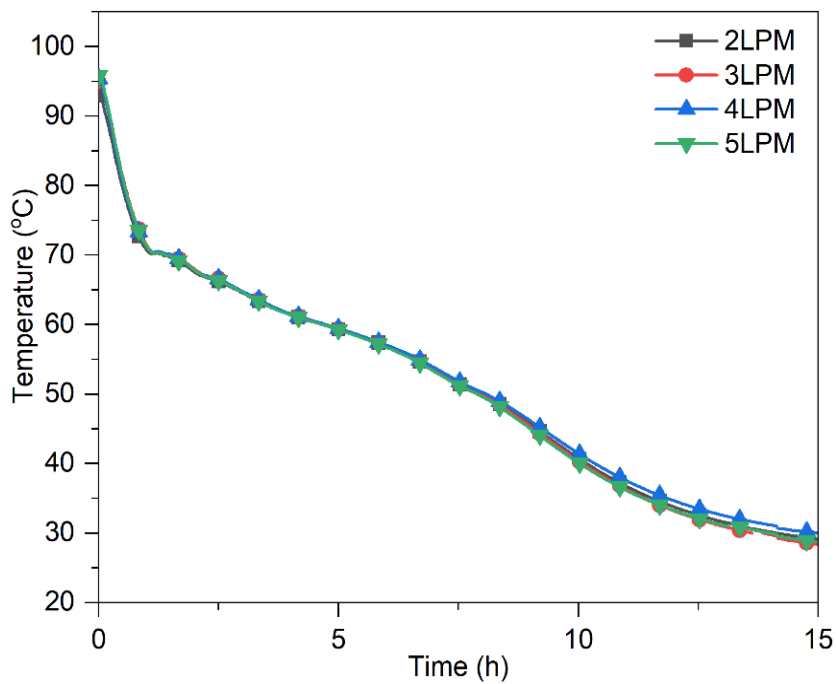
Figure 7.14. Effect HTF flow rate on discharging process.

The discharge fluid flows at a rate of 4 LPM and has a temperature of 26 °C. The temperature difference is approximately more than 1 °C during the initial 30 min owing to the sensible heat absorption by the copper tube and liquid PCM. With time advancement, heat transfer reduction occurs due to forming a solid PCM layer around the copper tube, decreasing the temperature gradient. The PCM heat transfer characteristics and the time required for energy discharge are studied for fluid inlet temperature of 26 °C and flow rates of 2, 3, 4, and 5 LPM. The heat transfer from solid PCM close to the copper tube to the HTF is minimal due to the thermal resistance created by solid PCM surrounding the copper tube. Similar to the DSC curve's solidification point, the solidification started at 70.5 ± 0.5 °C, as shown in Figure 7.14. No considerable degree of subcooling has been noticed before the nucleation trigger for all flow rates, indicating that flow rate has no significant effect on the solidification process. This is an advantage of shellac wax as a bio PCM. It is observed that the flow rate has no significant impact on the discharging process.

7.10 TEMPERATURE DISTRIBUTION INSIDE THE PCM DURING THE DISCHARGING PROCESS
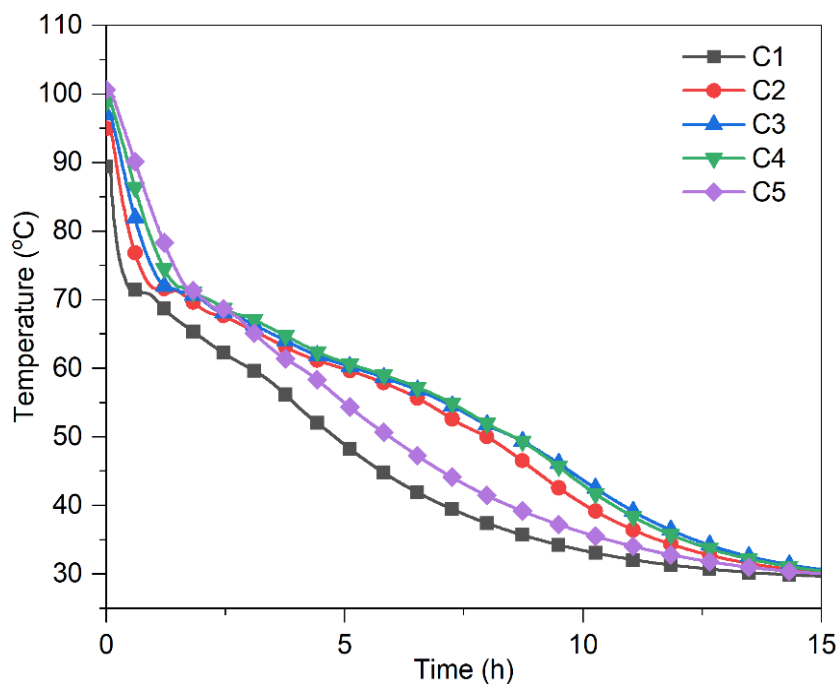
Figure 7.15. Temporal variation of the PCM temperature at the different axial probe locations during discharging process: $T_{cold,in}$ = 26 °C, and flow rate = 4.0 LPM.

The axial variation of temperature at location C (45.5 mm from the center axis) with time during the discharging process is shown in Figure 7.15. Due to more heat dissipation owing to direct contact with side and bottom walls reduce the PCM temperature faster at location C1(Figure 7.16, t=1 to 3 h). In contrast to the charging process, the solidification contour fronts propagate from bottom to top, as shown in Figure 7.16 (t=1 h). At the top location C5, due to the inner clearance volume of the LHTES unit, cooling occurs at a faster rate (t=3 h, Figure 7.16). However, the PCM in the middle portion (C2-C4 area) discharges the energy almost uniformly, as illustrated in Figure 7.16 (t=3 to 15 h). Figure 7.17 presents the temporal variation of PCM temperature at the same axial location 1 (bottom) during the discharging process. As anticipated, the temperature at all radial locations (A1, B1, and C1) uniformly releases the sensible liquid heat owing to the natural convective currents, evident in the discharge temperature contour (t=1 h bottom, Figure 7.16). Nucleation is initiated at A1 with an unnoticeable plateau and further releases sensible heat to the adjacent HTF tube (t=3 h, Figure 5.15).
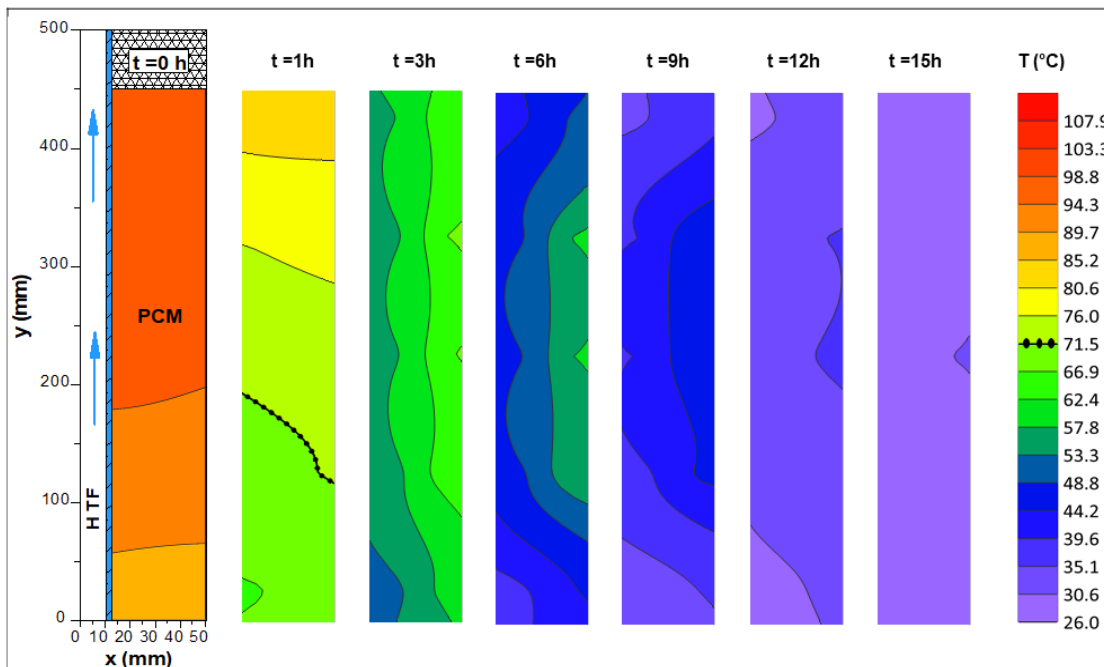
Figure 7.16. Temporal variation of temperature contours for discharging process: $T_{cold,in}$ = 26 ± 0.5 °C, and flow rate = 4.0 ± 0.2 LPM.
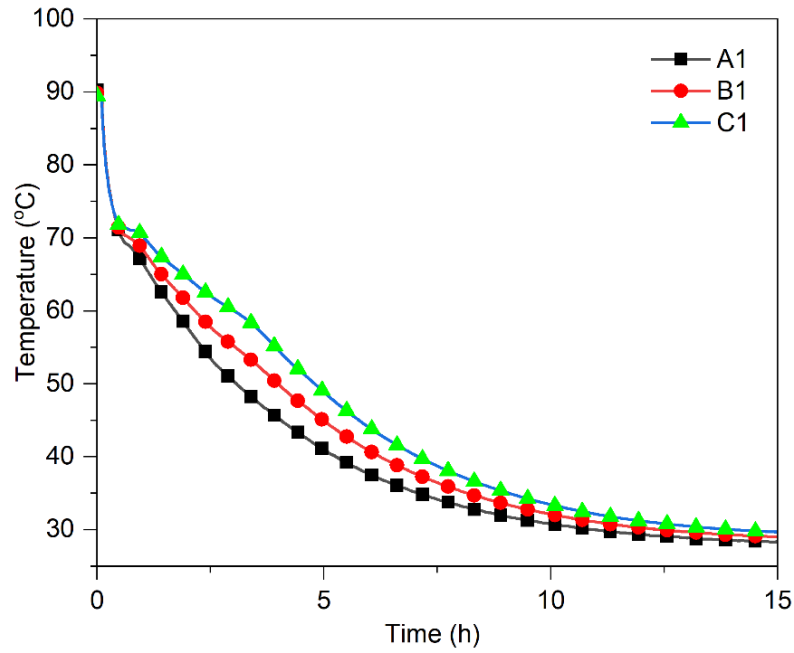
Figure 7.17. Temporal variation of the PCM temperature at the different radial probe locations during discharging process: $T_{cold,in}$ = 26 °C, and flow rate = 4.0 LPM.

7.11 THERMAL POWER, CUMULATIVE ENERGY, AND EFFICIENCY OF SHELLAC WAX-BASED LHTES UNIT.
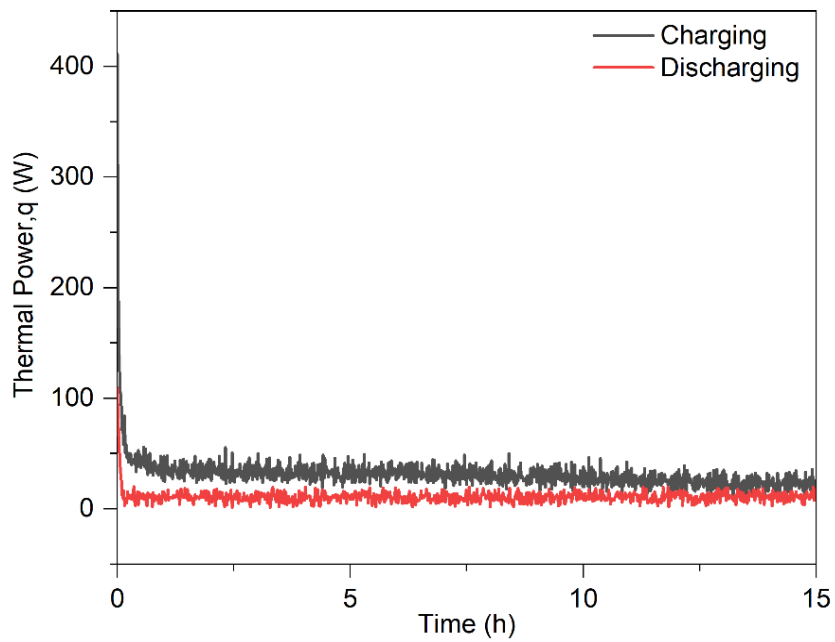
Figure 7.18. Instantaneous thermal power for charging ($T_{hot,in}$=110 °C) and discharging process ($T_{cold,in}$=26 °C) of fluid flow rate 4 LPM.

The instantaneous thermal power supplied and discharged at the specified fluid inlet temperature of $T_{hot,in}$ = 110 °C and $T_{cold,in}$= 26 °C, respectively, for a flow rate of 4 LPM is shown in Figure 7.18. As seen, the thermal power is varying over time during the charging or discharging process. Initially, the heat transfer rate into or from the LHTES system is high owing to the higher temperature gradient between HTF and the PCM. Further, as the charging proceeds, the heat transfer rate drops due to an increase in PCM temperature.

Table 7.4. The effect of HTF inlet temperature on the performance parameters measured, energy storage and discharge efficiency of LHTES unit ($T_{initial}$=26 °C and ṁ =4 LPM).

	$T_{hot,in}$ (°C)	$T_{pcm,f,av}$ (°C)	q_c (W)	Q_c (kJ)	$Q_{Max,s.}$ (kJ)	$Q_{s,c}$ (kJ)	η_c (%)
	100	84.5	20.7	2183	973.2	836.8	38.3
Charging	105	91.4	26.1	1942.3	1017.2	897.5	46.2
	110	95	29.9	1433.3	1061.2	929.2	64.8
	115	97.4	30.3	1351.4	1105.2	950.3	70.3
	120	99.5	30.6	1315.0	1144.1	966.2	73.4
	$T_{cold,in}$ (°C)	$T_{pcm,i,av}$ (°C)	q_c (W)	$Q_{s,d}$ (kJ)	$Q_{Max,d}$ (kJ)	Q_d (kJ)	η_d (%)
	26	83.1	10.5	824.4	1038.8	496.4	60.2
Discharging	26	90.5	10.7	889.6	1082.8	557.5	62.6
	26	94.5	10.7	924.8	1126.8	581.0	62.8
	26	97	10.8	946.8	1170.8	592.8	62.6
	26	99	10.9	947.1	1182.2	594.1	62.7

However, solid PCM around the heat transfer tube reduces the thermal power transfer from PCM to HTF during the discharge process. The average instantaneous thermal power for the flow rate of 4 LPM from the hot fluid to PCM is 29.9 W (110 °C), and from PCM to cold fluid is 10.7 W (26 °C). Further, quantitative results for different operating temperatures and flow rates are detailed in Tables 7.4 and 7.5.

Figure 7.19 (a) shows the cumulative energy supplied with time, uncertainties, and stored energy. Even with sufficient insulation, a partial amount of heat input is dissipated through the shell wall. The calculated heat loss ($\dot{Q}_{loss}$) for a specific charging process for the temperature of 110 °C and flow rate of 4 LPM is 7.9 ± 0.45 W, leading to a cumulative heat loss of 383.4 ± 21.8 kJ. The unaccounted heat loss based on theoretical energy storage is 120.7 ± 6.8 kJ. Energy storage efficiency increases with HTF inlet temperature, implying lower charging time would be critical in improving the LHTES unit's performance. A flow rate higher than 4 LPM reduces the temperature difference between inlet and outlet due to the fluid flow dynamics.

Table 7.5. The effect of HTF flow rate on the performance parameters measured, energy storage, and discharge efficiency of LHTES unit ($T_{initial}$=26 °C and $T_{hot,in}$= 110 °C).

	$\dot{m}$ (LPM)	$T_{pcm,f,av}$ (°C)	q_c (W)	Q_c (kJ)	$Q_{Max,s.}$ (kJ)	$Q_{s,c}$ (kJ)	η_c (%)
	2	92.9	29.5	1908.2	1061.2	910.7	47.7
Charging	3	94.5	32.0	1723.3	1061.2	924.8	53.6
	4	95	29.9	1433.3	1061.2	929.2	64.8
	5	95.1	34.1	1678.0	1061.2	930.0	55.4
	$\dot{m}$ (LPM)	$T_{pcm,i,av}$ (°C)	q_c (W)	$Q_{s,d}$ (kJ)	$Q_{Max,d}$ (kJ)	Q_d (kJ)	η_d (%)
	2	92.2	10.1	904.5	1126.8	515.4	56.9
Discharging	3	94.2	11.1	922.1	1126.8	545.0	59.1
	4	94.5	10.7	924.8	1126.8	581.0	62.8
	5	94.6	11.5	925.6	1126.8	564.5	60.9

Similarly, Figure 7.19(b) illustrates the cumulative energy received with time, uncertainties, and energy stored. The discharge efficiency listed in Tables 7.4 and 7.5 is calculated based on the stored energy available during the discharge to the HTF. No significant change in discharge efficiency is obtained with a change in operational parameters since the solid PCM formation around the tube hinders the parameter's influence on heat transfer between PCM and HTF.
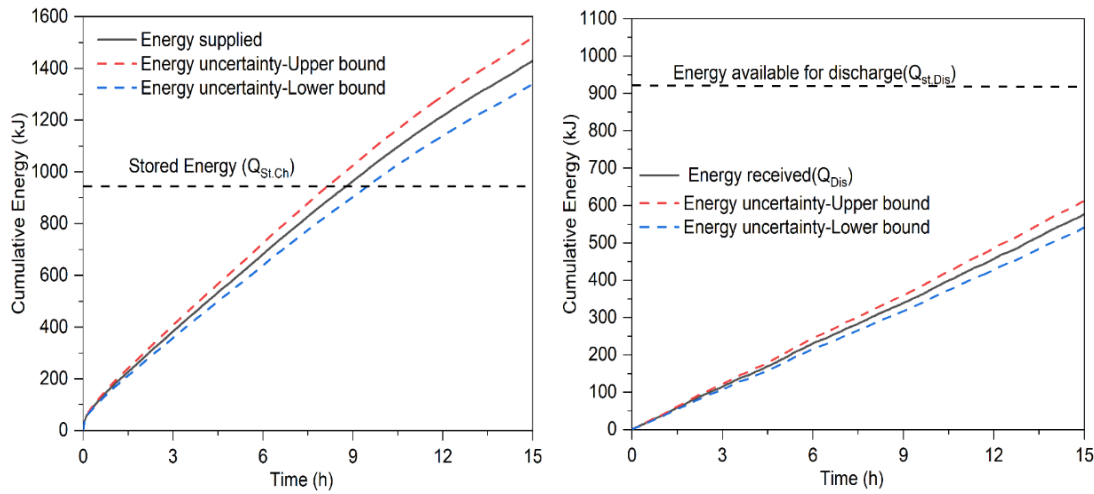
Figure 7.19. Cumulative energy (a) Supplied ($T_{hot,in}$=110 °C) and (b) Discharged ($T_{cold,in}$=26 °C) of fluid flow rate 4 LPM.

Based on this study, shellac wax as BPCM is efficient (73.4%) compared to existing organic PCMs like paraffin wax, stearic acid, and palmitic acid-based TES units (Kaygusuz 2001; Ozturk 2005).

7.12 CLOSURE

This chapter deals with the experimental performance analysis of shellac wax as BPCM in vertical shell and tube LHTES for an HTF with different inlet temperatures and flow rates. Finally, an optimum value of flow rate and inlet temperature of HTF for LHTES with shellac wax is presented, which can aid in prospective studies on shellac wax for sustainable energy storage. The next chapter deals with the numerical analysis of heat transfer improvement using the proposed tapered shell and tube CLHS unit.

CHAPTER-8

PERFORMANCE EVALUATION OF NOVEL TAPERED SHELL AND TUBE CASCADED LATENT HEAT THERMAL ENERGY STORAGE

8.1 INTRODUCTION

This chapter deals with the storage unit's geometrical design and its effect on the PCM's heat transfer behavior. The study was carried out numerically and compared the heat transfer performance of tapered type shell and tube CLHS model with that of the conventional cylindrical CLHS model, emphasizing the melting rate slowest melting portions (bottom) of the shell and tube unit. Thermal properties like transition temperature, latent, and specific heat of the three organic PCMs OM 42, OM 46, and OM 48 have been obtained using DSC. The same is employed in the 2-D numerical simulation carried out using the enthalpy-porosity method.

The properties of PCM, such as specific heat, transition temperature, and latent heat, are obtained using the DSC heat flow curves. The obtained values are given as input for the PCM properties in the numerical simulation. The heat transfer performance of the tapered type CLHS unit is then analyzed, and the same is compared to the conventional cylindrical type CLHS unit. The melting rate and the energy stored per unit time are compared to assess the superiority of the cascade type CLHS unit. Further, with the help of contours such as streamlines, velocity, melt fraction, and temperature, the detailed physics underlying the superiority is explained in detail, focusing on the convective currents.

8.2 COMPUTATIONAL DOMAIN

Figure 8.1 illustrates a schematic model of tapered type shell and tube CLHS and conventional cylindrical CLHS unit. 2-D models are considered to reduce the computational effort and to obtain the solution with acceptable accuracy. The annulus is filled with PCMs of different transition temperatures and is coupled with the heat transfer tube (copper), through which the HTF (water) is circulated. The inclination for the tapered model is chosen to keep the volume of the PCM fixed, equal to that in the cylindrical unit.
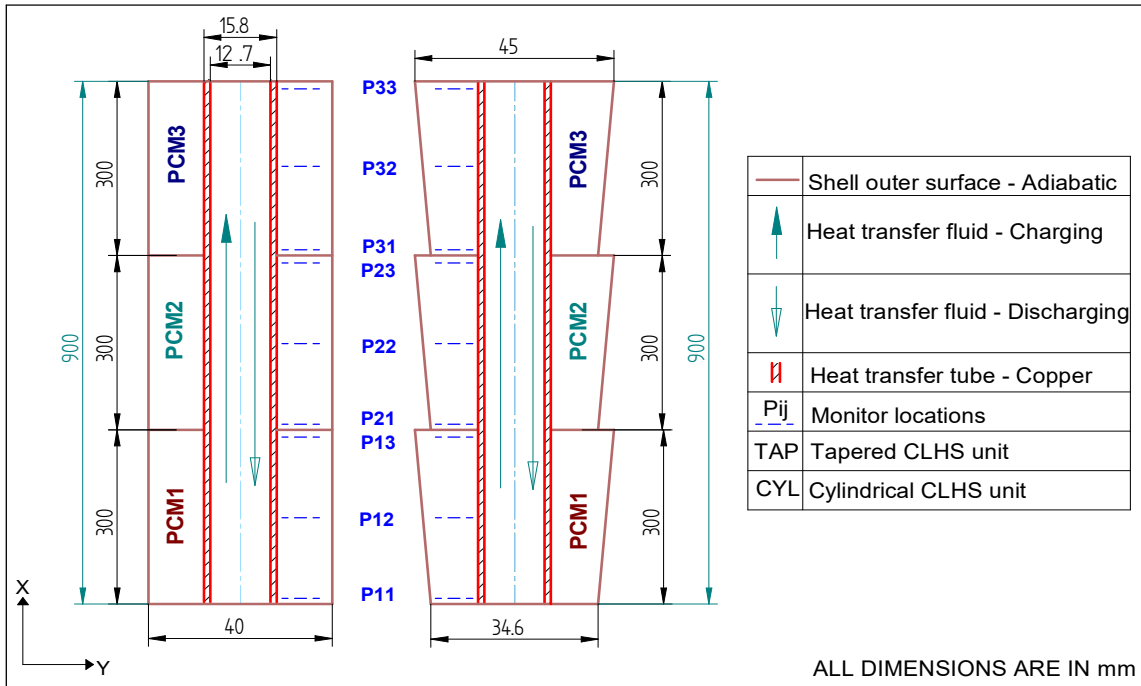
Figure 8.1. The dimension and thermocouple location of a cylindrical and tapered CLHS model.

8.3 NUMERICAL APPROACH

Heat transfer fluid flow and PCMs melting in the annulus are governed by a combination of Navier-Stokes equations and the energy equation. Initially, the PCMs are in the solid state, and heat transfer occurs predominantly via conduction. As the melting progresses, the convective currents are set up owing to the variation in density. CLHS is assumed to be at the ambient temperature (298 K) conditions before melting.

The phase change problem is analyzed based on the enthalpy-porosity method (fixed grid method) having single-phase governing equations (Brent et al. 1988b; Voller et al. 1987). This method, by default, includes an interface between solid-liquid during melting, known as the mushy zone. This technique is generally solved with the finite volume method (FVM), and no explicit condition needs to be considered at the phase front (Benmoussa et al., 2017; Voller and Peng, 1994). The following are the assumptions and boundary conditions employed to solve the below-mentioned governing equations.

➢ The HTF is considered as an incompressible and Newtonian fluid.

> ➢ The HTF inlet conditions, such as temperature and velocity, are invariant with time

> ➢ The HTF thermo-physical properties are temperature independent.

> ➢ Initially, it is assumed that the temperature inside the storage unit is uniform.

> ➢ PCMs are solid before the charging process and in the liquid phase before the discharging process.

> ➢ The outer shell surface is insulated.

> ➢ The computational domain is axisymmetric about the x-axis.

> ➢ For the density variation of PCMs, the Boussinesq approximation is employed.

The SIMPLE algorithm is adopted with pressure-velocity coupling to solve the governing equations. Momentum and energy equations are discretized through a second-order upwind scheme. The PRESTO scheme is employed to solve the pressure correction equations. Under relaxation, factors are set to 0.3, 0.5, 1, and 1 for pressure, momentum, energy, and liquid fraction, respectively. The residual convergence factor is set to 10^{-5}, 10^{-5}, and 10^{-6} for continuity, momentum, and energy equation. HTF operates in the turbulent flow regime, and the K-ε turbulence model is employed for the analysis. The governing equations solved are as follows,

Continuity equation

$$\frac{\partial \rho}{\partial t} + \nabla \left(\rho \cdot \vec{V} \right) = 0$$

(8.1)

Based on the enthalpy-porosity method, the entire PCM domain's energy conservation is expressed in total enthalpy and temperature below.

$$\frac{\partial \rho H}{\partial t} + \nabla \cdot \left(\rho v_{pcm} H \right) = \nabla \left(k \nabla T \right) + S$$

(8.2)

The total enthalpy is evaluated as

$$H = e + \left(L \cdot \beta \right)_{L}$$

(8.3)

$$e = e_{Ref} + \left[\left(\int_{T_{Ref}}^{T_s} c_{p,s,pcm} dT \right) + \left(\int_{T_l}^{T_f} c_{p,l,pcm} dT \right) \right]$$

(8.4)

Where e is the PCM total sensible enthalpy and e_{Ref} is the PCM sensible enthalpy at reference temperature T_{Ref}, β is the mass fraction that indicates the ratio of the mass of

liquid PCM to the total mass of the PCM and is related with each cell in the PCM domain given by Eq. 8.5 (Farag and Leopold 2009).

$$\beta = \begin{cases} 0 & T < T_{Solidus} \\ \dfrac{T - T_{Solidus}}{T_{Liquidus} - T_{Solidus}} & T_{Solidus} \le T \le T_{Liquidus} \\ 1 & T > T_{Liquidus} \end{cases}$$

(8.5)

By combining the Eq. (8.3) – (8.5), the energy conservation Eq. (8.2) can be simplified as:

$$\frac{\partial \rho e}{\partial t} + \nabla \cdot \left(\rho v_{pcm} e \right) = \nabla \cdot \left(k \nabla T \right) - \frac{\partial v_{pcm} \beta L}{\partial t} - \nabla \cdot \left(\partial v_{pcm} \beta L \right) + S$$

(8.6)

The momentum equation is written as

$$\frac{\partial \rho_{Ref} v_{pcm}}{\partial t} + \nabla \cdot \left(\rho_{Ref} vv \right) = -\nabla P + \nabla \cdot \left(\mu \nabla v_{pcm} \right) + \left(\rho - \rho_{Ref} \right) g + v_{pcm} A_s$$

(8.7)

The third term on the right-hand side of the (Eq. 8.7) is buoyancy due to the density difference between the solid and liquid PCM. According to the Boussinesq approximation (Eq. 8.8), the buoyancy force drives the natural convection and is related to PCM's linear thermal expansion coefficient.

Boussinesq approximation

$$\left(\rho - \rho_{Ref} \right) g = -\rho_{Ref} \alpha \left(T - T_{Ref} \right)$$

(8.8)

$$A_s = \frac{\left(1 - \beta\right)^2}{\beta^3 + \varepsilon} A_m$$

(8.9)

In Eq. 8.9, A_m is the mushy zone constant, and the recommended value is usually between 10^4-10^7 (Tan and Fok 2007). However, which signifies how quickly the phase front velocity is reduced to zero as when the PCM solidifies and ε is the small value ($\varepsilon=0.001$) to avoid the division by zero. The value of 10^5 has been used in the prior study (Assis et al. 2007), and the same is adopted herein.

8.3.1 Mean power of CLHS units

The average power is assessed to compare the performance of cylindrical and tapered CLHS units. Energy absorbed and released from PCM is given by Eq. (8.10) and (8.11). The total energy stored within the PCM domain summarizes the sensible heat and latent heat change, as provided in Eq. (8.12) (Meng and Zhang 2017).

$$Q_c = m_{HTF} c_{p,\text{HTF}} \left(T_{out} - T_{in} \right) \tag{8.10}$$

$$Q_d = m_{HTF} c_{p,\text{HTF}} \left(T_{in} - T_{out} \right) \tag{8.11}$$

$$Q_{st} = e + \left(m_{PCM} \times L \times \beta \right)_L \tag{8.12}$$

$$\text{where, } e = \left(\int_{T_{ref}}^{T_s} m_{PCM} c_{p,s,PCM} \, dt \right) + \left(\int_{T_l}^{T_f} m_{PCM} c_{p,l,PCM} \, dt \right)$$

The TES unit's average power during the charging and discharging process is the ratio of HTF energy released in and absorbed from the PCM to the corresponding time taken given in Eq. (8.13) and (8.14), respectively.

$$\overline{p_c} = \frac{Q_c}{t_c} \tag{8.13}$$

$$\overline{p_d} = \frac{Q_d}{t_d} \tag{8.14}$$

8.3.2 Time step and mesh sensitivity analysis

A 2-D axis-symmetric model of different mesh sizes (quadrilateral cells) is considered for tapered and cylindrical units to verify the cell size's solution dependency. Various mesh sizes and the respective time to attain steady-state temperature and melting fraction equal to 333 K and one, respectively, are given in Table 8.1. The mesh sensitivity analysis is performed methodically by increasing the cell density to ensure mesh independence on output results. The cylindrical and tapered units' quadrilateral cells are increased from 59,784 to 1,03,707 and 65,334 to 1,06,623, respectively, and have no significant effect on the output solution. Therefore, to minimize the computational cost, the optimum mesh size of 59,784 and 65,334 cells for cylindrical and tapered types has been chosen, respectively. Further, the time step of 0.05 s is

appropriate for the optimum mesh size to attain the energy equation's accuracy and convergence.

Table 8.1. Mesh sensitivity and computational cost analysis for cylindrical and tapered units.

	Mesh size	ST (333K) time (s)	MF (1) time (s)	Computational time (h)
Cylindrical				
Case 1	27888	9200	8550	51
Case 2	36000	9410	8750	59
Case 3	59784	9559	9100	71
Case 4	103707	9605	9140	91
Tapered				
Case 1	33042	7941	6915	53
Case 2	40425	8116	7165	63
Case 3	65334	8328	7400	75
Case 4	106623	8365	7480	94

8.3.3 Validation
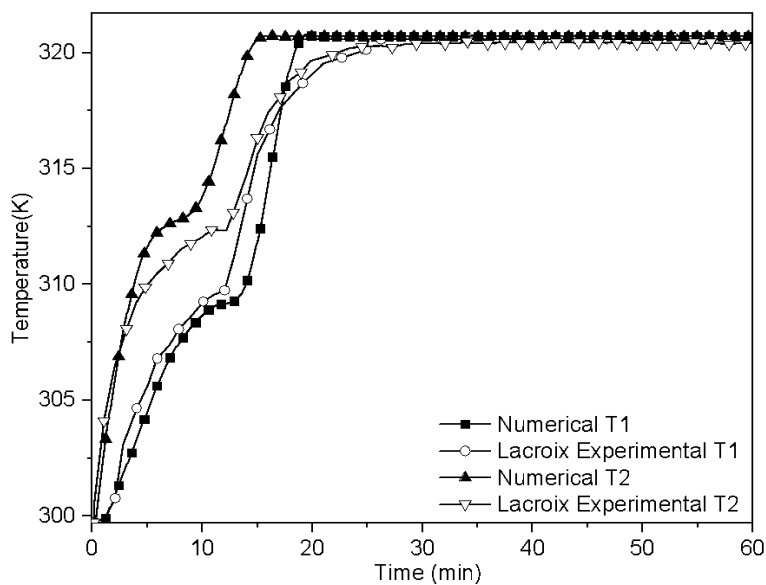
Figure 8.2. Numerical results validation with the experimental results (Lacroix 1993).

The results obtained with the present shell and tube LHTES unit are compared with the experimental model (Lacroix 1993).The temperature of PCMs during the charging

116

process is monitored at two different positions, as described in the experimental model.The results obtained have a mean deviation of 11 % from the experimental results (Lacroix 1993), indicating that the present methodology has acceptable accuracy (Figure 8.2). This deviation may be attributed to the fact that the shell wall is insulated and the considered mushy zone parameter, which might have significantly affected the melting rate.

8.4 DSC ANALYSIS

The DSC analysis of three organic PCMs (OM 42, OM 46, and OM 48) is shown in Figure 8.3.

(a)

(b)

(c)
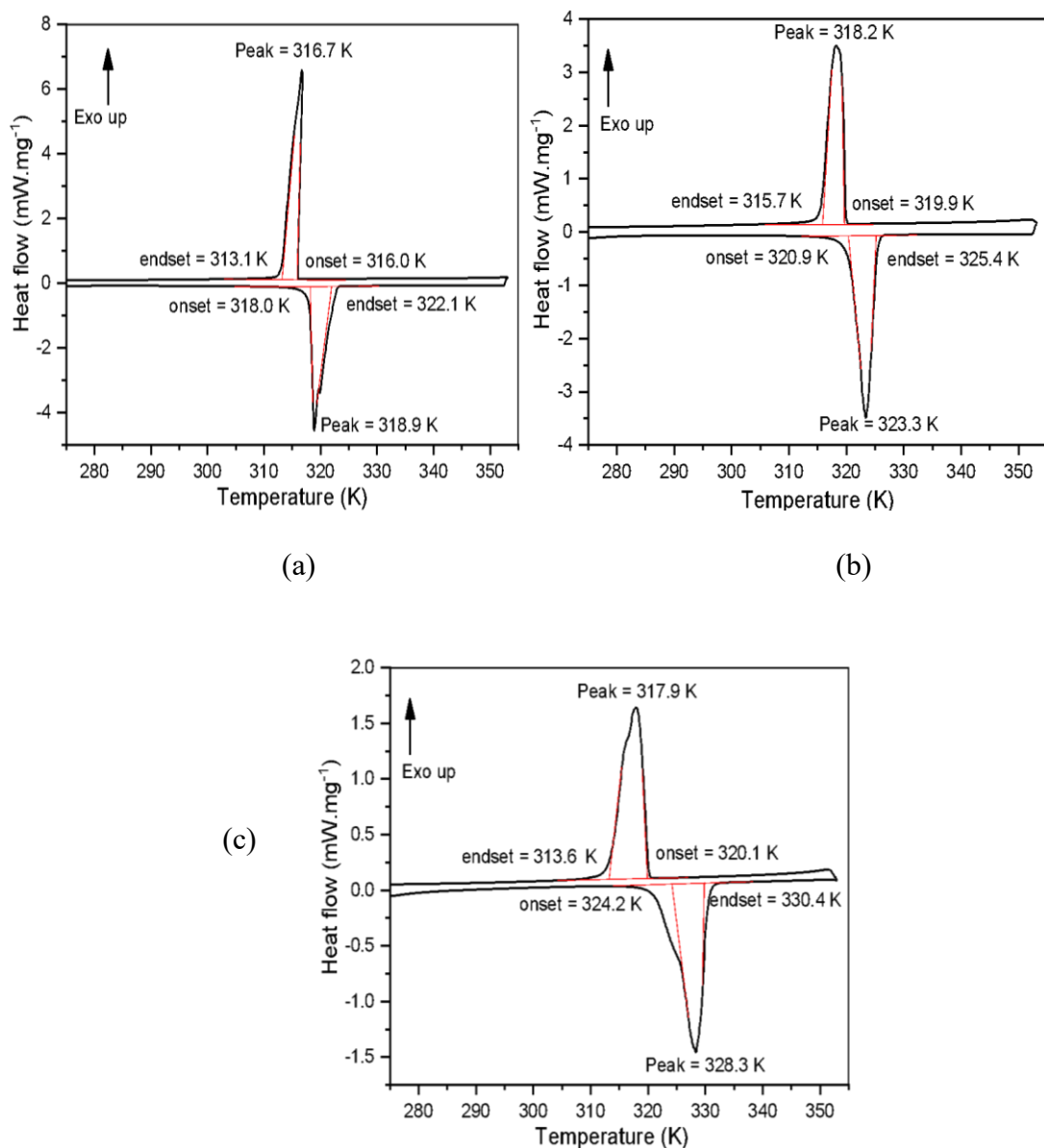
Figure 8.3. DSC heat flow curve (a) OM 42 (b) OM 46 (c) OM 48.

Table 8.2. Thermo-physical properties of PCMs.

PCMs	PCM1	PCM2	PCM3
Commercial name (PLUSS[R])	OM 48	OM 46	OM 42
[a]Melting temperature (K)	324.2	320.9	318
[a]Solidification temperature(K)	320.1	319.9	316
[a]Latent heat (kJ/kg)	85.6	123.8	131.2
	80.3	119.5	131.5
[a]Specific heat(kJ/kg·K) (Solid/Liquid)	2.0 / 2.3 (301 K / 333 K)	2.5 / 2.7 (301 K / 326 K)	2.7 / 2.7 (303 K / 328 K)
[b]Density(kg/m^3) (Solid/Liquid)	960 / 875 (301 K / 328 K)	917 / 880 (301 K / 328 K)	903 / 863 (303 K / 323 K)
[b]Thermal conductivity(W/m·K) (Solid/Liquid)	0.2 / 0.1 (278 K/ 333 K)	0.2 / 0.1 (278 K / 333 K)	0.19 / 0.1 (278 K / 333 K)
[b]Dynamic viscosity (Pa·s)	0.01755	0.01823	0.01979
[a]Linear thermal expansion coefficient (1/K)	0.0038	0.0042	0.0022
[b]Thermal stability (Cycles)	~2000	~2000	~2000

Note: [a]measured, [b]Ref.(PLUSS[R], 2019).

All three PCMs show sharp melting and solidification peaks, and zero slopes of the heat flow curves signify sensible heating in a solid and liquid state. This deviation may be attributed to the fact that the shell wall is insulated and considered a mushy zone parameter, significantly affecting the melting rate. Whereas in practical scenarios, heat dissipation occurs through the outer walls. With the validated methodology, further analysis is carried out. The sudden slope change indicates a transition region, and the heat flow peak signifies maximum endothermic and exothermic reactions during the phase transition process. Besides, it was noteworthy that OM 42, OM 46, and OM 48 have a narrow range of melting peaks at 318.9 K, 323.3 K, and 328.3 K, respectively,

signifying the mushy zone thickness of the PCMs employed is less. The latent and specific heat in the liquid and solid state of all three PCMs are listed in Table 8.2. Based on DSC and supplier data analysis, all three PCMs are suited for the CLHS system.

8.5 CHARGING PROCESS

The PCM temperature variations of the PCMs studied at different locations of cylindrical and tapered CLHS units are shown in Figure 8.4 ((a), (b), and (c)).

(a)

(b)

(c)
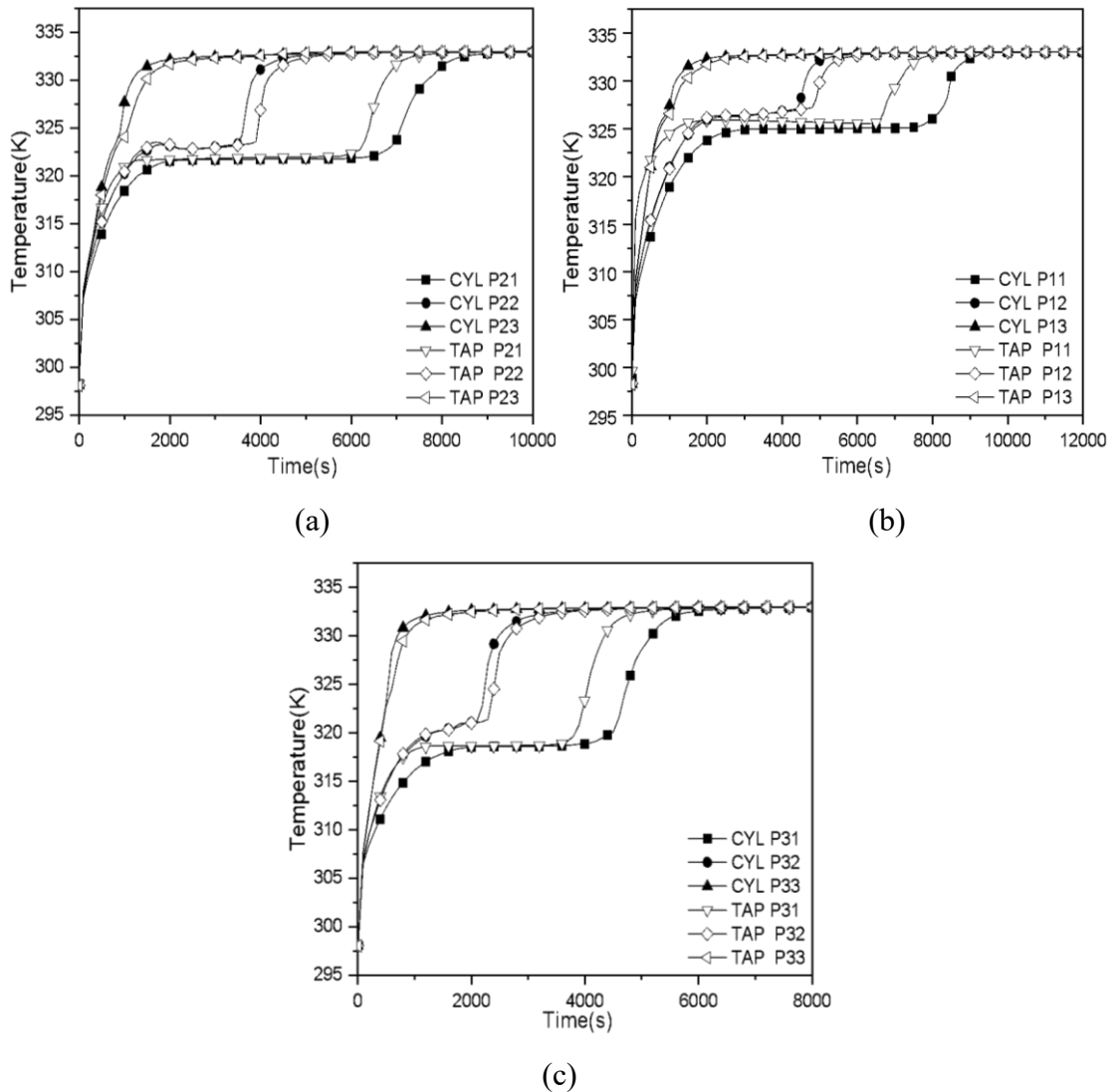
Figure 8.4. Comparison of temperature variation with charging time in tapered and cylindrical CLHS unit (a) PCM1 (b) PCM2 (c) PCM3.

Due to low density and lower onset melting point relative to PCM 1 and PCM 2, PCM 3 melts faster. The total time advanced to reach the steady-state for PCM 3 in the

cylindrical unit is 6000 s compared to 4900 s in the tapered unit. The PCM 2 followed a similar trend and attained steady-state in tapered and cylindrical units after 6600 s and 7900 s, respectively. Similarly, PCM1 reached the steady-state faster in tapered (t = 8330 s) than the cylindrical CLHS (t = 9560 s).

(a)

(b)

(c)

Figure 8.5. Variation of mass fraction with charging time in tapered and cylindrical CLHS unit (a) PCM1 (b) PCM2 (c) PCM3.

In both cases, the average temperature of the three PCMs decreased from top to bottom along with the cascaded storage unit. Owing to a lower transition temperature and higher temperature gradient with HTF, PCM 3 melted faster than PCM 2 and PCM 1.

Adjacent to the tube surface, heat conduction dominates due to the higher temperature gradient and PCM melts.

However, the bulk of the PCM remains in solid-state even after the onset of the melting of PCM adjacent to the tube surface. The part of the PCM melt reaches the top portion due to the influence of buoyancy-induced natural convective transport.

Figure 8.6. Charging contours of PCMs temperature (left) and a liquid mass fraction (right) (a) Tapered (b) Cylindrical, CLHS unit.

The time consumed for charging the cylindrical unit is more than a tapered CLHS model, as shown in Figure 8.4. The temperature gradient at various measured locations is smaller for the tapered unit than in the cylindrical CLHS unit. The local mass fraction variation with time for cylindrical and tapered units is shown in Figure 8.5. The mass fraction between 0 to 1 signifies a mixture of solid and liquid PCM, the mushy zone.

PCMs in the tapered unit require an average time of 7400 s to melt completely, whereas the cylindrical unit required 9100 s.
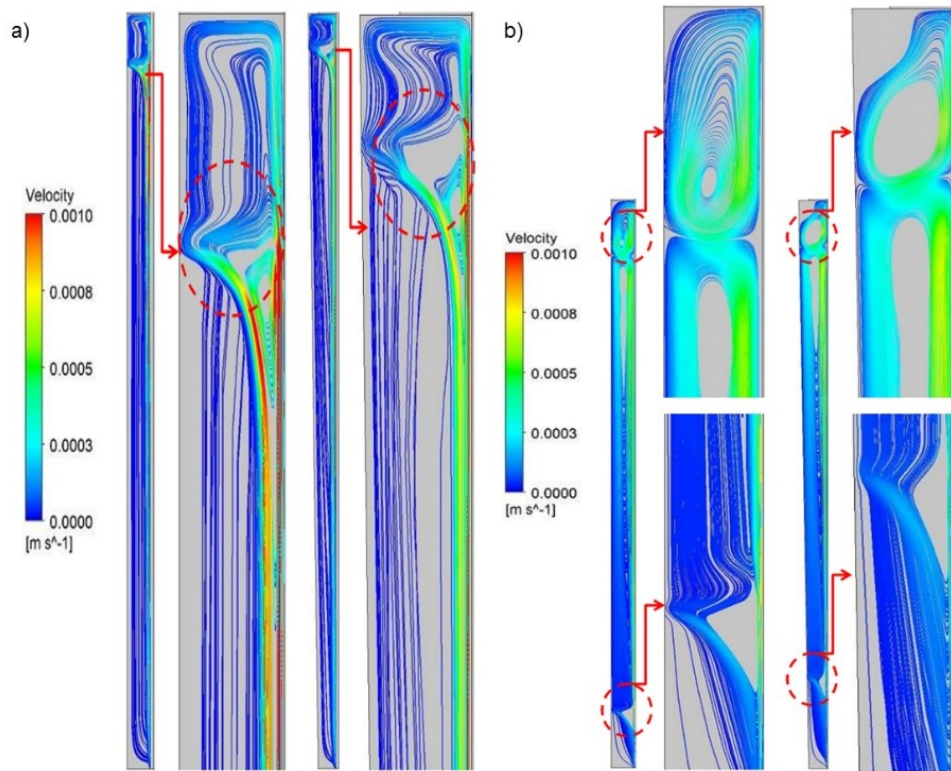
Figure 8.7. Streamlines during the charging process at (a) t = 2000s and (b) t = 7000s.

In the beginning, the HTF needed a specific time to transfer heat to PCM 2 and PCM 3, as they were positioned farthest from the inlet when compared to PCM 1. Hence for t < 360 s, the melted fraction of PCM 1 is higher than that of PCM 2 and PCM 3. Transient variation of temperature and mass fraction of 3 PCMs in cylindrical and tapered units are shown in Figure 8.6 (a and b). The temperature contour shows that during the initial time (t = 100 s), the isotherms are parallel to the shell tube, indicating the dominance of conduction heat transfer. As time progresses, the isotherms become curved for both units, showing that convection currents drive the melting rate of PCMs. However, the strength of the convective currents is different in cylindrical and tapered units. At time t = 8000s, the mass fraction at the bottom portion of PCM 2 and PCM 1 in the cylindrical unit indicates that the complete melting of PCM is not achieved, whereas, in the tapered unit, all the three PCMs have been completely melted. This has been a serious problem in cylindrical units, and extensive research has been carried out

to eliminate this with fins. However, the application of the fins at the bottom consumes space and also can cause thermal stratification. As a better alternative, a tapered cascade unit has been researched, and complete melting has been obtained simultaneously, as shown in Fig 8.6a.
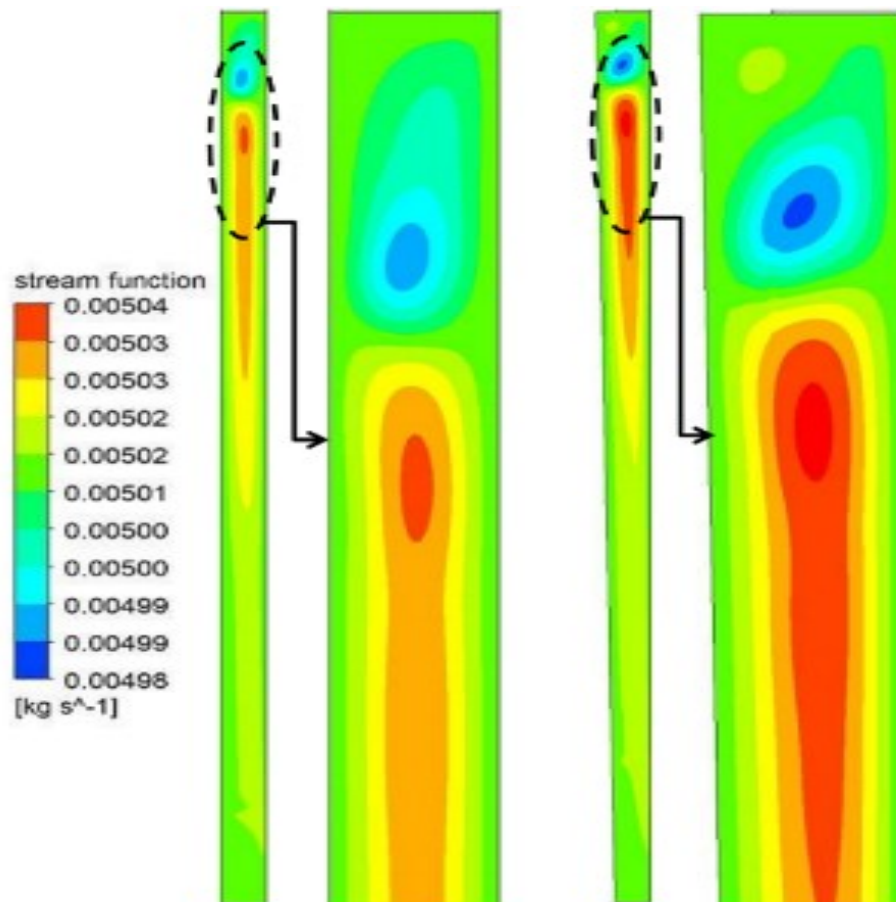
Figure 8.8. Stream function contour for the charging process at t = 7000 s.

The tapered unit's better performance relative to the cylindrical unit is attributed to the following physical aspects. Initially, in the absence of natural convection, the melting of PCM around the hot shell and tube surface is caused by conduction heat transfer. With time advancement (t = 7000 s), the melting front on the top becomes significant and deforms. Owing to this, the molten PCM rises upwards, replacing the colder PCM, creating a recirculating vortex which augments as PCM melts with time (Figure 8.7, a and b). Besides Figure 8.8, it is observed that the effect of natural convection is higher in tapered units compared to cylindrical ones. At the bottom, for t = 7000 s, the phase front lines' slope is higher for the cylindrical unit, indicating that conduction heat

transfer dominates in the liquid PCM (Figure 8.9(a)). Whereas, in the case of tapered CLHS units, the front phase lines at the bottom are less steep, indicating convective currents. A similar inference is drawn from the streamline contours at the bottom of both units (t = 7000 s). In the case of cylindrical units, the streamlines have a higher slope and are more inclined towards the shell and tube unit's far solid surface rather than towards the top. However, in the tapering unit, the streamlines are less steep and are directed towards the top. The same is reflected by the vortex's position and size formed at the bottom of both units (Figure 8.7(b)).
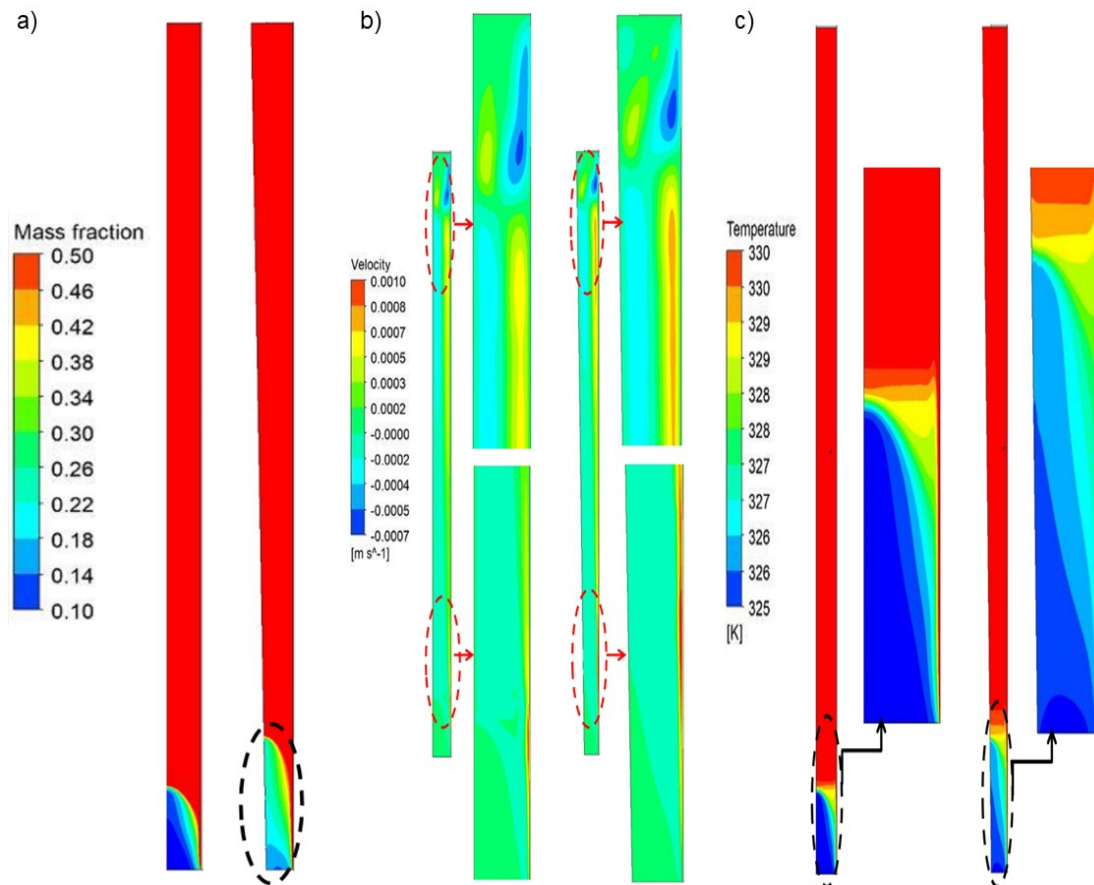
Figure 8.9. Charging process at t = 7000 s, (a) Mass fraction, (b) Velocity, and (c) Temperature contour.

In tapered units, the molten PCM's velocity adjacent to the shell wall at the bottom is higher than that in the case of cylindrical units (Figure 8.9(b)), indicating higher convective heat transfer in the tapered CLHS unit. Also, the temperature contours

(t = 7000 s) suggest that PCM melt at the bottom is stagnant in a cylindrical unit compared to the tapered CLHS unit (Figure 8.9(c)).

8.6 DISCHARGING PROCESS

After the PCM has been charged, it is equally important to know the charged PCM's rate, a vital aspect of designing any LHTES system.

(a)   (b)

(c)
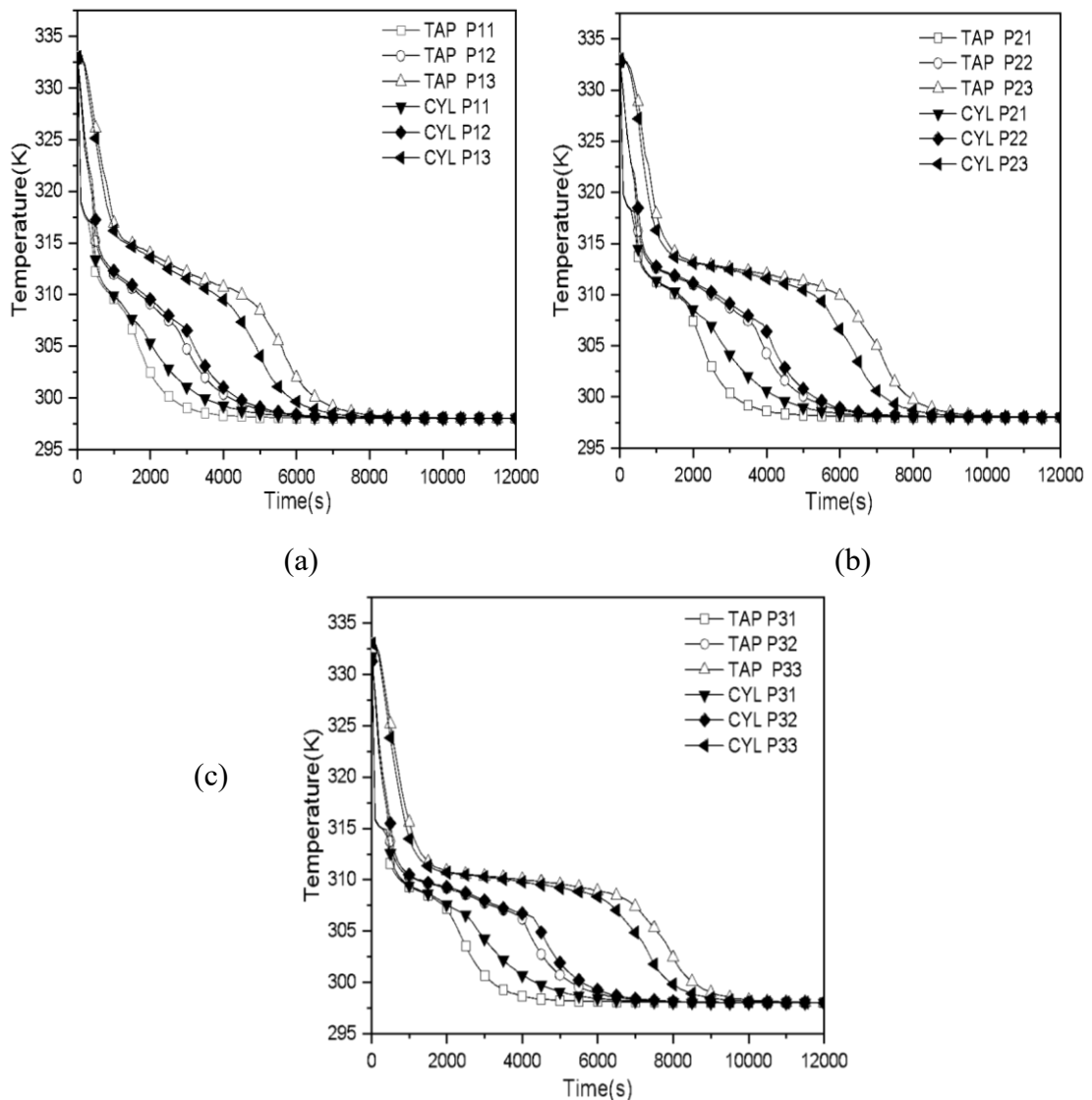
Figure 8.10. Comparison of temperature variation at various monitor locations (as mentioned in Figure 8.1) in the PCM unit with discharging time for tapered and cylindrical CLHS unit (a) PCM1 (b) PCM2 (c) PCM3.

The variation of temperature of the PCM units during the discharge period for both cylindrical and tapered units is shown in Figure 8.10 (a), (b), and (c). It is observed that temperature decreases rapidly during the initial phase of discharge. The liquid PCM's sensible cooling is attributed to the low specific heat and convection-dominated heat flow. With the advancement of time, the temperature-time curve approaches zero slopes owing to the release of latent heat and the dominance of the conduction mode of heat transfer.
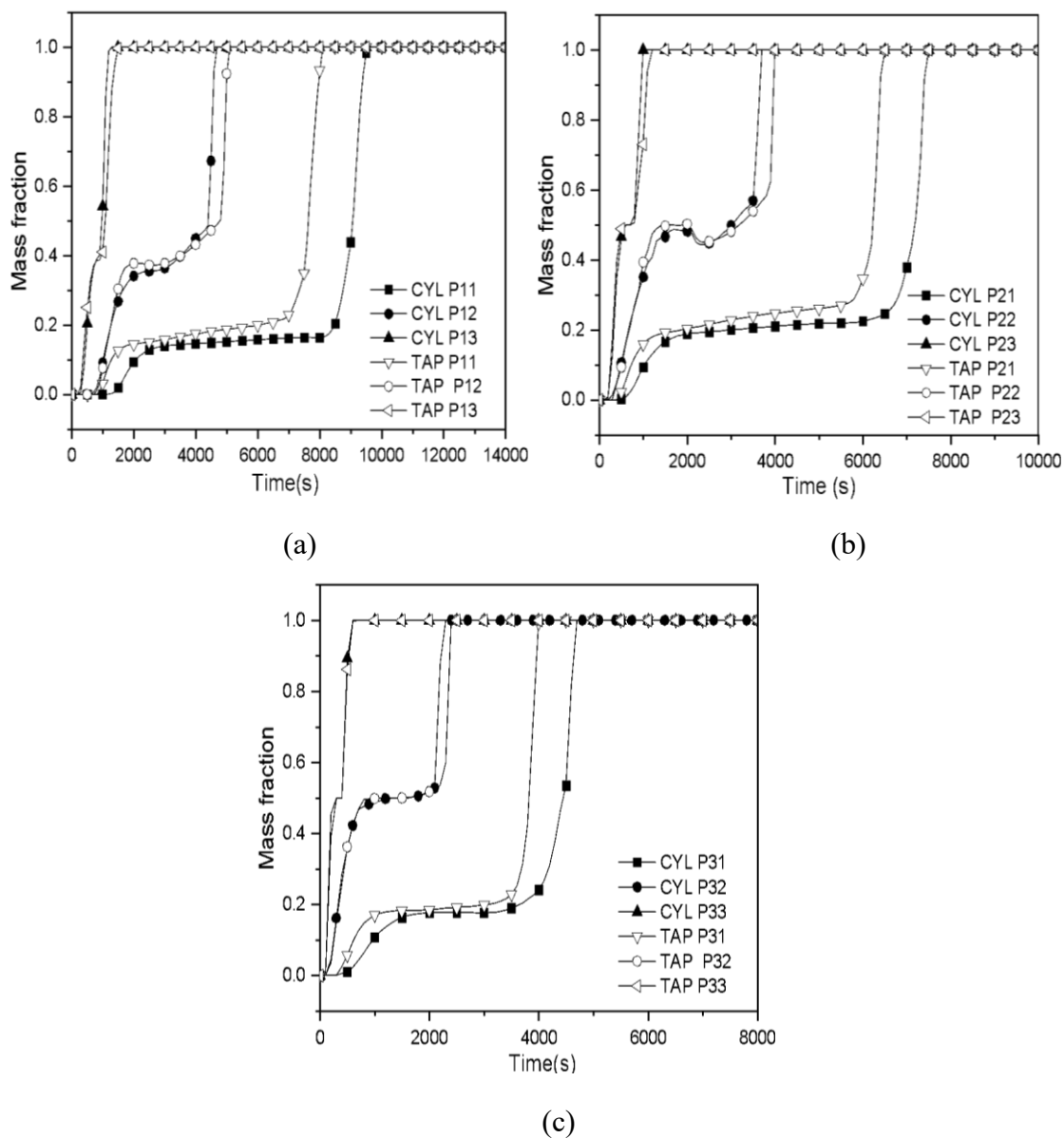

(a)   (b)

(c)
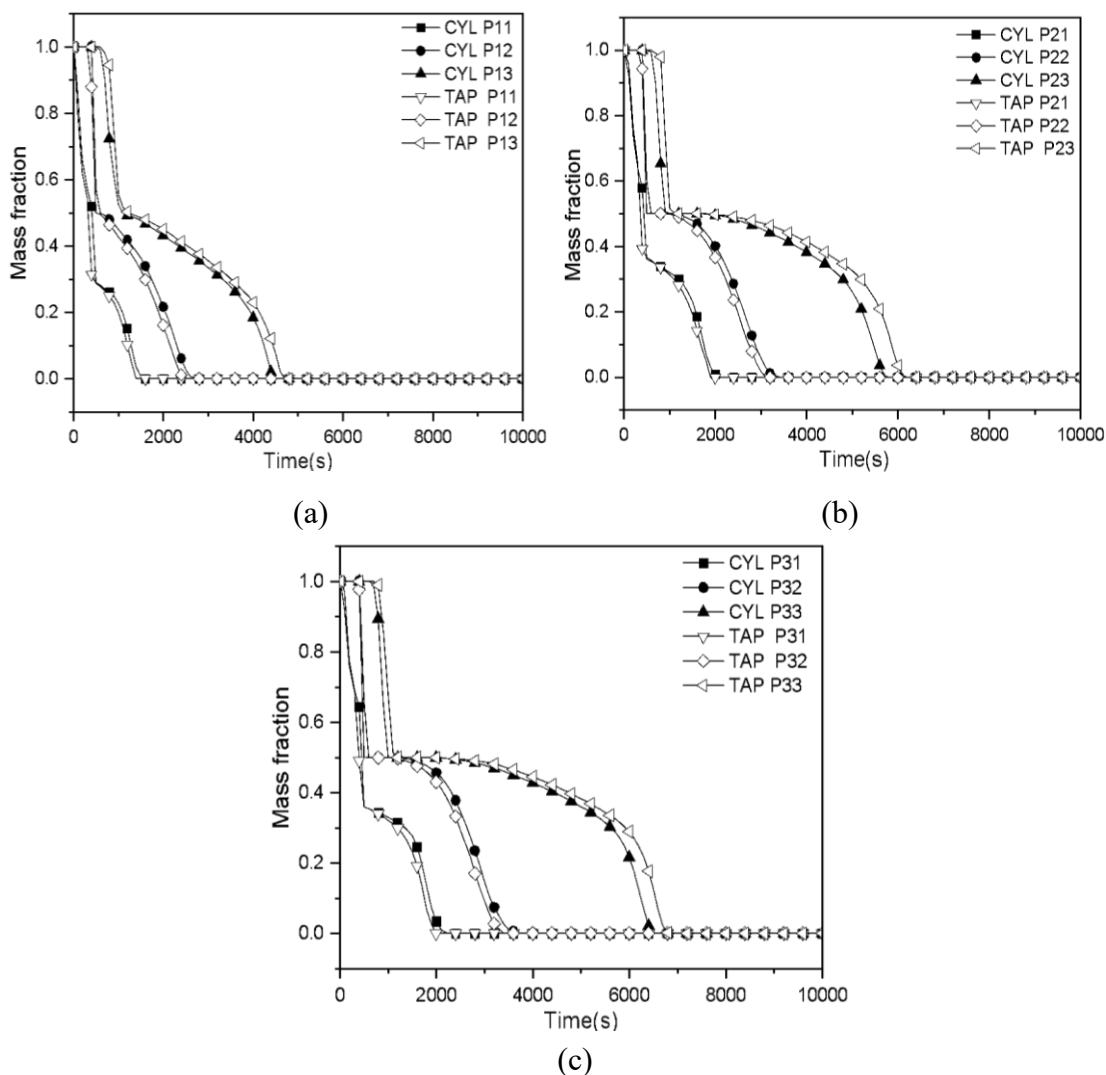
Figure 8.11. Comparison of mass fraction with discharging time in tapered and cylindrical CLHS unit (a) PCM1 (b) PCM2 (c) PCM3.

The temperature at the bottom reduces much faster than at the top level due to the PCM contiguous to the HTF tube solidifying first and forming a thin solid layer around the

tube. The low thermal conductivity of PCMs hinders the heat flow from the liquid PCM away from the tube surface. The heat transfer rate declined as the solid PCM around the HTF tube increased. Hence, conduction heat transfer between PCMs and HTF fluid dominated during the discharging process. On the other hand, natural convection prevails away from the HTF tube's surface, causing the hot liquid PCMs to move due to the buoyant force. Hence, the PCMs temperature at the bottom was lesser than at the top. The average temperature at positions 1 and 2 of the tapered unit dropped than that of the cylindrical cascaded unit, signifying that the energy discharge from the former is faster than the latter.
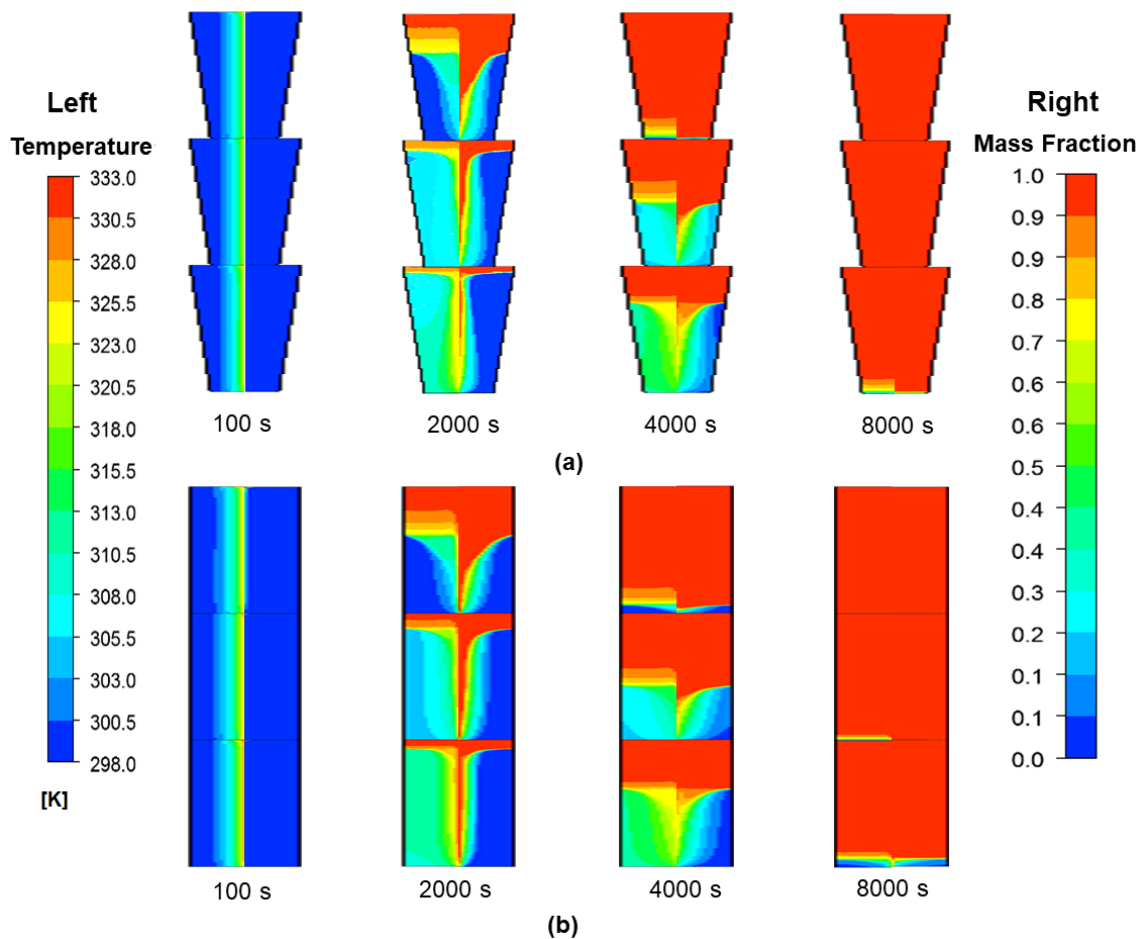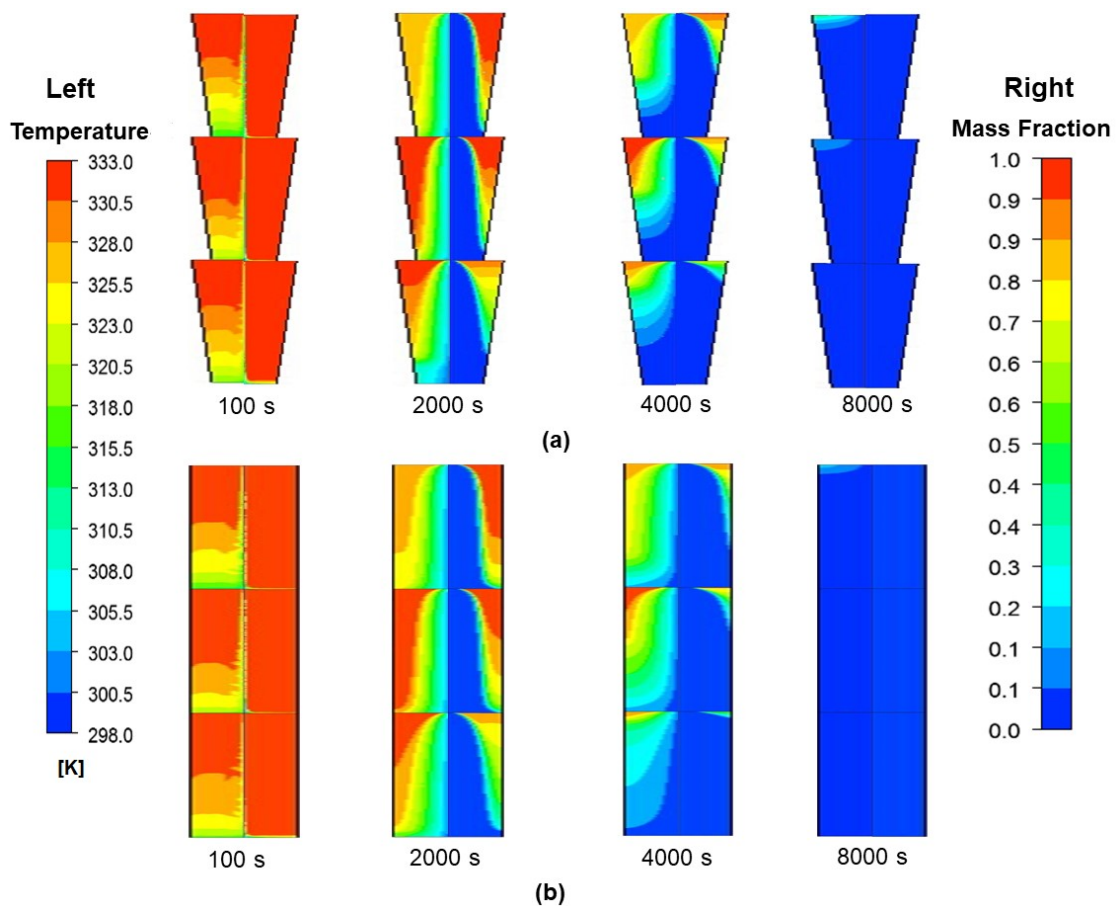

Figure 8.12. Discharging contours of PCMs temperature (left) and a liquid mass fraction (right) of (a) Tapered (b) Cylindrical, CLHS unit.

Whereas the temperature reduction at position 3 is lagging in tapered than that for cylindrical cascaded units, as shown in Figure 8.10 (a, b, and c). Unlike the charging process, the temperature at different locations attains the steady-state at nearly the same

time, which also quantifies that the energy recovered from both systems is almost the same. The comparison of mass fraction variation with time during the discharging process in tapered and cylindrical types is shown in Figure 8.11. There is no considerable difference in mass fraction rate for tapered and cylindrical cascaded units during the discharging period.

Further, upon exploring the mass fraction contours (Figure 8.12), it is observed that all the three PCMs in both the models solidified within 8000 s. The PCM 3 (OM 42) temperature drops slower during the discharging process than the other PCMs due to its lower transition temperature and higher latent heat than PCMs (OM 46 and OM 48). As shown in Figure 8.12a, the tapered model's initial temperature dropped to the crystallization temperature earlier than the cylindrical model due to the presence of convective currents in the liquid PCM. During the solidification process, the tapered unit corners take more time than the cylindrical unit owing to a reduction in conduction thermal resistance along the radial direction in the cylindrical unit.

8.7 MEAN POWER OF THE CYLINDRICAL AND TAPERED CLHS UNIT

The average powers of the two CLHS models are listed in Table 8.3. The HTF inlet mass flow rate is 0.0315 kg/s and is maintained constant throughout the numerical analysis for both models. The average power during the charging process is affected by the mode of heat transfer.

Table 8.3. The average power of the CLHS units.

Model	Cycle	Time, t (s)	Energy, e (kJ)	Mean power, $\overline{p}$ (kW)
Tapered	Charging	8330	175.1	0.0210
	Discharging	8450	171.8	0.0203
Cylindrical	Charging	9560	168.3	0.0176
	Discharging	8050	169.8	0.0208

Due to stronger convective heat transfer in the tapered unit. As the amount of energy stored is almost the same, the mean power mainly depends on heat charging and discharging. The obtained percentage increase in mean power for the tapered unit is 17.6 % higher than the cylindrical unit for a charging process.
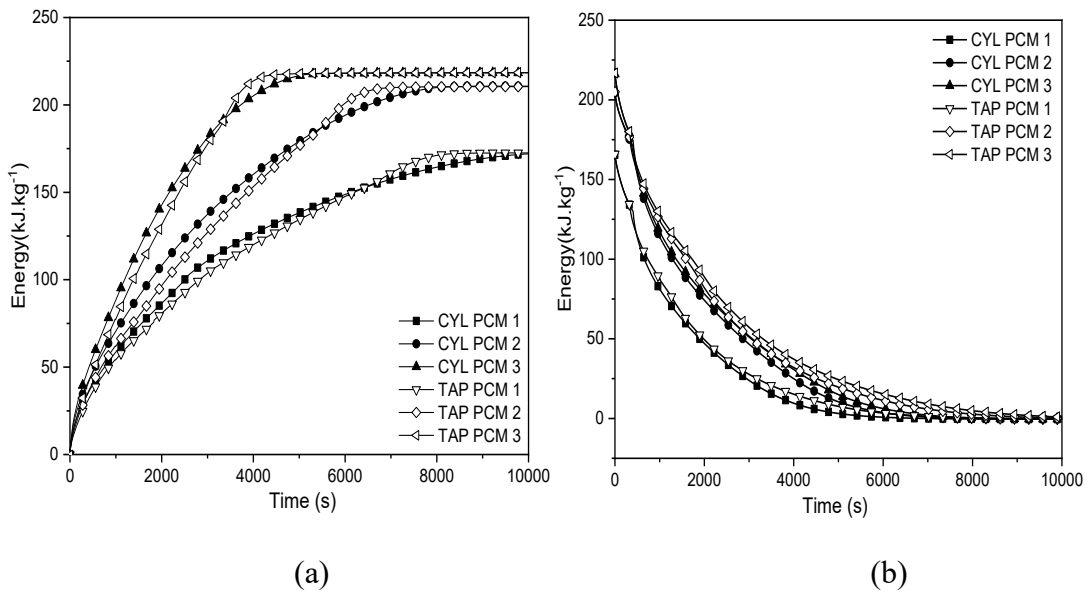
Figure 8.13. Specific energy comparison of cylindrical and tapered CLHS unit (a) Charging (b) Discharging process.
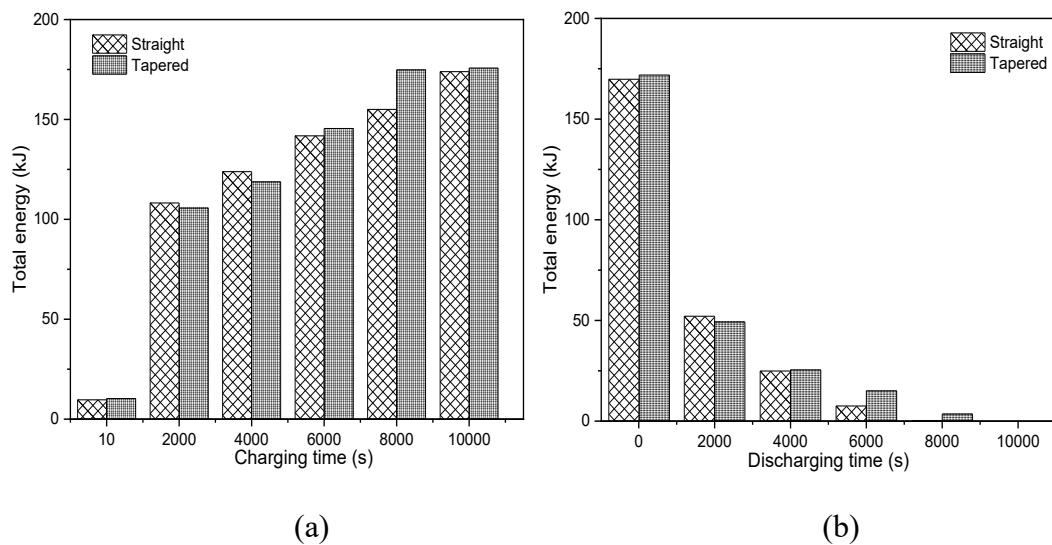
Figure 8.14. Total energy comparison of cylindrical and tapered CLHS model (a) Stored (b) Discharged.

However, for the discharging process, the mean power is 2.4 % lesser than the cylindrical tube. Hence, the rate of thermal energy stored is higher due to the effective utilization of the convection mode of heat transfer in tapered design. When analyzed in detail, it is observed that the overall percentage of energy stored for t < 2000 s is 62 % and 60% for cylindrical and tapered CLHS models, respectively. As the melt fraction increased, convective currents gained strength. Hence, the tapered unit absorbed the

remaining 40% in 6330 s in contrast to the cylindrical unit, which absorbed the remaining 38% of energy in 7560 s. This indicates the effective utilization of the convection mode of heat transfer in a tapered type CLHS system. Figure 8.13(a and b) shows the total energy stored and discharged in all the three PCMs for tapered and cylindrical CLHS models. The maximum energy stored and released is in PCM3>PCM2>PCM1 due to relatively lower melting temperature, highest sensible and latent heat of fusion of PCM3 attributed to its steeper temperature gradient with HTF. Comparing the total energy stored and discharged in two models for the fixed HTF inlet temperatures and the flow rate is shown in Figure 8.14(a) and (b), respectively. It is observed (Figure 8.14a) that the energy stored in a tapered and cylindrical unit reaches a maximum of around 8000 s and 10000 s, respectively, and after that remains constant in the charging cycle.

8.8 CLOSURE

The proposed tapered and existing cylindrical CLHS unit has been designed and modelled using an ANSYS workbench. The numerical methodology has been validated with previous experimental work to standardize it—comparing charging and discharging time, the total energy stored and released. Based on numerical results, the tapered type CLHS model utilizes convective heat transfer, effectively enhancing the melting rate of PCM without any additional structural configurations such as fins. The next chapter highlights the conclusions, key contributions of the present work, and suggestions for future work that have been discussed.

CHAPTER-9

CONCLUSIONS AND FUTURE SCOPE

9.1 CONCLUSION

This thesis is directed towards the thermophysical and performance analysis of BPCM for medium temperature applications like solar energy-assisted domestic water heating, food drying, waste heat recovery, etc. The conventional and non-conventional characterization techniques are adopted to characterize the commercially available BPCM and, importantly, Shellac wax as novel BPCM. Furthermore, experimentally evaluated shellac wax's energy storage and discharge performance using lab-scale shell and tube type TES unit with utmost importance for medium temperature applications and numerically compared the proposed novel tapered cascade unit's performance with the conventional cylindrical CLHS unit as the heat transfer enhancement technique.

➢ The effect of the vertical sample holder's aspect ratio on the PCM(OM46) subcooling in T-history measurement is evaluated and compared with the DSC results. The DOS is more in the DSC heat flow curve due to a higher cooling rate and lesser sample mass than the T-history analysis. I.R. contour at different cooling times shows that the T3 sample tube cools faster at a nearly uniform temperature. Nucleation triggers between the inner surface of the glass tube and the PCM are due to the adhesion force and are termed as heterogeneous nucleation. As the tube's diameter decreases or the aspect ratio increases, the cooling rate increases, affecting the high DOS value. T-history cooling with tube insulation reduces the heat transfer from the tube to the ambient, i.e., reducing the cooling rate and lowering the DOS. However, the increased diameter or the sample mass affects the sensible heat discharge time (t_{plt}) to attain plateau (melting temperature). However, the reduction in speed of solidification reduces the temperature level of the plateau. Because a significant fraction of sample mass below melting temperature absorbs more latent heat released by the nucleating site to increase the PCM temperature, reducing the latent heat released by the PCM. To accurately determine PCM's transition temperature and latent enthalpy in THM, it is recommended to use high aspect ratio tubes owing to the nearly uniform temperature inside the PCM. However, high

aspect ratio tubes take less time to attain plateau (t_{plt}). Also, choosing the lower cooling rate leads to a significant reduction in DOS.

➢ The thermal analysis of BPCM (OM55) checks the suitability and reliability of thermal properties for domestic solar water heating applications. Prime properties like transition and crystallization temperature, enthalpy of transition, and specific heat were evaluated and validated on bulk sample THM and DSC analysis.

➢ OM55 maximum stable temperature by TGA analysis is 154.6 °C, much higher than the DSWH application temperature range. OM55 is thermally stable within the operating condition. The maximum endothermic reaction indicated by DTA is 1.8 °C deviation with the DSC due to the measuring conditions and equipment accuracy.

➢ The thermal conductivity of OM55 obtained in TCA (TPS) is considerable, and it is higher than the supplier's nominal values (Transient line source method (TLS)). The TPS technique is a fast and precise method to measure the thermal conductivity and diffusivity of solids and liquids compared to the TLS method, which is more suitable for liquid than solid samples. DSC results depict a reasonable range of melting and solidification as 58.7 to 46.0 °C, respectively. The volumetric behavior of bulk OM55 is evaluated using four THM method trials, which indicates melting and solidification range as 59 ± 0.5 to 46 ± 0.5 °C respectively. However, THM trials' DOS and DSC analysis are 0.7 ± 0.1 °C and 0.9 °C respectively. No considerable difference in the subcooling effect has been observed between DSC and bulk sample THM. Calculation of isothermal enthalpy gives more insight into PCM thermal energy storage and discharge capacity and the storage system's design. However, to compare PCM properties and know the operating temperature for maximum energy storage and discharge, evaluating PCM's isothermal and non-isothermal enthalpy is essential. The DSC and THM study's outcome is that the OM55 operating temperature range for the optimum energy storage and discharge is 46 to 59 °C.

➢ Thermophysical and rheological characterization of shellac wax depicts shellac wax has aliphatic hydrocarbons, carboxylic acid, alcohol, and esters functional group (similar to beeswax and carnauba wax) Shellac wax, having a broad transition zone with a melting and solidification peak at 79.5 °C and 71.5 °C,

respectively, is thermally stable within the operating temperature. It has good enthalpy, sensible heat, and thermal conductivity values, which is the prime requisite property for PCM in storage applications. THM cooling rate curve is used to plot both first and second-order transition ranges, and it closely matches the DSC results. The comparison of THM and DSC enthalpy results signifies shellac wax as volume-dependent behavior. Shellac wax exhibits no significant change in thermal properties like transition temperature and latent heat after 300 thermal cycles.

➢ The melting and solidification behavior of shellac wax during the charging and discharging phases are studied employing a vertical shell and tube LHTES unit. The impact of operational parameters like HTF inlet temperature and flow rates on heat transfer characteristics of shellac wax are studied. Analysis of the charging process's temperature distribution curve and contours indicates that the PCM's heat transfer process is initiated by conduction. Later, it is dominated by convective currents.

➢ The inlet temperature of HTF significantly affects the heat transfer rate and complete melting process of shellac wax. The maximum reduction in melting time and storage efficiency is 42.2% and 73.4%, respectively, at 120 °C. During the charging process, as the flow rate increases from 2 to 4 LPM, a reduction of 43.6 % is obtained in melting time. However, a further increase in flow rate adversely affects the overall heat transfer coefficient resulting in no considerable improvement in melting time. The optimum flow rate and inlet temperature are obtained as 4 LPM and 120 °C, respectively yielding a charging efficiency of 73.4%, discharging efficiency of 62.6%, and maximum reduction in the melting time is 43.6% that shellac wax is a promising alternative for paraffin wax. It is evident from the experimental study that shellac wax is a suitable Bio-PCM for medium temperature range (60-80 °C) applications such as waste heat recovery, domestic water heating, food drying, etc.

➢ Computational analysis has been performed to investigate and compare the tapered and cylindrical CLHS model's heat transfer behavior. The liquid PCM accumulates in the shell's top surface during the charging cycle due to the buoyant force. The mean power for the tapered model during the charging cycle is 17.6%

higher than the cylindrical, attributed to convection heat transfer's dominance during the melting process. During the initial charging phase, 60% of the total energy is stored for the same charging time in both models. However, the time to store the remaining 40% of the total energy varied significantly for the two models due to the impact of natural convection. The tapered type CLHS model utilizes convection heat transfer, effectively enhancing PCM's melting rate without additional structural configurations such as fins. Hence is economically justifiable for higher energy storage for the same volume compared to conventional cylindrical CLHS units. This information helps the researchers carry out the experimental work on heat transfer enhancement and effective utilization of natural convection to select a geometrical design for the CLHS unit in solar-thermal energy storage systems.

9.2 KEY CONTRIBUTIONS OF THE PRESENT WORK

Following are the key contribution of the present work.

➢ Discussed the effect of sample tube aspect ratio on PCMs subcooling with T-history plots and optimized it.

➢ Proposed PCM isothermal enthalpy evaluation to determine latent heat energy storage and discharge capacity.

➢ Design of lab-scale shell and tube LHTES experimental setup.

➢ In a detailed thermophysical and performance analysis of shellac wax as novel BPCM.

➢ Proposed novel geometric configuration to enhance the PCM heat transfer in the LHTES system.

9.3 SCOPE FOR FUTURE WORK

➢ The study of tube aspect ratio effects on PCM subcooling can be extended to even inorganic materials. However, the inorganic material is more pronounced DOS than organic PCMs. Further, the possibility of nucleation temperature measurement at the outer tube surface and employing the controlled heating and cooling rate in the THM, which even more details the effect of tube aspect ratio on PCM subcooling.

➢ Shellac wax can be used for real site medium temperature applications like district heating, food drying, waste heat recovery, and solar thermal energy storage.

➢ Adopting the heat transfer enhancement techniques like multi-pass HTF tubes, fins, or changes in the geometrical configurations can enhance the shellac wax-based LHTES system's efficiency.

REFERENCES

Abhat, A. (1983). "Low-temperature latent heat thermal energy storage: heat storage materials." *Solar energy*, 30(4), 313-332.

Adine, H. A., and Qarnia, H. el. (2009). "Numerical analysis of the thermal behavior of a shell-and-tube heat storage unit using phase change materials." *Applied Mathematical Modelling*, 33(4), 2132–2144.

Akgün, M., Aydin, O., and Kaygusuz, K. (2007). "Experimental study on melting/solidification characteristics of a paraffin as PCM." *Energy Conversion and Management*, 48(2), 669–678.

Al-Abidi, A. A., Mat, S. bin, Sopian, K., Sulaiman, M. Y., and Mohammed, A. T. (2013). "CFD applications for latent heat thermal energy storage: A review." Renewable and Sustainable Energy Reviews, 20, 353-363

Agyenim, F., Hewitt, N., Eames, P., and Smyth, M. (2010). "A review of materials, heat transfer and phase change problem formulation for latent heat thermal energy storage systems (LHTESS)." *Renewable and Sustainable Energy Reviews*, Pergamon.

Aldoss, T. K., and Rahman, M. M. (2014). "Comparison between the single-PCM and multi-PCM thermal energy storage design." *Energy Conversion and Management*, 83, 79–87.

Anish, R., Mariappan, V., and Mastani Joybari, M. (2019). "Experimental investigation on the melting and solidification behavior of erythritol in a horizontal shell and multi-finned tube latent heat storage unit." *Applied Thermal Engineering*, 161, 114194.

Arena, S., Cau, G., and Palomba, C. (2015). "CFD simulation of melting and solidification of PCM in thermal energy storage systems of different geometry." *Journal of Physics: Conference Series*, IOP Publishing, 12051.

Assis, E., Katsman, L., Ziskind, G., and Letan, R. (2007). "Numerical and experimental study of melting in a spherical shell." *International Journal of Heat and Mass Transfer*, 50(9–10), 1790–1804.

Aswin, M., J, A. A., Dinesh, K., Gunaseelan, M., and P, J. A. P. v. (2017). "Performance Evaluation of Coil Heat Exchanger inside PCM Bed." *International Journal of Engineering Trends and Technology*, 45, 303–307.

Barreneche, C., Solé, A., Miró, L., Martorell, I., Fernández, A. I., and Cabeza, L. F. (2013). "Study on differential scanning calorimetry analysis with two operation modes and organic and inorganic phase change material (PCM)." *Thermochimica Acta*, 553, 23–26.

Badenhorst, H., and Cabeza, L. F. (2017). "Critical analysis of the T-history method: A fundamental approach." *Thermochimica Acta*, 650, 95–105.

Benmoussa, F., Benzaoui, A., and Benmoussa, H. (2017). "Thermal behavior of latent thermal energy storage unit using two phase change materials: Effects of HTF inlet temperature." *Case Studies in Thermal Engineering*, 10, 475–483.

Bezyan, B., Porkhial, S., and Mehrizi, A. A. (2015). "3-D simulation of heat transfer rate in geothermal pile-foundation heat exchangers with spiral pipe configuration." *Applied Thermal Engineering*, 87, 655–668.

Brent, A. D., Voller, V. R., and Reid, K. J. (1988a). "Enthalpy-porosity technique for modeling convection-diffusion phase change: Application to the melting of a pure metal." *Numerical Heat Transfer*, 13(3), 297–318.

Brent, A. D., Voller, V. R., and Reid, K. J. (1988b). "Enthalpy-Porosity Technique For Modeling Convection-Diffusion Phase Change: Application To The Melting Of A Pure Metal." *Numerical Heat Transfer*, 13(3), 297–318.

Cabeza, L. F., Zsembinszki, G., and Martín, M. (2020). "Evaluation of volume change in phase change materials during their phase transition." *Journal of Energy Storage*, 28(September 2019), 101206.

Cabeza, L. F., Barreneche, C., Martorell, I., Miró, L., Sari-Bey, S., Fois, M., Paksoy, H. O., Sahan, N., Weber, R., Constantinescu, M., Anghel, E. M., Malikova, M., Krupa, I., Delgado, M., Dolado, P., Furmanski, P., Jaworski, M., Haussmann, T., Gschwander, S., and Fernández, A. I. (2015). "Unconventional experimental technologies available

for phase change materials (PCM) characterization. Part 1. Thermophysical properties." *Renewable and Sustainable Energy Reviews*, 43, 1399-1414

Cellat, K., Beyhan, B., Güngör, C., Konuklu, Y., Karahan, O., Dündar, C., and Paksoy, H. (2015). "Thermal enhancement of concrete by adding bio-based fatty acids as phase change materials." *Energy and Buildings*, 106, 156–163.

Chen, C., Zhang, H., Gao, X., Xu, T., Fang, Y., and Zhang, Z. (2016). "Numerical and experimental investigation on latent thermal energy storage system with spiral coil tube and paraffin/expanded graphite composite PCM." *Energy Conversion and Management*, 126, 889–897.

Chernik, G. G. (1993). "Enthalpies of non-isothermal phase transitions in binary systems." *Thermochimica Acta*, 220, 37–54.

Chiu, J. N. W., and Martin, V. (2012). "Submerged finned heat exchanger latent heat storage design and its experimental verification." *Applied Energy*, 93, 507–516.

Chiu, J. N. W., and Martin, V. (2013). "Multistage latent heat cold thermal energy storage design analysis." *Applied Energy*, 112, 1438–1445.

Coates, J. (2006). "Interpretation of Infrared Spectra, A Practical Approach." *Encyclopedia of Analytical Chemistry*, 10815–10837.

Council, W.E., 2016. World Energy Resources report."

Cui, H., Yuan, X., and Hou, X. (2003). "Thermal performance analysis for a heat receiver using multiple phase change materials." *Applied Thermal Engineering*, 23(18), 2353–2361.

Dincer, I., and Rosen, M. A. (2001). "Energetic, environmental and economic aspects of thermal energy storage systems for cooling capacity." *Appl. Therm. Eng.*, 21(11), 1105–1117.

Dinker, A., Agarwal, M., and Agarwal, G. D. (2017). "Experimental assessment on thermal storage performance of beeswax in a helical tube embedded storage unit." *Applied Thermal Engineering*, 111, 358–368.

Domanski, R., and Fellah, G. (1996). "Exergy analysis for the evaluation of a thermal storage system employing PCMS with different melting temperatures." *Applied Thermal Engineering*, 16(11), 907–919.

Du, K., Calautit, J., Wang, Z., Wu, Y., & Liu, H. (2018). A review of the applications of phase change materials in cooling, heating and power generation in different temperature ranges. *Applied energy*, 220, 242-273.

Duan, X., Ryan, S., John, S., Stamp, J., and John, S. (2017). "Solar Thermal Energy Storage with Phase Change Material - Heat Exchanger Design and Heat Transfer Analysis.", *EEEP 2016*, 94, 370–372.

Ettouney, H., El-Dessouky, H., and Al-Kandari, E. (2004). "Heat Transfer Characteristics during Melting and Solidification of Phase Change Energy Storage Process." *Industrial & Engineering Chemistry Research*, 43(17), 5350–5357.

Faegh, M., and Shafii, M. B. (2017). "Experimental investigation of a solar still equipped with an external heat storage system using phase change materials and heat pipes." *Desalination*, 409, 128–135.

Fang, M., and Chen, G. (2007). "Effects of different multiple PCMs on the performance of a latent thermal energy storage system." *Applied Thermal Engineering*, 27(5–6), 994–1000.

Fleischer, A. S. (2015). *Thermal energy storage using phase change materials: fundamentals and applications*. Springer.

Franco, A. (2007). "An apparatus for the routine measurement of thermal conductivity of materials for building application based on a transient hot-wire method." *Appl. Therm. Eng.*, 27(14–15), 2495–2504.

Fan, L., and Khodadadi, J. M. (2012). "An experimental investigation of enhanced thermal conductivity and expedited unidirectional freezing of cyclohexane-based nanoparticle suspensions utilized as nano-enhanced phase change materials (NePCM)." *International Journal of Thermal Sciences*, 62, 120–126.

Farag, Y., and Leopold, C. S. (2009). "Physicochemical properties of various shellac types." *Dissolution Technologies*, 16(2), 33–39.

Farid, M. M., and Kanzawa, A. (1989). "Thermal performance of a heat storage module using pcm's with different melting temperatures: Mathematical modeling." *Journal of Solar Energy Engineering, Transactions of the ASME*, 111(2), 152–157.

Farid, M. M., Kim, Y., and Kansawa, A. (1990). "Thermal performance of a heat storage module using PCM's with different melting temperature: Experimental." *Journal of Solar Energy Engineering, Transactions of the ASME*, 112(2), 125–131.

Fortuniak, W., Slomkowski, S., Chojnowski, J., Kurjata, J., Tracz, A., and Mizerska, U. (2013). "Synthesis of a paraffin phase change material microencapsulated in a siloxane polymer." *Colloid and Polymer Science*, 291(3), 725–733.

Feliński, P., and Sekret, R. (2016). "Experimental study of evacuated tube collector/storage system containing paraffin as a PCM." *Energy*, 114, 1063–1072.

Gallart-Sirvent, P., Martín, M., Villorbina, G., Balcells, M., Solé, A., Barrenche, C., Cabeza, L. F., and Canela-Garayoa, R. (2017). "Fatty acid eutectic mixtures and derivatives from non-edible animal fat as phase change materials." *RSC Adv.*, 7(39), 24133–24139.

Gasia, J., Miró, L., Gracia, A. de, Barreneche, C., and Cabeza, L. F. (2016). "Experimental evaluation of a paraffin as phase change material for thermal energy storage in laboratory equipment and in a shell-and-tube heat exchanger." *Applied Sciences*, 6(4), 112.

Gunasekara, S. N., Pan, R., Chiu, J. N., and Martin, V. (2016). "Polyols as phase change materials for surplus thermal energy storage." *Applied Energy*, 162, 1439–1452.

Gunther, E., Hiebler, S., Mehling, H., and Redlich, R. (2009). "Enthalpy of phase change materials as a function of temperature: Required accuracy and suitable measurement methods." *International Journal of Thermophysics*, 30(4), 1257–1269.

Hawlader, M. N. A., Uddin, M. S., and Khin, M. M. (2003). "Microencapsulated PCM thermal-energy storage system." *Applied Energy*, 74(1–2), 195–202.

Hong, H., Kim, S. K., and Kim, Y. S. (2004). "Accuracy improvement of T-history method for measuring heat of fusion of various materials." *International Journal of Refrigeration*, 27(4), 360–366.

Hosseini, M. J., Ranjbar, A. A., Sedighi, K., and Rahimi, M. (2012). "A combined experimental and computational study on the melting behavior of a medium temperature phase change storage material inside shell and tube heat exchanger." *International Communications in Heat and Mass Transfer*, 39(9), 1416–1424.

Hosseinizadeh, S. F., Tan, F. L., and Moosania, S. M. (2011). "Experimental and numerical studies on performance of PCM-based heat sink with different configurations of internal fins." *Applied Thermal Engineering*, 31(17–18), 3827–3838.

Hu, W., and Yu, X. (2014). "Thermal and mechanical properties of bio-based PCMs encapsulated with nanofibrous structure." *Renewable Energy*, 62, 454–458.

Huang, M. J., Eames, P. C., and Norton, B. (2004). "Thermal regulation of building-integrated photovoltaics using phase change materials." *International Journal of Heat and Mass Transfer*, 47(12–13), 2715–2733.

Huang, M. J., Eames, P. C., Norton, B., and Hewitt, N. J. (2011). "Natural convection in an internally finned phase change material heat sink for the thermal management of photovoltaics." *Solar Energy Materials and Solar Cells*, 95(7), 1598–1603.

Ibrahim, N. I., Al-Sulaiman, F. A., Rahman, S., Yilbas, B. S., & Sahin, A. Z. (2017). Heat transfer enhancement of phase change materials for thermal energy storage applications: A critical review. *Renewable and Sustainable Energy Reviews*, *74*, 26-50.

Ji, C., Qin, Z., Dubey, S., Choo, F. H., and Duan, F. (2018). "Simulation on PCM melting enhancement with double-fin length arrangements in a rectangular enclosure induced by natural convection." *International Journal of Heat and Mass Transfer*, 127, 255–265.

Jmal, I., and Baccar, M. (2018). "Numerical investigation of PCM solidification in a finned rectangular heat exchanger including natural convection." *International Journal of Heat and Mass Transfer*, 127, 714–727.

Joshi, V., and Rathod, M. K. (2019). "Constructal enhancement of thermal transport in latent heat storage systems assisted with fins." *International Journal of Thermal Sciences*, 145(June 2018), 105984.

Jose Pereira da Cunha, and Philip Eames. (2016). "Thermal energy storage for low and medium temperature applications using phase change materials – A review." *Applied Energy*, 177, 227–238.

Joulin, A., Younsi, Z., Zalewski, L., Lassue, S., Rousse, D. R., and Cavrot, J. P. (2011). "Experimental and numerical investigation of a phase change material: Thermal-energy storage and release." *Appl. Energy*, 88(7), 2454–2462.

Kaygusuz Kamil, A. S. (2001). "Thermal Energy Storage System Using Some Fatty Acids as Latent Heat Energy Storage Materials." *Energy Sources*, 23(3), 275–285.

Kenisarin, M. M. (2010). High-temperature phase change materials for thermal energy storage. *Renewable and sustainable energy reviews*, 14(3), 955-970.

Kenisarin, M., & Mahkamov, K. (2007). Solar energy storage using phase change materials. *Renewable and sustainable energy reviews*, 11(9), 1913-1965.

Khillarkar, D. B., Gong, Z. X., and Mujumdar, A. S. (2000). "Melting of a phase change material in concentric horizontal annuli of arbitrary cross-section." *Applied Thermal Engineering*, 20(10), 893–912.

Khadraoui, A. El, Bouadila, S., Kooli, S., Guizani, A., and Farhat, A. (2016). "Solar air heater with phase change material: An energy analysis and a comparative study." *Appl. Therm. Eng.*, 107, 1057–1064.

Korti, A. I. N., and Tlemsani, F. Z. (2016). "Experimental investigation of latent heat storage in a coil in PCM storage unit." *Journal of Energy Storage*, 5, 177–186.

Koukou, M. K., Dogkas, G., Vrachopoulos, M. Gr., Konstantaras, J., Pagkalos, C., Lymperis, K., Stathopoulos, V., Evangelakis, G., Prouskas, C., Coelho, L., and Rebola, A. (2019). "Performance Evaluation of a Small-Scale Latent Heat Thermal Energy Storage Unit for Heating Applications Based on a Nanocomposite Organic PCM." *ChemEngineering*, 3(4).

Kravvaritis, E. D., Antonopoulos, K. A., and Tzivanidis, C. (2010). "Improvements to the measurement of the thermal properties of phase change materials." *Measurement Science and Technology*, 21(4).

Lacroix, M. (1993). "Numerical simulation of a shell-and-tube latent heat thermal energy storage unit." *Solar Energy*, 50(4), 357–367.

Lane GA. Solar heat storage—latent heat materials, vol. I. Boca Raton, FL: CRC Press, Inc.; 1983.

Lausecker, R., Badilita, V., Gleibner, U., and Wallrabe, U. (2016). "Introducing natural thermoplastic shellac to microfluidics: A green fabrication method for point-of-care devices." *Biomicrofluidics*, 10(4).

Ling, Z., Zeng, G., Xu, T., Fang, X., and Zhang, Z. (2015). "Performance of a Coil-pipe Heat Exchanger Filled with Mannitol for Solar Water Heating System." *Energy Procedia*, 75(January), 827–833.

Lázaro, A., Günther, E., Mehling, H., Hiebler, S., Marin, J. M., and Zalba, B. (2006). "Verification of a T-history installation to measure enthalpy versus temperature curves of phase change materials." *Measurement Science and Technology*, 17(8), 2168–2174.

Lazaro, A., Peñalosa, C., Solé, A., Diarce, G., Haussmann, T., Fois, M., Zalba, B., Gshwander, S., and Cabeza, L. F. (2013). "Intercomparative tests on phase change materials characterisation with differential scanning calorimeter." *Applied Energy*, 109, 415–420.

Levesque, B., Lavoie, M., & Joly, J. (2004). Residential water heater temperature: 49 or 60 degrees Celsius",5(4),11-12.

Li, G. (2015). "Energy and exergy performance assessments for latent heat thermal energy storage systems." *Renewable and Sustainable Energy Reviews*, Elsevier Ltd.

Ling, Z., Zeng, G., Xu, T., Fang, X., and Zhang, Z. (2015). "Performance of a Coil-pipe Heat Exchanger Filled with Mannitol for Solar Water Heating System." *Energy Procedia*, 75(January), 827–833.

Liu, M., Tay, N. H. S., Bell, S., Belusko, M., Jacob, R., Will, G., Saman, W., and Bruno, F. (2016). "Review on concentrating solar power plants and new developments in high temperature thermal energy storage technologies." *Renewable and Sustainable Energy Reviews*, 53, 1411–1432.

Lorente, S., Bejan, A., and Niu, J. L. (2014). "International Journal of Heat and Mass Transfer Phase change heat storage in an enclosure with vertical pipe in the center." *International Journal of Heat and Mass Transfer*, 72, 329–335.

Marín, J. M., Zalba, B., Cabeza, L. F., and Mehling, H. (2003). "Determination of enthalpy-temperature curves of phase change materials with the temperature-history method: Improvement to temperature dependent properties." *Measurement Science and Technology*, 14(2), 184–189.

Mehling, H., & Cabeza, L. F. (2008). Heat and cold storage with PCM (Vol. 308). Berlin: springer.

Meng, Z. N., and Zhang, P. (2017). "Experimental and numerical investigation of a tube-in-tank latent thermal energy storage unit using composite PCM." *Applied Energy*, 190, 524–539.

Moffat, R. J. (1988). "Describing the uncertainties in experimental results." *Experimental Thermal and Fluid Science*, 1(1), 3–17.

Murray, R. E., and Groulx, D. (2014). "Experimental study of the phase change and energy characteristics inside a cylindrical latent heat energy storage system: Part 1 consecutive charging and discharging." *Renewable Energy*, 62, 571–581.

Öztürk, H. H. (2005). "Experimental evaluation of energy and exergy efficiency of a seasonal latent heat storage system for greenhouse heating." *Energy Conversion and Management*, 46(9–10), 1523–1542.

Oró, E., Gracia, A. de, Castell, A., Farid, M. M., and Cabeza, L. F. (2012). "Review on phase change materials (PCMs) for cold thermal energy storage applications." *Appl. Energy*, Elsevier Ltd.

Peck, J. H., Kim, J. J., Kang, C., and Hong, H. (2006). "A study of accurate latent heat measurement for a PCM with a low melting temperature using T-history method." *International Journal of Refrigeration*, 29(7), 1225–1232.

Peiró, G., Gasia, J., Miró, L., and Cabeza, L. F. (2015). "Experimental evaluation at pilot plant scale of multiple PCMs (cascaded) vs. single PCM configuration for thermal energy storage." *Renewable Energy*, 83, 729–736.

PLUSS[R] India, Technical data sheet of the manufacturer https://www.pluss.co.in/productrange-PCM.php, 2019 (accessed 7 Jan 2020).

Pu, L., Zhang, S., Xu, L., and Li, Y. (2020). "Thermal performance optimization and evaluation of a radial finned shell-and-tube latent heat thermal energy storage unit." *Applied Thermal Engineering*, 166, 114753.

Pielichowska, K., & Pielichowski, K. (2014). Phase change materials for thermal energy storage. *Progress in materials science*, *65*, 67-123.

Putri, W. A., Fahmi, Z., Sutjahja, I. M., Kurnia, D., and Wonorahardjo, S. (2016). "Thermophysical parameters of coconut oil and its potential application as the thermal energy storage system in Indonesia." *Journal of Physics: Conference Series*, 739, 012065.

Rathgeber, C., Schmit, H., Hennemann, P., and Hiebler, S. (2014). "Calibration of a T-History calorimeter to measure enthalpy curves of phase change materials in the temperature range from 40 to 200° C." *Measurement Science and Technology*, 25(3), 35011.

Rudonja, N. R., Komatina, M. S., Živković, G. S., and Antonijević, D. L. (2016). "Heat transfer enhancement through pcm thermal storage by use of copper fins." *Thermal Science*, 20, s251–s259.

Ravotti, R., Fellmann, O., Lardon, N., Fischer, L. J., Stamatiou, A., & Worlitschek, J. (2019). Analysis of bio-based fatty esters PCM's thermal properties and investigation of trends in relation to chemical structures. *Applied Sciences*, *9*(2), 225.

Rudra Murthy, B. V., and Gumtapure, V. (2020). "Thermo-physical analysis of natural shellac wax as novel bio-phase change material for thermal energy storage applications." *J. Energy Storage*, 29(February), 101390.

Seddegh, S., Wang, X., Joybari, M. M., and Haghighat, F. (2017). "Investigation of the effect of geometric and operating parameters on thermal behavior of vertical shell-and-tube latent heat energy storage systems." *Energy*, 137, 69–82.

Seeniraj, R. v., and Lakshmi Narasimhan, N. (2008). "Performance enhancement of a solar dynamic LHTS module having both fins and multiple PCMs." *Solar Energy*, 82(6), 535–542.

Sharifi, N., Bergman, T. L., and Faghri, A. (2011). "Enhancement of PCM melting in enclosures with horizontally-finned internal surfaces." *International Journal of Heat and Mass Transfer*, 54(19–20), 4182–4192.

Sharma, A., Tyagi, V. V., Chen, C. R., and Buddhi, D. (2009). "Review on thermal energy storage with phase change materials and applications." *Renewable and Sustainable Energy Reviews*, 13(2), 318–345.

Sharma, S. D., Kitano, H., & Sagara, K. (2004). Phase change materials for low temperature solar thermal applications. *Res. Rep. Fac. Eng. Mie Univ*, *29*(1), 31-64.

Shi, J. N., Ger, M. D., Liu, Y. M., Fan, Y. C., Wen, N. T., Lin, C. K., & Pu, N. W. (2013). "Improving the thermal conductivity and shape-stabilization of phase change materials using nano graphite additives". *Carbon*, *51*, 365-372.

Shen, G., Wang, X., Chan, A., Cao, F., and Yin, X. (2020). "Investigation on optimal shell-to-tube radius ratio of a vertical shell-and-tube latent heat energy storage system." *Solar Energy*, 211, 732–743.

Shmueli, H., Ziskind, G., and Letan, R. (2010). "Melting in a vertical cylindrical tube: Numerical investigation and comparison with experiments." *International Journal of Heat and Mass Transfer*, 53(19–20), 4082–4091.

Shukla, A., Buddhi, D., & Sawhney, R. L. (2008). Thermal cycling test of few selected inorganic and organic phase change materials. *Renewable energy*, 33(12), 2606-2614.

Stanković, S. B., and Kyriacou, P. A. (2012). "The effects of thermistor linearization techniques on the T-history characterization of phase change materials." *Applied Thermal Engineering*, 44, 78–84.

Stanković, S. B., and Kyriacou, P. A. (2013). "Improved measurement technique for the characterization of organic and inorganic phase change materials using the T-history method." *Applied Energy*, 109, 433–440.

Stritih, U. (2004). "An experimental study of enhanced heat transfer in rectangular PCM thermal storage." *International Journal of Heat and Mass Transfer*, 47(12–13), 2841–2847.

Sundaram, P., Tiwari, R. K., and Kumar, S. (2016). "Experimental Performance Study of Helical Coil Thermal Storage Unit Filled with PCM." *International Journal of Chem Tech Research*, 9(07), 611–618.

Solé, A., Miró, L., Barreneche, C., Martorell, I., and Cabeza, L. F. (2013). "Review of the T-history method to determine thermophysical properties of phase change materials (PCM)." *Renewable and Sustainable Energy Reviews*, Elsevier Ltd.

Suppes, G. J., Goff, M. J., and Lopes, S. (2003). "Latent heat characteristics of fatty acid derivatives pursuant phase change material applications." Chemical Engineering Science, 58(9), 1751–1763.

Sukontasukkul, P., Uthaichotirat, P., Sangpet, T., Sisomphon, K., Newlands, M., Siripanichgorn, A., & Chindaprasirt, P. (2019). Thermal properties of lightweight concrete incorporating high contents of phase change materials. *Construction and Building Materials*, 207, 431-439.

Tan, F. L., and Fok, S. C. (2007). "Thermal management of mobile phone using phase change material." *Proceedings of the Electronic Packaging Technology Conference, EPTC*, 836–842.

Tay, N. H. S., Belusko, M., and Bruno, F. (2012a). "An effectiveness-NTU technique for characterising tube-in-tank phase change thermal energy storage systems." *Applied Energy*, 91(1), 309–319.

Tay, N. H. S., Bruno, F., and Belusko, M. (2012b). "Experimental validation of a CFD model for tubes in a phase change thermal energy storage system." *International Journal of Heat and Mass Transfer*, 55(4), 574–585.

Tay, N. H. S., Bruno, F., and Belusko, M. (2012c). "Experimental validation of a CFD and an ε-NTU model for a large tube-in-tank PCM system." *International Journal of Heat and Mass Transfer*, 55(21–22), 5931–5940.

"Thermal Energy Storage (TES) Methods." (2010). *Thermal Energy Storage*, John Wiley & Sons, Ltd, 83–190.

Ushak, S., Gutierrez, A., Galleguillos, H., Fernandez, A. G., Cabeza, L. F., and Grágeda, M. (2015). "Thermophysical characterization of a by-product from the non-metallic industry as inorganic PCM." *Solar Energy Materials and Solar Cells*, 132, 385–391.

Valan, A. A., Sasmito, A. P., and Mujumdar, A. S. (2013). "Numerical performance study of paraffin wax dispersed with alumina in a concentric pipe latent heat storage system." *Thermal science*, 17(2), 419–430.

Voller, V. R., Cross, M., and Markatos, N. C. (1987). "An enthalpy method for convection/diffusion phase change." *International Journal for Numerical Methods in Engineering*, 24(1), 271–284.

Voller, V. R., and Peng, S. (1994). "An enthalpy formulation based on an arbitrarily deforming mesh for solution of the Stefan problem." *Computational Mechanics*, 14(5), 492–502.

Voller, V. R., and Prakash, C. (1987). "A fixed grid numerical modelling methodology for convection-diffusion mushy region phase-change problems." *International Journal of Heat and Mass Transfer*, 30(8), 1709–1719.

Vyshak, N. R., and Jilani, G. (2007). "Numerical analysis of latent heat thermal energy storage system." *Energy Conversion and Management*, 48(7), 2161–2168.

Wang, Y., Wang, L., Xie, N., Lin, X., and Chen, H. (2016). "Experimental study on the melting and solidification behavior of erythritol in a vertical shell-and-tube latent heat thermal storage unit." *International Journal of Heat and Mass Transfer*, 99, 770–781.

Wu, Z. G., and Zhao, C. Y. (2011). "Experimental investigations of porous materials in high temperature thermal energy storage systems." *Solar Energy*, 85(7), 1371–1380.

Xu, Y., He, Y. L., Li, Y. Q., and Song, H. J. (2016). "Exergy analysis and optimization of charging-discharging processes of latent heat thermal energy storage system with three phase change materials." *Solar Energy*, 123, 206–216.

Wang, S., Faghri, A., and Bergman, T. L. (2012). "A comparison study of sensible and latent thermal energy storage systems for concentrating solar power applications." *Numer. Heat Transf. Part A Appl.*, 61(11), 860–871.

Wiki PCM, Approaches to determine the values of supercooling. https://thermalmaterials.org/wiki-pcm/supercooling, 2019 (accessed 2 Feb. 2020).

Yagci, O. K., Avci, M., and Aydin, O. (2019). "Melting and solidification of PCM in a tube-in-shell unit: Effect of fin edge lengths' ratio." *Journal of Energy Storage*, 24.

Yang, X., Lu, Z., Bai, Q., Zhang, Q., Jin, L., and Yan, J. (2017). "Thermal performance of a shell-and-tube latent heat thermal energy storage unit: Role of annular fins." *Applied Energy*, 202, 558–570.

Yavari, F., Raeisi Fard, H., Pashayi, K., A. Rafiee, M., Zamiri, A., Yu, Z., Ozisik, R., Borca-Tasciuc, T., and Koratkar, N. (2011). "Enhanced Thermal Conductivity in a Nanostructured Phase Change Composite due to Low Concentration Graphene Additives." *J. Phys. Chem. C*, 115(17), 8753–8758.

Yinping, Z., Yi, J., and Yi, J. (1999). "A simple method, the -history method, of determining the heat of fusion, specific heat and thermal conductivity of phase-change materials." *Measurement Science and Technology*, 10(3), 201–205.

Zalba, B., Marın, J. M., Cabeza, L. F., & Mehling, H. (2003). Review on thermal energy storage with phase change: materials, heat transfer analysis and applications. *Applied thermal engineering*, 23(3), 251-283.

Zhang, H., Wissen, R. M. J. van, Nedea, S. v, and Rindt, C. C. M. (2014). "Characterization of sugar alcohols as seasonal heat storage media-experimental and theoretical investigations." *Advances in Thermal Energy Storage*, EUROTHERM, 99.

Zhang, S., Zhang, L., Yang, X., Yu, X., Duan, F., Jin, L., and Meng, X. (2017). "Experimental investigation of a spiral tube embedded latent thermal energy storage tank using paraffin as PCM." *Energy Procedia*, 105, 4543–4548.

Zheng, H., Zhang, R., Zhang, H., Feng, Y., Li, K., and Zhang, W. (2011). "Thermal analysis of four insect waxes based on differential scanning calorimetry (DSC)." *Procedia Engineering*, 18, 101–106.

Zhang, Z., & Fang, X. (2006). Study on paraffin/expanded graphite composite phase change thermal energy storage material. *Energy Conversion and Management*, *47*(3), 303-310.

Zhang, N., Yuan, Y., Yuan, Y., Cao, X., & Yang, X. (2014). Effect of carbon nanotubes on the thermal behavior of palmitic–stearic acid eutectic mixtures as phase change materials for energy storage. *Solar energy*, *110*, 64-70.

Zhang, Y., Wang, L., Tang, B., Lu, R., & Zhang, S. (2016). Form-stable phase change materials with high phase change enthalpy from the composite of paraffin and cross-linking phase change structure. *Applied energy*, 184, 241-246.

APPENDIX-A

A1. DESIGN, FABRICATION, AND CALIBRATION OF IN-HOUSE T-HISTORY EXPERIMENTAL SETUP

Design of water bath tank, cooling chamber, and different accessories of THM as shown in Figure A.1.
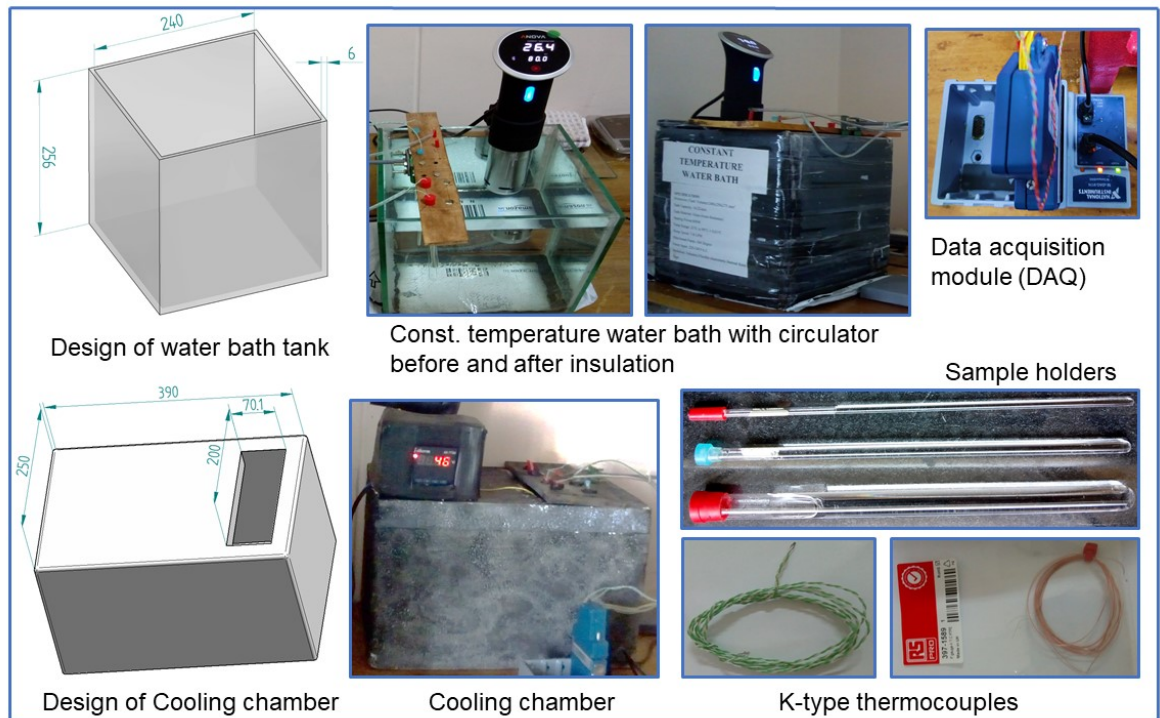
Figure A.1. Design and accessories of THM.

A2. CALIBRATION OF CONSTANT TEMPERATURE WATER BATH

Constant water bath temperature was calibrated using a pre-calibrated ultra-precise RTD sensor with an accuracy of $\pm 1/10 \, (0.3 + 0.005 \, |T|)$ °C. The water bath temperature varied as 85 °C, 90 °C, and 95 °C. Ultra-precise RTD sensor records temperature at three positions (Figure A.2.) along with the water height (i.e., 220mm (A), 120mm (B), and 20 mm (C) from the top surface of the water) and along the width (1, 2, 3 and 4) as listed in the Table A1. Further, the calculated average and uncertainty of all three temperatures listed in the table indicate the uncertainty or deviation increases as the water bath temperature increases. The maximum uncertainty or accuracy of the water bath is chosen as ± 0.5 °C.
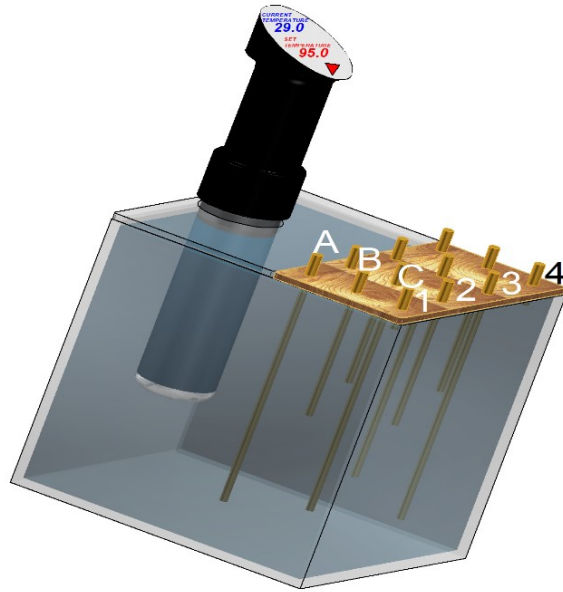
Figure A.2. Temperature sensors position during the calibration of constant temperature water bath.

Table A.1. Calibration of constant temperature water bath.

Ultra Precise RTD sensor	1	2	3	4	Average
Set temperature at 85 °C					
A (220mm)	85.2	85.3	85.4	85.3	85.3
B (120mm)	85	84.9	84.9	85	84.9
C (20mm)	84.8	84.7	84.7	84.6	84.7
Average ± SD					**84.9 ± 0.3**
Set temperature at 90 °C					
A (220mm)	90.4	90.5	90.3	90.4	90.4
B (120mm)	90.1	89.9	90	90.1	90.0
C (20mm)	89.8	89.7	89.6	89.7	89.7
Average ± SD					**90.0+0.35**
Set temperature at 95 °C					
A (220mm)	95.6	95.4	95.5	95.4	95.4
B (120mm)	95.2	94.9	95.1	95.1	95.0
C (20mm)	94.6	94.5	94.4	94.4	94.4
Average ± SD					**95.0±0.5**

A3. CALIBRATION OF THERMOCOUPLES BY COMPARISON TECHNIQUE

Four K-type thermocouples were calibrated through a reference calibration ultraprecise immersion RTD sensor (DIN 1/10, Class A, Omega^{TM}: P-M-1/10-1/4-4-0-P-3) of an accuracy $\pm 1/10$ $(0.3 + 0.005 \,|T|)$ °C [https://in.omega.com/pptst/P-ULTRA_RTD.html] At the same position (120mm depth from the topwater surface), two thermocouples of each probe dia. 0.2mm and 0.075mm and RTD sensors were recorded after attaining the steady-state by varying the constant water bath temperature from 30, 40, 50, 60, 70, 80, 90, and 95 °C.

The temperature difference between the thermocouples and reference is the correction temperature, denoted as $\Delta T_{Correction}$.

$$\therefore \Delta T_{correction} = T_{Reference} - T_{Thermocouple} \tag{A1}$$

$T_{Reference}$ is the reference temperature of the ultraprecise RTD sensor, and $T_{Thermocouples}$ is the temperature measured by each thermocouple.

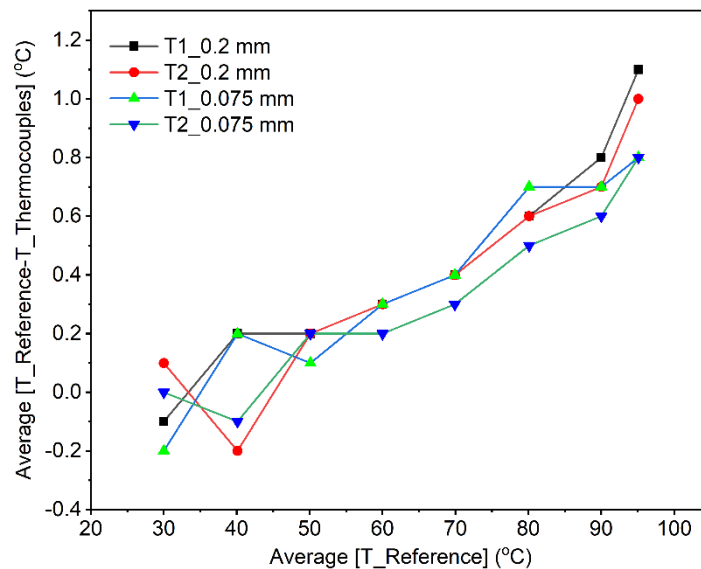Figure A.3. Average correction temperature VS Average reference temperature.

The correction temperature is stable only for specific water bath temperatures. Still, it varies considerably for different water bath temperatures. The average value of $\Delta T_{correction}$ is calculated at each temperature from 30 to 95 °C. The linear relationship

between the average corrected temperature and reference temperature is shown in Figure A.3. The linear fitting results are outlined in Table A2.

$$\Delta T_{correction} = m.T_{reference} - n \tag{A2}$$

Where m is the fitting curve slope, n is the intercept, and R' is the correlation coefficient

Table A.2. Results of thermocouple calibration.

Thermocouples	m	n	R'	Uncertainty δT (°C)
T1_0.2 mm	0.0155	-0.564	0.958	0.12~0.1
T2_0.2 mm	0.0148	-0.567	0.928	0.16~0.2
T1_0.075 mm	0.0141	-0.538	0.965	0.1
T2_0.075 mm	0.0124	-0.487	0.959	0.1

According to Eq. (A1) and (A2), the reference temperature can also be expressed in this form, i.e., Eq.(A3)

$$T_{medium} = T_{reference} = \frac{T_{thermocouples} + n}{1 - m} \tag{A3}$$

The overall uncertainty is calculated using the error propagation equation, the root sum square of bias, and random errors.

$$\delta T = \sqrt{B_e^2 + R_e^2} \tag{A4}$$

Where δT is the overall uncertainty of the thermocouples, B_e is the bias error, and R_e is the random error. Bias error is the temperature difference between the true and the measured value of the medium (T_{Medium}) as the thermocouples calibrated with reference ultra-precise RTD sensor, the bias error of the thermocouples is the accuracy of the reference sensor, which is $\pm 1/10$ (0.3 + 0.005 |T|) °C. The standard deviation of measured data at a specific temperature is established as a random error—the overall uncertainty of thermocouples δT is listed in Table A2.

A4. MATLAB CODING FOR SPECIFIC HEAT AND ENTHALPY CALCULATION IN THE THM.

```
function [j3]=Find_Enthalpy_Thermal_Delay_Heating_All_Tubes_Multi_Graph()
ta10=input('enter the maximum(Temperature) time index for 10mm:');
tb10=input('enter the minimum(Temperature) time index for 10mm:');
ta5=input('enter the maximum(Temperature) time index for 5mm:');
tb5=input('enter the minimum(Temperature) time index for 5mm:');
ta3=input('enter the maximum(Temperature) time index for 3mm:');
tb3=input('enter the minimum(Temperature) time index for 3mm:');
mw10=input('enter the mass of 10mm water:');
mt10=input('enter the mass of 10mm test tube:');
mp10=input('enter the mass of 10mm pcm:');
mw5=input('enter the mass of 5mm water:');
mt5=input('enter the mass of 5mm test tube:');
mp5=input('enter the mass of 5mm pcm:');
mw3=input('enter the mass of 3mm water:');
mt3=input('enter the mass of 3mm test tube:');
mp3=input('enter the mass of 3mm pcm:');
Cpt=input('enter the specific heat of test tube:');
Cpw=input('enter the specific heat of water:');
num=xlsread('T-history analysis.xlsx');
M10=(mt10*Cpt+mw10*Cpw)/mp10;
N10=(mt10*Cpt)/mp10;
M5=(mt5*Cpt+mw5*Cpw)/mp5;
N5=(mt5*Cpt)/mp5;
M3=(mt3*Cpt+mw3*Cpw)/mp3;
N3=(mt3*Cpt)/mp3;
[~,~,~,H,MN,S]=datevec(num(:,3));
num(:,11)=H*3600+MN*60+S;
T10=zeros([100000,1]);
H10=zeros([100000,1]);
Q10=zeros([1000000,1]);
```

```
T5=zeros([100000,1]);
H5=zeros([100000,1]);
T3=zeros([100000,1]);
H3=zeros([100000,1]);
Cpmatrix10=zeros([10000,1]);
Cpmatrix5=zeros([10000,1]);
Cpmatrix3=zeros([10000,1]);
t1_10=num(ta10,11);
t0_10=num(tb10,11);
t1_5=num(ta5,11);
t0_5=num(tb5,11);
t1_3=num(ta3,11);
t0_3=num(tb3,11);
p10=polyfit(num(ta10:tb10,11),num(ta10:tb10,8),11);
q10=polyfit(num(ta10:tb10,11),num(ta10:tb10,9),11);
r10=polyfit(num(ta10:tb10,11),num(ta10:tb10,10),11);
p5=polyfit(num(ta5:tb5,11),num(ta5:tb5,6),11);
q5=polyfit(num(ta5:tb5,11),num(ta5:tb5,7),11);
r5=polyfit(num(ta5:tb5,11),num(ta5:tb5,10),11);
p3=polyfit(num(ta3:tb3,11),num(ta3:tb3,4),11);
q3=polyfit(num(ta3:tb3,11),num(ta3:tb3,5),11);
r3=polyfit(num(ta3:tb3,11),num(ta3:tb3,10),11);
c=1;d=1;e=1;
for i=t1_10:0.005:t0_10
    if(i+0.005<t0_10)
        kp_10=polyval(p10,i);
        mp_10=polyval(p10,i+0.005);
        kw_10=polyval(q10,i);
        mw_10=polyval(q10,i+0.005);
        T10(c,1)=(kp_10+mp_10)/2;
        pc10=abs(polyval(polyint(p10),i)-polyval(polyint(p10),i+0.005));
        w10=abs(polyval(polyint(q10),i)-polyval(polyint(q10),i+0.005));
```

```matlab
        a10=abs(polyval(polyint(r10),i)-polyval(polyint(r10),i+0.005));
        Cp10=(abs(M10*(((abs(kw_10-mw_10)*(pc10-a10)))/((w10-a10)*(abs(kp_10-
mp_10))))-N10));
        Cpmatrix10(c,1)=Cp10;
        if(c>1)
            H10(c,1)=H10(c-1,1)+abs((Cp10)*(mp_10-kp_10));
        else
            H10(c,1)=(Cp10)*(mp_10-kp_10);
        end
        Q10(c,1)=((mp10)*(-1)*Cp10)/1000;
        if(Cpmatrix10(c,1)<40000)
        c=c+1;
        end
    end
end
for i=t1_5:0.005:t0_5            %%%% 5 mm
    if(i+0.005<t0_5)
        kp_5=polyval(p5,i);
        mp_5=polyval(p5,i+0.005);
        kw_5=polyval(q5,i);
        mw_5=polyval(q5,i+0.005);
        T5(d,1)=(kp_5+mp_5)/2;
        pc5=abs(polyval(polyint(p5),i)-polyval(polyint(p5),i+0.005));
        w5=abs(polyval(polyint(q5),i)-polyval(polyint(q5),i+0.005));
        a5=abs(polyval(polyint(r5),i)-polyval(polyint(r5),i+0.005));
        Cp5=(abs(M5*(((abs(kw_5-mw_5)*(pc5-a5)))/((w5-a5)*(abs(kp_5-mp_5))))-
N5));
        Cpmatrix5(d,1)=Cp5;
        if(d>1)
            H5(d,1)=H5(d-1,1)+abs((Cp5)*(mp_5-kp_5));
        else
            H5(d,1)=(Cp5)*(mp_5-kp_5);
```

```matlab
        end
     %Q5(d,1)=((mp5)*(-1)*Cp5)/1000;
     if(Cpmatrix5(d,1)<30000)
     d=d+1;
      end
   end
end
for i=t1_3:1:t0_3                    %%%% 3 mm
   if(i+1<t1_3)
     kp_3=polyval(p3,i);
    mp_3=polyval(p3,i+1);
     mw_3=polyval(q3,i+1);
     T3(e,1)=(kp_3+mp_3)/2;
     pc3=abs(polyval(polyint(p3),i)-polyval(polyint(p3),i+1));
     w3=abs(polyval(polyint(q3),i)-polyval(polyint(q3),i+1));
     a3=abs(polyval(polyint(r3),i)-polyval(polyint(r3),i+1));
     Cp3=(abs(M3*(((abs(kw_3-mw_3)*(pc3-a3)))/((w3-a3)*(abs(kp_3-mp_3))))-
N3));
     Cpmatrix3(e,1)=Cp3;
      if(e>1)
        H3(e,1)=H3(e-1,1)+abs((Cp3)*(mp_3-kp_3));
      else
         H3(e,1)=(Cp3)*(mp_3-kp_3);
      end
     %Q3(e,1)=((mp3)*(-1)*Cp3)/1000;
      if(Cpmatrix3(e,1)<30000)
     e=e+1;
      end
   end
end
%j1=plot(T10(1:c-1,1),H10(1:c-1,1),T5(1:d-1,1),H5(1:d-1,1),T3(1:e-1,1),H3(1:e-
1,1));
```

%j2=plot(T10(1:c-1,1),Cpmatrix10(1:c-1,1),'g',T5(1:d-1,1),Cpmatrix5(1:d-1,1),'b');%,T3(1:e-1,1),Cpmatrix3(1:e-1,1),'r-o');;;;

j3=plot(T10(1:c-1,1),Q10(1:c-1,1),T5(1:d-1,1),Q5(1:d-1,1),T3(1:e-1,1),Q3(1:e-1,1));

A5. LabVIEW CODING

The program has been coded using the LabVIEW platform, as shown in Figure A.4, to acquire the T-history sample and reference temperature data with respect to time.
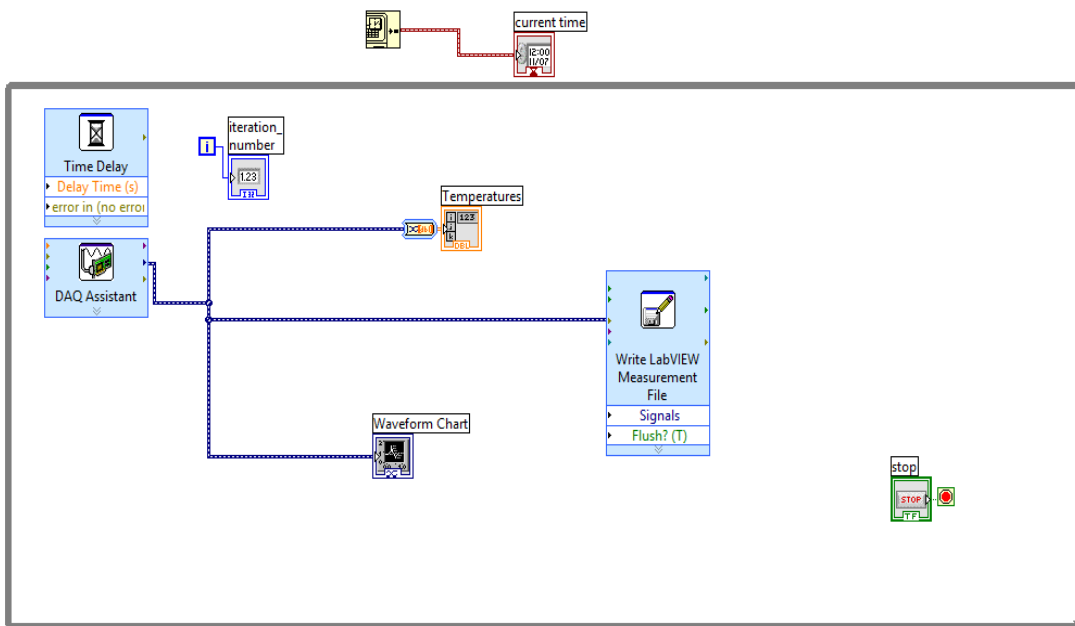

Figure A.4. LabVIEW circuit to obtain T-history sample and reference temperature with time.

APPENDIX-B

B1. DESIGN, FABRICATION, AND CALIBRATION OF LAB-SCALE SHELL AND TUBE LHTES EXPERIMENTAL UNIT

The improvement of design and fabrication of shell and tube experimental setup takes place in three stages, as shown in Figure B1. Initial stage: This is the shop floor person's work. But the fabrication work in this stage does not meet all the required design and delayed work. In the same condition, we bought to our lab and modified the HTF hot tank dimension, included the stirrer, changed the control board, thermocouples, nitrile foam insulation to HTF tank and LHTES unit with leakage proof checking to meet all the requirements to conduct the performance study of BPCM in shell and tube LHTES unit, i.e., as shown in Figure B1(b). We worked on the formal experiment using commercial BPCM(OM-55). A problem identified during the discharging cycle was that HTF cooling using a radiator and fan did not effectively extract complete heat from the LHTES unit. Further to overcome this, the second stage, including the cooling unit, consists of a compressor, evaporator, PID controller, SSR and refrigerant (R-134), etc., as shown in Figure B1(c). The detailed design of hot, cold fluid tanks and different components used in lab-scale shell and tube LHTES experimental setup is shown in Figure B2.

(a) Initial stage of fabrication   (b) First stage of setup with air cooling   (c) Second stage modification with compressor cooling
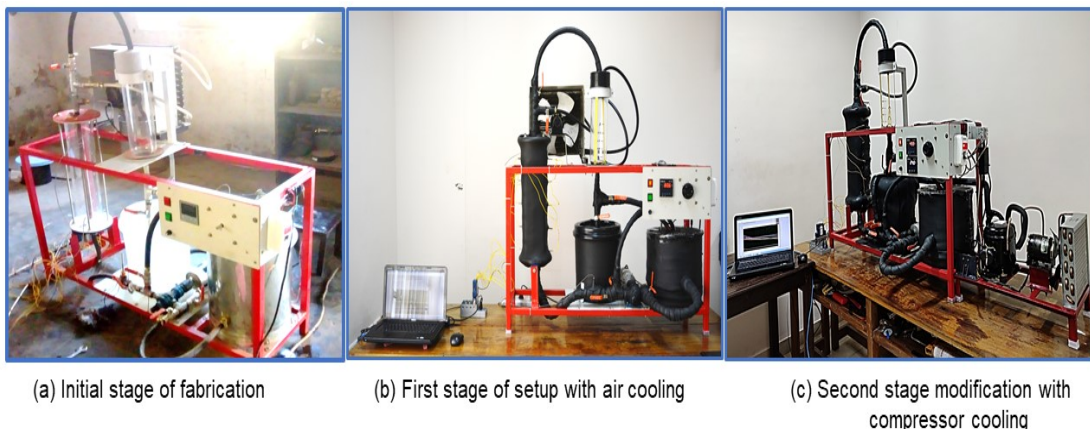
Figure B.1. Fabrication stages of lab-scale shell and tube LHTES experimental setup.

HTF flow rate measured using measuring flask, i.e., evaluating the time required to collect one liter of HTF. It is certain to know the uncertainty in flow measurement before starting the formal experiment. The uncertainty of flow measurement was

performed at different flow rates of 2,3,4 and 5 LPM with five repeated trials of period one hour each and calculated the mean and standard deviation as listed in Table B1. The calibration results of flow measurement give the relation that

$\pm (0.05 \cdot \text{flow rate})$ LPM   (B1)

For a flow rate varied between 2 to 5 LPM.

Figure B.2. Design of HTF tanks and individual parts of shell-tube LHTES unit.

Table B.1. Calibration of flow measurement by repeatability.

Flow rate (LPM)	Trial 1 Time (s)	Trial 2 Time (s)	Trial 3 Time (s)	Trial 4 Time (s)	Trial 5 Time (s)	Uncertainty($\delta\dot{m}$) LPM
2	60.0	62.2	57.6	57.8	63.0	0.09 ~ 0.1
3	60.1	57.6	57.1	62.7	58.8	0.14 ~ 0.1
4	60.2	58.2	63.8	62.0	58.4	0.19 ~ 0.2
5	59.5	57.5	57.5	62.5	63.0	0.29 ~ 0.2

B2. CALIBRATION OF THERMOCOUPLES

Fifteen K-type thermocouples used to measure the PCM temperature inside the shell and tube LHTES were calibrated using the procedure as explained in appendix-A. The linear relationship between the average corrected temperature and reference temperature is shown in Figure B3. The linear fitting results are outlined in Table B2. The accuracy of the fifteen K-type thermocouples from the calibrated results is ±0.5.
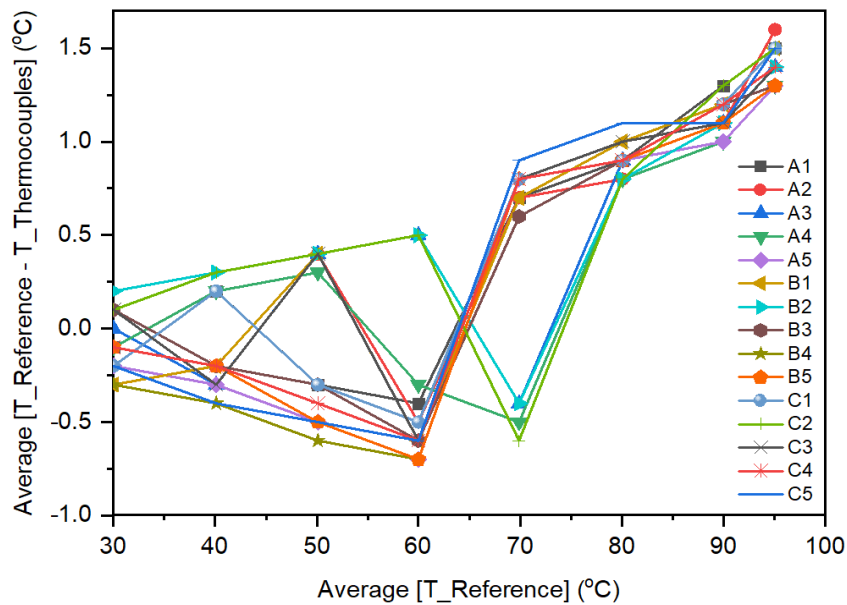

Figure B.3. Average correction temperature Vs. Average reference temperature.

Table B.2. Calibration of K-type thermocouples used to measure the BPCM temperature distribution inside the LHTES unit.

Thermocouples	m	n	R'	Uncertainty δT (°C)
A1	0.02631	-1.2199	0.847	0.46
A2	0.02542	-1.1621	0.838	0.46
A3	0.02128	-0.9205	0.761	0.50
A4	0.01831	-0.8418	0.669	0.56
A5	0.02800	-1.5158	0.835	0.51
B1	0.02799	-1.3402	0.858	0.46
B2	0.01533	-0.4498	0.643	0.50
B3	0.02489	-1.2280	0.807	0.50

B4	0.03213	-1.7819	0.864	0.51
B5	0.02714	-1.4232	0.814	0.53
C1	0.02681	-1.2760	0.840	0.48
C2	0.01805	-0.6250	0.633	0.61
C3	0.02375	-1.0422	0.786	0.51
C4	0.02811	-1.4356	0.844	0.49
C5	0.03171	-1.6799	0.862	0.51

LIST OF PUBLICATIONS

International Journals

1. Rudra Murthy B.V. and Veershetty Gumtapure "T-history analysis of aspect ratio effect on subcooling and solidification behavior of phase change material in vertical glass tubes." *Thermal Science*, 25 (7) 2020: 326-338. SCI Index IF=1.62.

2. Rudra Murthy B.V., Veershetty Gumtapure "Thermal property study of the fatty acid mixture as Bio-phase change material for solar thermal energy storage usage in domestic hot water application," *Journal of energy storage, Elsevier,* 25 (2019):100870, SCI Index IF=6.58.

3. Rudra Murthy B.V. and Veershetty Gumtapure "Thermophysical analysis of natural shellac wax as novel bio-phase change material for thermal energy storage applications." *Journal of Energy Storage*, 29 (2020): 101390, SCI Index IF=6.58.

4. Rudra Murthy B.V., Kumara Thanaiah and Veershetty Gumtapure "Experimental investigation of Shellac wax as potential Bio-based phase change material for medium temperature thermal energy storage applications." *Solar Energy,* 231(2022):1002-1014. SCI Index IF=5.7.

5. Rudra Murthy B.V., Kottayat Nidhul and Veershetty Gumtapure "Performance evaluation of novel tapered shell and tube cascaded latent heat thermal energy storage." *Solar Energy*, 214(2021): 116087. SCI Index IF=5.7.

International Conferences

1. Rudra Murthy B.V. and Veershetty Gumtapure "Thermal Analysis of Bio-Phase Change Material for Latent Heat Thermal Energy Storage Application in Processing Industries", International Symposium on Advanced Materials for Industrial and Societal Applications (NMD-ATM 2019), Indian Institute of metals (IIM), Kovalam Thiruvananthapuram, India, Nov 13-16, 2019.

BIO-DATA

NAME: RUDRA MURTHY B.V.

DATE OF BIRTH: 15-11-1984

Mobile No.: +91-7829760803

Email: rudra.royalmech@gmail.com

Address:

Bettadasathenahally Village, Holenarasipura Taluk

Hassan District, Karnataka-573211

EDUCATIONAL QUALIFICATION:

Examination	Board/Institute	Academic Year	Percentage/ CGPA
Ph.D. (Course work)	National Institute of Technology Karnataka, Surathkal	2016-2017	8.25
M.Tech (Thermal Science and Engineering)	University Visvesvaraya College of Engineering, Bangalore	2010-2012	87.5
B.E. (Mechanical Engg.)	Visvesvaraya Technological University, Belgaum	2002-2006	62.8

PROFESSIONAL EXPERIENCE:

Name of the company/Institute	Designation	From	To
Hindustan Aeronautics Limited (HAL), Aerospace Division, Bangalore	Contract Engineer	August 2006	August 2007
K.V.G. College of Engineering, Sullia	Assistant Professor	October 2007	May 2016